Universitat Autònoma de Barcelona

Epitaxial growth of (001)-oriented anatase films on ferroelectric buffer layers

Adrián Crespo Villanueva

Epitaxial growth of (001)-oriented anatase films on ferroelectric buffer layers

Adrián Crespo Villanueva

Doctoral thesis in Materials Science

September 2022

Supervisors

Dr. Xavier Torrelles Albareda, Dr. Francesco Carla and Dr. Felip Sandiumenge Ortiz

Academic Tutor

Dr. Xavier Torrelles Albareda

Advanced Structural and Functional Characterization Group

Institut de Ciència de Materials de Barcelona (ICMAB-CSIC)

ICMAB
INSTITUT DE CIÈNCIA DE MATERIALS DE BARCELONA
EXCELENCIA SEVERO OCHOA

Dr. Xavier Torrelles Albareda, research scientist at the Institut de Ciència de Materials de Barcelona – Consejo Superior de Investigaciones Científicas, **Dr. Francesco Carla**, Principal Beamline Scientist at Diamond Light Source and **Dr. Felip Sandiumenge Ortiz**, research scientist at the Institut de Ciència de Materials de Barcelona – Consejo Superior de Investigaciones.

CERTIFY THAT

Adrián Crespo Villanueva has carried out under their direction the doctoral research entitled "Epitaxial growth of (001)-oriented anatase films on ferroelectric buffer layers". This work has been done within a PhD program in Materials Science at the department of chemistry of Universitat Autònoma de Barcelona.

For that record they sign this certificate. Bellaterra, September 2022.

Dr. Xavier Torrelles Albareda

Dr. Francesco Carla

Dr. Felip Sandiumenge Ortiz

Acknowledgments

I would like to express my gratitude to all who have been involved in this project and facilitated my research journey by their support.

First, I would like to thank my supervisors: Xavier Torrelles, Felip Sandiumenge and Francesco Carla, for your pertinent guidance, support and continuous encouragement needed to accomplish this thesis. In particular, I thank Xavier Torrelles for giving me the opportunity to do this thesis.

I would like to acknowledge the support of other participators and collaborators in my work. To start with Jose Manuel Caicedo Roque, José Santiso and Jessica Padilla for the training in the PLD technique and for the assistance with the growth and characterization of my samples. Also, to David Serrate from Universidad de Zaragoza for his patience during the PFM measurements. I extend my gratitude towards all research group members and research collaborators at Diamond Light Source. I thank Philip Mousley, Jonathan Rawle and Hadeel Hussain.

I am deeply thankful to Greg Cabailh, Maurizio de Santis Veronique Langlais, it was always a great pleasure to work and discuss with you. You turned the beamtimes into a much easier and even funnier experience.

I would also like to thank the support of and help of the technical services staff. Thanks to the technical staff of the AFM service Maite Simón and Andrés Gomez. To Belén Ballesteros and Francisco Belarre for their assistance with the TEM measurements. To Ana Esther and Marcos Rosado for her assistance with the SEM. I thank also to Gustau Català for the ferroelectric measurements.

I am grateful for the friendships I have made through ICMAB! Special thanks to everyone for the good moments we shared together and the endless support. I also would like to express my gratitude to all my friends Ana, Arnau, Bea, Carmen, Christian, Darla, Laura, Mel, Meryem, Mónica, Niki, Sergi, Valeria, Virginia and so many more... Thank you all!

Finally, huge thanks go to my family for their encouragement, patience throughout the doctoral project.

Financial Support

I also like to acknowledge the financial support by the Spanish Government (Project numbers: RTI2018-098537-B-C21 and CEX2019-000917-S, SEV-2015-0496 founded by MCIN) and the EFA194/16/TNSI funded by Interreg POCTEFA Program.

Resumen

El óxido de titanio es interesante, entre otras cosas, para la conversión fotovoltaica de la luz en electricidad. Las dos superficies más estudiadas del TiO_2 son el rutilo (110) y la anatasa (101). El rutilo es la superficie más estable termodinámicamente a altas temperaturas, mientras que la anatasa es la más estable a temperatura ambiente, así como la más fotoactiva. Sin embargo, actualmente la anatasa-TiO_2 (001) promete una mayor actividad fotocatalítica que la anatasa-TiO_2(101), debido al mayor número de sitios activos de Ti en la superficie de la anatasa (001). Por otra parte, se sabe que la presencia de iones Ti^{3+} puede mejorar la actividad fotocatalítica al actuar como puntos de absorción de electrones, suprimiendo finalmente la recombinación. Estos iones se forman normalmente por la reducción de iones Ti^4 a Ti^{3+} debido a la formación de vacantes de oxígeno.

En este trabajo crecemos películas de anatasa orientadas (001) mediante deposición de láser pulsado sobre $SrTiO_3$(001) para investigar las propiedades estructurales y electrónicas de estas superficies. El análisis de los patrones LEED indica el desarrollo de una reconstrucción superficial (4x1)/(1x4), que es una manifestación de la deficiencia de oxígeno. La difracción de rayos X indica que sólo se obtiene la orientación cristalina de la anatasa (001). La topografía de la superficie de las películas de anatasa puede ajustarse en función de la temperatura, como se observa en las mediciones de AFM. Además, el AFM muestra que la dimensión lateral de los dominios ordenados se extiende hasta el rango de 100-200nm. Además, se muestra un trabajo preliminar de TiO_2 depositado sobre heteroestructuras ferroeléctricas $BaTiO_3/SrTiO_3$ con el objetivo final de investigar el acoplamiento entre la ferroelectricidad y la eficiencia fotocatalítica.

Además, se investigaron las condiciones de deposición de las perovskitas ferroeléctricas $BaTiO_3$ y $BiFeO_3$. Las películas de BTO crecieron (001) orientadas con superficies lisas y diferentes relaciones *c*/*a* dependiendo de las condiciones de crecimiento. Por otro lado, pequeñas variaciones en la temperatura provocan cambios notables en la morfología superficial y la estequiometría de las películas delgadas de BFO.

Summary

Titania is of interest among others for the photovoltaic conversion of light to electricity. The two most studied surfaces of TiO_2 are the rutile (110) and the anatase (101). Rutile provides the most thermodynamically stable surface at higher temperatures, whereas anatase is the most stable one at room temperature as well as the most photoactive. However, currently anatase-TiO_2 (001) holds promises of greater photocatalytic activity than anatase-TiO_2(101), as the anatase (001) surface has the higher number of Ti active sites. On the other hand, it is known that the presence of Ti^{3+} ions may improve the photocatalytic activity by acting as electron hole traps eventually suppressing the recombination. These ions are formed by the reduction of Ti^{4+} ions to Ti^{3+} due to the formation of oxygen vacancies.

In this work we grow (001)-oriented anatase films by Pulsed Laser Deposition on $SrTiO_3$(001) to investigate the structural and electronic properties of these surfaces. The analysis of LEED patterns indicates the development of a (4x1)/(1x4) surface reconstruction, which is a manifestation of oxygen deficiency. X-Ray diffraction indicates that only the anatase (001) crystal orientation is obtained. The surface topography of anatase films can be tuned as function of temperature as observed from AFM measurements. Moreover, AFM shows that the lateral dimension of the ordered domains extends up to the 100-200nm range. Additionally, a preliminary work of titania deposited on ferroelectric $BaTiO_3/SrTiO_3$ heterostructures is shown with the final aim of investigating the coupling between the ferroelectricity and the photocatalytic efficiency.

Furthermore, the deposition conditions of the ferroelectric perovskites $BaTiO_3$ and $BiFeO_3$ were investigated. BTO films grew (001) oriented with smooth surfaces and different *c*/*a* ratios depending on the growth conditions. On the other hand, small variations in temperature results in notable changes in the surface morphology and stoichiometry of BFO thin films.

Objectives

The study of the structural and electronic properties of TiO_2 surfaces, among them anatase (001), needs highly crystalline samples suitable for advanced surface characterization techniques such as diffraction and photoemission techniques under operando conditions. The main objective of this project is to gain an in-depth understanding of the growth process of anatase (001) thin films to produce high quality films to be used as model systems to study their properties. Another objective would be the study of its heteroepitaxy with ferroelectric (FE) films, with the intention of improving the photocatalytic response of anatase (001) surfaces. To this end, two different ferroelectric materials: $BaTiO_3$ and $BiFeO_3$ were selected.

The tasks of this thesis can be summarized as follows:

- Preparation of high quality TiO_2-anatase (001) oriented thin films to be used as models for the investigation of the photocatalytic water splitting reaction that occurs at its surface. The study of the structural and electronic properties of those titania films.

- Optimization of $BaTiO_3$ and $BiFeO_3$ ferroelectric thin films growth conditions for the preparation of TiO_2/FE heterostructures.

Contents

List of figures

List of tables

1. Introduction

1.1. Motivation

The increase in population linked with the improvement of lifestyle standard is demanding more energy consumption. Nowadays, fossil fuels still play a dominant role in global energy systems leading to the emission of greenhouse gases such as carbon dioxide related with the climate change problem. Many renewable energy sources are available including geothermal, wind, hydropower and solar that can be considered as alternatives to fossil fuels consumption, but each of them has limitations which just make them a possibility under certain conditions. The expected gradual reduction of fossil fuel reserves combined with its serious impact for the environment have accentuated the urge to develop new sustainable energy sources for the human society.

Hydrogen could be a possible alternative to conventional fossil fuels because of its non-contaminant emissions and its possible application for fuel cells. However, in the present days around the 90% of hydrogen is produced from fuel fossil energies. Therefore, a renewable method to obtain hydrogen must be investigated. Among all the possible new ways of producing hydrogen for energy proposes solar photocatalytic water splitting (PWS) arises as a promising way to produce hydrogen[1,2].

Research on tunable catalysts[3–5] and methods of controlling the activity of catalyst constitutes a breakthrough research field in the PWS area. These new families of catalysts are expected to have a high impact on the design and improvement of materials properties leading to energy alternatives that could compete with existing technologies. This work could be framed as a first step towards achieving these objectives.

1.2. Photocatalysis

The main contribution of this work to this field focuses on the synthesis and study of the structural and electronic properties of highly active TiO_2 surface electrodes for their possible applications as photocatalyst on photocatalytic water splitting (PWS) processes.

1.2.1. Principles of photocatalysis

Catalysis is the process of increasing in the rate of a chemical reaction by the addition of a reagent, the catalyst, that is not itself consumed and decreases the free enthalpy of the reaction. Thus, photocatalysis is the initiation or change in the rate of a chemical reaction, under the action of UV, visible or IR light in the presence of a material called photocatalyst[6,7].

Heterogeneous photocatalysis starts when a semiconductor is in contact with the reactant and then it is irradiated by light of the suitable energy ($E \geq E_g$), which excite electrons and promote them from the valence band (VB) to the conduction band (CB) generating an electron-hole pair (*Figure 1.1*).

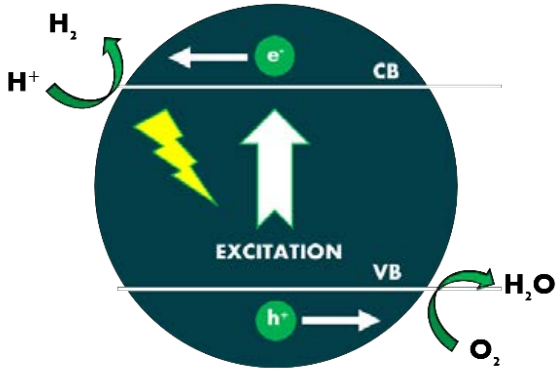

Figure 1.1: Principle of water splitting using semiconductor photocatalysts.

These photocarriers can recombine again when electrons return to its original energetic level through a non-radiative transition and the photon energy is lost as heat. But if the electron-hole pair diffuse through the catalyst and reach its surface they may react with the adsorbed species and start the chemical transformations through interfacial charge transfer reactions.

The overall quantum yield is the parameter used to evaluate the photocatalytic activity of a material[8] and it can be defined by *Equation 1.1*:

$$Quantum\ yield\ (\%) = \frac{Number\ of\ reacted\ electrons}{Number\ of\ absorbed\ photons} \times 100 \qquad (1.\ 1)$$

For the overall water splitting case, the photogenerated electrons reduce water to form hydrogen and the holes oxidize water molecules to give oxygen[9,10]:

$$H_2O + 2h^+ \rightarrow 2H^+ + \frac{1}{2}O_2 \qquad E^0_{oxidation} = -1.23\ eV \qquad (1.\ 2)$$

$$2H^+ + 2e^- \rightarrow H_2 \qquad E^0_{reduction} = 0\ eV \qquad (1.\ 3)$$

The position of the CB and VB, in a semiconductor (SC) photocatalyst, is a crucial point for the reaction to start. The bottom level of the CB must be more negative than the hydrogen redox potential, while the highest level of the VB must be more positive than H_2O oxidation level. Therefore, the minimum bandgap that a SC must have to be appropriate for water splitting is 1.23 eV [11]. Some suitable photocatalysts are shown in *Figure 1.2*.

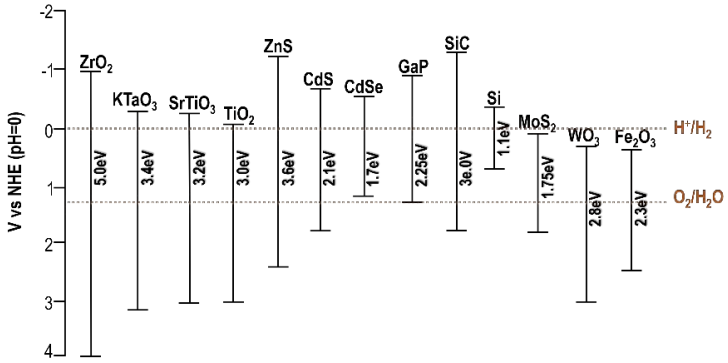

Figure 1.2: Relationship between band structure of semiconductors and redox potentials of water splitting.

For TiO_2 the energy needed to start the PWS requires UV light (λ≤ 388nm) to obtain photogenerated charge carriers (*Eq. 1.4*)

$$TiO_2 \xrightarrow{h\vartheta} h._{VB}^{+} + e_{CB}^{-} \qquad (1.4)$$

Those species can work as electron donors (D) or acceptors (A). The holes react with electron donor species oxidizing them, while the CB electrons are involved in the reduction of electron accepting molecules.

In the case of the water splitting, as it takes place in aqueous environment, holes can oxidize OH^- or water molecules to produce ·OH radicals (*Eq. 1.5*), which are extremely oxidizing agents (E^0=-2.8V)[12].

$$OH^- + h._{VB}^{+} \rightarrow \cdot OH \qquad (1.5)$$

·OH radicals can participate in oxidant reactions with D present in the electrolyte (*Eq. 1.6*). Also, electrons in the conduction band can be trapped by molecular oxygen adsorbed in the TiO_2 (*Eq. 1.7*), which is reduced to generate superoxide radical anions (*Eq. 1.8*). This anion can continue reacting with H^+ to produce hydroperoxyl radicals, which further electrochemical reduction produce hydrogen peroxide (*Eq. 1.9*).

$$\cdot OH + D_{aq} \rightarrow D_{aq}^{+} + OH^- \qquad (1.6)$$

$$O_{2+}e_{CB}^{-} \rightarrow O_2^{\cdot -} \qquad (1.7)$$

$$O_2^{\cdot -} + H^+ \rightarrow \cdot OOH \qquad (1.8)$$

$$\cdot OOH + \cdot OOH \rightarrow H_2O_2 + O_2 \qquad (1.9)$$

The energies of the HOMO and LUMO levels of the reactant molecules and their relative's position to the redox potential of the reaction determines the suitability of a catalyst for a specific reaction[8,12,13].

Additionally, the photocatalytic processes can be tuned by employing electrochemical methods. This process is known as photoelectrochemistry (PEC). PEC is based on the combination of a photoactive catalyst with electrochemistry. The possibility to apply an external potential improves the efficiency of charge separation by driving the photogenerated charge carriers away from the surface. PEC also gives the opportunity to measure properties such as the kinetics of electron and hole transfer, among others. The principals involved in PEC are the same as for photochemical systems, but with a different set-up (*Figure 1.3*). In PEC water splitting overall reaction takes place at two different electrodes, while in photochemical reactions, there is a semiconductor-electrolyte junction at which the water splitting reaction takes place[14].

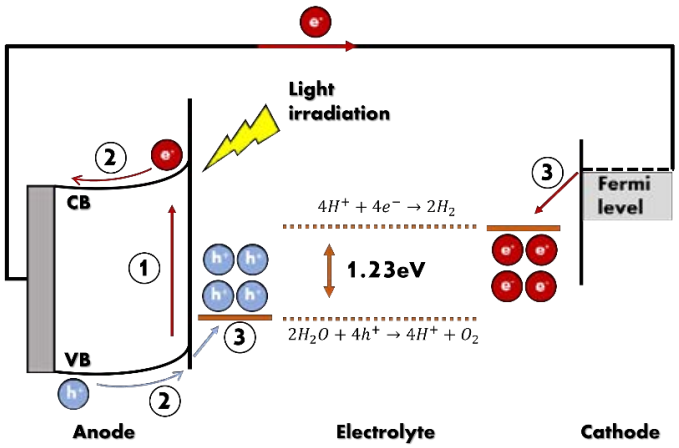

Figure 1.3: Schematic representation of the PEC WS process in a common PEC WS system consisting of a photoanode and a metal counterpart. (1) Absorption of radiation by the photoelectrode and charge carrier generation, (2) Separation and transport of charge carriers to the electrode surface, (3) Oxidation of water at the anode and H^+ reduction at the cathode.

As mentioned above, the rapid recombination of the photogenerated charge carriers on the photocatalysts is one of the limiting factors of PC. To solve that problem the effect of the spontaneous polarization of ferroelectric materials has emerged as an effective strategy to increase the life time of the charge carriers enhancing the photocatalytic activity[15]. Also, crystallinity affect the recombination probability, as defects can act as trapping and recombination centres for the photogenerated charge carriers[14].

1.2.2. Titanium dioxide

There is a high number of semiconductors with photocatalytic properties such as metal oxides (e.g. ZnO, WO_3)[16,17], metal sulphides (e.g CdS) or selenides (e.g. CdSe)[18,19]. Among them TiO_2 appears as an attractive photocatalyst because is abundant, cheap, it has good stability to photocorrosion, it is non-toxic and more importantly it shows high photocatalytic activity [20–23].

TiO_2 is an oxide that has three different polymorphs: (a) rutile, (b) anatase and (c) brookite illustrated in *Figure 1.4*. The different lattice parameters and the bandgap of the different polymorphs is summarized in *Table 1.1*. All the polymorphs are constituted by the same TiO_6 octahedra building block, where each titanium atom is coordinated to six oxygen atoms (TiO_6). The crystal structures differ by the distortion of the octahedral and by the assembly patterns of the octahedral chains. In rutile the octahedral are connected by

the edges, while in anatase the TiO_6 are connected by their vertices and in brookite, both vertices and edges are connected[24].

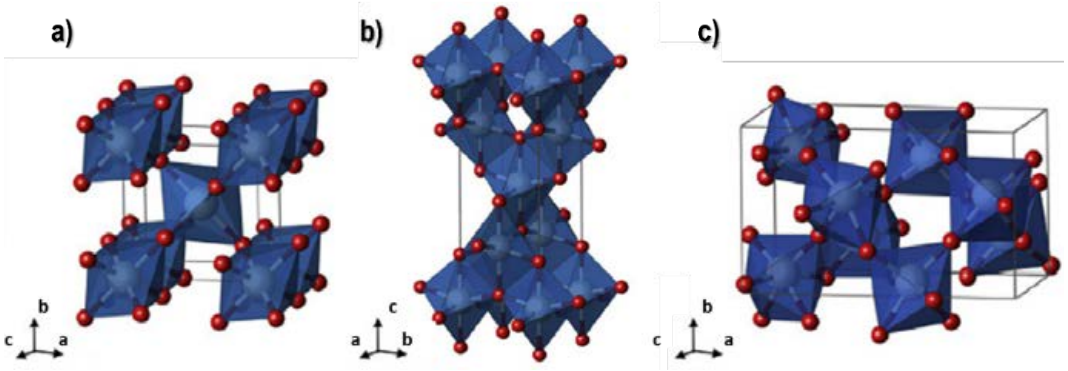

Figure 1.4:Titanium dioxide polymorphs. (a) rutile, (b) anatase, (c) brookite. The small red spheres represent the oxygen atoms, the big grey ones are the titanium atoms, while the blue polyhedral shapes show the orientation in space of the TiO_6 octahedra.

Phase	Crystal Structure	*a* (Å)	*b* (Å)	*c* (Å)	Bandgap energy (eV)
Rutile	Tetragonal	4.59	4.59	2.96	3.0
Anatase	Tetragonal	3.78	3.78	9.51	3.2
Brookite	Orthorhombic	9.16	5.43	5.13	3.26

Table 1.1 Crystal structure, lattice parameters and bandgap energy of the different TiO_2 polymorphs.

These polymorphs have different photocatalytic behaviors. Anatase and rutile are commonly used as photocatalysts since brookite is relatively unstudied due to the complexity of obtaining enough amount to perform photocatalytic studies. However, anatase is considered to have the best photocatalytic properties[25]. Luttret et al[26] evaluated the photocatalytic activity of TiO_2 samples (anatase and rutile) by decomposition of an organic dye and reported a greater photocatalytic activity to the anatase films due to its higher bandgap, the presence of an indirect bandgap and to the fact that anatase reaches its maximum photoactivity with a thickness of 5nm indicating that charge carriers can originate from much deeper in the bulk increasing the photocatalytic activity of the anatase. Additionally, to these results Kavan et al[27] presented a work done by electrochemical impedance showing that anatase has a 0.2eV more negative flatband potential leading to a better matching of the LUMO level of molecular oxygen which could increase the photoreactivity. Moreover, it has been reported that mixtures of anatase and rutile express higher photocatalytic activity than each of them separately[28,29].

Furthermore, the photocatalytic activity of anatase is related to the facet exposed to the reaction (*Figure 1.5*). These variations are associated to three different elements, (a) each facet has a distinctive band structure, which regulates the separation efficiency of the photogenerated charge carriers[30], (b) the preferential transport direction of those carriers depending on the facet structure is a crucial factor in photocatalysis[25,31,32] and (c) depending on the photocatalytic reaction one facet can work better than another[33–35].

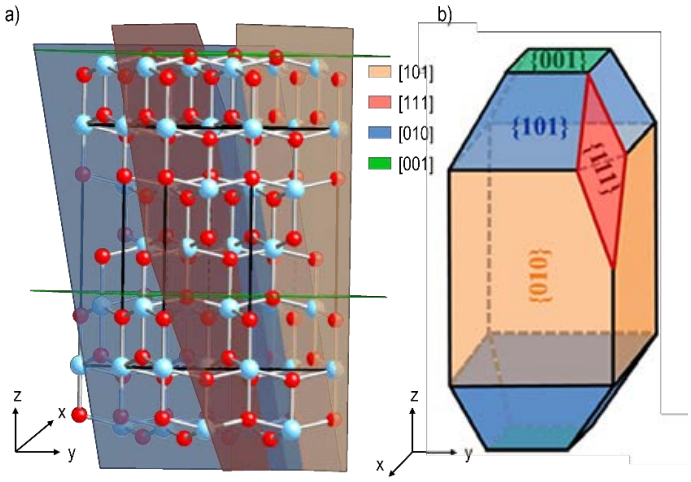

Figure 1.5:Schematic illustration of (101), (010), (001)] and (111) facets of anatase: (a) molecular simulation model, (b) crystal mode.

However, TiO_2, in all phases, has two main disadvantages. Firstly, the fast recombination of the charge carriers decreases the photocatalytic time activity. Secondly, its bandgap around ~3-3.2 eV only permits titania to absorb the UV portion of the spectrum, which corresponds to the 5% of all the solar spectrum[36]. These limitations have motivated investigations to modify the absorption edge of titania and techniques to prevent the fast recombination of the electron-hole pairs generated during the photoreaction[30,37].

1.3. Thin films and heterostructures

The study of surfaces and interfaces is one of the most interesting topics because is where critical processes such as catalysis or corrosion happen. Therefore, thin film growth arises as crucial for their capability to be used to study structure-properties relations in a more controlled manner. Although crystals have a regular structure, surface atoms are arranged differently from bulk atoms (e.g., lower coordination or different chemical environment) leading to new properties. Thus, to comprehend the evolution of any surface process the surface structure and chemistry must be known. However, film's structure commonly has less quality than single crystals, which could limit their use as model systems to study material's properties. For that reason, the efforts are pointing to the preparation of high quality epitaxial thin films.

Epitaxial growth

Epitaxy refers to the oriented growth of a crystalline material on the top of a single crystal substrate. The orientation is described by the Miller indices. Epitaxial growth can be classified in (a) homoepitaxy when the film grown is identical to that of the substrate and (b) heteroepitaxy when they are different. In heteroepitaxial growth a mismatch between the substrate's lattice and the grown film lattice can be defined as:

$$f = \frac{a_{substrate} - a_{film\ bulk}}{a_{film\ bulk}} \qquad (1.\ 10)$$

Where $a_{film\ bulk}$ and $a_{substrate}$ are the in-plane lattice constants of the deposited material and the substrate, respectively[38]. This mismatch leads to bi-axial stress on the film, which ideally deforms elastically and grows matching the substrate's lattice parameters. The deformation of the a_{film} compared to its $a_{film\ bulk}$ is described by:

$$\varepsilon = \frac{a_{film} - a_{film\ bulk}}{a_{film\ bulk}} \qquad (1.\ 11)$$

In the present days, the high quality of epitaxial thin films allows the study of the electronic and structural properties of materials. Moreover, the combination of different materials in heteroepitaxial structures gives us the opportunity to find a whole new set of properties[39–41].

1.3.1. Perovskites

The perovskite structure refers to the mineral $CaTiO_3$. The structure of a perovskite is characterized by the formula ABO_3 with a cubic structure (*Pm-3m*), where A is occupied by a divalent or trivalent cation and B is a trivalent or tetravalent cation (*Figure 1.6*). In the unit cell, A cations are located at the corners of the cube while the B ions are in the center of the unit cell surrounded by an octahedron of oxygen ions[42] . However, the cubic structure of the ideal perovskite structure can be affected by the variation of the cationic ionic radius and by ion displacements with respect to the oxygen sublattice, which leads to a diminution in the unit cell symmetries such as tetragonal, orthorhombic, monoclinic, or rhombohedral that can influence the electric and magnetic properties[43]

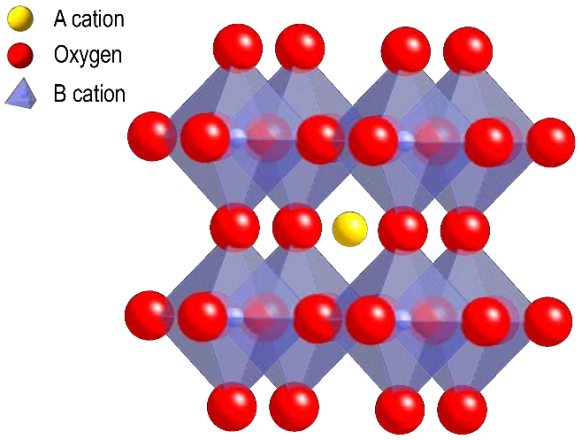

Figure 1.6: Scheme of a typical perovskite structure.

The perovskites used in the framework of this project will be briefly defined:

Strontium Titanate ($SrTiO_3$)

$SrTiO_3$ (STO) crystal is a perovskite (*Pm-3m*) with a lattice parameter of 3.905Å. The Ti^{4+} ions are surrounded by six O^{2-} ions, while the Sr^{2+} ions are surrounded by four TiO_6 octahedra and have 12-fold cuboctahedral coordination. For the (100) planar direction, the STO surface displays two different

terminations. One arranged with alternating layers of TiO_2 planes and another one by alternating SrO plane, since STO is formed by an alternating stacking of these two atomic planes[44]. On the other hand, STO (111) contains stacking of two hexagonal surface structures of SrO_3^{4-} and Ti^{4+} (*Figure 1.7*). The perfect epitaxial growth of TiO_2 on STO substrates would be on a TiO_2 terminated STO as the anatase is also composed by a vertical stack of alternating TiO_2 planes[45].

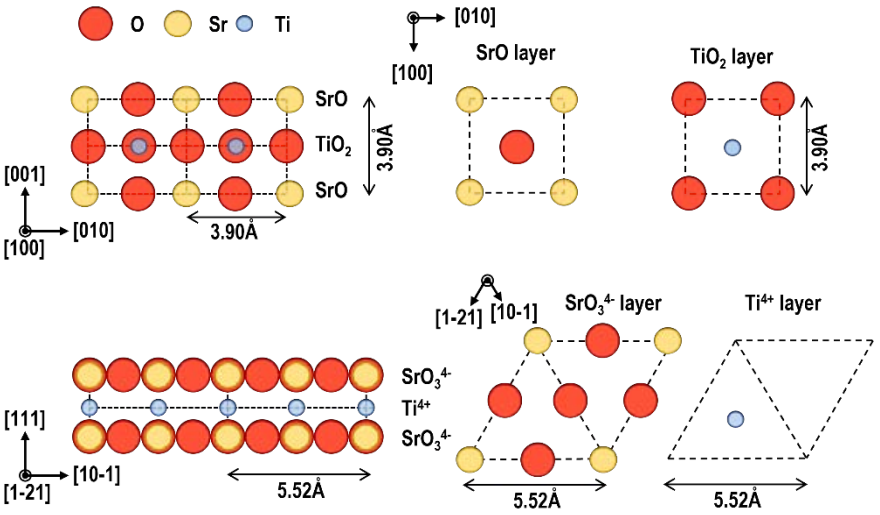

Figure 1.7: Schematic representation of cross-sectional crystal structures (left panel) and two possible ideal termination layers (right panel) from a crystallographic point of view for [001] and [111] orientated $SrTiO_3$ substrates. Figure adapted from A. Biswas et al. Appl. Phys. Lett. 98, 051904 (2011)[46]

STO was chosen as the substrate material for its chemical and compositional stability and for its lattice parameter similar to those of the perovskite's oxides selected in this project. The [100] and [111] orientations were picked to promote the growth of high epitaxy thin films as the mismatch between the desired materials and the STO is small resulting in a compressive mismatch promoting the out of plane parameter expansion enhancing the polarization in that direction.

Barium Titanate ($BaTiO_3$)

$BaTiO_3$ (BTO) is one of the most studied ferroelectrics perovskites oxides due to its interesting properties such as high critical temperature ($T_C \approx 120$ºC), high dielectric constant[47] and its spontaneous polarization ($26\mu C/cm^2$)[48]. BTO thin films have many applications such as non-volatile memories[49], optical modulators[50] and photoelectrochemical cells[51,52]. Above its T_C BTO presents a cubic phase (a=4.01Å), but below T_C BTO passes through certain phase transitions (*Figure 1.8*). The most relevant phase, for this project, is the transition from cubic to tetragonal where the *c*-axis suffers an elongation by a displacement of the Ti^{4+} from the unit cell's center (see inset *Figure 1.8*). This new symmetry can be induced by substrate strain engineering to obtain a remanent polarization (P_r) around 250% higher than bulk $BaTiO_3$[53].Two more transitions occur by reducing the temperature from tetragonal to orthorhombic below 0ºC and from orthorhombic to rhombohedral below -90ºC[43,54].

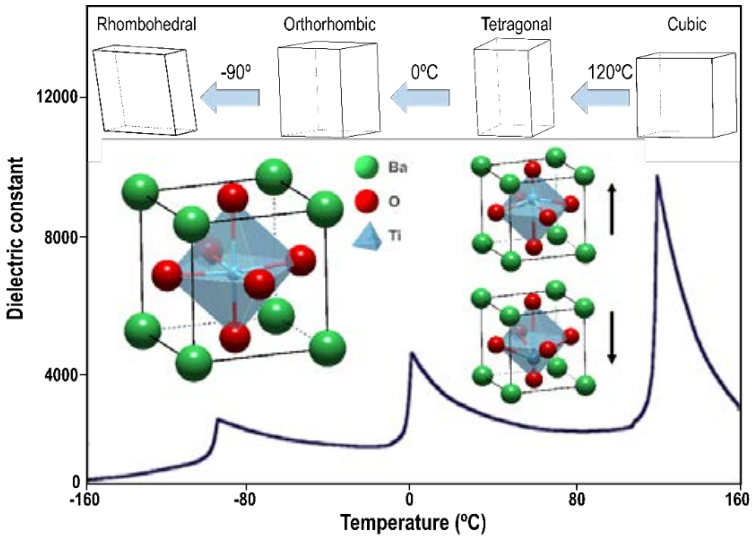

Figure 1.8: Temperature phase diagram of BTO including the transition from cubic to tetragonal, to orthorhombic and to rhombohedral. The insets show BTO in cubic structure and the tetragonal structures for up and down polarization (indicated by a black arrow). The displacements are over dimensioned for better visualization.

Bismuth ferrite ($BiFeO_3$)

$BiFeO_3$ (BFO) is one of the most studied multiferroics and most promising lead-free piezoelectric materials which displays multiferroic behavior at room temperature[55,56]. Multiferroic materials exhibit ferroelectric or anti-ferroelectric properties in combination with ferromagnetic or anti-ferromagnetic properties. Bulk BFO has rhombohedral symmetry (*R3c*) with a pseudocubic cell parameter of 3.96Å and an 89.4° rhombohedral angle (*Figure 1.9*). The polarization vector of BFO follows the [111] direction of the perovskite structure with high saturation polarization ($P_s \approx 90 \mu C/cm^2$)[57,58]. However, ferroelectric thin films can suffer polarization fatigue[59], which will result in losing the control of its properties. As published by Baek et. Al. [60], along the [111] direction BFO suffers a decrease of the polarization from ~115 $\mu C/cm^2$ to ~57 $\mu C/cm^2$ after 10^6 P-E cycles, while on the [100] direction it remains constant at approximately 55 $\mu C/cm^2$. Thus, BFO will be grown on (111) and (100) STO oriented. The ferroelectric properties of BTO and BFO films are related to the strain: [61–64], doping[65,66] , vacancies[67] or the growth conditions.

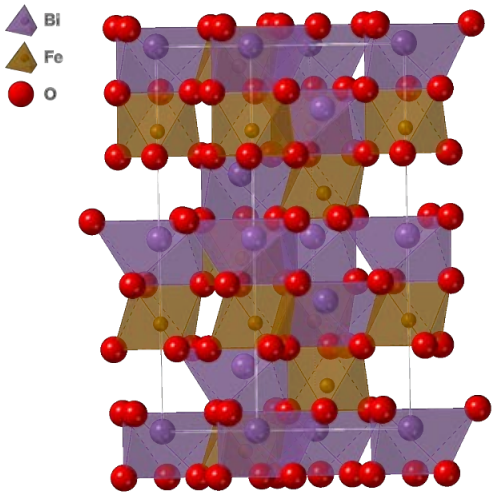

Figure 1 9: BFO schematic structure.

2. Experimental techniques

In this chapter an overview of the experimental setups and techniques for sample preparation and characterization used during this PhD are described. It will be divided in three parts. The first one is devoted to the preparation techniques employed to prepare the samples as well as the in-situ equipment's of the used set-ups. The second part is related to the conventional characterization techniques carried out at laboratory facilities. Finally, the two main experimental techniques employed in synchrotron facilities: Surface X-ray Diffraction (SXD) and X-ray Photoemission Spectroscopy (XPS) are explained followed by a brief description of the beamlines employed for those experiments.

2.1. Preparation techniques

This section is focused on the two main techniques used to prepare the thin films as well as the equipment available in the set-ups of those techniques. Thin films presented in this work have been mainly grown by Pulsed Laser Deposition (PLD). The PLD set-up used is located at the Institut Català de Nanociència y Nanotecnologia (ICN2) and was manufactured by SURFACE systems+technology GmbH&Co.KG. This chamber allows in-situ monitoring of thin films deposition with reflection high-energy electron diffraction (RHEED) technique. TiO_2 films in the nanometric range were grown at the Néel Institute by Molecular Beam Epitaxy (MBE) using a UHV set-up composed by a preparation chamber coupled to an analysis chamber. The latter is equipped with a commercial scanning tunnelling microscope (Omicron VT STM/AFM), a low-energy electron diffractometer (LEED) and an Auger electron spectrometer (AES).

2.1.1. Pulsed Laser Deposition

PLD is a physical vapor deposition technique (PVD) consisting of a high-energy pulsed excimer laser used to vaporize a target material to prepare thin films. *Figure 2.*1 illustrates a typical PLD set-up and the PLD employed in this thesis. The laser beam is driven into a vacuum chamber and focused on a target. After laser exposure, the target material vaporizes into a plasma plume that condenses onto a substrate, stuck in a holder with silver paint, to form a thin film.

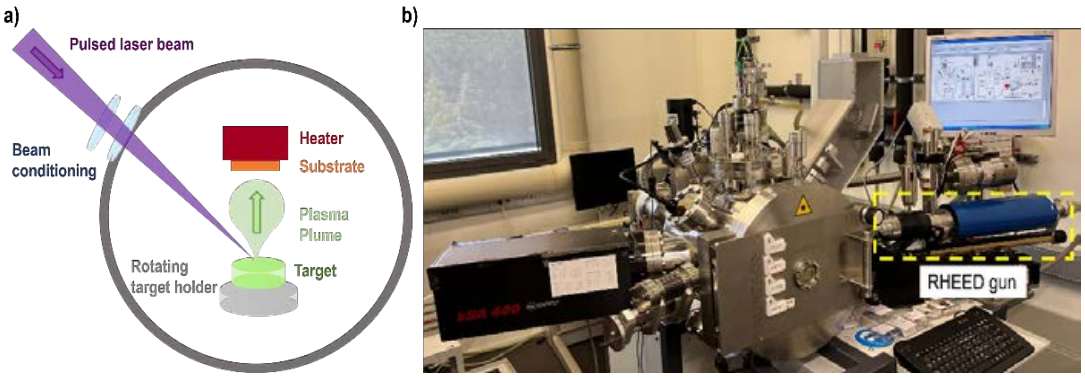

Figure 2.1:(a) general sketch of a PLD set-up and (b) picture of the PLD used in the ICN2.

Before deposition, the vacuum chamber is pumped to the base pressure (~10^{-4} mTorr). The target is rotated and toggled to preserve a homogeneous surface. To maintain constant the target conditions for all depositions an ablation of it is done before each deposition, while protecting the substrate to avoid the plasma plume to reach its surface. The PLD process can be summarized in four stages. The first stage implies photon absorption at the target surface. During this stage, temperature around the target's focused area increases up to thousands of Kelvins leading to the second stage where a thin surface layer of the target material vaporizes and forms a plasma plume, which expands perpendicularly to the surface. The third stage involves the plasma plume expansion until it reaches the substrate's surface. The last stage corresponds to the thin film growth and starts when the material of the plume arrives at the substrate. These processes are strongly conditioned by the laser parameters, substrate conditions and the background pressure.

The last stage of the PLD process can be initiated by three principal modes of thin film growth[68] illustrated in *Figure 2.2*:

a) Layer-by-layer (Frank van der Merwe): where one monolayer is finished before the new layer starts to grow giving rise to a 2D type growth
b) Island growth (Volmer-Weber): in that case the interaction between the coming ad-atoms is stronger than the interaction with the substrate consequently 3D islands nucleate and grow on the substrate.
c) Layer-plus-island (Stranski-Krastanov): such growth mode is a combination of the previous two. The process starts as a 2D growth where the film increases its elastic energy until it reaches a maximum. Then, the formation of the islands relaxes the film strain leading to a continuous film with discrete islands on the top.

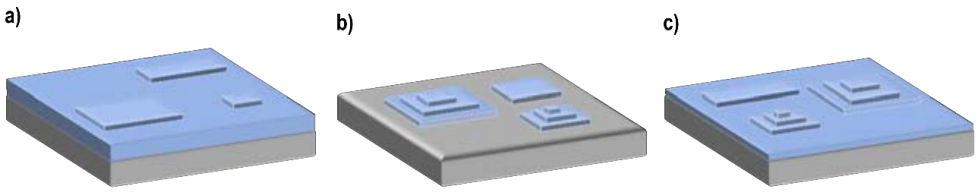

Figure 2.2 Different growth modes: (a) Layer-by-layer, (b) Island growth and (c) Layer-plus-island.

2.1.1.1. Reflection high-energy electron diffraction

RHEED is a technique for surface structural analysis of crystalline materials. The RHEED set-up consists of an electron beam source, of energy usually around 5-30 KeV, directed at a glancing angle (0-5º) on the sample surface inside a vacuum chamber. Diffracted electrons arrive to a phosphorescent screen giving rise to diffraction patterns as shown in *Figure 2.3a.* The spot's intensity of the reflected beam depends on the steps density on the surface. As the RHEED intensity is sensitive to film roughness, the growth process leads to characteristic intensity oscillation of the RHEED spots during the deposition, usually corresponding to the completion of a single monolayer (ML) (*Figure2.3b*).

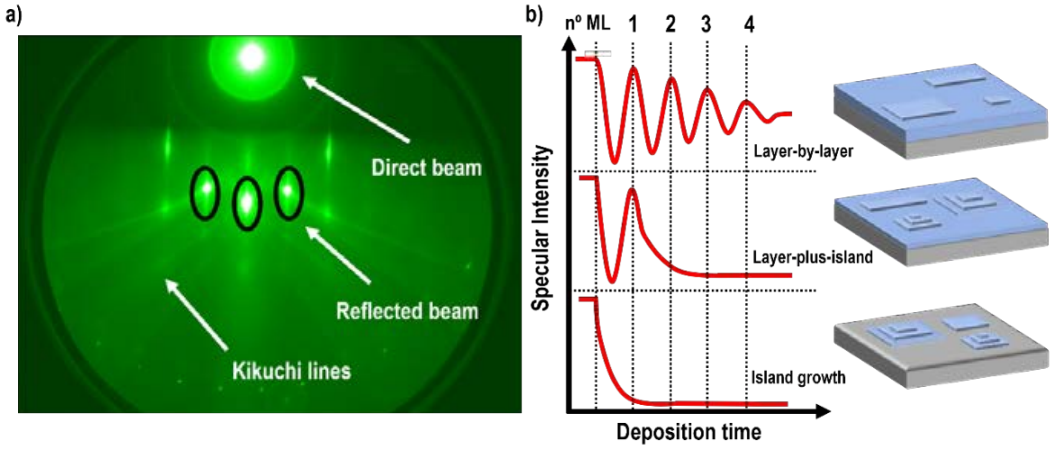

Figure 2.3: (a) Typical RHEED pattern of a bare STO substrate and (b) Characteristic RHEED intensity oscillations for each growth mode.

2.1.2. Molecular beam epitaxy

MBE is a PVD technique used to grow layer-by-layer monocrystalline thin films in an UHV environment by condensation of a molecular flux of the desired metal evaporated in an effusion cell (*Figure 2.4*). Differing from the PLD technique, MBE presents a slow deposition rate, calibrated measuring the variations of the resonance frequency of a quartz crystal balance, caused by the metal deposition on it[69].Thus, UHV conditions must be acquired to avoid impurities, as well as preventing gas phase collisions of the molecules heading the substrate. If the metal evaporation occurs in a properly oxygen environment metallic oxides are obtained by reactive deposition.

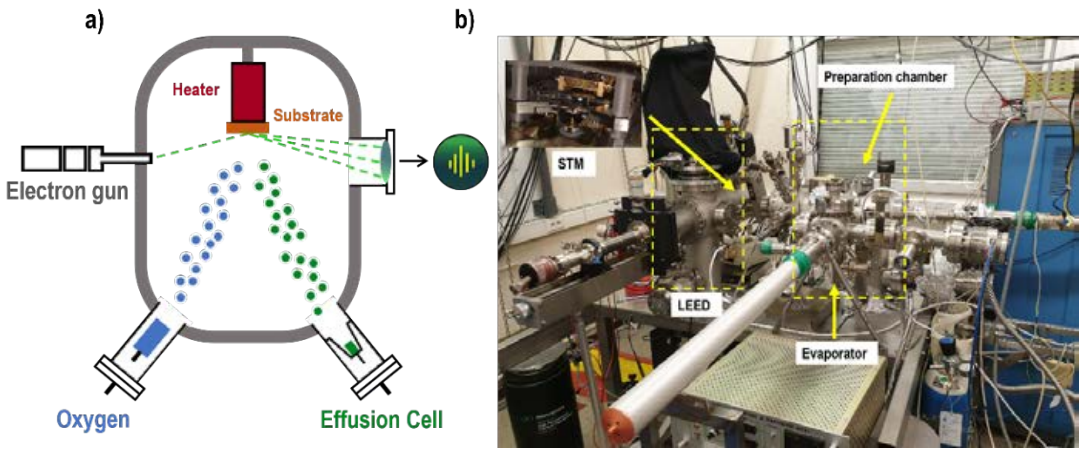

Figure 2. 4: (a) Scheme of an MBE set-up adapted from Nunn, W et.al., Journal of Materials Research 36, 4846–4864 (2021)[70] *and (b) picture of the used MBE at the Néel Institute.*

2.1.2.1. Low Energy Electron Diffraction

Low energy electron diffraction (LEED) is a surface sensitive characterization technique that provides information about the crystallographic quality and structure of the deposited films such as the atomic symmetry or the arrangement of the unit cell. Electrons produced at an electron gun are sent to the sample's surface to diffract. Then, diffracted electrons arrive at a fluorescent screen to form the LEED pattern, which reflects the surface crystal structure of the material (*Figure 2.5*). For this project, LEED has been used to check the STO substrates quality as we as to study possible surface reconstructions of the TiO_2 deposited films.

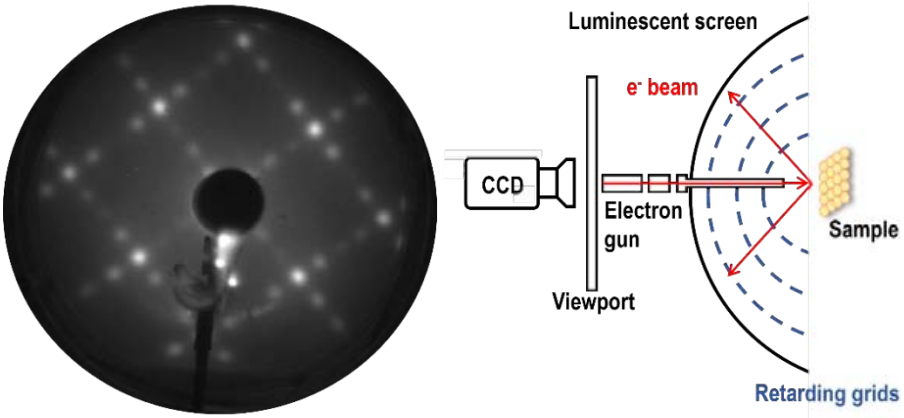

Figure 2.5: (a) *LEED pattern of a TiO_2/STO sample (b) Schematic of LEED apparatus: The Electron gun is directed towards the sample and the grids ensure only elastically scattered electrons to reach fluorescent screen.*

2.1.2.2. Auger electron spectroscopy

The principle of Auger electron spectroscopy (AES) is illustrated in *Figure 2.6*. Initially the electron beam hits the sample with enough energy to eject a core electron (1). The hole produced by the beam is then filled

by a secondary electron from a higher energy level (2). The energy gain is transferred to a tertiary electron, called Auger electron, that is ejected (3).

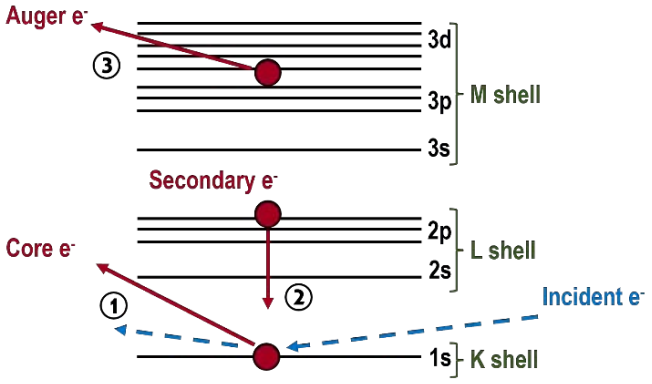

Figure 2.6: Schematic diagram of the Auger process.

The kinetic energy of the Auger electrons depends on the core-shell energy levels which is specific for each element, while the intensity of the peak depends on the quantity of the element present in on the sample. Thus, AES is used to identify elements present in the surface of the sample by the energy of the emitted electrons. AES was used to check the cleanliness of the substrates and the homogeneity of the coating after the film's deposition.

2.1.2.3. Scanning tunnelling microscopy

The scanning tunnelling microscope (STM) is a powerful tool for investigating the surface properties, mainly of metals and semiconductors, which provides real-space atomic resolution images of the surface topography. The working principle of STM is based on the quantum mechanical tunnelling effect where electrons can tunnel through a narrow potential barrier between an atomically sharp tip and preferably conductive sample while a voltage between them is applied (*Figure 2.7*).

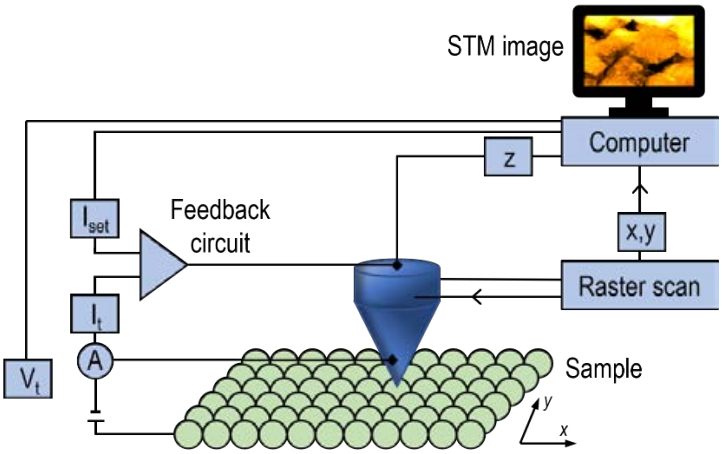

Figure 2.7:A schematic structure of the STM setup.

Equation 2.1 describes the tunnelling current (I):

$$I \propto U\, e^{-A\sqrt{\varphi d}} \qquad (2.\ 1)$$

Where *d* is the distance between the sample and the tip, U the applied voltage, A is a constant and φ the barrier height depending on the electronic structures of the tip and the sample. STM can work at constant height mode and constant current mode[71]. STM (Omicron VT STM/AFM) has been used to better understand the TiO_2 surface reconstruction.

2.2. Conventional characterization

This section is devoted to the techniques used to fully characterize the samples. The standard conventional techniques are those that usually equip laboratories to perform an initial assessment on the structural, electronic, magnetic, chemical etc. properties of the synthesized material. Some of these techniques used in this work are described in the subsections below.

2.2.1. X-Ray diffraction

Crystal structure

A crystal can be described as a periodical three-dimensional arrangement of atoms called crystal lattice. The unit cell describes the minimum set of elements which repeated generate the whole crystal lattice. Unit cell characteristics can be expressed with six lattice parameters: the three lengths of the cells edge and the angles between them (*a*, *b*, *c*, α, β, and γ) as illustrated in *Figure 2.8*.

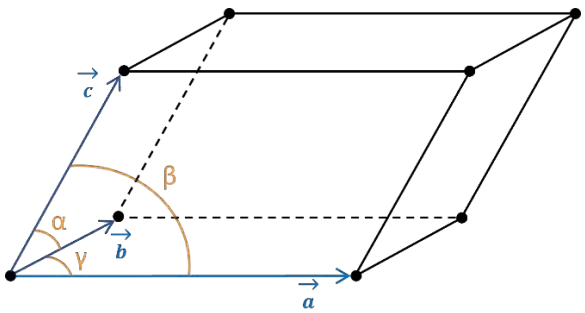

Figure 2.8: Unit cell definition with lengths a, b, c, and angles between the sides given by α, β, γ.

Crystals present symmetry transformations whereby microscopic (atoms, ions, molecules) elements (vertices, faces or edges of a polyhedral body) are made to coincide. The basic symmetry operations that lead to the repetition of any motif are translation, rotation, inversion, and rotation-inversion. There are 14 different possibilities of unit cells called Bravais lattices, where parallel planes separated by a distance (d-spacing) are described by three integers known as Miller Indices (h,k,l)

Diffraction is the process that happens when light is scattered by a periodic array producing constructive interference only at specific angles. The scattering of x-rays from crystal lattices gives rise to diffraction patterns, that contain valuable information about the arrangement within the crystal (structure and lattice parameters). X-ray diffraction (XRD) is based on Bragg's Law (*Equation 2.2*), where λ is the wavelength of

the X-ray beam, θ is the scattering angle, n is the diffraction order and d_{hkl} are the interplane distance of the atomic lattice with *hkl* Miller index.

$$2d_{hkl}\sin\theta = n\lambda \qquad (2.\ 2)$$

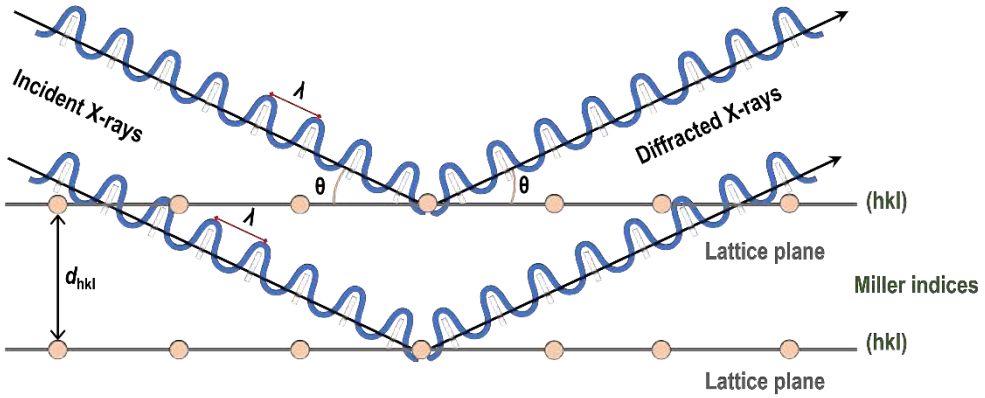

Figure 2.9: Scheme of x-ray diffraction.

The scattering amplitude of a crystal with N_1, N_2 and N_3 unit cells along three axes defined by the vector a_1, a_2, a_3 can be described by *Equation 2.3*:

$$A_q = A_0\left(\frac{e^2}{mc^2R_0}\right)F(q)\sum_{n_1=0}^{N_1-1}\sum_{n_2=0}^{N_2-1}\sum_{n_3=0}^{N_3-1}\exp\left(iq\cdot(n_1a_1+n_2a_2+n_3a_3)\right) \qquad (2.\ 3)$$

Where *e* and *m* are the electron's charge and mass, R_0 the distance to the observer, A_0 the amplitude of the oncoming wave, q is the momentum transfer and F_q the structure factor, which can be expressed by *Equation 2.4*:

$$F(hkl) = \sum_j e^{-\vec{G}_{hkl}\cdot\vec{R}_j}\cdot f_j^{hkl} \qquad (2.\ 4)$$

$\vec{G}_{hkl}$ is a reciprocal space vector, $\vec{R}_j$ corresponds to the base vector and f_j^{hkl} is the atomic dispersion factor. The N-slit interference function is defined in *Equation 2.5*:

$$S_N(x) = \sum_{n=0}^{N-1}\exp(ixn) = \frac{1-\exp(ixN)}{1-\exp(ix)} \qquad (2.\ 5)$$

Now the diffracted amplitude can be defined as a product of slit functions (*Equation 2.6*):

$$A_q = A_0\left(\frac{e^2}{mc^2R_0}\right)F(q)S_{N_1}(q\cdot a_1)S_{N_2}(q\cdot a_2)S_{N_3}(q\cdot a_3) \qquad (2.\ 6)$$

In large 3D structures the N-slit interference function tends in the limit to a periodic array of δ functions with 2π/a spacing. Thus, the maximum intensity reaches its maximum only along well-defined directions where the Laue equations are fulfilled simultaneously:

$$q \cdot a_1 = 2\pi h \qquad (2.\ 7)$$

$$q \cdot a_2 = 2\pi k \qquad (2.\ 8)$$

$$q \cdot a_3 = 2\pi l \qquad (2.\ 9)$$

Hence, the diffracted intensity is zero except at discrete points. The square of *Equation 2.6* gives us the equation for the intensity at h,k,l point as a function of the reciprocal lattice vectors (b_1,b_2,b_3):

$$I_{hkl} = \left| E_e \frac{e^2}{mc^2 R_0} F(hb_1 + kb_2 + lb_3) N_1 N_2 N_3 \right|^2 \qquad (2.\ 10)$$

To characterize thin films a MRD PANalytical X'PERT PRO located at the ICN2 was used. This equipment has a 4-circle goniometer which allows the identification of the different phases present in the thin films, the study of the lattice parameters and the epitaxial relationship between films.

2.2.2. Atomic force microscopy

Atomic force microscopy (AFM) is englobed inside scanning probe microscopies (SPM), and it is mainly used to obtain topographical information about samples surfaces. AFM is based on the scan of a sharp tip over the surface of a sample (*Figure 2.10a*), while sensing the interaction between them. Forces between the tip and the sample cause the cantilever to deflect, the tip is attracted by the sample at bigger distances and repelled at closer distances (*Figure 2.10b*). These interaction forces are measured by the deflection of the cantilever which is detected by a laser beam focused on the end of the cantilever and reflected into a photodetector[72,73].

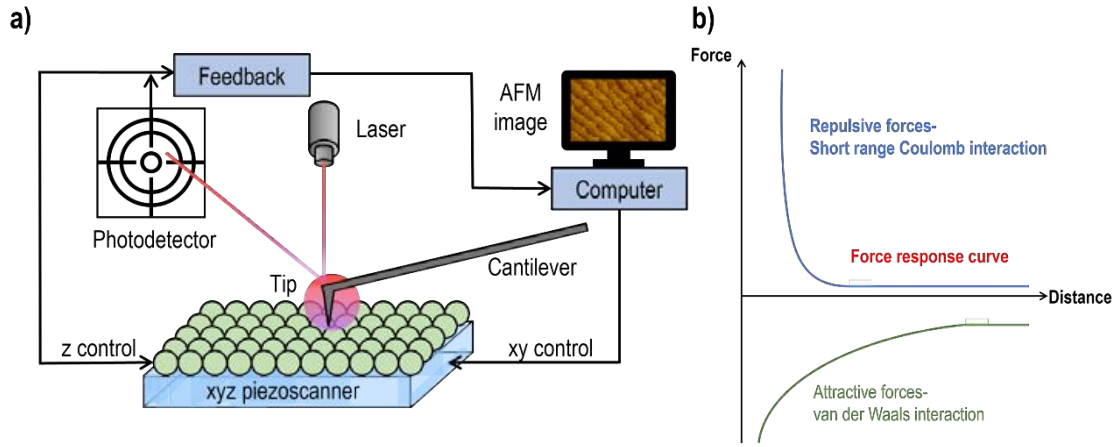

Figure 2.10:(a) illustration of a typical AFM set-up with the main components and (b) Force-Distance plot showing the interaction of an AFM tip with the surface

Several modes of AFM can be used, but the most common imaging modes are:

- Contact mode: the tip is always in contact with sample surface. Through the cantilever deflection it is possible to measure the interaction between the sample and the tip. The cantilever deflection is maintained constant by the feedback system that adjust the z piezo.

- Tapping mode: in intermittent contact mode, the tip scans the surface while the cantilever is oscillating near its resonance frequency. The tip remains in contact with the surface only at the minimum of each oscillation. As the tip is closer to the surface its oscillation amplitude decreases and when the distance is increased, the amplitude is also increased. Then, this oscillation is controlled by the feedback system, which will provide topographical information of the surface.

AFM has been used to obtain information about the surface morphology of composite and single-phase thin films. The measurements were carried out with an Agilent 5100 SPM based in the Scanning Probe Microscopy Service at ICMAB handled by the technical staff.

2.2.3. Scanning electron microscopy

Scanning electron microscopy (SEM) is formed by an electron source, electromagnetic lenses, and an electron detector as depicted in *Figure 2.11*. The electron beam is accelerated and focused on the sample using the electromagnetic lenses. When the electron beam hits and penetrates the sample, it is deflected in an elastic scattering mode, where electrons do not lose kinetic energy, or in an inelastic scattering mode, where the electron beam interacts with the sample, and they lose and transfer their kinetic energy to the atomic nuclei. This interaction leads to the generation of secondary electrons, backscattered electrons, characteristic x-rays, photons etc. These generated elements are used to obtain information about the sample. Backscattered electrons (BSE) are produced by elastic scattering and are captured to form BSE images. Backscattered coefficient is dependent on the atomic number (Z) of the specimen, thus elements with higher Z will appear brighter than those with lower less Z number. By inelastic scattering secondary electrons are produced. Only secondary electrons produced close to the surface may be able to escape from the sample. Since secondary electrons are mainly affected by surface variations, they provide topographical information about the sample[74].

The SEM images presented in this thesis were obtained using the QUANTA FEI 200 FEG-ESEM installed at ICMAB, and the HR-SEM Magellan located at ICN2.

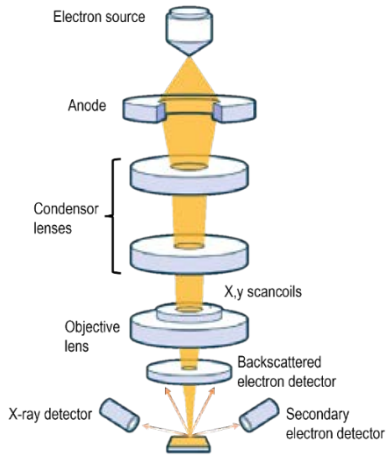

Figure 2.11: Schematic illustration of a SEM adapted from SEM vs TEM, Gleichmann, Nicole, Technology Networks (2020)[75]

2.2.4. Transmission electron microscopy

The transmission electron microscope (TEM) consists of an electron source, electromagnetic lenses, and an electron detector as illustrated in *Figure 2.12*. A very thin, electron transparent sample is located along the electron beam. Then, the electron beam passes through the sample which modifies it and imprints its image. After that, the beam is magnified by lenses and detected by a fluorescence phosphorus screen or a CCD camera.

In TEM, the back focal plane contains de diffraction pattern. An aperture can be inserted to generate a diffraction pattern from a selected area of the sample. High resolution TEM (HRTEM) is a phase contrast imaging mode that allows the imaging of the atomic structure. In scanning-TEM (STEM) mode the electron beam is converged into a small electron probe that scans across the sample to form an image. Image acquisition in STEM is slower than in TEM and must be done using different detectors. High angular dark field images are obtained from electrons incoherently scattered at high angles (Rutherford scattering from the nucleus), where the angle of the scattered electron depends on the size of the atom nucleus. Therefore, the contrast on HAADF images comes from the Z number where heavier atoms will scatter more leading to more signal and thus will appear brighter in the image compared to lighter atoms. Also, STEM can be used for chemical analysis by using electron dispersive X-ray spectroscopy (EDX), where an electron from the inner shell of an atom is ejected when is reached by a high energy electron beam emitting a photon, which is characteristic for each element. However, EDX works better for heavy elements and the limited energy resolution of the EDX detector can lead to peak-overlap problems. TEM can be used to perform electron energy loss spectroscopy by the analysis of the energy distribution of inelastically scattered electrons that have come through the sample. From the energy-loss events we can obtain information about the chemical composition and the electronic structure of the specimen atoms (e.g., valence state)[76].

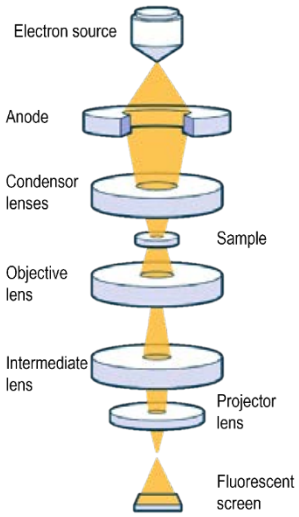

Figure 2.12:Schematic illustration of a TEM adapted from SEM vs TEM, Gleichmann, Nicole, Technology Networks (2020)[75].

The samples for TEM characterization were prepared region by precision ion polishing system (PIPS) and focused ion beam (FIB) to obtain an ultra-thin electron transparent sample. In the framework of this thesis, TEM was used to study the structure of TiO_2 films and the BFO films. TEM characterization was done with a FEI Tecnai F20 S/TEM of the electron microscopy unit of the ICN2, and the aberration corrected Titan electron microscope at the Instituto de Nanociencia y Materiales of Zaragoza (INMA).

2.3. Synchrotron characterization

During the realization of this thesis many experiments have been carried out in different synchrotron facilities to get deeper information on the structural and electronic properties of the films. This section will focus on the specific beamlines that have been used to achieve the pursued objectives. It will be divided in two parts according to their specific area of application: photoemission or diffraction.

2.3.1. Surface X-Ray diffraction

Surface X-ray diffraction (SXRD) is a powerful technique to study the structure of the topmost layer of samples. In this kind of experiments the x-ray beam incident on to the sample is at glancing angles. Thus, the beam penetration depth is reduced, and the surface sensitivity is increased. However, the diffraction intensities have a major contribution from the bulk due to the low surface-bulk ratio. Thus, high photon flux is needed, and synchrotron radiation is typically required to perform SXRD measurements.

When diffraction occurs at the surface of a crystal the diffracted intensity can be obtained adapting *Equation 2.10* with a_3 along the surface normal and the signal of the top monolayers is calculated by setting N_3=1. This equality represents a loss of translational periodicity in the a_3 direction due to its truncation by the surface. That would produce rods or bars with a continuous distribution of intensity along this direction (L) for each discrete reflection (H, K). Those rods are called crystal truncation rods (CTRs) since they arise from a crystal being truncated. If we consider a 3D truncated crystal diffraction, we can obtain a more realistic model for crystal surface diffraction. Here, the intensity distribution perpendicular to the surface is obtained by the sum of the bulk reflections and the surface CTR. In the case of a surface reconstruction, fractional order reflections (FORs) are observed where surface reconstruction specific diffuse intensity is observed perpendicular to the surface at non-integer reciprocal H and/or K values[77,78].

The intensity distribution for a 2D lattice and for a CTR can be expressed by the following equations:

$$I_{2D} = \left| E_e \frac{e^2}{mc^2 R_0} F(q) N_1 N_2 \right|^2 \qquad (2.\ 11)$$

$$I_{CTR} = \left| E_e \frac{e^2}{mc^2 R_0} F(q) N_1 N_2 \right|^2 \frac{1}{2\sin^2(q \cdot \frac{a_3}{2})} \qquad (2.\ 12)$$

From the SXD data analysis lattice parameters, surface relaxation and reconstruction phenomena can be studied since the intensity distribution depends on those parameters. The refinement of the surface structure from the obtained SXD data was done using the ROD program based on the calculus of the structure factor. A brief introduction to the software can be found in "ROD: a program for surface X-ray crystallography, E. Vlieg J. Appl. Cryst. (2000), 33, 401-405[79]". Surface X-ray diffraction experiments were carried out at Diamond Light Source (DLS), the national UK's synchrotron facility, formed by 32 different beamlines and at the European Synchrotron Radiation Facility (ESRF), which since 2020 has become the world's first fourth-generation high-energy synchrotron. Both beamlines were used to (a) study the surface structure of the anatase (100) (surface reconstruction, average structure of the film and that at the interface to evaluate the effects of misfit strain at the initial stages of film growth) and (b) study the termination of the BTO and BFO film structure as well as their interfaces.

2.3.1.1. I07: Surface and Interface Diffraction

Beamline I07 is a hard X-ray diffraction beamline (8-30 keV) committed to the study of surfaces and interfaces using grazing incidence angle X-ray scattering methods as SXRD, GIXD, XRR and GISAXS.

The study of the TiO_2 surface and BFO films was done at the experimental hutch 2 (EH2) devoted to experiments where UHV sample preparation is required. EH2 holds a 2+3 diffractometer oriented to operate with the sample surface in the vertical plane i.e. the surface normal direction is located in the horizontal plane with a large environmental chamber (*Figure 2.13*) formed by a three-vessel system: a load-lock chamber, a buffer chamber equipped with LEED, SPM, and facilities to clean the sample and an analysis chamber which contains an extra LEED and an X-ray source for XPS[80].

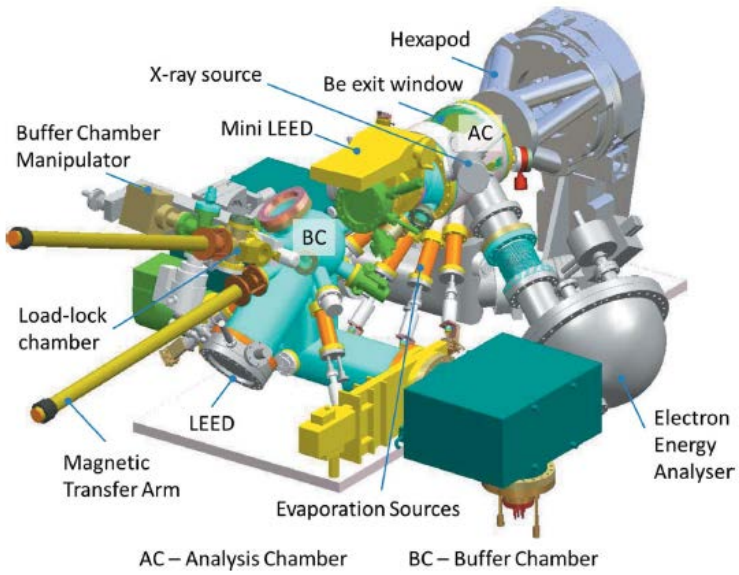

Figure 2.13: Schematic outline of the UHV chamber from EH2. Figure extracted from Nicklin, C.,et.al. J. Synchrotron Radiat. ***23****, 1245–1253 (2016)*[80].

2.3.1.2. BM32-IF: InterFace Beamline

BM32-IF is a Collaborating Research Groups (CRG) beamline dedicated to the study of surfaces and interfaces. BM32 diffractometer can be seen in *Figure 2.14*. To align and focus the x-ray beam two mirrors and a double crystal monochromator is used. The sample is placed on a goniometer inside an UHV chamber coupled to an MBE, RHEED and AES to be used during the X-ray characterization. Then, the beam is reflected into a 2-D detector, which allows the 2D visualization of the reciprocal space.

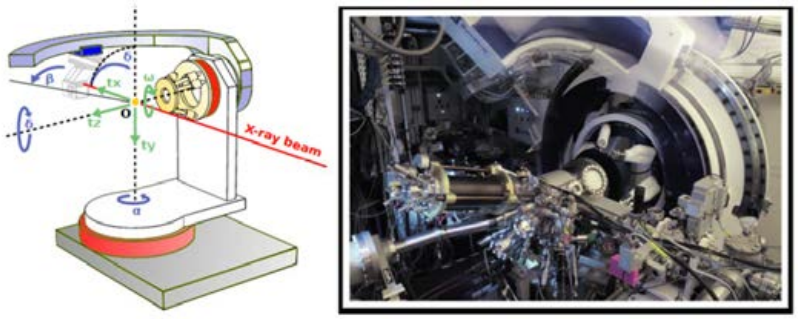

Figure 2.14: (a) Schematic outline and (b) actual set-up of the z-axis diffractometer at the beamline BM32 at ESRF Figure extracted from Sant R., doctoral thesis[81].

2.3.2. X-Ray photoelectron spectroscopy

X-ray photoemission spectroscopy (XPS) is a quantitative surface sensitive spectroscopic technique based on the photoelectric effect[82] (*Figure 2.15*) that enables the identification of the elemental and chemical composition of the outer layers (0-10nm) of the studied sample.

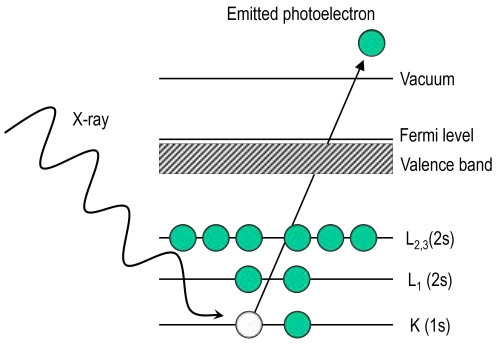

Figure 2.15:Basic principle of photoemission process: the energy of the photon is transferred to a core level electron, then the excited photoelectron is ejected into vacuum after overcoming the work function near the surface, leaving a core hole.

The photoelectric effect happens when an electromagnetic radiation with energy hv can induce electron ejection. Electrons are ejected with a kinetic energy (E_k) from the core level toward the analyser. The electrons are ejected if the energy of the incident photons is higher than the binding energy of the former. The kinetic energy of the ejected electron measured at the hemispherical analyser is described in *Equation 2.13*:

$$E_{bin} = E_{pho} - \quad (E_{ki} + \varphi) \qquad (2.\ 13)$$

Here E_{bin} corresponds to the binding energy for the core level, E_{pho} is the photon energy used in the measurement, E_{ki} is the kinetic energy of the ejected electron from the measured material and φ is the work function related to the XPS spectrometer. The surface sensitivity of this techniques is related to the short mean free path of the electrons in the material. Even though x-rays penetrate around hundreds of nanometers through the material, the ejected electrons have very short inelastic mean free path (IMFP)[83–85]. Thus, the electrons detected are from the first nanometers of the sample. *Figure 2.16* represents the general behavior of the IMFP of an electron vs its kinetic energy. For example, a typical lab x-ray photon source using AlKα (1487 eV) allows to study the topmost 2.5 nm of the sample, while synchrotron facilities allow a wide range of energies from soft x-rays (50-1500 eV) and Hard X-rays (up to 10 KeV) which allow higher surface sensitivity as well as the study of interfaces, faster measurements, and better resolution[86,87].

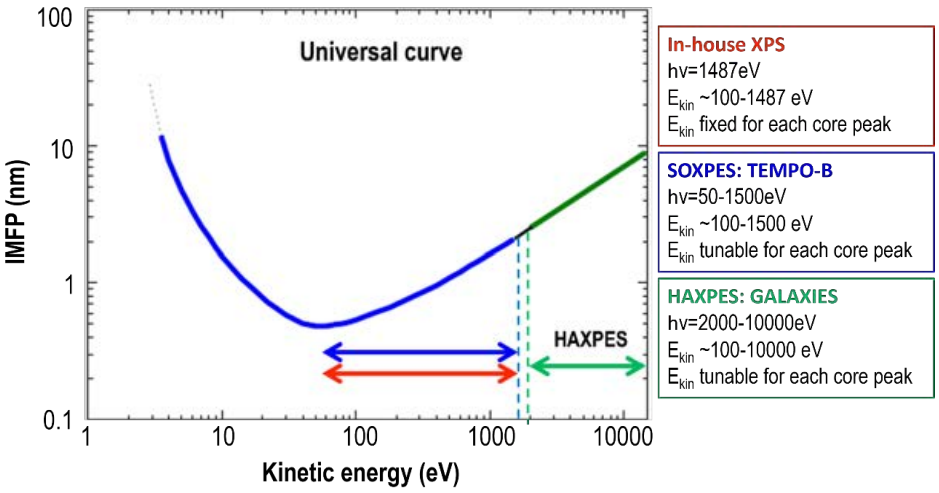

Figure 2.16: General IMFP of electrons vs its kinetic energy.

A typical XPS spectra is shown in *Figure 2.17.* The x axis is assigned to the binding energy (BE) in eV and the position of each peak is characteristic of the different elements for a particular electronic state or at a particular chemical environment[88,89], while the y axis defines the intensity typically in count per second. Different peaks can be seen in the spectrum, which are on a background that increases toward high binding energy, and step-like on the high BE side of each relevant peak, caused by inelastic collisions of the photoelectrons upon leaving the sample. The background is formed by contributions from secondary electrons at high BE, while at low BE Bremsstrahlung radiation predominates. The peaks present in the spectrum can be classified into three types: photoemission from core levels, photoemission from valence bands and peaks coming from x-ray excited Auger emission.

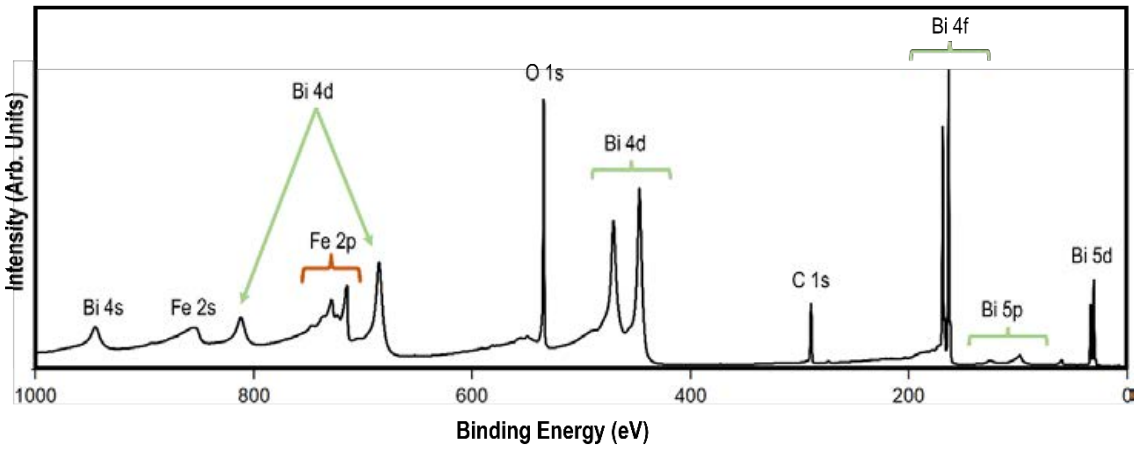

Figure 2.17: XPS spectra of a $BiFeO_3/SrRuO_3/SrTiO_3$ film (hv = 750 eV, Epass= 20 eV,Estep=0.1eV).

The most intense and well-defined peaks are the core level peaks, which represent the electronic structure of the sample. These peaks present spin-orbit splitting, except for the s levels[90,91]. The core levels are referenced by the principal atomic quantum number n (n=1, 2, 3…) which correspond to the main electronic layers around the atom's nucleus. The orbital angular momentum of the ejected electron is indicated by a second number l (l=0, 1, 2, 3… related with s, p, d, f orbitals). The third number presents the angular momentum number (|l - s |<j< |l + s|), with s the spin angular momentum (s =1/2, ms = (±1)/2). Thus, a doublet related to two different possible states with different binding energies can be observed (*Figure 2.18*). The intensity ratio (or branching ratio) between peaks depends on the orbital. *Table 2.1* shows the spin-orbit splitting for different orbitals, the corresponding j values, and ratios of the peak area.

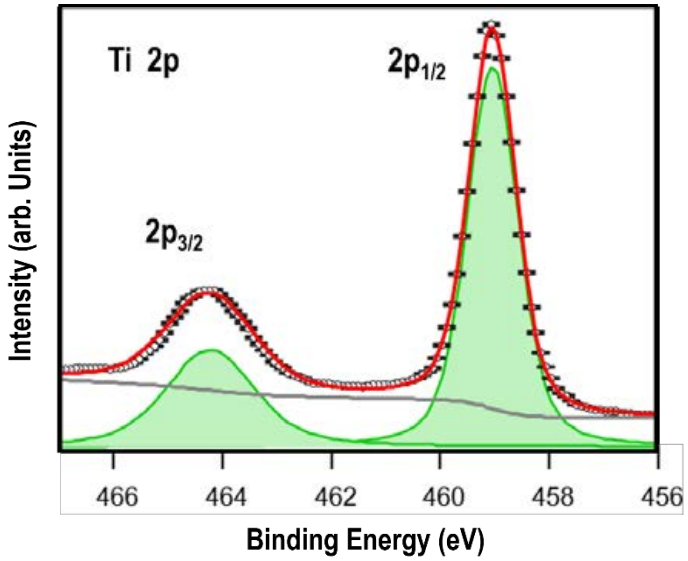

Subshell	J=l±s	Area ratio
s	1/2	-
p	1/2 3/2	1:2
d	3/2 5/2	2:3
f	5/2 7/2	3:4

Table 2.1: Spin-orbit splitting j values and ratios of the peak area.

Figure 2.18:Ti 2p spectrum illustrating the 2p spin-orbital splitting.

XPS intensity for a given element depends on several conditions such as the concentration, its position on the system, the exciting photon energy[92,93] or the measurement conditions. The analysis of the core level spectra allows the identification of elements present in the sample. A correct fitting of the XPS data requires

appropriate selection of the line shape for the core level peaks and background. The photoemission peaks could be described as a Voigt function: a convolution of a Gaussian and a Lorentzian function, where the Lorentzian function is related with the lifetime of the core hole and where the Gaussian function presents the contribution of the analyzer resolution and the photon source[94] for a synchrotron. On the other hand, it is essential to remove the continuous background to keep only the photoelectric contribution. This can be done by fitting the background with different models such as linear, Shirley[95,96] or Tougaard[97].

The valence band is composed of electrons involved in delocalized or bonding orbitals, with BE between 0 and 20 eV. A band structure results as the levels in this region are very closely spaced (*Figure 2.19*). TiO_2 has a bandgap of around ~3.2eV, which needs a particular preparation method to make it suitable for electron-based techniques. After cycles of ion sputtering and annealing TiO_2 presents a degree of non-stoichiometry that appears mainly as two kinds of point defects, bridging oxygen vacancies at the surface and interstitials titanium species[98–100]. These defects lead to a band gap state (BGS), which appears at about 0.8 eV below the Fermi Level (E_F)[101]. Several reports by Yim et al.[100] ,Henrich et. al.[101] and Schaub et. Al. [102] studied the origin of the band gap state of rutile TiO_2. The results suggested that oxygen vacancies were responsible for the band gap state on TiO_2, as it appears after the bombardment, when point defects are created and it disappears after the exposure to oxygen when the surface is healed. This theory is called the O-vacancy model, which proposes that when oxygen vacancies appear, two excess electrons related with each vacancy are transferred to empty *3d* states of adjacent five-coordinated Ti sites, creating two Ti^{3+} sites. The excess of electrons could affect the surface chemistry of the TiO_2[103,104].

However, other published works suggest that the BGS intensity can be related to the Ti^{3+} interstitials[105–107]. Wendt et. Al. based on STM, photoelectron spectroscopy measurements and DFT calculations discovered that in addition to filling the surface vacancies oxygen atoms adsorbed at the five coordinated titanium come from the reaction of molecular oxygen with the reduced TiO_2 surface. The STM images revealed that the adsorbed oxygen atoms were in excess with respect to what is expected if we assume that the oxygen vacancies as the only adsorption site. Thus, they proposed that BGS can also come from Ti interstitials.

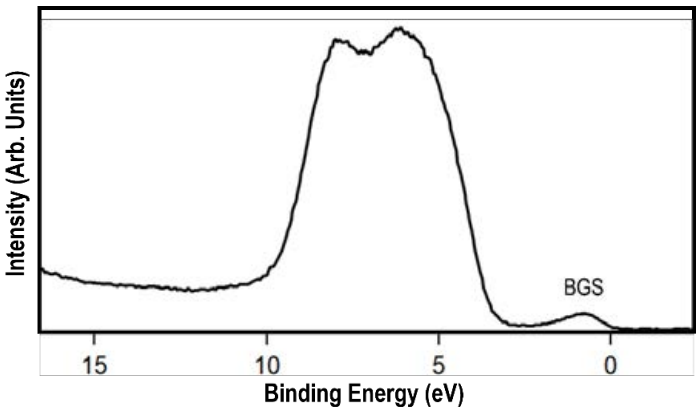

Figure 2.19: X-ray photoelectron spectra of the valence band region of the anatase (001) thin film (hv = 750 eV, Epass= 20 eV,Estep=0.1eV, UHV).

During this thesis two synchrotron radiation based XPS experiments were carried out at SOLEIL, a third-generation synchrotron operating since 2008 located in Saint-Aubin (France) formed by 29 different beamlines which work in a broad range of wavelengths from THz radiation to hard X-rays.

2.3.2.1. TEMPO beamline at SOLEIL

TEMPO beamline (Time Resolved Experiments on Materials with Photoelectron Spectroscopy) is devoted to the study of the electronic and magnetic properties of materials close to the surface by standard and time-resolved photoemission in the soft X-ray range (50 to 1500 eV). At the TEMPO beamline, it is also possible to perform high-quality band structures studies by angle-resolved photoemission (ARPES), as well as absorption measurements at different edges in the soft X-ray energy range[108].

TEMPO branch B (*Figure 2.20*) dedicated to Near Ambient Pressure X-ray Photoelectron Spectroscopy (NAP-XPS) was employed to investigate the key surface intermediates involved in the photocatalytic process of the anatase under oxygen and water pressure, up to the mbar range, in presence and absence of UV light to better understand the TiO_2 intermediate steps appearing before water dissociation process.

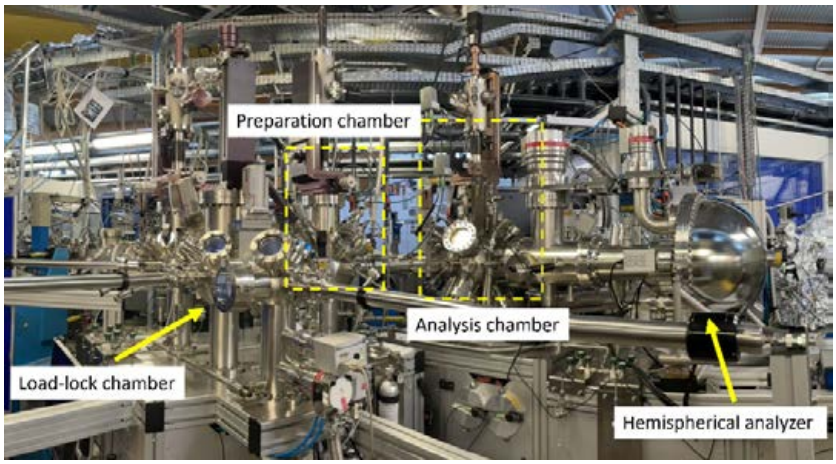

Figure 2.20: Picture of TEMPO-B beamline at SOLEIL synchrotron.

2.3.2.2. GALAXIES beamline at SOLEIL

GALAXIES beamline focuses on X-ray scattering (IXS) and on hard X-ray photoelectron spectroscopy (HAXPES). The objectives were: 1) to determine the depth profile of Bi and Fe concentrations along the islands type structures present in some samples. 2) To repeat the same procedure on BFO films grown epitaxially without islands. 3) To check the presence or absence of metallic bismuth (Bi^0) at the samples. For that purpose, the HAXPES end-station dedicated to hard X-ray high kinetic energy photoelectron (0-12keV) spectroscopy was used. The end-station set-up can be seen in *Figure 2.21*. It is mainly formed by an UHV-chamber equipped with an electron analyser, a sample manipulator, and a gas cell. A secondary chamber, connected to the main one, is used for sample loading and basic sample treatments. Electrons are detected by a hemispherical SCIENTA EW4000 electron analyser which allows wide angular openings

to increase the number of electrons collected by the detector compared to regular hemispherical analysers[109].

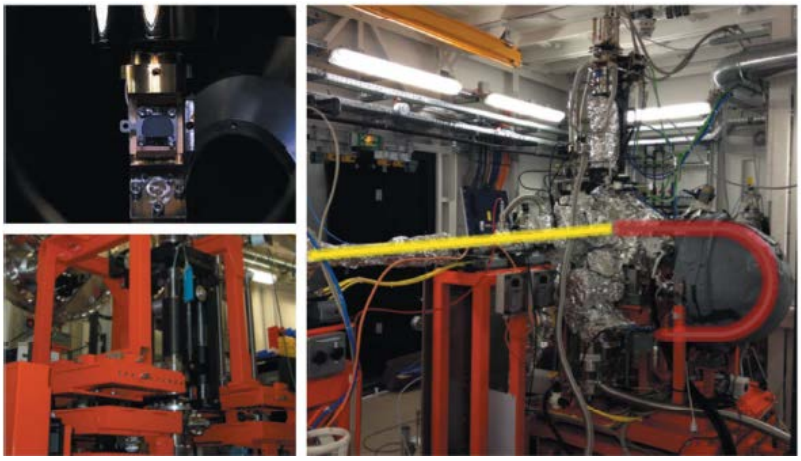

Figure 2.21: Photographs of the HAXPES endstation with the sample mounted on the manipulator, the gas cell, and a view of the hemispherical analyzer. Figure extracted from Krishnan, P. et al., Sci. Rep. 7, 43298 (2017) [109].

3. Thin films preparation and characterization

This chapter is focused on the optimization of the growth parameters for the deposition of TiO_2, $BaTiO_3$, $BiFeO_3$ and TiO_2/BTO/STO (100) thin films and its characterization.

Firstly, the effect of pressure and temperature will be studied for the TiO_2 films grown by PLD, as well as the influence of the annealing treatments on the final quality of those films. Additionally, a comparison between samples deposited by two different chemical vapour deposition techniques: PLD and MBE will be discussed. Knowing how to obtain pure phases of anatase (001) films is crucial to link the surface structure of the resulting films with their possible photocatalytic activity.

Secondly, the evolution of the *c*-lattice parameter of the BTO will be investigated changing several deposition parameters such as deposition rate, temperature, pressure, and thickness. Afterwards, the preparation of BFO films on STO (100) and (111) substrates will be discussed.

Finally, a preliminary study on the preparation of TiO_2/BTO/STO (100) heterostructures has been done. The final objective is to investigate the possibility of combining the ferroelectric properties of the ferroelectric films with the titania to enhance its photocatalytic activity.

3.1. Substrates preparation

$SrTiO_3$ (STO) substrates (CrysTec, 5x5x0.5mm) with (100) and (111) orientations were used to grow the selected materials. To grow a high-quality thin film, substrates must be clean, flat and with the lowest roughness possible. Thus, the as-received STO (100) substrates were previously treated to obtain Ti-STO terminated atomically flat surfaces by annealing them at 1000ºC for 1 hour in air and ulterior sonication in deionized water etching for 15 minutes [110]. *Figure 3.1* shows AFM images of a STO substrate at each stage of the process. *Figure 3.1a* presents the as-received substrate. *Figure 3.1b* illustrates the STO after the annealing process, where the white dots correspond to SrO and SrO hydroxide which have an ionic bonding nature with the STO. For that reason, deionized water is effective to remove these impurities as they are soluble materials. The result of the water etching can be seen in *Figure 3.1c* where atomically flat STO has been obtained with a roughness about ~0.75 Å. The main advantages of using this procedure are the innocuousness of the required chemical products, as well as the absence of vacuum conditions, which facilitates their handling.

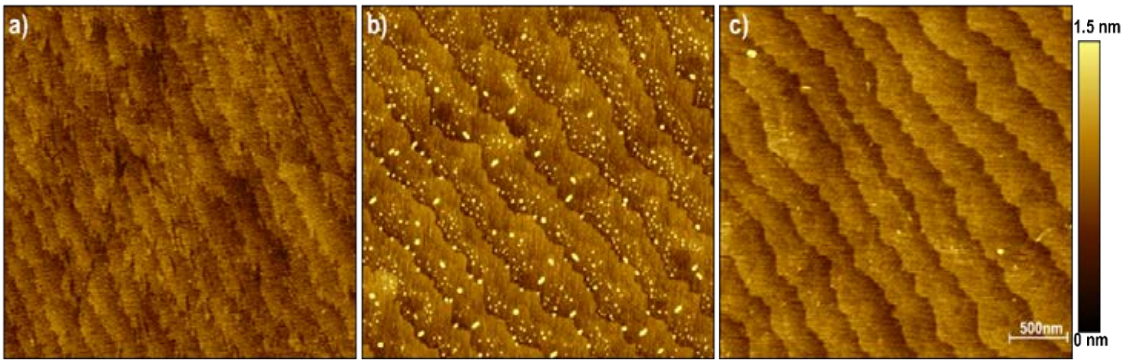

Figure 3.1: 3x3 μm² AFM images of STO (100) substrates (a) bare STO, (b) after annealing (1000ºC, 1h) and (c) after H_2O etching.

The previous cleaning process was also tested on STO substrates with (111) orientation. However, in this case the method decreases the surface's quality (*Figure 3.2*). The bare STO (111) substrate presents a smooth surface (*rms* ~0.9 Å), whereas after the annealing the superficial roughness increases to 0.35nm. Thus, STO (111) substrates were not cleaned for the deposition of thin films.

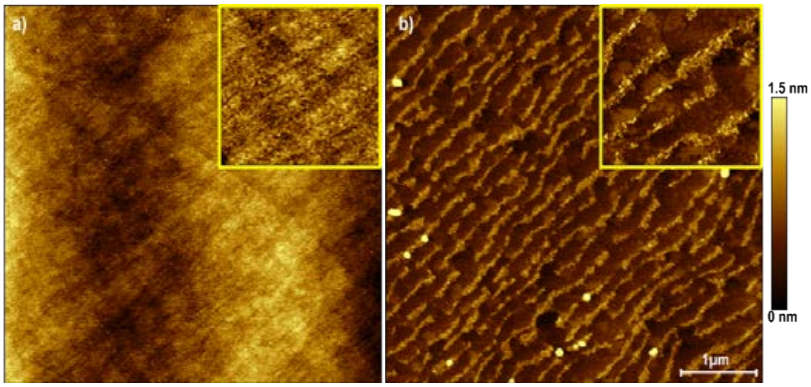

Figure 3.2: 5x5 μm² AFM images of STO (111) substrates (a) bare STO, (b) after H_2O etching.

For the MBE preparations, STO (100) substrates were further cleaned in-situ. The AES indicates that the substrate introduced in the UHV-chamber has carbon contamination on its surface, as well as traces of calcium (*Figure 3.3a black curve*). These contaminants were removed applying an additional cleaning process that involved two successive cycles of Ar^+ ion sputtering (0.6 keV, $P_{Ar}= 5\cdot10^{-6}$ mbar, t=5minutes) and annealing at 850ºC under an $P_{O2}=10^{-6}$mbar (*Figure 3.3a red curve*). The LEED pattern was used to evaluate the crystallographic quality of the STO substrate. *Figure 3.3b* shows a diffuse pattern of the STO before the cleaning process, while after it, a sharp pattern is obtained indicating good STO quality and an optimal design of the surface cleaning procedure (*Figure 3.3c*).

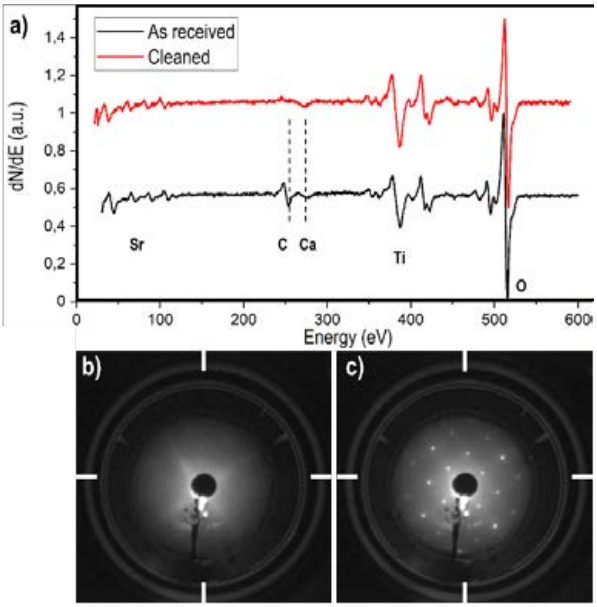

Figure 3. 3: a) AES of the STO (100) as received (black) and after cleaning (red) and LEED pattern of (b) bare STO and (c) cleaned STO substrates. LEED pattern recorded at 100eV. The solid lines indicate the principal directions [100] or [010].

3.2. TiO_2 growth conditions

This section will be divided according to the growth technique employed for the deposition of the TiO_2 anatase (001) films, PLD or MBE. The aim is to obtain high quality epitaxial anatase thin films with the best surface and crystallinity as possible independently of the growth technique used. The anatase (001) facet is considered to be the most active for photocatalytic applications[26,111,112], however the difficulty to synthesize it in the laboratory[113] combined with its low presence in nature[114] makes crucial to develop a method to prepare anatase (001) surfaces with large crystal terrace sizes at low cost to continue in the knowledge of the structural and electronic properties of this surface and for its application. During the optimization of the growth conditions of the anatase (001) films, certain phenomena related to the film's lattice parameters and recrystallization processes were detected showing a certain dependence on the growth and annealing temperature, respectively. Once the growth conditions were determined, a subsequent study was carried out based on temperature to optimize the quality of the film. The objective of this study is to increase the degree of crystallinity of the film and the size of the terraces present on the film's surface.

3.2.1. PLD growth

A commercially available TiO_2 target (diameter: 5cm, purity: 99.99%, Mateck) was used to prepare the titania thin films by PLD. Reports on the preparation of TiO_2 thin films investigate a wide range of growth conditions[115–118]. Considering the studies present in the literature, we examined a range of oxygen pressures (10 mTorr, 85 mTorr and 120 mTorr) at a deposition temperature of 600 ºC. Afterwards, a series of different growth temperature (600ºC-925ºC) were tested at a certain growth pressure (85 mTorr). The energy density of the laser was set to ~1.8J/cm^2 with an approximately deposition rate of 0.033 nm/pulse. All the anatase

films grown on $SrTiO_3$(100) by PLD show heteroepitaxial growth. In order to compare the measurements between different samples, all the films shown in this section were grown with the same number of pulses (1500 pulses), which is equivalent to a thickness of about 50 nm.

The RHEED observation during the deposition of a TiO_2 film grown on bare STO (100) is presented in *Figure 3.4*. *Figure 3.4a* corresponds to the RHEED pattern of the substrate, while *Figure 3.4b* is the final RHEED pattern of a TiO_2 sample. During the experiment the specular spot intensity, marked with a circle, was monitored. The decrease of the specular RHEED intensity at the initial growing stage (*Figure 3.4c*) indicates the formation of islands but keeping their registry with the main crystallographic (001) directions of the substrate surface (3D growth).

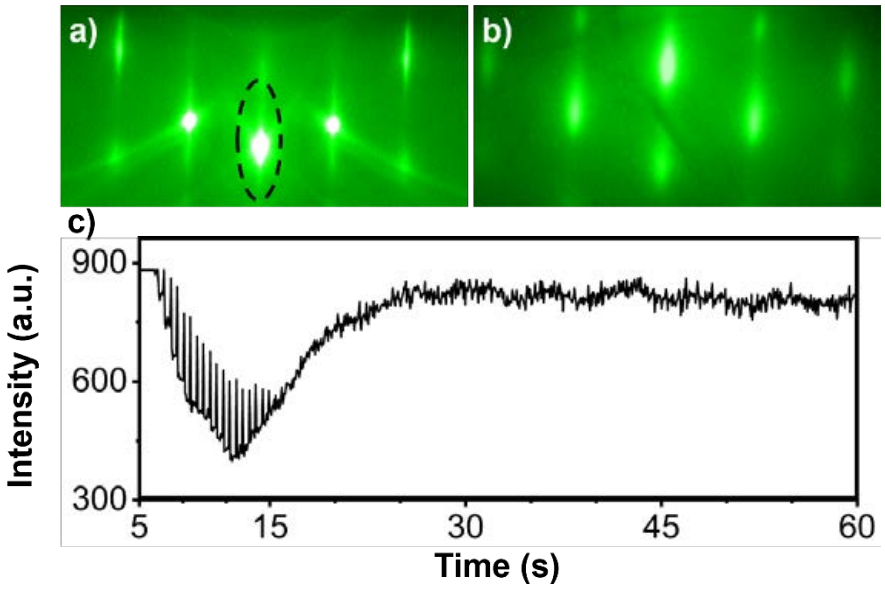

Figure 3.4 RHEED pattern of (a) bare STO reflections before deposition and (b) TiO_2/STO reflections after deposition. The discontinuous ellipse in (a) indicates the peak used to track the intensity during the film growth, shown in (c).

The growth mechanism seen in *Figure 3.4* is similar with the results obtained by Radovic et.al.[45], that proposed a three stage mechanism: Sr-diffusion to the STO surface, islands formation and step flow growth. In the initial stage of the growth, titanium atoms reach the substrate's steps and interact with the strontium present on the substrate's surface and grows in a pseudomorphic mode. In the 2nd step, isolated anatase islands block the Sr-segregation process to the interface between them. The formation of islands is compatible with a Volmer-Weber growth mode where the balance between surface and interface energies favours the formation of islands. The 3rd stage involves growth through the flow of crystal steps where the spaces between adjacent islands are filled.

3.2.1.1. Influence of oxygen pressure

First the influence of the oxygen pressure was tested maintaining the substrates at identical deposition temperatures (600ºC). *Figure 3.5* illustrates the different sample's topography a function of the oxygen pressure. All samples present a granular-like surface, but films grown at low pressure present an inhomogeneous surface with a dispersion of the island sizes varying from 20 to 40 nm, while samples prepared at medium and high oxygen pressures have a regular island size around 35nm. A further increase in pressure could not be tested as at 120mTorr pressure our PLD pumping system reaches its stability limit because the gas inlet flow is greater than the pumping capacity of the turbomolecular pump.

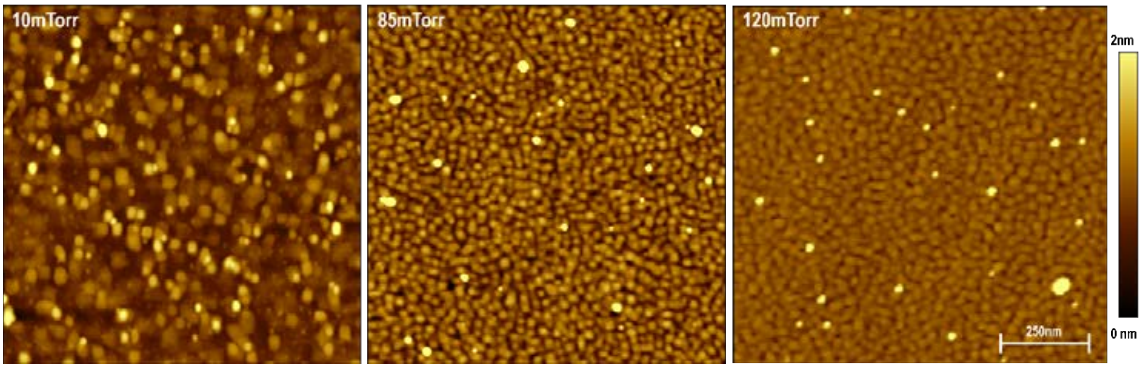

Figure 3.5:1x1 μm² AFM images of TiO_2 films prepared by PLD at different oxygen pressures.

The XRD of films grown at low (10mTorr), medium (85mTorr) and high (120mTorr) oxygen pressures are similar to those shown in *Figure 3.6,* which correspond to films deposited at comparable conditions. The anatase peaks move towards lower angles at 10 mTorr, while at higher pressures the peak position remains constant indicating a bigger out-of-plane lattice parameter at low pressure. This behavior will be discussed afterwards. 85mTorr was the pressure selected to grow the anatase thin films as the surface seems more homogeneous.

3.2.1.2. Influence of growth temperature

The study as a function of temperature was performed maintaining the same oxygen pressure (85 mTorr) and laser parameters (Energy density: ~1.8J/cm^2) in the range 600 to 925ºC. The structural quality of the films was monitored using conventional XRD: θ-2θ geometry. The measured diffraction patterns shown a systematic shift of the anatase (001) peaks towards lower 2θ -angles, indicating to an expansion of the *c*-lattice parameter, with increasing temperature. The different growth temperatures for the PLD films are listed in *Table 3.1*. All films have similar thicknesses (~50nm) owing to the identical number of pulses during the PLD deposition. TS is assigned to TiO_2 grown on STO (100) substrates.

TiO_2 film	TS_01	TS_02	TS_03	TS_04	TS_05	TS_06	TS_07	TS_08
T(ºC)	600	650	700	750	800	875	925	600

Table 3.1: List of the TiO_2 thin films on STO substrates, grown by PLD, with their corresponding growth temperature.

The x-ray diffractograms of all TiO_2 PLD-deposited samples only contain reflections from the STO substrate and the TiO_2-anatase film (001). An example is given in *Figure 3.6* where the diffraction patterns of two films grown at 600°C (black) and 925°C (red) are shown. Peaks corresponding to the substrate and the film are indexed as STO (S00L) and anatase (A00L), where L corresponds to the out-of-plane Miller index. Reflections A (004) and A (008) are close to 2θ=37.6º and 80.5º, respectively. The measured diffraction patterns for all the samples show a systematic shift of the anatase (00L) peaks towards lower 2θ -angles with increasing temperature. The red colour x-ray pattern of *Figure 3.6* is shifted to lower angles respect to the black colour x-ray pattern. This shift is associated to an expansion of the *c*-lattice parameter of the film.

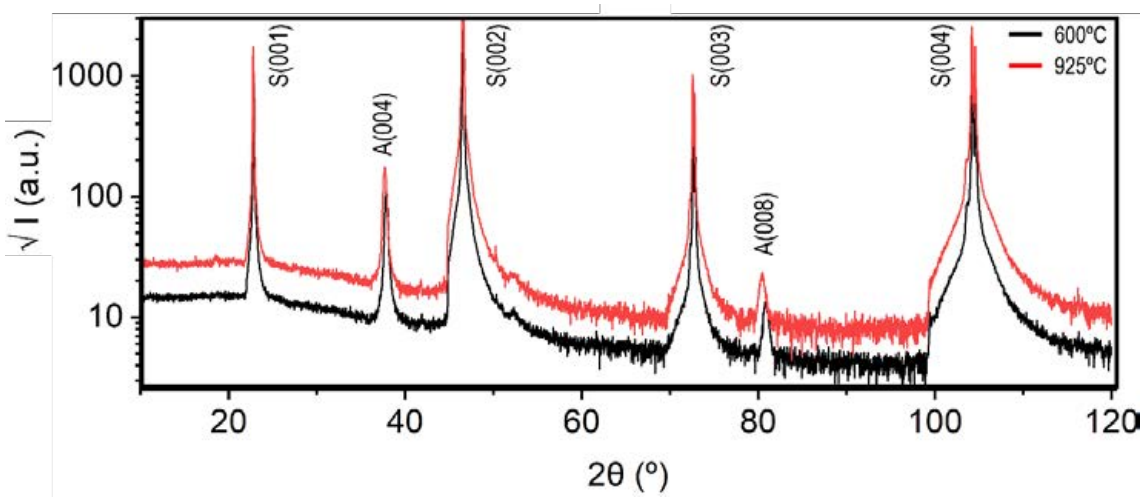

Figure 3.6: X-Ray diffractogram of samples prepared at 600ºC (black) and 925ºC (red).

These shifts are better observed in *Figure 3.7* that shows the (004) and (008) anatase peaks of two films grown at 600ºC (*Figure 3.7a*) and 875ºC (*Figure 3.7b*) before (black) and after (red) annealing them at 900ºC during 6 hours in air using a ceramic oven. As expected, the peak shift is much smaller in *Figure 3.7b* than in *Figure 3.7a*, due to the proximity of the growth and the annealing temperature (875ºC and 900ºC). Additionally, the x-ray diffractogram of a sample prepared at 600ºC and annealed consecutively at 700ºC, 800ºC and 900ºC in air for 6 hours each displayed in *Figure 3.7c* shows that the shift evolves gradually with the annealing temperature. These results confirm the peak shift dependence on the last temperature applied, annealing or growth.

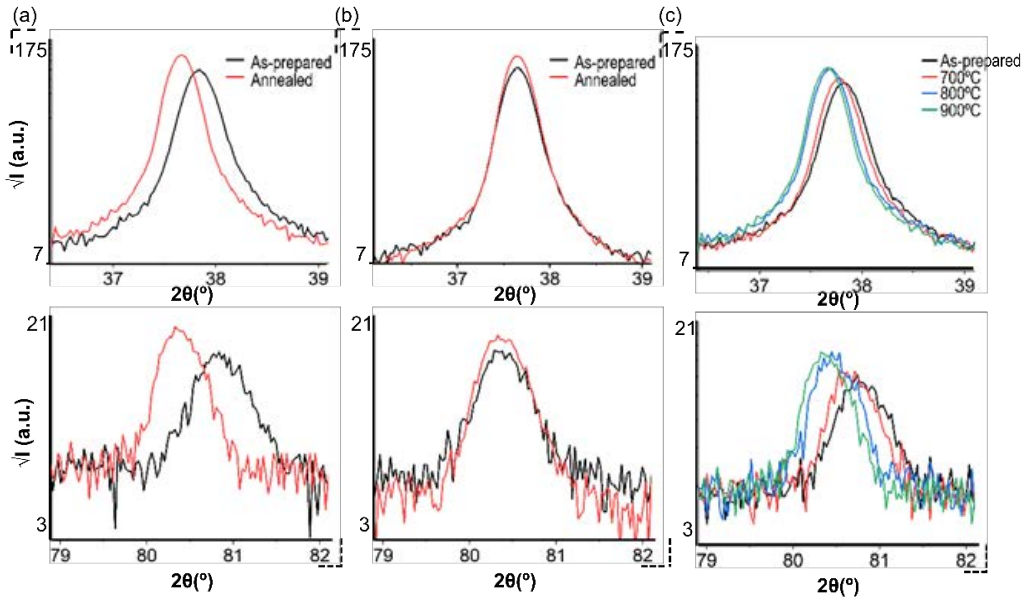

Figure 3.7: X-ray diffractogram zoom into the anatase (004) and (008) peaks for samples prepared at (a) 600ºC and (b) 875ºC before (black) and after (red) annealing them at 900ºC for 6 hours in air and (c) a sample prepared at 600ºC and annealed successively at various temperatures (700, 800 and 900ºC) for 6 hours in air.

The expansion of the *c*-lattice parameter of the anatase (001) film (from 9.5014 to 9.5464 +/- 0.0005 Å in the range 600 – 925 ºC) as a function of the growth temperature is represented in *Figure 3.8* (black dots). This parameter (c_{film}) has been normalized to the bulk *c*-lattice parameter (c_{bulk}) of the tetragonal anatase crystal at room temperature (a_{bulk} = 3.7845 Å, c_{bulk} = 9.5143 Å)[119] defined by the expression:

$$c_{norm} = \frac{c_{film}}{c_{bulk}} \qquad (3.\ 1)$$

All TiO_2 shifts were measured at RT either after the growth process or the annealing treatment. From *Figure 3.8* it can be observed that the magnitude of the shift depends on the final temperature: growth temperature and annealing treatment. *Figure 3.8* also shows the evolution of the domain or terrace size (red dots), obtained from the analysis of AFM images (see *Figure 3.10*).

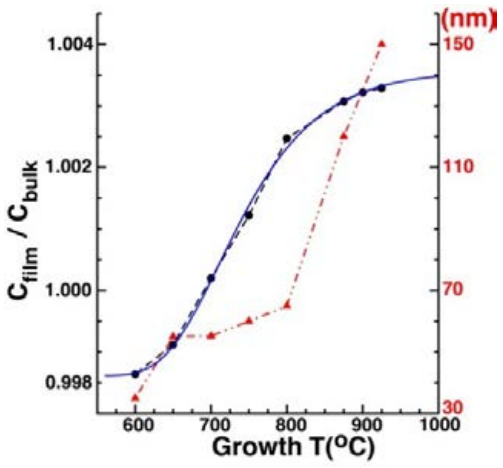

Figure 3.8: Variation of the average domain size (red dots) of the 'as- prepared' anatase (001) films as a function of the growth T; (black dots) Dependence of the normalized c lattice parameter of the anatase (001) films on T; Fitting (blue curve) of the experimental points (black dots) to a Gumbel distribution.

Reflectivity measurements were performed to determine the film thickness values of the samples listed in *Table 3.1*. *Figure 3.9* shows an example of a XRR curve obtained for sample TS_01, grown at 600ºC, after its PLD deposition resulting in a thickness of around 52nm.

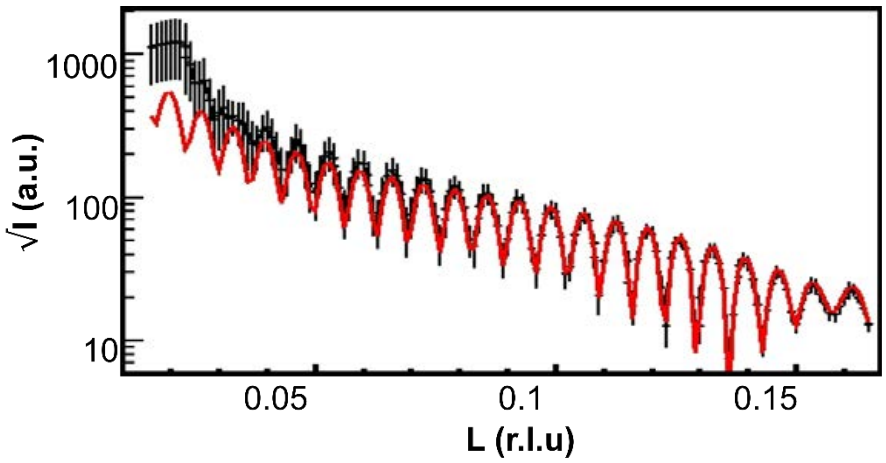

Figure 3.9: Reflectivity curve before the annealing treatments for the as-prepared sample deposited at 600ºC (TS_01). Fit (red) of the experimental reflectivity curve (black) for the anatase (001) film, expressed in units of the Miller index L corresponding to the STO cell (r.l.u. = reciprocal lattice units).

Table 3.2 contains the film thicknesses and crystallite sizes (D) of the samples listed *Table 3.1* in using Snell's law and Williamson-Hall formalisms, respectively[120,121], as well as the size of the islands that cover the surface of the samples. The crystallite sizes (CS) derived from the WH-plots are close to 40nm in good agreement with the approximately 50 nm thickness of the samples obtained by XRR. The difference between the crystallite size and the real thickness could be related to the disorder regions seen in the interface between STO and TiO_2 and the topmost layers of the film observed in TEM (see section *3.2.1.5.TEM characterization).*

TiO_2 film	Thickness (±1 nm)	CS (± 6 nm)	Island size (± 2 nm)
TS_01	52	39	35
TS_02	44	41	55
TS_03	49	40	56
TS_04	50	50	60
TS_05	44	39	65
TS_06	51	49	120
TS_07	54	45	150
TS_08	54	45	150

Table 3.2: Summary of the thicknesses, crystallite sizes and island size of the samples prepared at various temperatures.

The analysis of the XRD data shows only contributions from the STO (100) substrate and the anatase (001) films. The shift evolution of the anatase peak position to lower Bragg angle reveals an expansion of the *c* lattice parameter with temperature (*Figure 3.8*) and an increasing crystallinity of the film confirmed by the width reduction and the intensity gain of the anatase peaks. The out-of-plane lattice parameter evolution

with temperature can be predicted by using a cumulative distribution function (CDF) of the Gumbel distribution[122] (blue line in *Figure 3.9*) defined by the expression:

$$c_{norm}(calc) = p + q\ (e^{-e^{-(T-\mu)/\beta o}}) \qquad (3.\ 2)$$

The exponential part, CDF(x:μ,β)= $-e^{-(x-\mu)/\beta o}$, is a probability distribution function defined between 0 and 1. Hence, the parameter p: is a background baseline that shifts the function to values of $c_{norm}(T)$ close to 1; q: is a scaling function able to reduce the Gumbel distribution in the range $0.990 < c_{norm}(T) < 1.004$; T: is the temperature variable; μ: is the mode of the distribution; and βo: is related with the standard deviation of the distribution. Other functions as power laws were tested, but the best results were obtained with the Gumbel distribution (fit correlation value: 0.9989). The possibility of fitting the obtained parameters allows the preparation of samples with the desired morphology and island size, which is known to affect the photocatalytic activity of titania[123,124]. It is possible to distinguish between a compressive strain regime at temperatures below 700ºC where c_{norm} values are smaller than one reaching a maximum 0.20% compression of the c_{film} at 600ºC and tensile strain regime at higher temperatures where the c_{film} expands up to 0.33% at 925ºC. *Table 3.3* contains the lattice parameters obtained for all the as-prepared samples presented throughout this section:

Growth temperature (Cº)	*a* (Å) ±0.006	*c* (Å) ±0.005
600	3.773	9.501
650	3.772	9.513
700	3.774	9.524
750	3.766	9.533
800	3.775	9.538
875	3.777	9.539
925	3.771	9.541

Table 3.3: Anatase (001) film's lattice parameters for the as-prepared samples obtained by RSM.

The in-plane lattice parameters remain almost constant at all the growth temperatures and very close to the bulk value, while the out-of-plane lattice parameters changes following the relation expressed in *Equation 3.2*. Additionally, SXRD experiments carried out on the IF-BM32 beamline at the ESRF synchrotron for a sample prepared at 875ºC (~80nm thick) and an MBE sample (~8nm thick) have a 3.7784 ± 0.0005Å and 3.7811+/- 0.0005Å in-plane lattice parameter, respectively, leading to a compressive strain compared to the a_{bulk} of about 0.16% for the PLD sample and 0.09% for the MBE sample. Further discussion on the SXRD experiments will be presented in *Chapter 4: Surface Structure*.

The evolution of the surface morphology of the anatase (001) films grown by PLD as a function of the growth temperature is shown in *Figure 3.10*. Zoom images are included for those films that have the smallest island sizes (600ºC < T < 800ºC). All the sample's surfaces are formed by different size and shape islands. The island size is defined as the lateral dimensions of those islands obtained from the AFM images. The AFM images show an increasing island size with temperature in consistency with the expected higher surface

diffusion kinetics. In the low temperature range (600-800ºC) the island size, presents small variations starting at 35nm for 600ºC increasing up to 60nm for samples prepared at 800ºC. However, anatase (001) films grown at temperatures above 875ºC show island sizes greater than 100 nm achieving the maximum size of about 150 nm for samples prepared at 925ºC. These sizes could allow these films to be used to perform some electronic experiments in synchrotron facilities, i.e., NAP-XPS, since the long-range order is not a critical parameter for this technique, but do not allow them to be used as model systems for surface structural determination. For this reason, these surfaces still need to increase their terrace size more than a factor of 5 for such purposes.

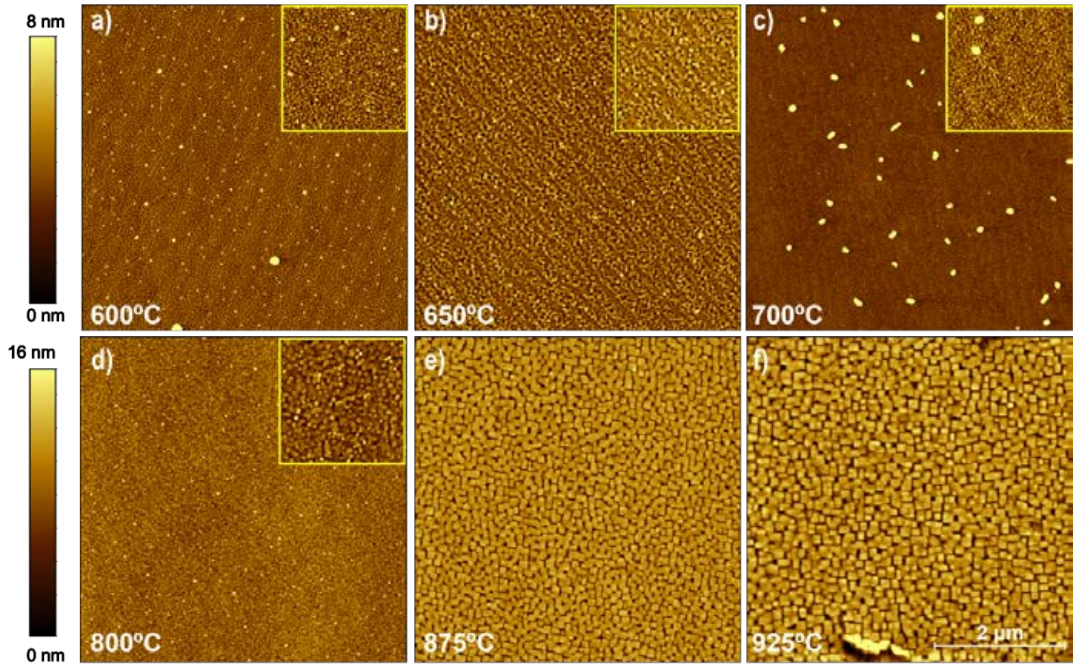

Figure 3.10: 5x5 µm² AFM images of TiO_2 films prepared by PLD showing the evolution of their surface morphology with growth temperature. Images with smaller film island sizes (600-800ºC) show an inset zoom of 1x1 µm² for better visualization.

3.2.1.3. Influence of annealing temperature

In order to increase the quality of the films, the samples were further annealed. Sample TS_08 was prepared at 600ºC and subsequently annealed at different temperatures (600ºC, 700ºC, 800ºC and 900ºC for 6h in air) to improve the quality of the film surface. The x-ray diffractograms taken at each stage of the procedure is shown in *Figure 3.7c* revealing that the shift of the anatase peaks occurs gradually and follows the same behaviour as for the samples deposited at a certain temperature. In conclusion the annealing and growth temperature have the same effect.

Figure 3.11 contains the AFM images that show the evolution of the sample's morphology with annealing stage. The initial film presents a granular-like topography with an average island size of 35nm which transforms into a flat terraced-like surface with terrace sizes of around 120nm after the different annealing treatments revealing the possibility of generating large, ordered terraces regardless of the growth temperature. The as-prepared sample has circular-shaped islands on its surface which after annealing at

700ºC change to square-shaped islands. The coalescence of the islands into a more uniform film surface occurs at 800ºC and reaches its maximum at 900ºC forming a terraced morphology.

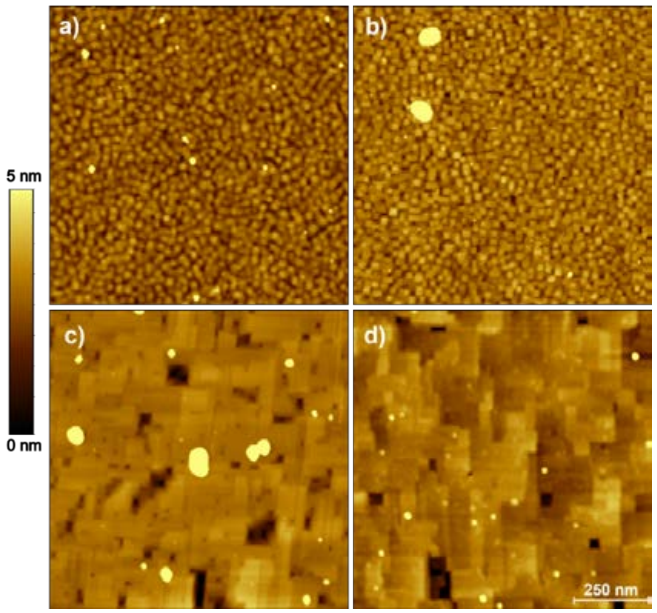

Figure 3.11: 1x1 µm² AFM images of (a) a sample prepared at 600ºC and after annealing consecutively at 700ºC, (c) 800ºC and (d) 900ºC for 6 hours.

In the low temperature regime (600-700ºC), hereinafter referred as R1, the film evolves from compressed to slightly expanded along the *c*-axis. Furthermore, the morphological changes seem to be minimum (*Figure 3.11 a* and *b*), just a small variation in the island shape from circular-like to square-like can be observed. Above R1 the islands spread over the surface and coalesce leading to a terraced surface. This restructuring of the surface could explain the large intensity gains in the XRD within the temperature range comprised between 800ºC and 900ºC. The effect of the different annealing steps applied to sample TS_09 in R1 could produce a rearranging of the ordered oxygen vacancies, inferred from TEM observations (section *3.2.1.5 TEM characterization)*, with no major changes in the surface morphology. However, at higher temperatures when the out of plane lattice parameter expands, the film's surface rearranges forming bigger terraces increasing the intensity of the anatase reflections[125]. It has been demonstrated that successive annealing stages (6 hours each) at progressive increasing temperatures in air have the effect of smoothing the film surface transforming the morphological granular-like surface into a flatter one formed by flat terraces.

To check time's relevance in the annealing processes, a larger annealing time was selected: 12 hours instead of 6 hours. *Figure 3.12* corresponds to a sample prepared at 750ºC and annealed following the above-mentioned process. Compared to the previously sample grown at 600ºC which increased its island size up to 120nm, in this case the islands size increases to an average value of about 300nm proving that the annealing time is a critical parameter to obtain bigger terraces. These results are consistent with previously reported articles[126,127].

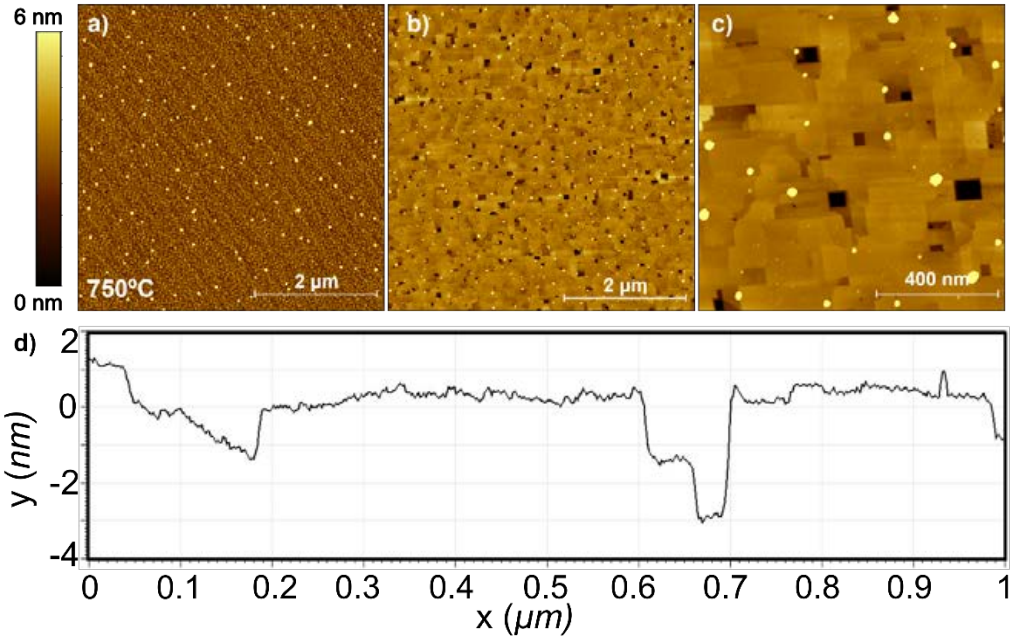

Figure 3.12: AFM images of (a) a sample prepared at 750ºC (b and c) annealed at 900ºC for 12 hours in air (d) profile of image c.

Annealing at temperatures slightly lower to the anatase/rutile phase transition temperature (950ºC) for longer periods of time (12 hours) using samples grown at temperatures at 925ºC with an initial terrace size of 150 nm allows obtaining bigger terraces of about 650 nm, as shown in *Figure 3.13*.

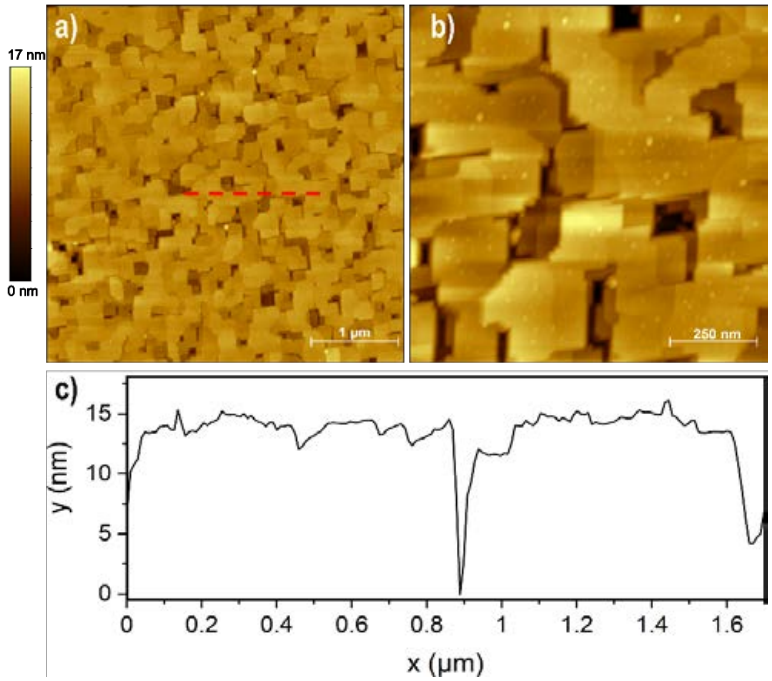

Figure 3.13: (a) 4x4 µm² and (b) 1x1 µm² AFM image of a sample grown at 925ºC and annealed at the same temperature for 12 hours (c) line profile of the red line in (a).

The effect of high temperature annealing (T > 950ºC) was also investigated to set an approximate value of the phase transition temperature of the anatase film to establish a secure temperature interval in heat treatments. The x-ray diffractogram of samples annealed at 950ºC have weak contributions from the three TiO_2 phases indicating that the phase transition starts to occur. The phase transition temperature depends

on the technique employed to obtain the TiO_2 films as it depends on the amount of defects, the morphology and the quantity of grain boundaries[128]. Further increase in the annealing temperature up to 1000ºC gives the x-ray diffractogram shown in *Figure 3.14*. According to the indexation of the rutile and brookite peaks in the diffractogram of *Figure 3.14*, the rutile phase growth with orientation (110) with respect to the STO substrate. The brookite seems to grow with two orientations (001) and (100) although this phase looks residual when comparing its intensity with those of the anatase and rutile.

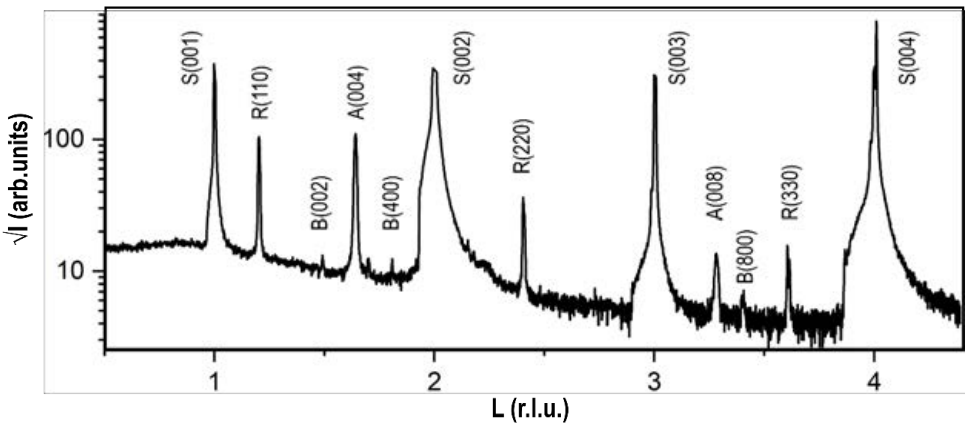

Figure 3.14:XRD diffractogram of a sample annealed at 1000º C. Main TiO_2 phases are rutile (R) and anatase (A). Weaker peaks belong to the brookite phase (B).

It has been proved that the maximum useful annealing temperature to improve the flatness of the anatase (001) film surfaces is 925ºC. At this temperature, the maximum expansion of the out-of-plane lattice parameter is achieved (*Figure 3.8*), while at 950ºC the phase transition from anatase to rutile starts to appear. The temperature range between 925ºC and 950ºC offers a possible window to improve the film's quality before the transition to rutile occurs.

3.2.1.4. TEM characterization

TEM observations were carried out to investigate the microstructure of the TiO_2 samples. The cross-section images (Figure *3.15a* and *b*) of a sample prepared at 875ºC shows a terraced surface in agreement with the corresponding AFM images (*Figure 3.10e*). The TiO_2/STO interface typically shows dark contrasts which indicate the occurrence of residual strains likely associated with the first growth stages. Inspection of *Figures 3.16a* and *b* also show that these interfacial strains are not laterally continuous but the interface alternate 100-200 nm long strained and non-strained segments. The origin and distribution of these interfacial strains is not well understood yet. A selected area diffraction (SAD) pattern of the anatase film viewed along the [100] STO zone axis illustrated in *Figure 3.15c* shows sharp spots that indicate perfect epitaxy. Additionally, the SAD pattern taken across the anatase-STO interface (*Figure 3.15d*) revealing a sharp epitaxial relationship between the film and the substrate along the main crystallographic directions.

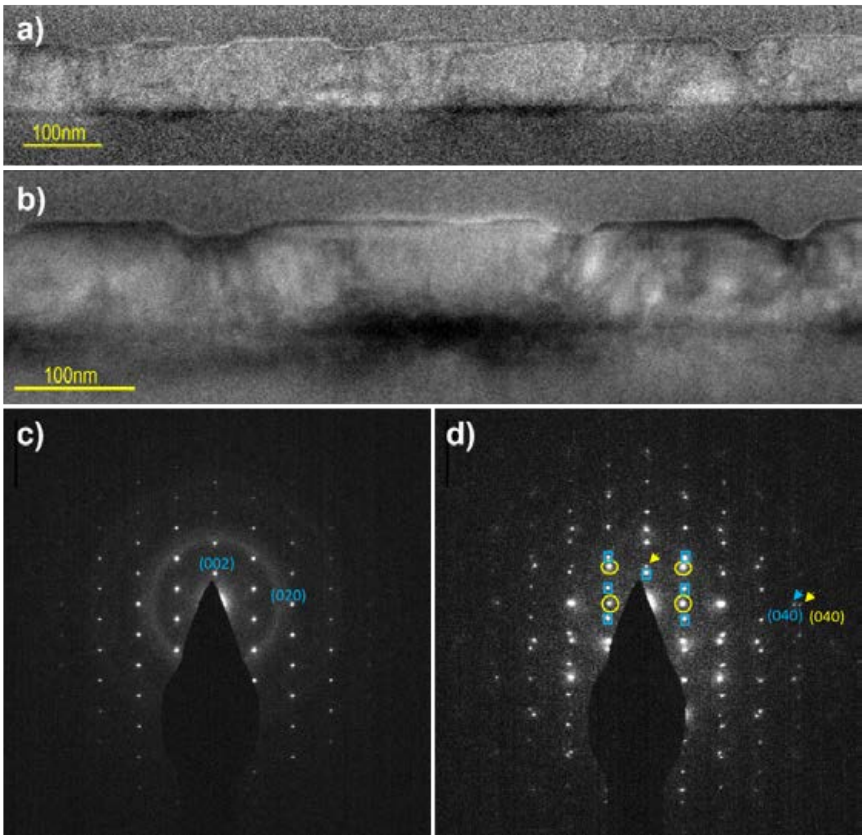

Figure 3.15: (a), (b) cross-section images and SAD pattern taken along the [100] STO zone axis of (c) anatase film and (d) anatase/STO interface, yellow symbols correspond to STO and blue symbols to A. The two arrows at the (040) reflections show splitting, indicating misfit relaxation.

The high-resolution image shown in Figure *3.16a* clearly shows that the terraces are atomically flat. The top-most layers exhibit a darker contrast and a dilation of the lattice along the [001] direction, indicating strain on the surface compared to the bulk (*Figure 3.16b*). Geometrical phase analysis (GPA) was carried out to study the strain through the uppermost layers of the film. *Figure 3.16c* and *Figure 3.16d* show the evolution of the in-plane and out-of-plane strain, respectively. It is observable that on the most superficial layers of the terraces, far from the columnar defects, the strain distribution is homogeneous, while at the surface the strain increases giving rise to the dark contrast areas seen on the surface (*Figures 3.15a* and *b*). These variation could be explained by disorder induced by the prohibitive high surface energy of the anatase (001) surface[129,130].

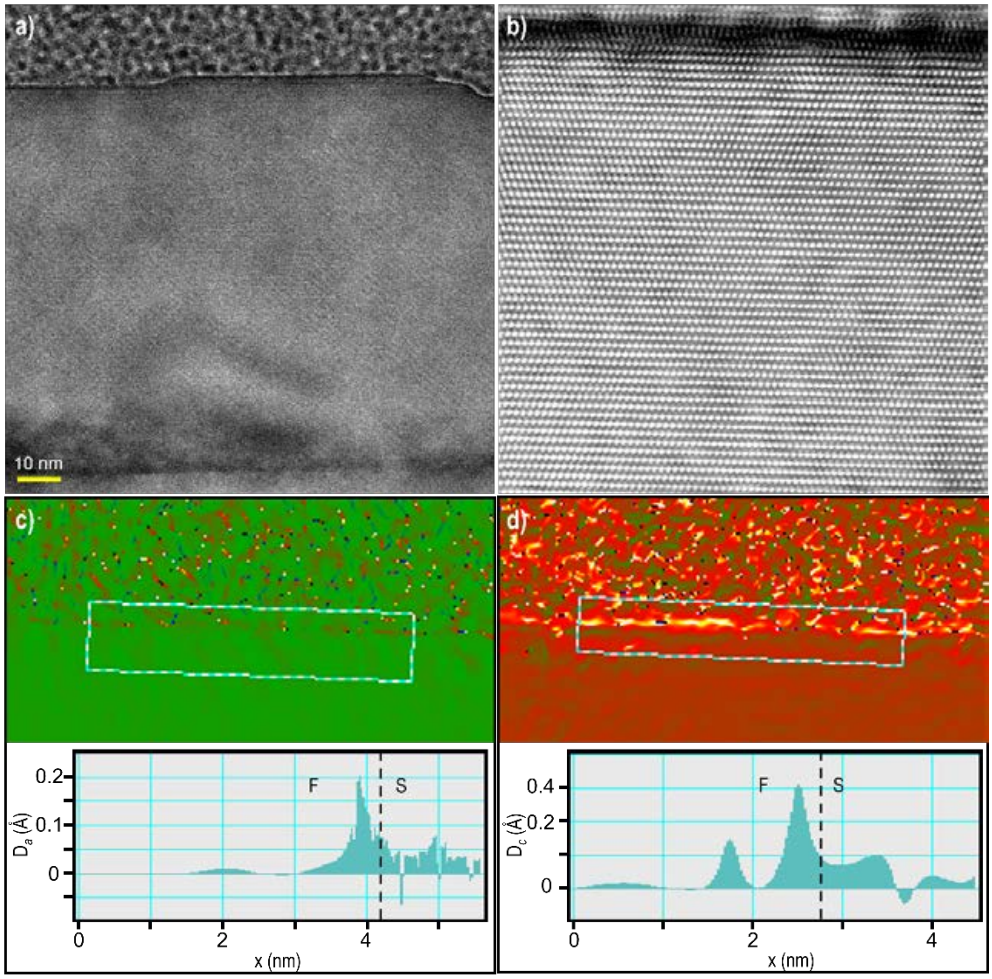

Figure 3.16: (a-b) HRTEM image of the TiO_2 film along the [100] STO zone axis, GPA analysis of the topmost layers for the anatase films of (c) in-plane strain and (d) out of plane strain. The discontinuous black line indicates the end of the bulk of the film (F) and its surface (S).

Periodic contrast modulations are clearly seen in *Figure 3.17a* on a region of the film free of extended defects with an atomically flat (001) terrace. These modulations lead to different spots in the fast Fourier transform (FFT) close to the expected anatase reflections (*Figure 3.17b*). The superlattice spots are mainly arranged along the [0 -1 3] * reciprocal space direction (arrowed in the FFT), indicating a period comprised in the range 1.30-1.39nm. *Figure 3.17c* is a filtered image showing the modulation in more detail.

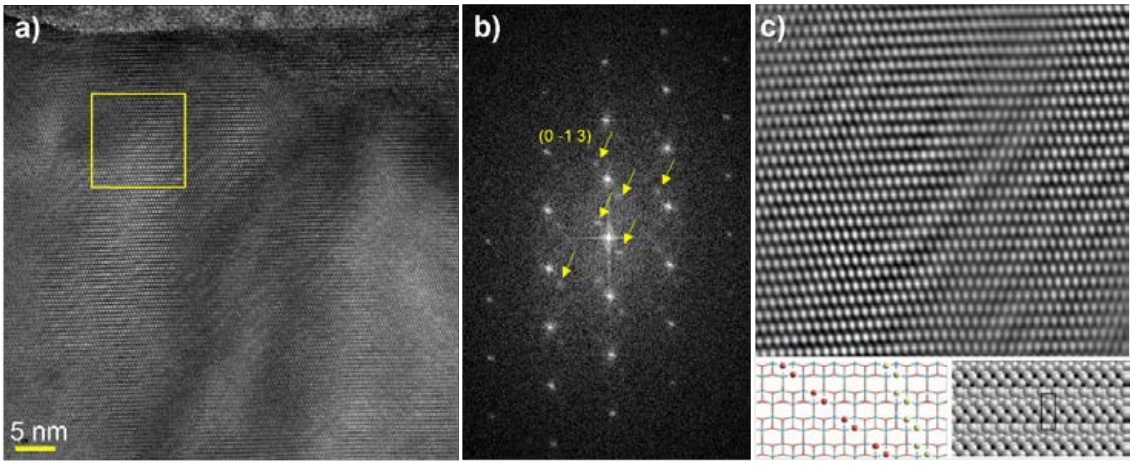

Figure 3.17: (a) HRTEM image along the (001) STO axis, (b) FFT of the marked area in (a) and (c) Filtered image. Insets in (c) structural models for Magneli-like anatase phase, wire-frame model viewed down the (010) direction (left) and ball model (right) extracted from Ciancio et.at.[131]*c*

These structural modulations have been typically attributed to the formation of Magnéli-like (Ti_nO_{2n-x}) phases along {013} shear planes[131]. The insets displayed in *Figure 3.17c* are the structural models presented by Cianco et.al[131] for Magnéli-like phases in anatase. Recently, Knez D. et.al.[132] assign the presence of these modulations to the formation of ordered distributions of oxygen vacancies, arranged in periodic superstructures, with changing oxygen concentration within the thin film, without crystallographic shear planes. Thus, the modulations that we observe in our film are indicative of oxygen deficiency, which is confirmed by the presence of Ti^{3+} as it will be described in *Chapter 5: Water and oxygen interface with anatase (001) thin films*. The intensity of the superlattice spots varies markedly depending on the studied area.

Figure 3.18a shows a columnar defect of the film at boundary of a terrace bounded by a (013) plane. *Figure 3.18b* illustrates an area of the film with a perfect structure, showing a flat terrace, where the left facet bounding the terrace is also (013) oriented. On the other hand, *Figure 3.18c* displays a flat terrace bounded by a rough vicinal facet.

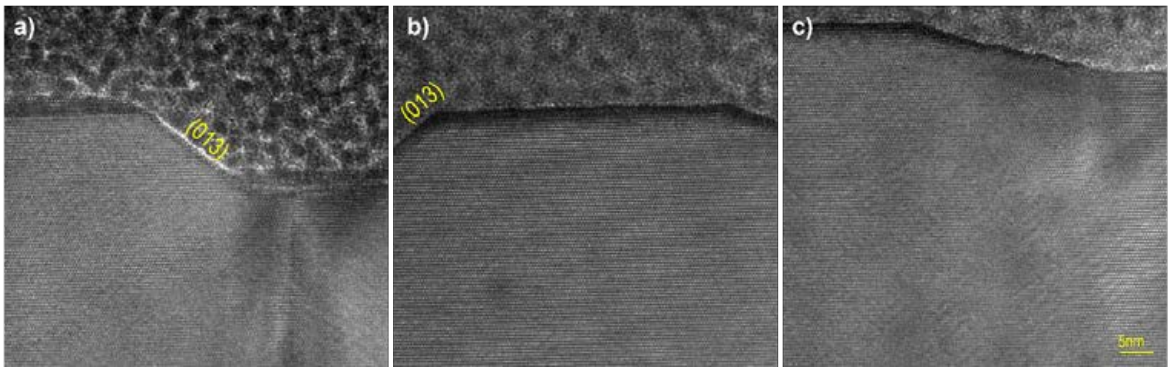

Figure 3.18: HRTEM images with different vicinal facet orientations.

Figure 3.19a shows a region of the film with (011) defects. Such defects involve a small tilt, as indicated by the splitting of the (004) reflection in the FFT (*Figure 3.19b*). The dark contrasts indicate that these defects

are associated with strong strains. The nature of these defects is still unclear. We note that a (101) twin would involve a much larger tilt angle compared with the one present on these defects.

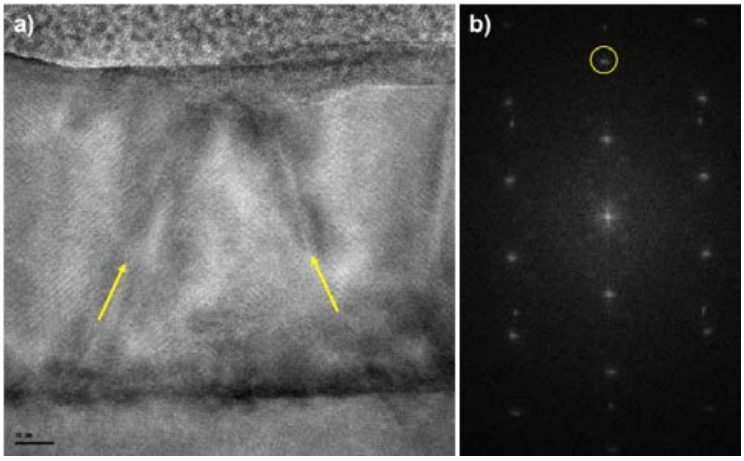

Figure 3.19: (a) HRTEM image showing (011) defects (marked with arrows) and (b) FFT indicating the (004)) reflection splitting.

3.2.2. MBE growth

The starting point to grow MBE samples was the PLD growth conditions. However, the best growth conditions were optimized by a collaborator[133]. This section will focus on the comparison of samples prepared by MBE with those grown by PLD to prove the possibility of getting same quality and same properties of TiO_2 thin films independently of the growth technique employed for their preparation.

TIO_2 films grown by MBE were deposited evaporating Ti on STO hold at 650ºC and with an oxygen pressure inside the chamber of 10^{-6} mbar with a previously calibrated titanium flux of 0.012 Å/s. The deposition of 8nm of titanium corresponds to a 16nm thick layer of TiO_2 anatase. This relation is maintained for all samples. To check the homogeneity of the coating AES spectra was measured. In *Figure 3.20* the Sr peaks are residual and almost no visible once TiO_2 is deposited proving that the film is fully covered. The small oscillation appearing at the lowest kinetic energy could indicate that small areas of the STO surface could be irradiated through the holes formed in the regions between adjacent domains as those present in *Figure 3.22*.

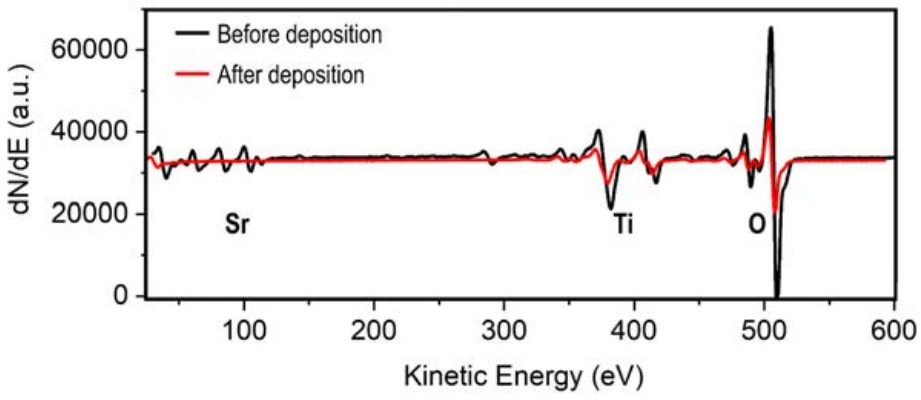

Figure 3.20: AES spectra before (black) and after (red) TiO_2 deposition.

Just after the deposition, all the MBE samples present a diffuse LEED pattern with broad spots indicating a bad-ordered film structure. To obtain a sharp pattern, samples were annealed ex-situ (850ºC, 6hours) and then re-introduced in the UHV chamber for being cleaned by a soft Ar^+ sputtering (10^{-6} mbar, 500eV, 2 minutes) and by heating it up in oxygen (850ºC, 10^{-6} mbar of O_2, 30 minutes). The following LEED pattern changes and now presents sharp pattern with two domains of the (4x1) reconstruction of (100) anatase [134]. A two-domain structure, formed by a (4x1) and (1x4) reconstructions, comparable to those reported by Herman et al.[135] and by Hengerer et al.[136] is seen. All samples presented this reconstruction except the thinnest deposit of 2nm of anatase. The important fact is that we can obtain the same type of reconstruction of samples independently of the growth technique. *Figure 3.21* shows the comparison of the LEED patterns of two samples one grown by MBE, with the above-mentioned conditions, and one by PLD, deposited at 875ºC similar to the one presented in *Figure 3.10e*. The as-prepared PLD sample LEED pattern presents a diffuse pattern; however, after a short cleaning process under the same conditions used to improve the MBE sample, the same (4x1) surface reconstruction appears. Thus, demonstrates that we can grow good quality anatase (100) with similar surface structures by two different techniques.

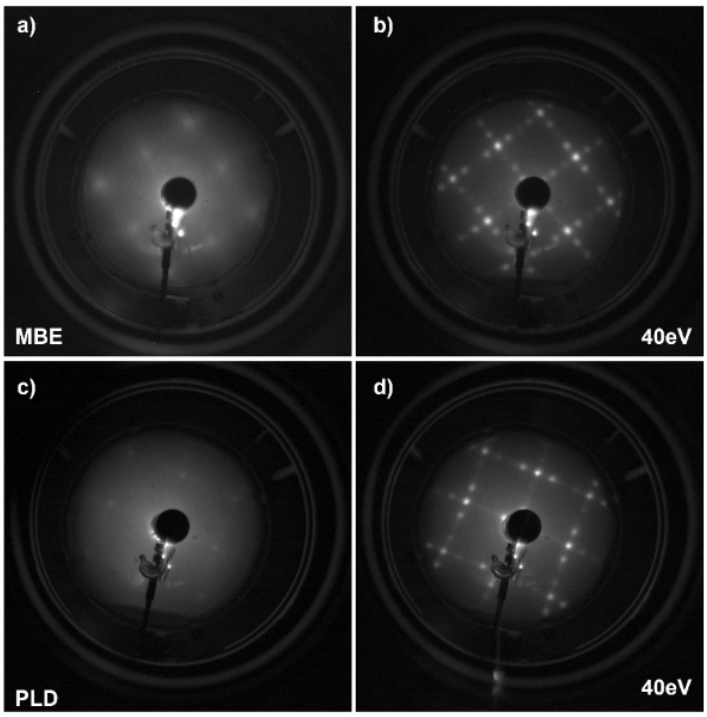

Figure 3.21: LEED pattern of an 8 nm thick anatase film prepared by MBE (top): (a) sample as deposited and (b) sample after annealing ex-situ at 850ºC. LEED pattern of a 55 nm thick anatase film prepared by PLD (bottom): (c) sample as deposited and (d) sample after annealing at 850ºC.

To investigate the atomic structure and surface morphology of anatase (001) and to understand better the surface reconstruction STM images were taken. *Figure 3.22a* is an AFM image of an 8nm thick MBE sample. The terraces of this sample present flat terraces of approximately 100nm, which analyzed in detail by STM (*Figure 3.22b*) show that each terrace is probably formed by 2 smaller islands. From the STM image it is possible to see that anatase presents well-defined regions with parallel rows of atoms along the [100]

crystallographic direction of the STO surface with an average separation of about 1.5 nm, displayed in the profile shown in *Figure 3.22c*, which is approximately four times the (1x1) unit cell distance (~15.12Å).

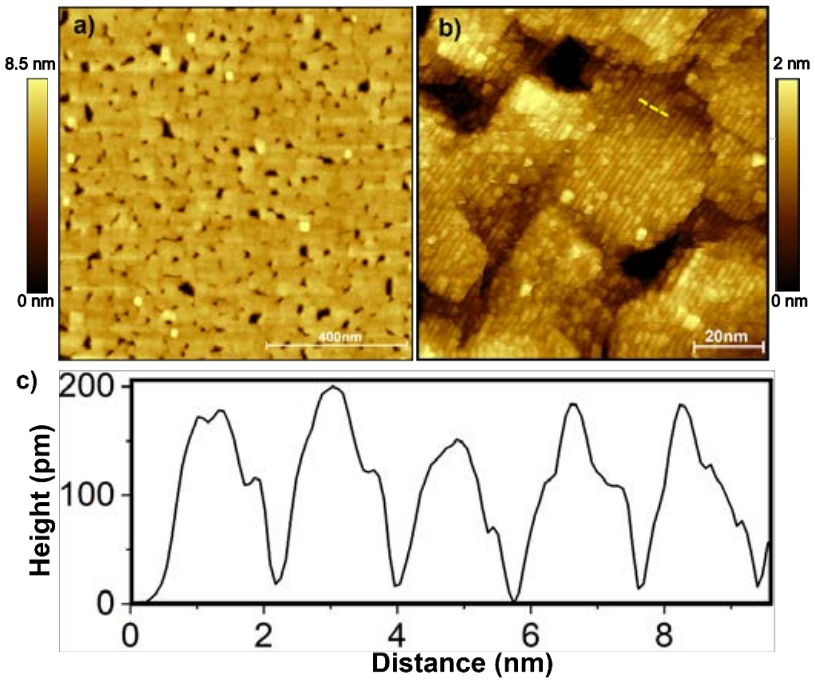

Figure 3.22:(a) 1x1 μm² AFM image and (b) STM image of an 8 nm thick anatase (001) film. At the nanometer scale the typical rows of the (4x1)/(1x4) reconstruction are observed (c) line profile of the yellow line.

Comparing samples grown by PLD and MBE, the typical flat terrace sizes obtained from PLD after thermal treatment are larger than those from MBE, which could be explained by their different thicknesses, 50nm vs 8nm, respectively. *Figure 3.11* shows holes between adjacent islands, that are filled during the annealing stages when the small islands coalesce, which makes the surface of the films more homogeneous. Thus, the thickness of the film is relevant to provide the necessary material to fill these gaps and homogenize the surface during coalescence.

3.2.3. Discussion

The presence of oxygen vacancies observed in our films can modify the magnitude of the lattice parameters of the film. Thus, the evolution of the c-lattice parameters must be related with the different arrangement and the variable concentration of those vacancies along the anatase (001) film. A larger out-of-plane lattice parameter compared to the bulk one could be explained by oxygen vacancies, as they are known to expand the unit cell[137,138]. XRD measurements done on the films deposited at different oxygen pressures reveal that the *c*-lattice parameter decreases at higher pressures keeping the temperature constant at 600ºC, which is consistent with the expected less amount of the oxygen vacancies when the pressure is increased. Additionally, it has been noticed that above 85 mTorr the out-of-plane lattice parameter remains stable at a certain temperature meaning that the minimum amount of oxygen vacancies in the film is achieved in this range.

Annealing processes at higher temperatures (T>950ºC) results in the coexistence of anatase and rutile, as presented in *Figure 3.15*. The positions of the anatase films peaks in the XRD revert to those of the anatase bulk ($c_{film}=c_{bulk}$) when the formation of rutile starts around 925ºC. A further increase of the temperature would induce the complete transformation from anatase crystal to rutile. From our XRD measurements, it is observed that the anatase-rutile transition occurs progressively and that the XRD intensities of the anatase peaks, with the presence or absence, of rutile are very similar and compatible with this type of transition[139].

A limitation to obtain bigger terraces on the TiO_2-anatase surface could be related with the PLD deposition rate. It has been demonstrated that the deposition time is relevant during the growth process. It increases the mobility of the specimens adsorbed on the STO surface allowing a more uniform growth[140]. However, it was not possible to reduce the laser's frequency, since 1Hz was the limit of our system. At this frequency, a 50 nm thick film grows in about 25 minutes (1500 pulses). In contrast, MBE techniques would employ 12 hours at typical growth rates of 0.012 Å/s. A longer deposition time leads to higher terraces sizes, as it could substitute the annealing process according to the results obtained by Du Y. et al, which deposited about 96 monolayers of TiO_2 with MBE (deposition rate ~0.012 Å/s) and obtained terraces of large platelets with an average lateral domain size of ~400 nm[140]. For these reasons, the anatase film synthesis involves two steps: growth at a given temperature plus a long annealing in air or oxygen at high temperatures. These steps allow the anatase grains to coalesce into a flat terraced surface (*Figure 3.12*). The samples prepared by PLD, and MBE shown in *Figures 3.13* and *3.23* generate patterns of coalescence of islands like those observed by other authors[140,141] with similar sizes, however, some differences between them are noted. The 10 nm film synthesized by PLD at 800ºC by Liu G. et. Al.[141] indicates that island coalescence is reached at the temperature of growth, however, the work does not offer any information on whether or not any post-heat treatment was applied to the film. In our 50 nm anatase thin films, coalescence is achieved after annealing at temperature between 800ºC and 900 ºC. The samples prepared at any growth temperature by PLD, without post annealing, never coalesce as evidenced in *Figure 3.11*. Consequently, annealing of the film at high temperatures is mandatory to induce coalescence of the grains. The large domain sizes achieved by MBE at a deposition temperature of 750ºC of Du Y. et al.[140] are recovered in our thick-film samples after a long air annealing at high temperatures.

3.2.4. Conclusions

We have grown epitaxial anatase (001) TiO_2 films by two different techniques: PLD and MBE. The film quality obtained from both techniques is similar after annealing treatments. The effects of the deposition temperature on the film growth have been studied, as well as the role of the temperature and time during the film annealing process. It is possible to control the average size of the anatase (001) surface terraces, almost independently of the deposition temperature by performing a long post-growth annealing at high temperatures (900ºC during 6 to 12 hours) in air or oxygen. For 50nm thick films the post-growth annealing processes can transform the film's surface from a granular-like morphology into a terraced-like morphology,

increasing the average lateral domain size of these terraces up to 400nm. A greater increase in the terraces size has been found when the initial grain size was bigger, as shown in *Figure 3.14*, where starting from an average size of 150nm is possible to obtain terraces sizes around 650nm, which highlights the importance of the annealing time and temperature as well as the initial grain size. The measurement of the bandgap for all samples should be done to evaluate the photocatalytic performance for the different morphologies obtained.

It has also been proved that the maximum useful annealing temperature to enlarge the flatness of the anatase (001) film surfaces is 925ºC. At this temperature, the maximum expansion of the lattice parameters is achieved, while at 950ºC the phase transition from anatase to rutile begins to appear.

In addition, the evolution of in- and out-of-plane lattice parameters with temperature for the anatase films has been described. The first ones remain almost constant with temperature, while the *c* lattice parameter expands gradually with temperature. This behaviour has been assigned to the presence of oxygen vacancies, which lead to the anatase peaks shifts observed in the x-ray diffractograms taken for samples prepared at different oxygen pressures at a certain temperature and for samples grown at various temperatures at the same pressure.

We have observed, independently of the growth technique employed (PLD or MBE), the 4x1/1x4 anatase surface reconstruction in UHV conditions after two successive cycles of Ar^+ ion sputtering (0.6 KeV, P_{Ar} = $5 \cdot 10^{-6}$ mbar, t=5min) and annealing at 850ºC under an oxygen pressure of 10^{-6} mbar. The quality of those films permitted the realization of photoemission and surface diffraction experiments, that are described below.

3.3. $BaTiO_3$ growth conditions

One of the objectives of this work is to obtain high quality epitaxial BTO films to combine its ferroelectric properties with TiO_2 films to build heterostructures to check their possible applications in photocatalysis experiments. To accomplish this objective, different ferroelectric films were prepared. These films constitute the precursor work, for later studies on the behaviour of their remnant polarization when combined with other heteroepitaxial films, i.e., TiO_2.

In this section, the film growth process of BTO (diameter:5cm, purity: 99.99%, Mateck), is described. The objective is to obtain the maximum polarization along the (001) direction. Thus, these films were grown on STO (100) substrates due to the small mismatch between their respective in-plane lattice parameters resulting in a compressive mismatch that promotes the out of plane parameter expansion enhancing the polarization in that direction. For ferroelectric characterization BTO was grown on a layer of $SrRuO_3$ deposited on STO (100) or directly on STO (100) doped with Nb (STO-Nb) ($SrTiO_3$: Nb 0.5 wt%, CrysTec, 5x5x0.5mm). BTO films were grown at three different rates (2Hz, 5Hz and 10Hz), the effect of the oxygen

background pressure (1mTorr-100mTorr) was checked, and the influence of the growth temperatures was also evaluated (600-750ºC). The compressive misfit resulting from the BTO deposition on STO favors the out of plane polarization and according to J. Lyu et.al. also, it could enhance the polarization along the [001] direction. Recently, a study published by Li, Z. et.al. says that "it could be understood that the polarization is associated with the lattice parameter of c-axis and the tetragonality value (c/a)"[142]. Thus, the aim is to obtain the flattest surface achievable to have the best layer to grow TiO_2 on it and the higher *c*-lattice parameter as possible. For that reason, the criteria to select the best growth conditions have been the position of the (002) BTO reflection (P) with the roughness of its surface (*rms*), the nominal thickness (t) of the samples, as well as the crystallite size (CS) obtained with the Scherrer equation. Scherrer gives dimension of the coherence domain in the direction normal to the diffraction plane, in this case the (002). It is noticeable that the CS does not perfectly match the thickness, which it indicates that there is a non-crystalline part in the film. These results are consistent with the TEM images that will be presented in *Section 3.5 Heterostructures,* where the interface between BTO and STO seems to be rough and shows strong and extended strain contrasts (*Figure 3.68*). *Table 3.4* summarizes the samples that will be presented through this section, where BS indicates BTO grown on STO (100) substrates, BS_{Nb} corresponds to BTO deposited on STO-Nb (100) substrates and BSS is assigned to BTO grown on STO (100) with an $SrRuO_3$ buffer layer. The number of pulses was maintained at 1500 for all the samples corresponding to ~50nm thick, except those indicated on *Table 3.4*.

Label	Conditions	P (º)	*c* ±0.01 (Å)	t ±1 (nm)	CS ±5 (nm)	*rms*±0.02 (nm)
BS_01	2Hz. 700ºC,1mTorr, 3800 pulses	43.88	4.12	78.3	51.09	0.19
BS_02	2Hz. 700ºC,50mTorr, 3800 pulses	44.06	4.10	75.6	41.92	0.21
BS_03	2Hz. 700ºC,100mTorr, pulses	45.17	4.01	79.2	60.24	0.25
BS_{Nb}_01	2Hz. 700ºC,1mTorr	43.29	4.175	48.1	36.60	0.25
BS_{Nb}_02	5Hz. 700ºC,1mTorr	43.47	4.159	47.2	41.90	0.38
BS_{Nb}_03	10Hz. 700ºC,1mTorr	43.58	4.149	45.8	33.44	0.27
BS_{Nb}_04	2Hz. 700ºC,10mTorr	43.49	4.157	46.5	25.04	0.38
BS_{Nb}_05	2Hz. 700ºC,50mTorr	44.80	4.041	48.3	55.98	0.5
BS_{Nb}_06	2Hz. 700ºC,100mTorr	45.11	4.015	49.3	46.52	1
BS_{Nb}_07	2Hz. 600ºC,1mTorr	43.03	4.199	47.7	36.39	0.41
BS_{Nb}_08	2Hz. 650ºC,1mTorr	43.49	4.157	48.2	27.66	0.32
BS_{Nb}_09	2Hz. 750ºC,1mTorr	43.61	4.146	45.1	22.24	0.22
BSS_01	2Hz. 700ºC,1mTorr	43.68	4.139	46.2	38.89	0.28
BSS_02	2Hz. 700ºC,10mTorr	43.78	4.131	48.6	33.62	0.32
BSS_03	2Hz. 700ºC,20mTorr	43.78	4.131	47.5	19.42	0.33
BSS_04	2Hz. 700ºC,40mTorr	43.88	4.121	45.6	29.23	0.31
BSS_05	2Hz. 700ºC,1mTorr, 800 pulses	43.594	4.147	29.3	24.05	0.33
BSS_06	2Hz. 700ºC,1mTorr	43.83	4.126	50.3	28.83	0.29
BSS_07	2Hz. 700ºC,1mTorr, 2400 pulses	43.996	4.111	81.2	33.87	0.33
BSS_08	2Hz. 700ºC,1mTorr, 3800 pulses	44.082	4.104	124.8	41.92	0.31
BSS_09	2Hz. 700ºC,1mTorr, 4500 pulses	44.164	4.096	152.3	48.25	0.35

Table 3.4: Sample list of BTO deposited films on different conditions. All samples, except for the ones that is indicated, present an average thickness of ~50nm.

3.3.1. $BaTiO_3$ on STO (100)

First, BTO conditions were optimized to grow on STO (100) substrates. The initial temperature was set to 700ºC, and the laser energy was fixed at 90mJ as previous results in our group[143] indicated that BTO grew with good quality on STO substrates with those parameters.

The BTO growth was monitored in-situ by RHEED for the sample BTO_STO_01, prepared at 700ºC and at 1 mTorr. The first image (*Figure 3.23a*) corresponds to the bare clean STO substrate RHEED pattern. Kikuchi lines (KL), produced by inelastic scattering processes, usually appear on highly crystalline flat substrates. *Figure 3.23b* is the RHEED pattern obtained after the deposition of the BTO film.

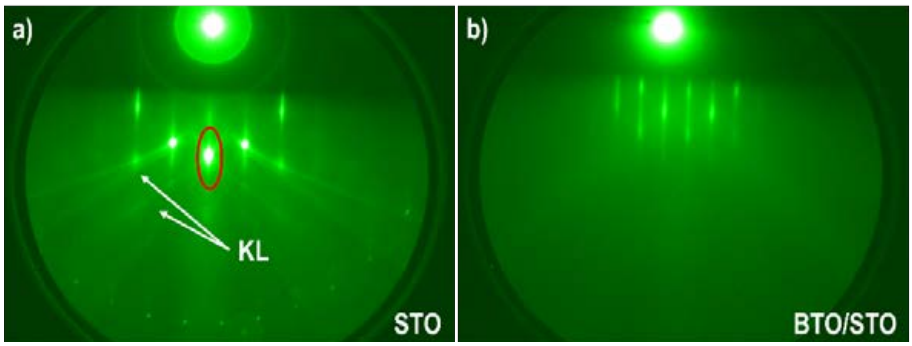

Figure 3.23: RHEED patterns obtained along [100] azimuthal direction for (a) STO (001) and (b) BTO (001).

The intensity of the circled spot was monitored to obtain the specular RHEED intensity plotted in *Figure 3.24*. The intensity oscillations at the beginning of the deposition indicate a layer-by-layer growth mode.

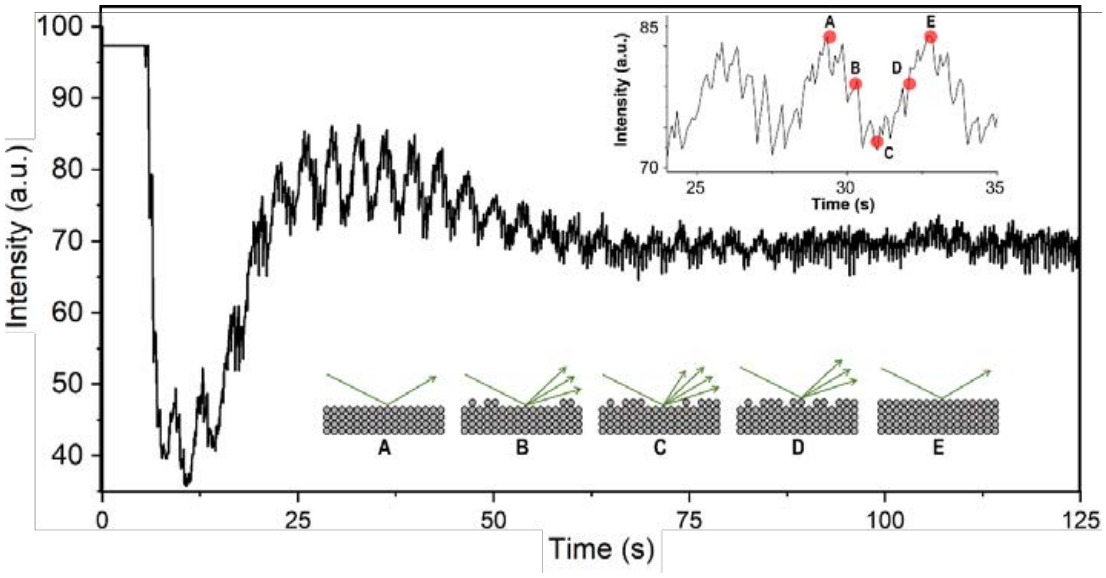

Figure 3.24: Specular spot intensity obtained during the growth of BTO at 700ºC, 1mTorr and 2Hz. Insets show an amplified region. The red dots indicate at which growth stage is the layer.

Approximately every 10 pulses 1 monolayer (ML) is finished and a maximum corresponding to a fully terminated layer is obtained (spots A and E), which is a ~0.4Å/pulse growth rate. The immediate rise of grains density when the vaporized material is deposited on the surface provokes an intensity decrease after

each pulse. Then, intensity dramatically increases as the grain's density reduces. After 250 pulses, the intensity oscillations are clearly seen, indicating a layer-by-layer growth of the first 25 monolayers. In short, BTO films deposited at 1mTorr, 700ºC and 2Hz give rise to flat samples (*rms*< 0.20nm) with a layer-by-layer growth mode.

The effect of growing at different oxygen pressures was tested to elucidate at which pressure BTO presents the higher *c* lattice parameter value. *Figure 3.25* shows several x-ray diffractograms corresponding to ~80nm thick films prepared at the same conditions (700ºC, 90mJ, 2Hz) except for the oxygen pressure at 100mTorr (blue), 10mTorr (red) and 1mTorr (black). The (00*L*) reflections are marked with S and B for the substrate and the BTO, respectively. BTO grows perfectly (001) oriented, as no other reflections coming from other phases or orientations can be seen. BTO reflection shift to lower 2θ angles as the growth pressure decreases. Thus, indicates an increase of the *c* lattice parameter from 4.01Å at 100mTorr to 4.12Å at 1mTorr, which could lead to an enhancement of the polarization along the (001) direction[62,142].

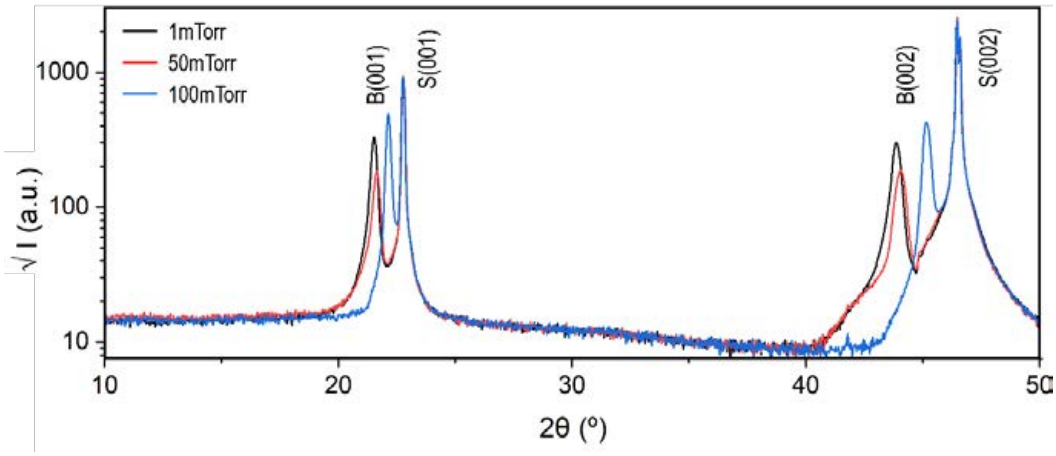

Figure 3.25: XRD θ-2θ scan of BTO samples prepared at 1mTorr (BS_01),10mTorr (BS_02) and 100mTorr (BS_03).

The morphology of the prepared samples was studied by AFM to investigate the surface topography changes with pressure (*Figure 3.26*). At 1mTorr, a 2d terrace-like morphology can be appreciated in the AFM images, nevertheless the 1x1 μm^2 indicates a more granular-like surface (insets in *Figure 3.26*). At higher oxygen pressures (10 and 100mTorr), the 2d terraced-like morphology is no longer observable. Additionally, the surface roughness does not seem to be affected by the oxygen pressure. At 1mTorr the surface roughness is *rms*~0.19nm. At higher pressures, the *rms* roughness slightly increases to 0.21nm and to 0.25nm for the samples deposited at 10mTorr and 100mTorr, respectively.

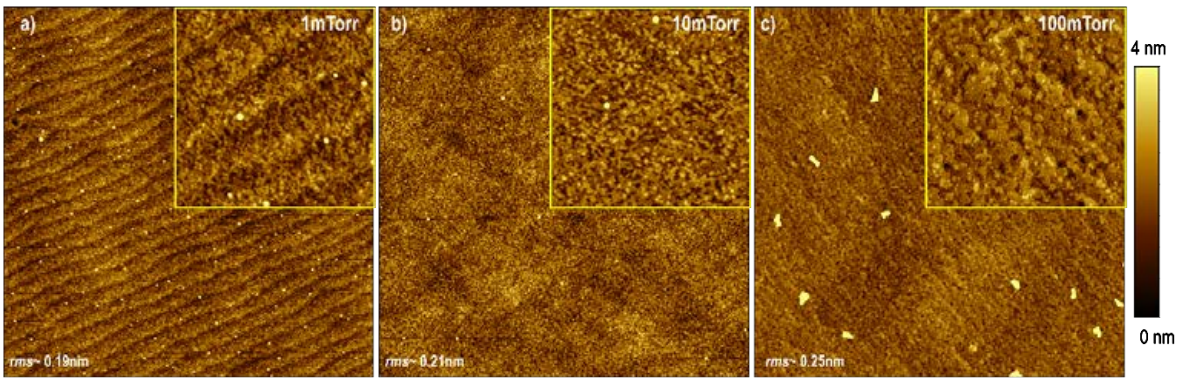

Figure 3.26: 5x5 μm² AFM images of samples prepared at (a) 100mTorr, (b) 10mTorr and (c) 1mTorr. Insets show 1x1 μm² AFM images.

High quality epitaxial BTO films on STO (100) substrates were obtained at all the pressures selected. Nonetheless, the best deposition pressure for our objectives was 1 mTorr, as it presents the higher *c*-lattice parameter and the flattest surface. However, to measure the ferroelectric properties of BTO it must be grown over a conductive layer. For this reason, BTO was grown on STO-Nb and on $SrRuO_3$ (SRO).

3.3.2. $BaTiO_3$ on STO-Nb

These films were also grown on conductive STO doped with niobium substrates (STO-Nb) ($SrTiO_3$: Nb 0.5 wt%, CrysTec, 5x5x0.5mm). In STO-Nb substrates, the Nb^{5+} atoms substitute the Ti^{4+} atoms when is incorporated to the STO structure[144,145]. In addition, STO-Nb lattice parameters are slightly different compared to STO (3.908 vs 3.905Å)[144] and the roughness of the surface is also higher (*rms* ~0.1nm). Thus, a range of temperatures (600ºC-750ºC), oxygen pressures (1-100 mTorr) and different deposition rates (2Hz, 5Hz and 10Hz) were tested for ~50nm thick BTO/STO-Nb thin films.

Influence of the deposition rate

First, the deposition rate was checked by fixing the other parameters with the optimized conditions of section *3.3.1. BaTiO3 on STO (100)* (700ºC, 1mTorr, 90mJ) films. The x-ray diffractogram (*Figure 3.27*) reflects a small variation in the BTO peak position depending on the rate used. The growth rate has a small effect on the c-lattice parameter, as summarized in the inset of *Figure 3.27*, compared to other deposition parameters such as pressure or temperature.

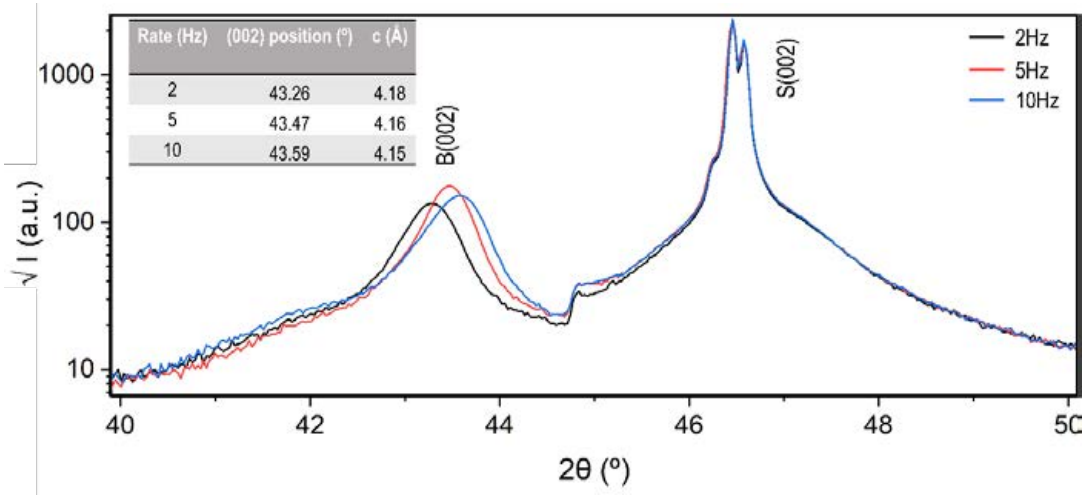

Figure 3.27: XRD θ-2θ scan of BTO deposited at different growth rates: 2Hz (BS_{Nb}_01), 5Hz (BS_{Nb}_02) and 10Hz (BS_{Nb}_03). The inset summarizes the different deposition parameter, the (002) BTO reflection position and the c parameter of the prepared films.

The AFM images (*Figure 3.28*) show similar surfaces independently on the deposition rate presenting a granular-like topography. There is no clear correlation between the deposition rate used and the roughness of the obtained film. Depositing at 5Hz gives rise to the highest surface roughness (*rms* ~0.38nm), while at 10Hz and 2Hz decreases to 0.27nm and 0.25nm, respectively.

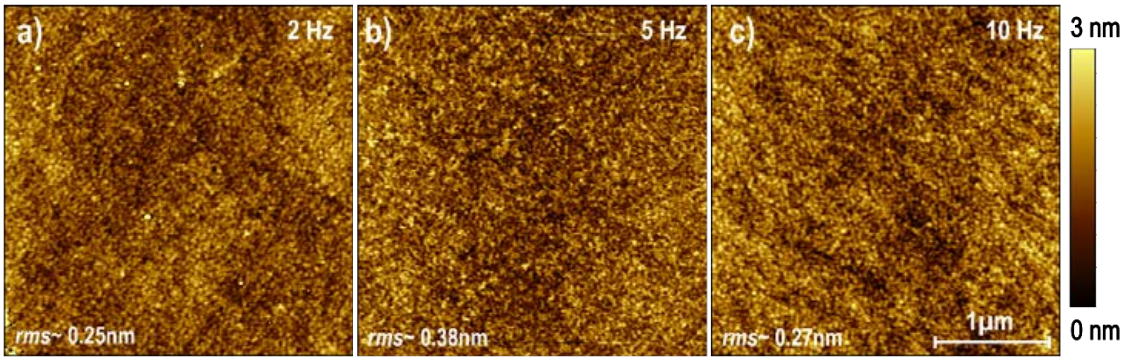

Figure 3.28: 3x3µm² AFM images of BTO deposited at different growth rates with their corresponding surface roughness.

From the results obtained the deposition rate selected was 2Hz, as it shows the highest *c*-lattice parameter and the flattest surface.

Influence of the oxygen pressure

The influence of pressure on the growth of BTO is illustrated in the x-ray diffractograms shown in *Figure 3.29*. From the analysis of the (002) reflection we can see a strong impact on the out-of-plane lattice parameter of the films. Pressures above 50mTorr tend to decrease the out-of-plane lattice parameter where the c_{film} of the BTO completely matches the c_{bulk}. The *c*-lattice parameter varies inversely with the oxygen pressure. It starts at 4.02Å when BTO is deposited at 100mTorr and achieves a maximum of 4.18Å for the films grown at 1mTorr, which is a difference of the 3.85% respect to the c_{bulk}. S.B. Mi et.al.[146] presents a 3% larger c_{film} compared to the c_{bulk} for a sample prepared at low deposition pressure (~1.5mTorr). Additionally,

Hiltunen, J. et.al.[147] studied the influence of the oxygen pressure on the lattice parameters with the same tendency as ours. As the gas pressure increases, the *c* lattice parameter decreases. A. P. Chen[148] investigated the oxygen pressure effect on the structural properties of BTO obtaining similar *c*-values to ours at different oxygen pressures e.g. 4.2 Å vs 4.18 Å for films deposited at low pressures, respectively. The obtained lattice parameters are similar to values reported in literature [146,147148].

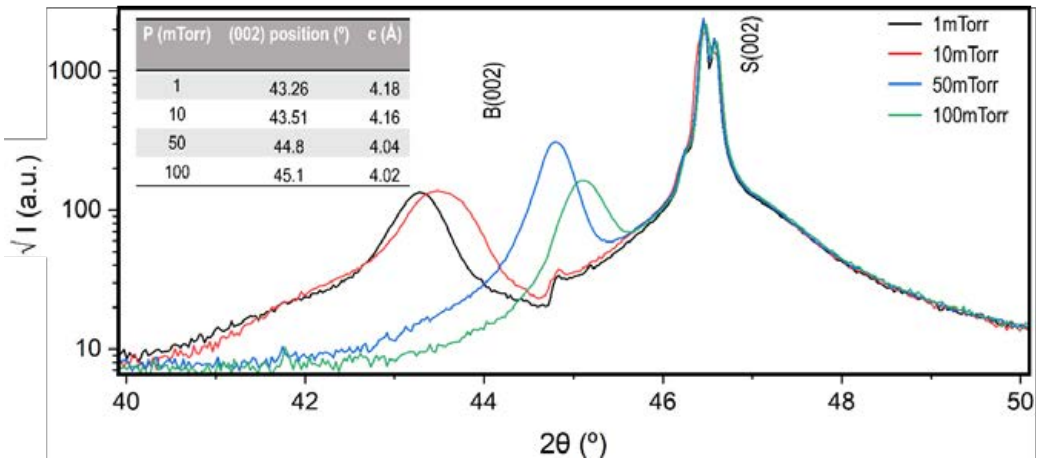

Figure 3.29: XRD θ-2θ scan of BTO thin films grown at different oxygen pressures: 1 mTorr (BS_{Nb}_01), 10 mTorr (BS_{Nb}_04), 50 mTorr (BS_{Nb}_05) and 100 mTorr (BS_{Nb}_06). The inset summarizes the different deposition parameters, the (002) BTO reflection position and the c parameter of the prepared films.

Figure 3.30 presents the different morphologies obtained for the BTO films deposited at different oxygen pressures. Samples deposited at pressures below 50 mTorr have a similar granular-like surface consisting of small islands of sizes around ~45nm (*Figure 3.30 a-c*). On the other hand, the surface of the sample grown at 100mTorr is filled with pit holes and flat islands with sizes around 90nm. The surface roughness tends to increase with the deposition pressure starting from a *rms*~0.25 nm for sample BS_{Nb}_01 (1mTorr) to 1 nm for the sample prepared with the highest pressure (100 mTorr).

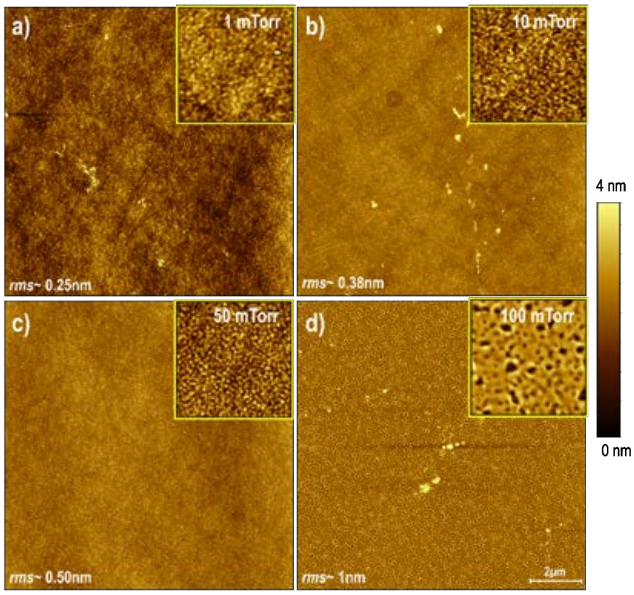

Figure 3.30: 10x10µm² AFM images of BTO grown on STO at different oxygen pressures. Insets show 1x1 µm² AFM images.

The pressure selected to deposit BTO on STO-Nb substrates was 1mTorr, as it has been demonstrated that gives the biggest out of plane lattice parameter and the best surface.

Influence of Temperature

Lastly, the influence of 4 different temperatures was checked. From results obtained in our group[143], which studied the BTO deposition at 600 and 700ºC, it was decided to test that range (600-750ºC). The x-ray diffractograms for the prepared samples are shown in *Figure 3.31*. The peaks of the (002) BTO reflections at 600ºC and 650ºC appear at lower Bragg angles compared to those obtained at the higher temperatures used. At 750ºC a double peak is observed, which indicates the presence of two different out-of-plane lattice parameters. The observed lattice parameters are similar to values reported in literature [149,150].

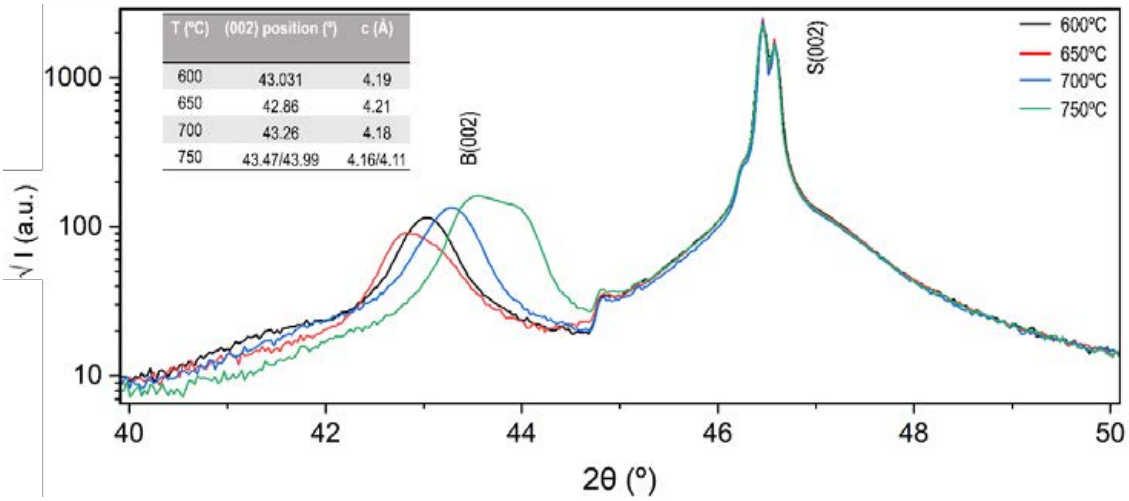

Figure 3.31: XRD θ-2θ scan of BTO samples deposited at a different temperature: 600ºC (BS_{Nb}_07), 650ºC (BS_{Nb}_08), 700ºC (BS_{Nb}_01) and 750ºC (BS_{Nb}_09). The inset summarizes the different deposition parameter, the (002) BTO reflection position and the c parameter of the prepared films.

Comparing the AFM images (*Figure 3.32*), sample BS_{Nb}_07, deposited at 600ºC, presents the highest roughness and a granular-like surface formed by islands of different shapes and sizes. At moderate temperatures (650-700ºC) the morphology of the surface is similar presenting a granular-like surface with regular shapes and sizes. On the other hand, a 2d terrace-like morphology can be appreciated for sample BS_{Nb}_09, deposited at 750ºC. Despite samples grown at low temperatures have a higher out-of-plane lattice parameter, the film that was grown at 700ºC shows better crystallinity and roughness (CS:37 nm and *rms*~0.25nm) compared to those films (CS: 36nm and *rms*~0.41nm at 600ºC and CS:28nm and *rms*~0.32 at 650ºC). Consequently, 700ºC was selected as the best growth temperature together with 2Hz of deposition rate and the oxygen pressure of 1mTorr.

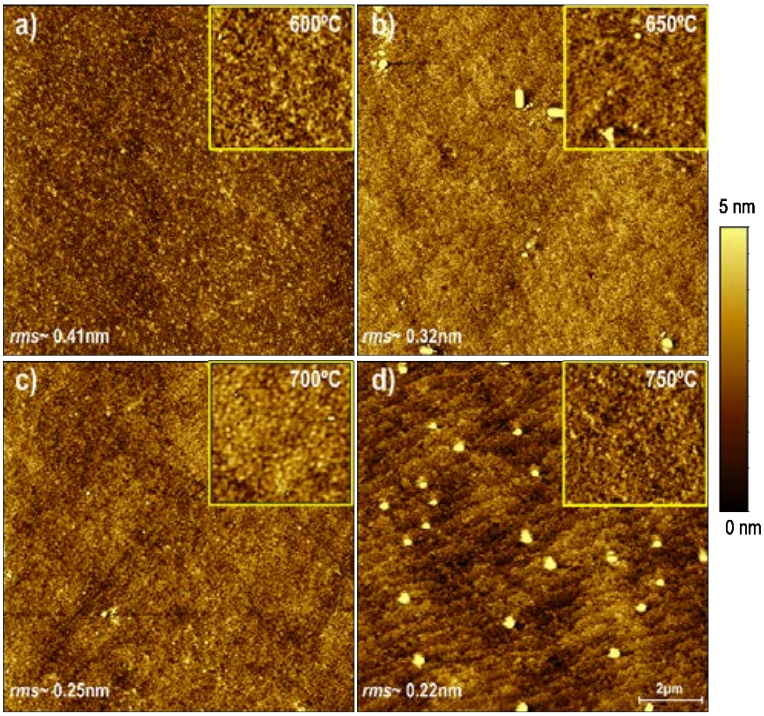

Figure 3.32: 5x5um² AFM images for samples prepared at different temperatures.

3.3.3. $BaTiO_3$/SRO on STO (100)

As an alternative to STO-Nb, we also grew BTO using an SRO buffer layer as a bottom electrode. Since SRO thin films are widely applied as conducting layers in epitaxial multilayered heterostructures of complex oxides. SRO is a perovskite with an orthorhombic symmetry at room temperature, the difference in length of the A-O bond compared to the B-O length leads to a rotation in the BO_6 octahedra. This rotation produces a distorted pseudocubic perovskite structure with a pseudocubic lattice parameter of 3.93Å, which provides good lattice matching with STO[151,152].

From the previous results, it has been noticed that the parameter most affecting to the roughness of the surface and the value of the out of plane lattice parameter is the oxygen pressure region below 50mTorr. Thus, it was the only parameter adjusted for the BTO/SRO/STO heterostructures. Additionally, the effect of the thickness in the evolution of the *c*-lattice parameter was studied.

The SRO growth parameters used were: 635ºC, 100 mTorr, 90mJ[153] and 15nm were deposited to obtain fully strained SRO layers. All the films deposited grew following the (001) orientation as seen on the x-ray diffractograms obtained from samples grown at different oxygen pressures (*Figure 3.33*). The (002) BTO reflections are broader at higher pressures (20 and 40mTorr) compared to those at lower pressures (10 and 1mTorr), where the peaks are better defined reflecting a larger crystallite size on the film. The position of the (002) peak remains almost constant for all the studied pressures. Additionally, Laue fringes, can be observed between the BTO reflection and the SRO peak, which indicate a sharp interface between the film

and the STO. Laue oscillations originate from interference events within the film due to the high crystal quality of the superlattices[154,155]. The presence of these fringes is usually used to confirm the good quality growth of films[156], their homogeneity and the uniformity of the film and smoothness, meaning that having a smooth and planar up and bottom interfaces[157]. This behavior is very common in oxides thin films[158,159]. These oscillations reflect the thickness of the deposited SRO layer.

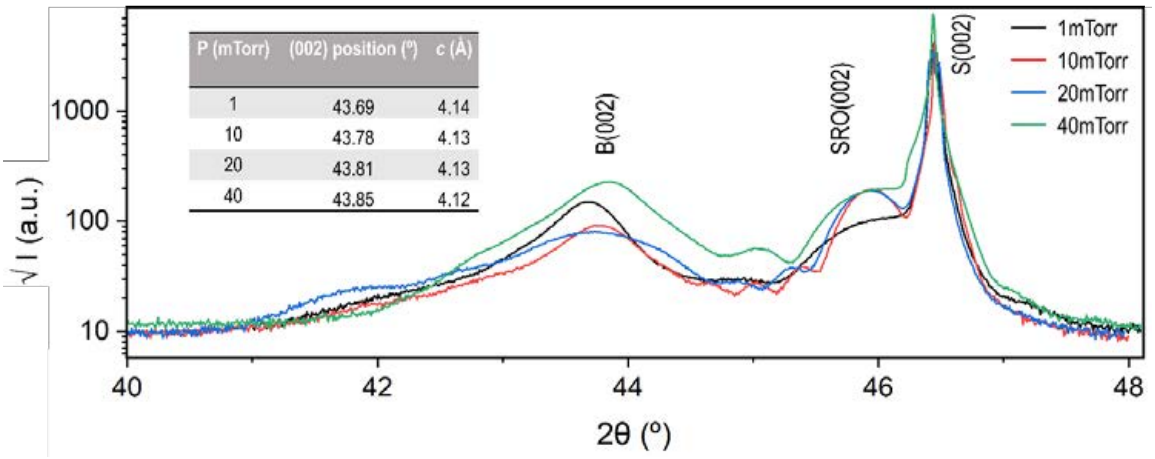

Figure 3.33: XRD θ-2θ scan of BTO/SRO/STO thin films prepared at a range of oxygen pressures: 1mTorr (BSS_01), 10mTorr (BSS_02), 20mTorr (BSS_03) and 40mTorr (BSS_04). The inset summarizes the different deposition parameter, the (002) BTO reflection position and the c parameter of the prepared films.

The AFM images (*Figure 3.34*) show a characteristic topography where the surface is not completely covered, and trenches have appeared along the STO step edges. However, the topography, for all the samples, inside the terraces presents a granular morphology with high density of small islands (*rms*~0.3nm). According to Choi et al., 2001[160], the terminating layer of the STO influences the initial growth of SRO thin films. When the initial TiO_2-terminated STO substrate is heated in the PLD system before deposition, some Sr can diffuse to the surface and relocates preferentially along the step edges. The presence of strontium affects to the uniformity of the SRO layer. The growth speed of the SRO is dependent on the STO termination, being faster on the B-sites (TiO_2) than on the A-sites (SrO). This different growth velocities leads to the trenches observed in the BTO/SRO/STO heterostructures, which will influence the macroscopic transport properties of the sample[161]. This topography has been previously reported in several studies[162–164]. The Sr diffusion into the step edges during the SRO deposition process is the cause that prevents the acquisition of fully covered and flat surfaces. It can be observed a tendency towards eliminating the trenches by lowering the BTO deposition oxygen pressure. However, better SRO growth conditions should be found to avoid the appearance of these trenches.

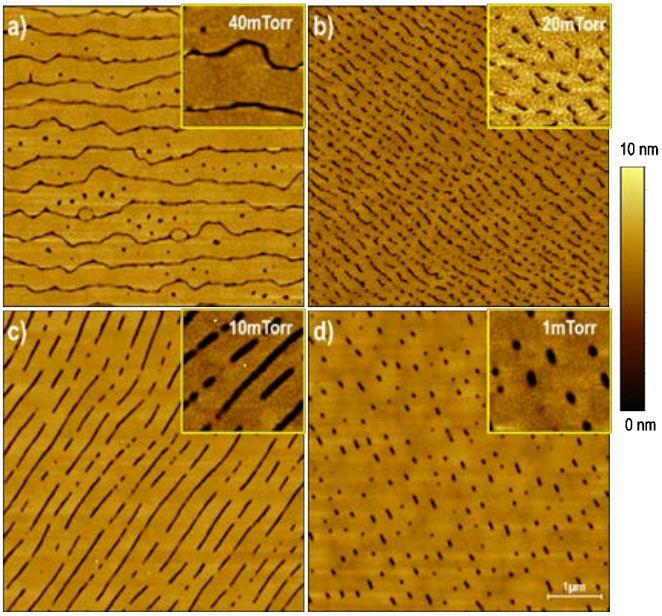

Figure 3.34: 5x5 AFM images of the BTO/SRO/STO samples prepared at different oxygen pressures.

The best conditions to obtain flat 2d-like BTO are 1mTorr and 700ºC as observed in the previous experiments.

Thickness influence

BTO was deposited on SRO/STO with different thicknesses (30-150nm) to investigate its effect on the deposited film. The (002) BTO reflection of the films shifts gradually towards the position of the bulk value indicating a decrease of the out-of-plane lattice parameter with increasing thickness (*Figure 3.35*). The film peaks become narrower in thicker samples, as the relaxed part of the film dominates the diffraction intensity. This behavior is typical for gradual strain relaxation by insertion of misfit dislocations into the heterostructure when the film thickness exceeds its critical thickness [165–168]. The thickness of the mismatched BTO layer must be small to accommodate the mismatch strain coherently with the STO substrate.

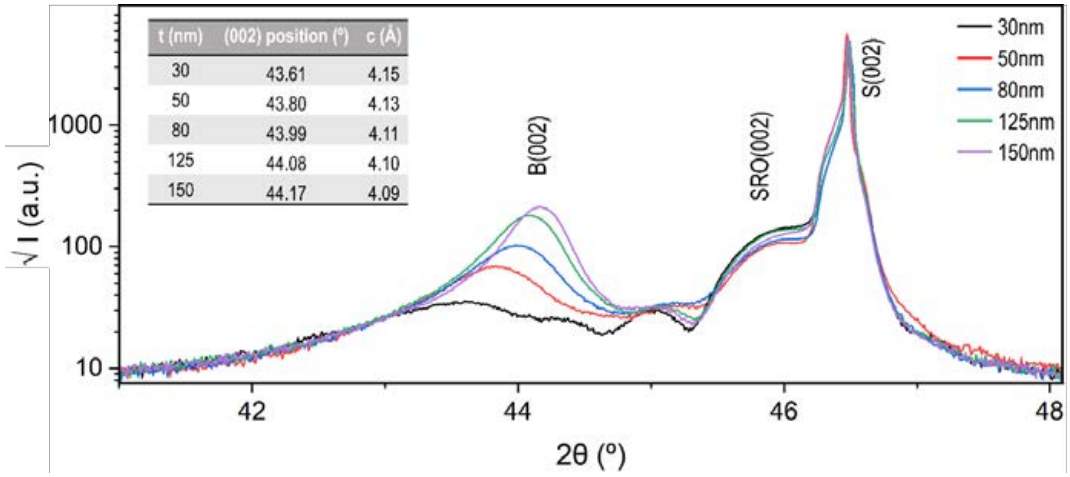

Figure 3.35: XRD of BTO/SRO/STO samples with different thicknesses: 30nm (BSS_05), 50nm (BSS_06), 80nm (BSS_07). 125nm (BSS_08) and 150nm (BSS_09). The inset summarizes the different thickness, the (002) BTO reflection position and the c parameter of the prepared films.

The in-plane lattice parameters were obtained from reciprocal space maps (RSM) around the (-103) reflection. *Figure 3.36* shows two RSMs, one of a completely strained BTO film (~30nm) and another of a fully relaxed BTO (~150nm) both grown on SRO/STO. The main contribution to these RSM comes from the STO substrate. Both samples have a small contribution of the SRO conductive layer, which is fully strained with the STO. The BTO of the 150nm thick sample presents two intensity maxima: one aligned with the STO and another one slightly shifted (*Figure 3.36a*) and a much more intense one, which means that the strained fraction is very small. On the other hand, the thinnest sample the BTO contribution is almost perfectly aligned with the STO substrate contribution (*Figure 3.36b*), indicating that the BTO in-plane lattice parameters are coherently strained to the STO substrate (*a*=3.905Å). The lattice parameters obtained for the different thicknesses are summarized in *Table 3.5*.

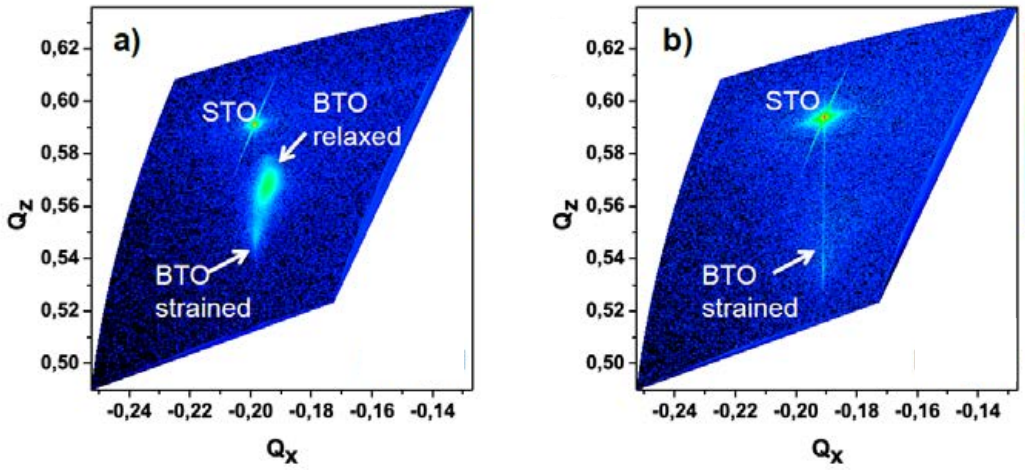

Figure 3.36: RSM of (a) 150nm thick (BSS_09) and (b) 30nm thick BTO film (BSS_05) BTO film.

	Cell parameters ± 0.01 (Å)	
Thickness (nm)	**a**	**c**
30	3.90	4.15
50	4.03	4.13
80	4.02	4.11
125	4.01	4.10
150	4.03	4.08

Table 3.5: Summary of the BTO cell parameters obtained from RSM as a function of the film thickness

The BTO thin films show a systematic decrease of the tetragonality (*c*/*a* relation) with increasing thicknesses as BTO relaxes when more material is deposited. BTO grows completely strained below 50nm, whereas above that thickness BTO grows with similar parameters of those of the bulk. Thus, the polarization in thinner samples is expected to be higher due to a greater cation displacement respect to the anions of the BTO.

3.3.4. Conclusions

We have optimized the conditions for the deposition of BTO on different STO (100) substrates: doped with niobium and without doping to achieve thin films with smooth surfaces (*rms* roughness ~0.2nm). It has been demonstrated that the pressure used to deposit the sample is the parameter, beside thickness, that affects the most the final *c*-lattice parameter. The obtaining of BTO with larger out-of-plane lattice parameters is related with the use of low pressures (1mTorr) and moderate temperature (700ºC). The RHEED monitorization during the PLD deposition has demonstrated that the growth occurs layer-by-layer up to 25ML.

3.4. $BiFeO_3$ growth conditions

The deposition of single-phase films containing volatile elements, such as (Pb,Zr)TiO_3, $BiMnO_3$ or $BiFeO_3$ need accurate optimization growth conditions. For this reason, the BFO target employed has an excess of 10% Bi to compensate the Bi volatility (diameter: 5cm, purity: 99.99%, Mateck), which with the right conditions will be lost during the deposition[169–171]. BFO was grown on top of two different crystallographic orientations of STO the (111) and the (100). STO (111) is suited to obtain the maximum polarization since as explained in *section 1.31*, the polarization vector of BFO follows the (111) direction. Furthermore, BFO films were grown on conducting heteroepitaxies of SrRuO3/STO to allow the measurement of the ferroelectric properties[172].

The obtaining of pure BFO thin films is known to only happen in a narrow parameter range. Béa H. et.al.[170] found a small gap around 580ºC and 10^{-2} mbar (~8mTorr) to get single phase (001)-oriented BFO, for higher pressures they detect the presence of Bi_2O_3, whereas at lower oxygen pressures α-Fe_2O_3 was noticed. You L. at.al.[173], using a stoichiometric PLD target, discovered that the Bi/Fe ratio in the films increases with the deposition pressure, without Fe_2O_3 formation. They propose a broad pressure window between 1-20mTorr at 700ºC to obtain pure BFO without detecting impurities. Additionally, Wang J.et.al [174] obtained pure phase epitaxial BFO on SRO/STO heterostructures by growing it at 670ºC at 20 mTorr. Jiang et.al. [171] investigated about the deposition parameters that could affect the morphology and the BFO growth on SRO/STO pointing out that the oxygen pressure and the deposition temperature are the most critical parameters to the final result. The empty circles in *Figure 3.37* indicate the different compositions and growth mechanisms obtained by Jiang et.al. [171] for the ranges of deposition temperatures 650-750ºC and oxygen pressures 7-180mTorr (~1-24 Pa). Outside these ranges, the formation of other phases like Bi_2O_3, α-Fe_2O_3 or Fe_2O_3 can occur. These impurities have a huge effect on the properties of the film for example reducing the remanent polarization with the Bi/Fe ratio[56,173].

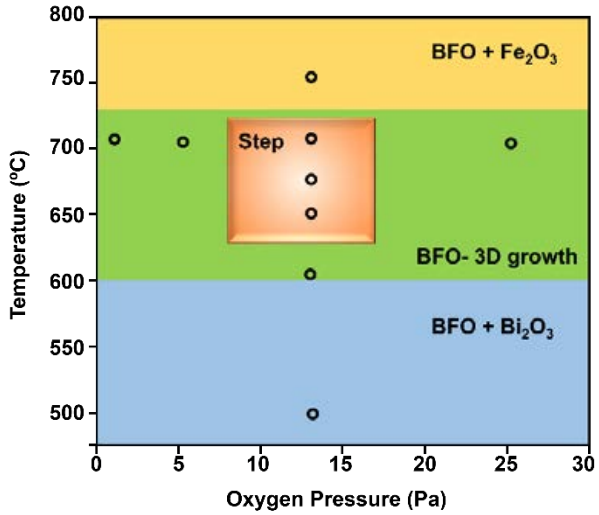

Figure 3.37: Growth diagram for BFO thin films Jiang Z. et.al[171]. The open circles are the results obtained by Jiang Z. et.al work.

Considering these studies, we have chosen 2Hz, 650ºC, 100mTorr (~13.3Pa) and 1000 pulses as a starting point and investigated the effect of the temperature for films grown on SRO on (100) and (111) oriented STO substrates. The cooling rate after deposition was set to 7ºC/min.

Our initial objective was to obtain single phase BFO (001)-oriented thin films with a fully covered surface. However, an unexpected island morphology was found, that could be interesting for the generation of nanostructures. Thus, we were interested in understanding the formation of those nanostructures. Despite the x-rays diffractograms show a peak around 2θ= ~45º assigned to the BFO (002) reflection, the TEM analysis reveals that bismuth is barely present. The preparation of samples with identical deposition conditions leads to relevant differences on the sample's morphology. This phenomenon will be discussed throughout this section. Inhomogeneous

3.4.1. $BiFeO_3$/SRO on STO (100)

The samples that will be presented through this section are summarized in *Table 3.6*. BFSS and BFS corresponds to BFO deposited on SRO/STO (100) and on STO (100), respectively. P corresponds to the 2θ position of the BFO (002) reflection in and h is the height of the islands measured with AFM.

Label	nº pulses	Temperature (ºC)	P (º)	Island's morphology	h ±2 (nm)
BFSS_01*	1000	650	45.04	Covered surface	-
BFSS_02*	1000	700	44.64	Trapezoidal	30
BFSS_03*	2000	700	44.75	Trapezoidal	48
BFSS_04	2000	700	44.65	Trapezoidal	53
BFSS_05	2000	700	44.72	Dendrites + rectangles	51
BFSS_06	2000	700	44.81	Big dendrites	49
BFSS_07	2000	700	44.64	Rectangles	47
BFSS_08	2000	700	44.67	Trapezoidal+ squares	45
BFSS_09	2000	700	44.76	Trapezoidal + rectangles	46
BFS_01	2000	700	44.68	Inhomogeneous trapezoidal+dendrites	55

*Table 3.6: Sample list of the $BiFeO_3$ thin films All samples have been deposited at 100mTorr and 5Hz, except those indicated with a * that were grown at 2Hz.*

The influence of two different temperatures (650ºC and 700ºC) were tested for BFO grow on SRO/STO (100). 30nm of SRO were deposited in identical conditions than those used in the *BTO/SRO_STO section*[153]: 635ºC, 100mTorr and 2Hz. The HR x-ray diffractogram for those samples indicates the presence of BFO (002) oriented and a low intensity peak at ~49.5º assigned to the α-Fe_2O_3 (220) reflection is detected (*Figure 3.38*).

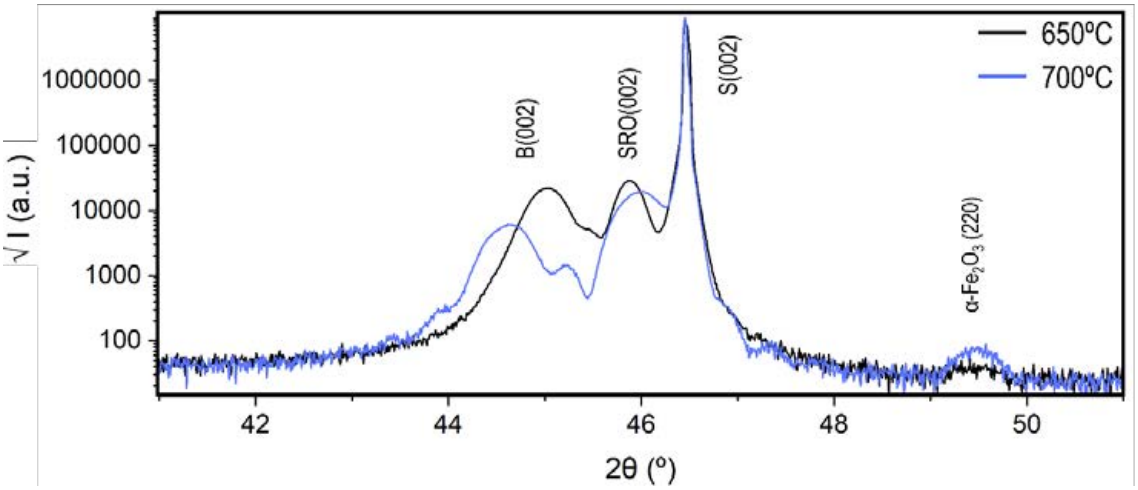

Figure 3.38: HR-XRD θ-2θ scan of BFO/SRO/STO (100) films deposited at 650ºC (BFSS_02) and 700ºC (BFSS_03).

The surface morphology studied with AFM shows considerable differences between the surface morphology of the two deposited BFO thin films. *Figures 3.39(a-b)* illustrate the topography of BFSS_01, deposited at 650ºC, which presents a totally covered surface with a surface roughness of about ~0.35nm (*Figure 3.39c*).

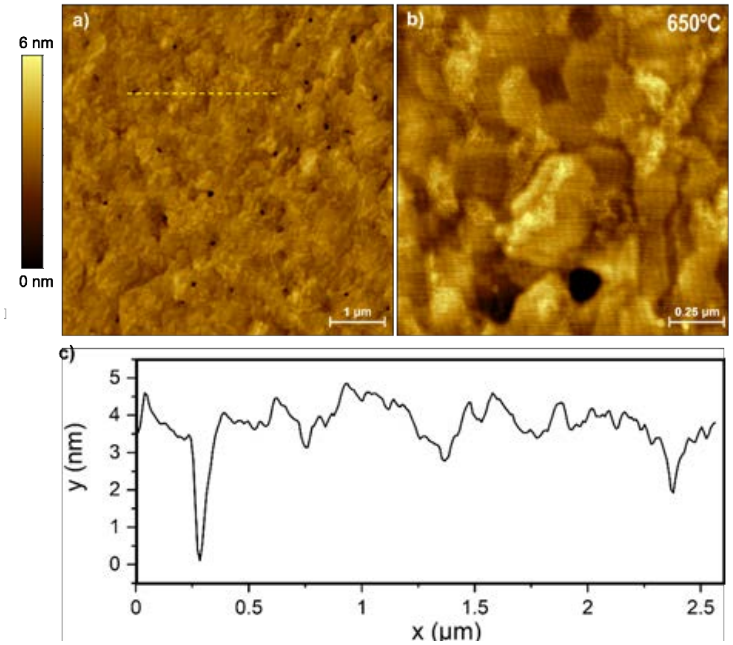

Figure 3.39: BFSS_01 AFM images of (a) 5x5µm² (b) 1x1µm². And (c) line profile of the yellow line of (a)

On the other hand, unexpectedly, BFSS_03, grown at 700ºC, shows an interesting island-like topography (*Figure 3.40*). This sample's surface is built of regular islands (~30nm height) of sizes ranging from 350nm to 900nm with an average size of ~600nm.It is worth mentioning that the surface of these islands is almost flat as can be seen in the height profile presented in *Figure 3.40c*. As with the BTO/SRO/STO thin films, the SRO does not completely cover the substrate creating trenches along the (100) direction of the STO substrate. However, in this deposition these defects seem to act as nucleation centres for the BFO islands and as a result the islands present a certain degree of organization, this topic will be discussed afterwards with SEM studies.

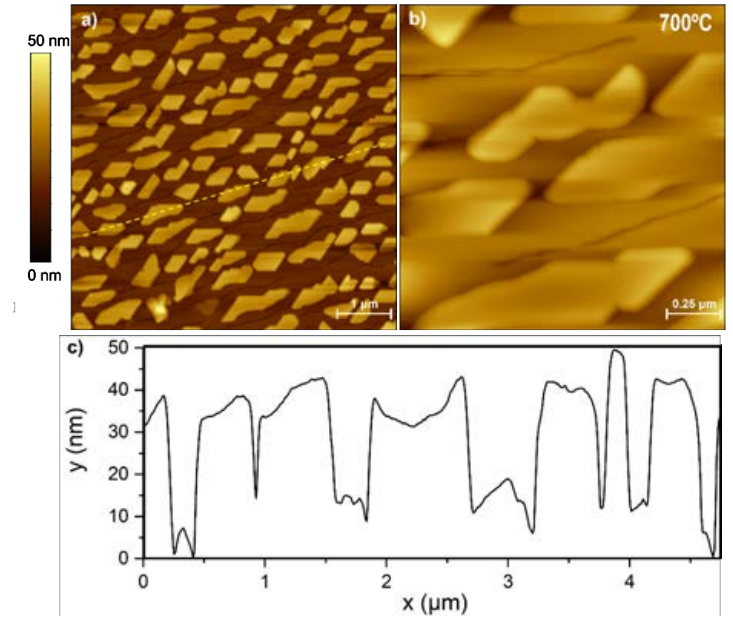

Figure 3.40: BFSS_02 AFM images of (a) 5x5µm² (b) 1x1µm². And (c) line profile of the yellow line of (a)

Despite the presence of a small peak of α-Fe_2O_3 in the x-ray diffractogram, 700ºC was chosen as the deposition temperature to investigate the formation of the island's topography given its interest in the generation of nanostructures. Typically, these self-assembled structures are grown by depositing the material over a template that is removed afterwards as reported by Jeon, J. et.al[175] who grew BFO on an anodized aluminium oxide template to obtain circular BFO nanoislands. Another method to obtain BFO nanoislands was reported by Sun, F. et. Al.[176] and consisted on growing BFO on LAO with a conductive buffer layer. Then, well ordered polystyrene (PS) sphere arrays were stacked onto these films to act as a mask. Afterwards, Ar^+ ion sputtering was used to remove the PS mask to obtain the desired BFO structures. However, Ma J. et al.[177,178] reported the formation of rectangular- and square-shaped rhombohedral phase BFO islands in a tetragonal phase BFO matrix by PLD deposition of BFO on $LaAlO_3$ (001) with a thin (La,Sr)MnO_3 buffer layer. BFO nanoislands are of special interest due to their intrinsic ability to particular topological domain states due to constrained geometries or boundary conditions[179–181]. Thus, we decided to redirect the focus of this work to the characterization of these structures.

First, the influence of thickness and deposition rate on the stability of these islands was tested by growing two new samples under the same deposition conditions (700ºC, 100mTorr), but at two different deposition rates (2Hz and 5Hz) and higher number of pulses (nº pulses = 2000). The objective was to control the degree of coverage and size of the islands. The x-ray diffractogram (*Figure 3.41*) obtained for those samples, independently of the growth rate, present the same pattern as the thinner sample, but the intensity of the α-Fe_2O_3 (220) reflection increases.

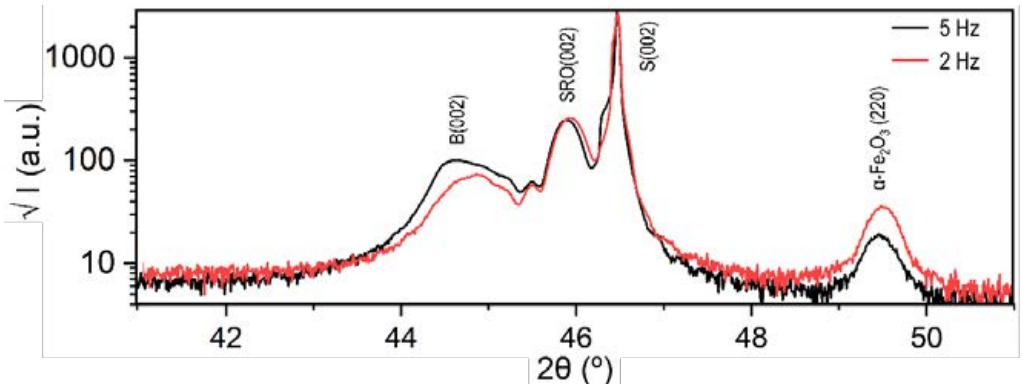

Figure 3.41:HR XRD θ-2θ scan of a BFO/SRO/STO (100) thin film deposited at 700ºC, 100mTorr, 2000 pulses and various deposition rates: 2 Hz (red) (BFSS_04) and 5Hz (black) (BFSS_05).

The effect of doubling the number of pulses increases the islands height from 30nm to ~50nm. However, the island's density is much higher than in the previous deposition maintaining the same average size of the islands (~600nm). The new islands morphology seems to have a more trapezoidal shape compared to the thinner sample (*Figures 3.42* and *3.40*). The comparison of the AFM images for the samples deposited at different growth rates reveals that higher deposition rates leads to higher density of islands. The surface of some islands (yellow ellipsoids in *Figure 3.42*) seems to have a variation in height within the islands, which

could be an indicative of the coexistence of ferroelastic domains. This phenomenon is more noticeable in the sample deposited at 5Hz than in sample BSS_03 (2Hz) where the islands are flatter.

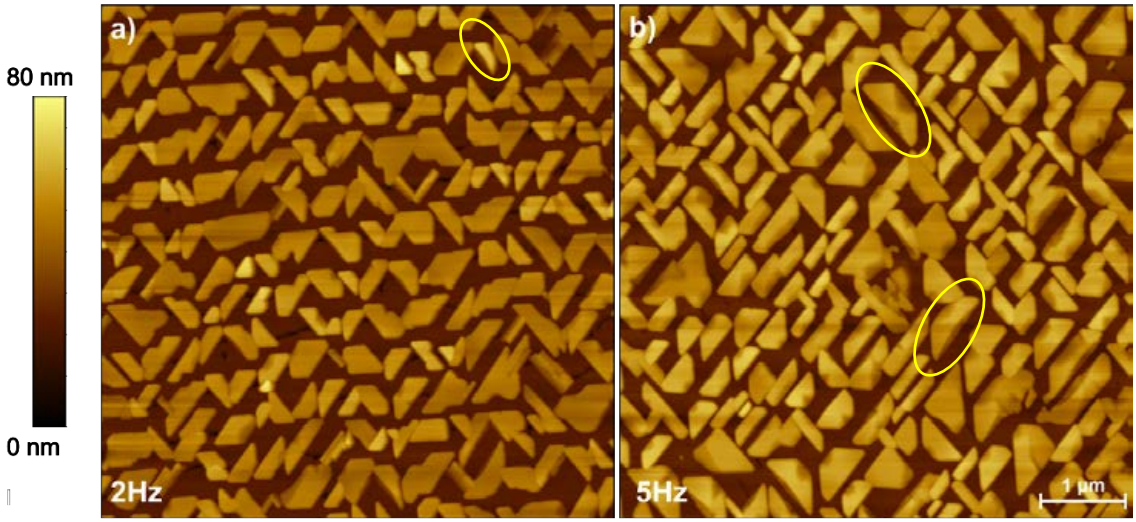

Figure 3.42: 5x5µm² AFM images of BFO/SRO/STO (100) thin films deposited at (a) 2Hz (BFSS_03) and (b) 5Hz (BFSS_04).

SEM observations were carried out to better understand the surface of the samples. We used the electron backscattered detector, which is more sensitive to channeling effects, and therefore to crystal orientation. The resulting images obtained from the sample deposited at 2Hz (*Figure 3.42a*) are shown in *Figure 3.43*, while *Figure 3.44* shows the acquired images for the BFO grown at 5Hz (*Figure 3.42b*).

The analysis of the SEM images for sample BFSS_03, deposited at 2Hz, reveal some new features. *Figure 3.43a* and *b* correspond to BSE images taken at the centre of sample's BFSS_04, which present areas of high density of islands with lengths around ~600nm. In *Figure 3.43b*, the islands are thin enough to be transparent for the electrons and allow the underlaying SRO trenches to be seen. On the other hand, *Figures 3.43c* and *d* are secondary electron images taken at the edges of the sample. These areas present lower density of islands compared to the centre of the sample. *Figure 3.43c* shows an area with almost no material deposited, nevertheless it is clear that the SRO trenches act as a nucleation centre for the islands as seen on the circled spots. This behaviour can be better observed in *Figure 3.43d*, where islands are in an intermediate state with lengths of approximately ~250nm following the [100] direction of the SRO trenches.

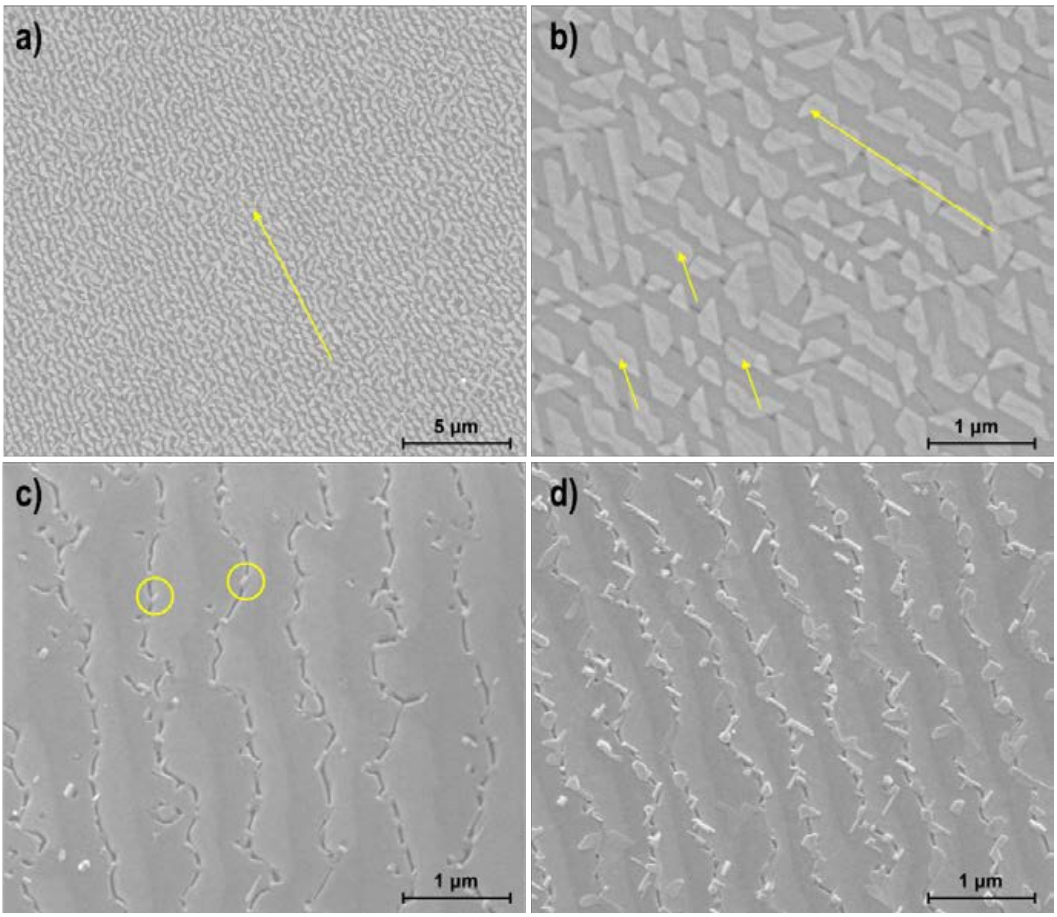

Figure 3.43: (a-b) BSE mode images and (c-d) secondary electrons mode images of BFO/SRO/STO (100) film deposited at 2Hz.

Comparing the SEM images of the edges for both samples (*Figure 3.43d* and *Figure 3.44b)*, it seems that the different BFO morphologies at these regions depend on the deposition growth rate leading to dendritic structures at 5Hz, whereas at 2Hz small islands appear. This behaviour could be related to the different amount of material that reaches the surface at the initial growth of the BFO nanoislands, being lower at 2Hz than at 5Hz. Comparing *Figures 3.44c* and *3.44d* corresponding to a SE and BSE images, respectively, contrast changes can be seen on the BSE image within the islands that are not visible on the SE image that could reflect the coexistence of domains.

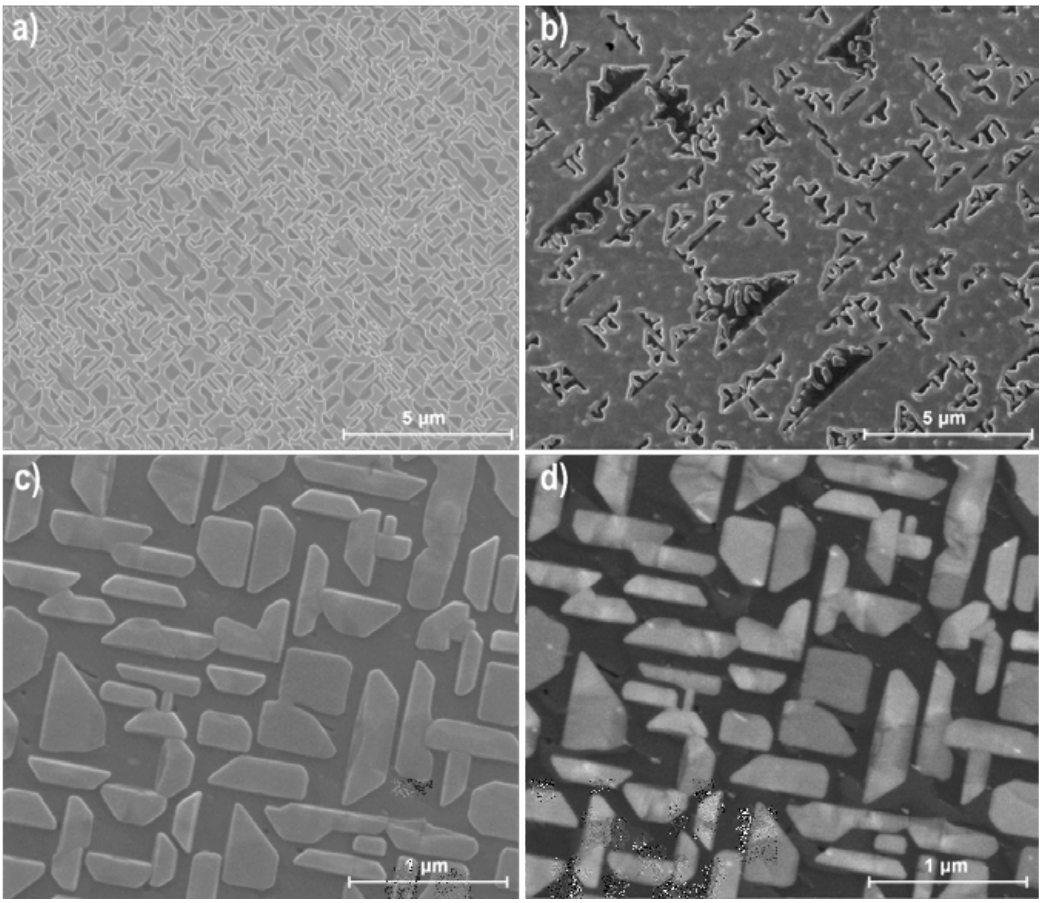

Figure 3.44: (a-c) SE images and (d) BSE image of a BFO/SRO/STO (100) thin film deposited at 5Hz. Note that on Figures a-b the islands appear darker than the substrate.

The deposition conditions at the edges of the samples seem to be slightly different from the center ones by the presence of dendritic-like structures, which may be an indication of an inadequate solidification process far from the equilibrium.

The lack of reproducibility is proved below, where the variability of samples deposited at identical nominal conditions (700ºC, 100mTorr and 5Hz with a cooling rate of 7ºC/min) is shown. Samples BFSS_05 and BFFS_06 have dendritic-like structures covering the surface but with different density coverages. *Figure 3.45a* presents small dendritic structures combined with rectangular islands, while sample BFSS_07 (*Figure 3.45b*) has a maze-like surface full of dendrites. In both cases, the dendrites as well as the rectangular islands, grow along the [100] and [010] crystal directions of the substrate.

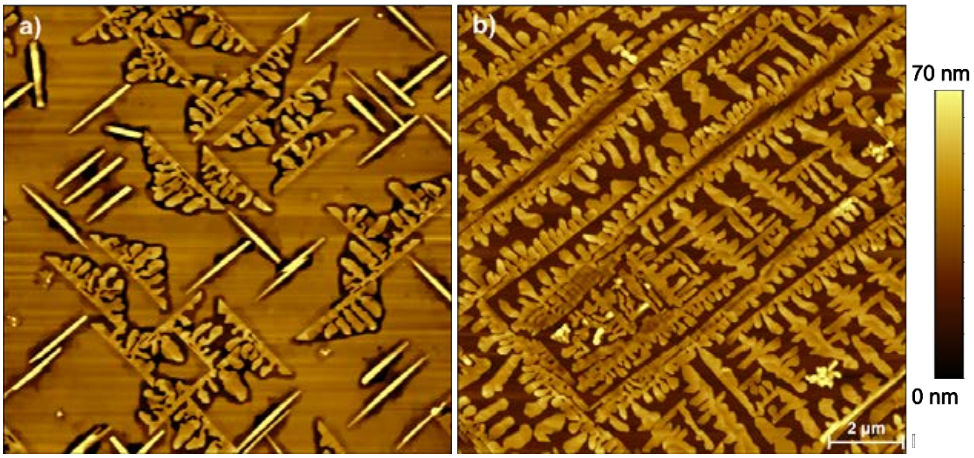

Figure 3.45: 5x5µm² AFM images of samples (a) BFSS_05 and (b) BFSS_06.

Additionally, to the dendritic structures, rectangular-shaped structures were obtained in absence of the trapezoidal islands with uncovered areas as it is detailed in *Figure 3.46*. Furthermore, the rectangles seem to have a variation in height within the rectangle-shaped islands as happened with sample BFSS_04 (*Figure 3.42b*):

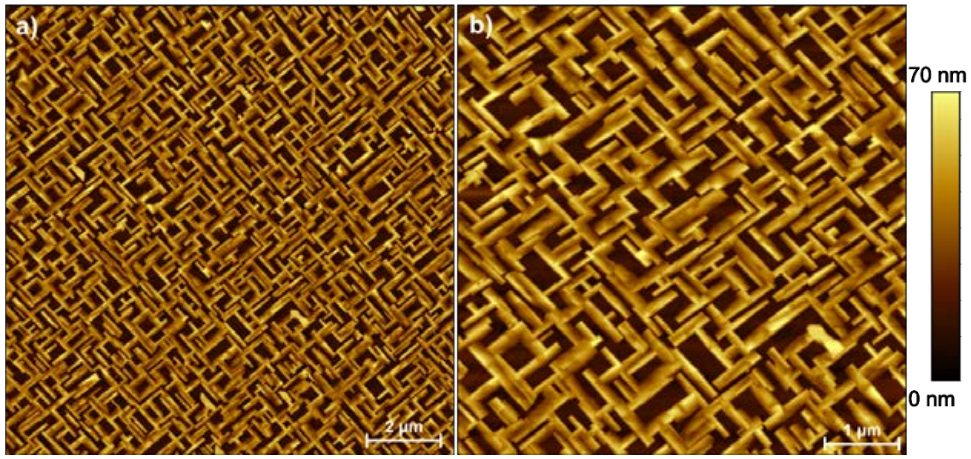

Figure 3.46: (a) 10x10 µm² and (b) 5x5µm² AFM images of sample BFSS_07.

Nonetheless, samples BFSS_08 and BFSS_09 present a similar topography to the samples BFSS_02-04, but with small differences. *Figure 3.47a* details the morphology of sample BFSS_08 where is possible to see small islands on the SRO trenches, as well as the trapezoidal islands. On the other hand, sample BFSS_09 (*Figure 3.47b*) shows a combination of the characteristic trapezoidal islands and the rectangular shaped islands seen in *Figure 3.46.*

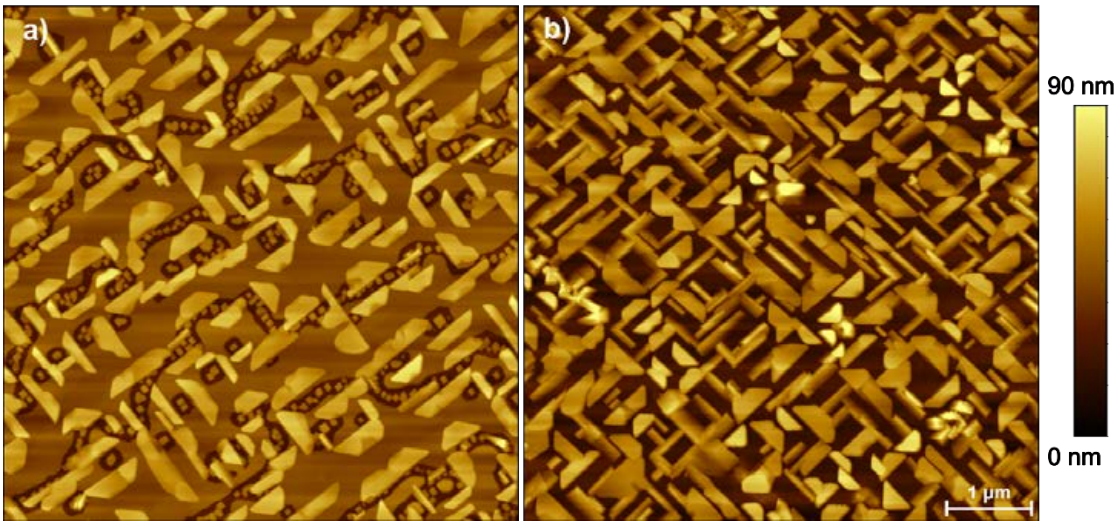

Figure 3.47: 5x5µm² AFM images of sample (a) BFSS_09 and (b) BFSS_10.

An example of growing BFO without the SRO-formed trenches is given in *Figure 3.48* for sample BFS_01, where BFO was deposited on STO (100) without the SRO layer maintaining the other conditions (700ºC, 100mTorr, 5Hz and 2000 pulses). In this sample, the absence of the SRO trenches results into a surface covered by particles that could not form the islands observed in the other samples. The 10x10 µm² AFM image (*Figure 3.48a*) shows an inhomogeneous covering of the STO surface with different size structures with no specific order. A detailed look into the surface of sample BFS_01 shown in *Figure 3.48b*, shows two types of structures with different shapes: trapezoidal islands (red) and bigger dendrite-like structures (blue) similar to the morphologies previously seen.

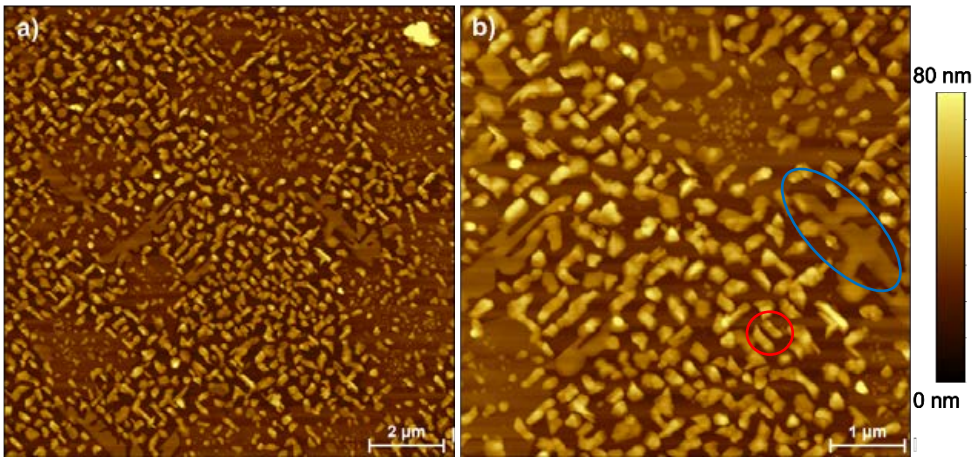

Figure 3.48: (a) 10x10µm² and (b) 5x5µm² AFM images of sample BFS_01

It has not been possible to determine the factors affecting the geometry of the formed 3D islands, since at the same nominal deposition conditions different geometries have been obtained: trapezoidal islands (*Figure 3.42*), rectangular shaped for sample BFSS_07 (*Figure 3.46*) and a combination of both geometries in sample BFSS_09 (*Figure 3.47b*). This lack of reproducibility strongly suggests that small deviations in growth conditions out of our control induces large modifications in growth mechanism. However, all samples

present some similarities: the XRD of the samples are almost identical to the one presented in *Figure 3.41*, where 4 different peaks assigned to BFO (002), α-Fe_2O_3 (220), SRO (002) and STO (002) can be seen. Additionally, all the structures have approximately the same height (~50nm) and grow following the [100] and [010] directions of the STO. It has been observed that the trenches observed in the SRO surface act as preferential nucleation sites for BFO and promotes the formation of islands. We note that BFO deposited on STO lacking such defects, under the same conditions, grows in a continuous fashion (*Figure 3.48*).

TEM characterization

The sample BFSS_05 (700ºC, 100mTorr, 5Hz, 2000 pulses) was studied by STEM-HAADF. From that sample two lamellas were prepared for observation along [100] and [110] axis. Both lamellas present the same features, therefore only the lamella prepared to observe along the [100] axis will be shown. The low magnification images of the 45º cut indicates that the buffer SRO layer is deteriorated by the presence inclusions. The SRO looks granulated in the form of nanoparticles. Despite the grainy texture present in the SRO buffer layer, it looks like the islands still grow epitaxially with the substrate. Additionally, BFO islands appear with two types of contrasts dark and bright (*Figure 3.49*), which is consistent with the contrast variations detected within the islands seen in the BSE images.

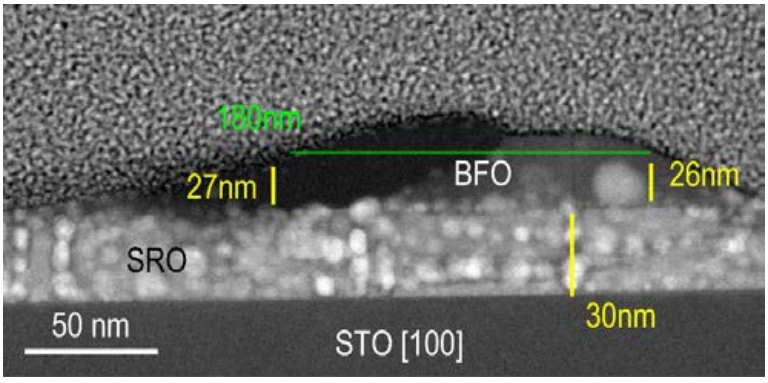

Figure 3.49: Low magnification image of the island/buffer/substrate ensemble viewed along the [100] axis.

A high-resolution image is shown in *Figure 3.50a*. The inclusions in the SRO buffer are embedded in a coherent matrix which still preserves the epitaxial relationship with the STO substrate. Such inclusions are also present in the island, particularly in the neighborhood of the interface. On the right-hand side of F*igure 3.50b,* vertical superstructure contrasts in the SRO matrix suggest local structural modifications that could be induced by stoichiometric unbalance caused by the segregation of the inclusions.

Similar contrasts are observed in the BFO island. The origin of such structural modifications is unclear but, again, are thought to be caused by stoichiometric modifications associated with the segregation process. The FFT spectra obtained from the substrate and from the BFO island exhibit the same cubic pattern demonstrating their epitaxial relationship (*Figures 3.50c and d*).

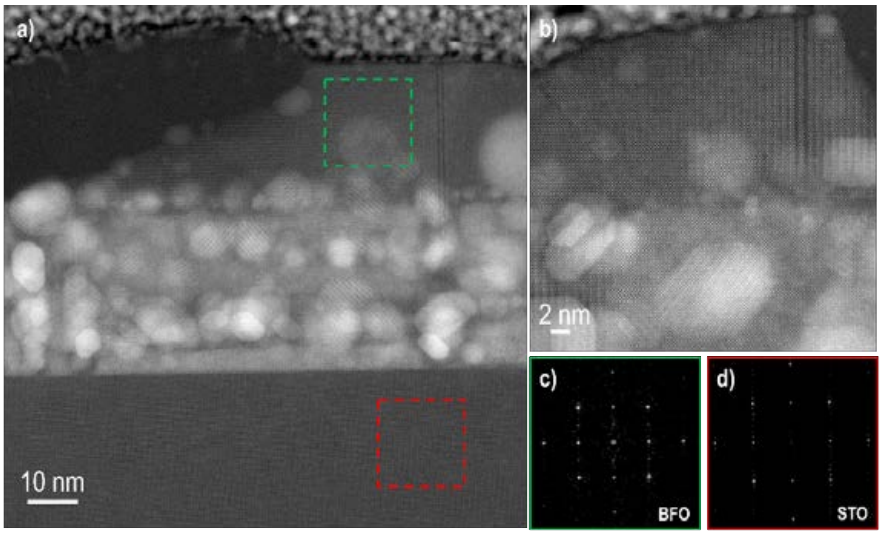

Figure 3.50: (a-b) HRTEM images along the [100] STO axis, (c-d) SAD pattens of the marked areas in (a).

Figure 3.51 presents an EDX mapping of Bi, Sr, Fe, Ru and O through the island/buffer/substrate ensemble. It can be clearly observed that Bi segregates from the island and forms Bi-rich inclusion on the SRO surface. Bismuth diffusion into the buffer layer is also observed, giving rise to a heterogeneous distribution. On the other hand, the island appear Fe depleted near the interface, and Fe is seen to diffuse into the SRO layer. Sr from the latter is also observed to diffuse into the island, particularly in Fe depleted zones. The Ru mapping indicates that this cation remains confined within the SRO buffer but exhibits a heterogeneous distribution consistent with the granular structure observed in HAADF. Altogether, these results indicate a dramatic degree of interdiffusion which destabilizes the structural framework of the original phases.

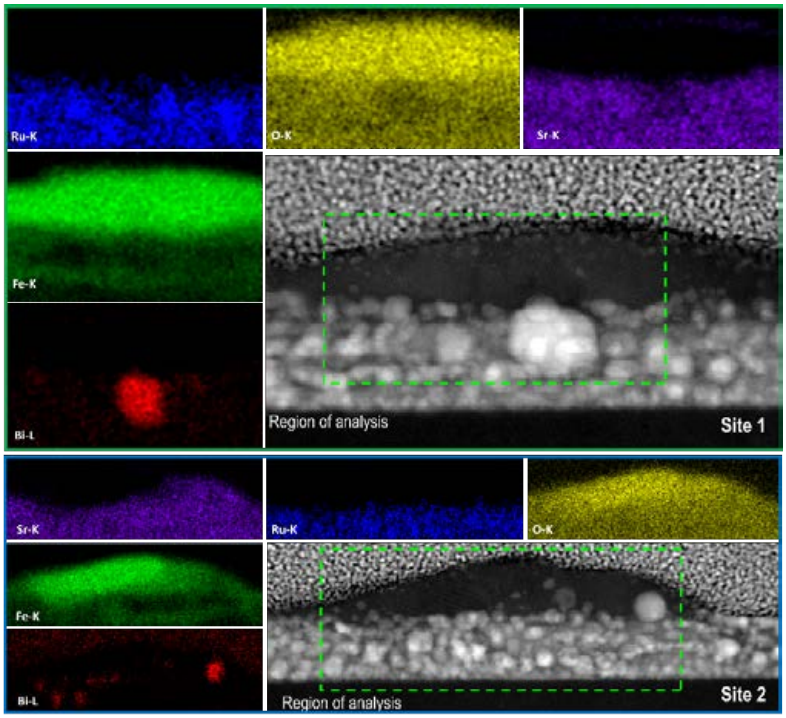

Figure 3.51: EDX mapping of Bi, Sr, Fe, Ru and O through the island/buffer/substrate ensemble. Bi, Sr, Fe, Ru and O are identified by the colours red, purple, green, blue and yellow, respectively.

Figure 3.52 depicts the TEM/EDX spectra of two different regions, that revealed Sr diffusion into the islands (B, D regions) and demonstrate the bismuth segregation into small particles (A, C regions). Thus, confirming that the islands observed are mainly formed by iron oxide.

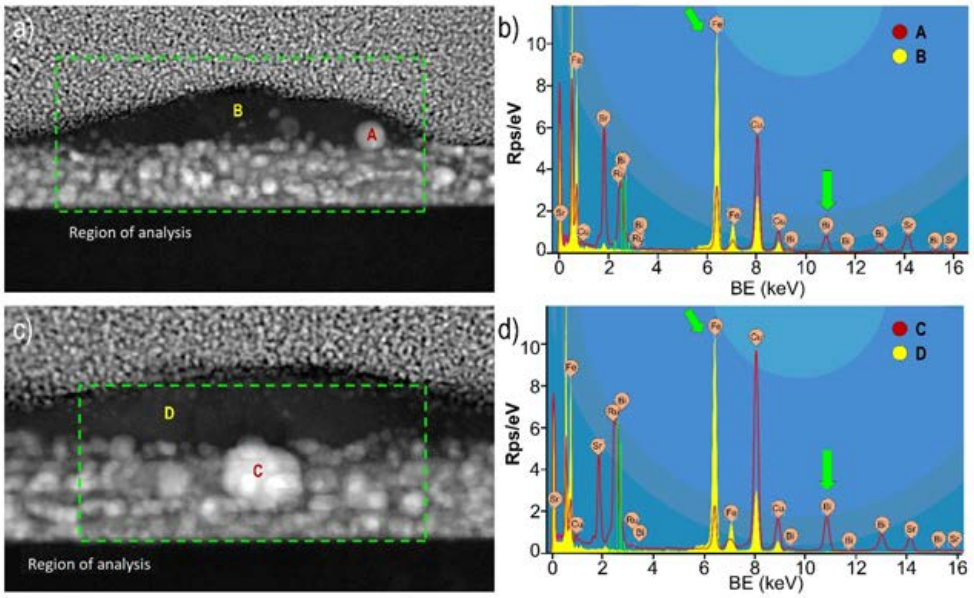

Figure 3.52: (a,c) Low magnification image of the island/buffer/substrate ensemble viewed along the [100] axis with their respective EDX analysis (b,d).

The EDX mapping of the island displayed on *Figure 3.53a* is shown in *Figures 3.53b* and *c*, where strontium and iron are clearly identified. The EDX mapping shows that the central part of the island is formed mainly by iron, while there is a small amount of strontium that has diffused into the island structure, as shown in the composition profiles (*Figure 3.5d*).

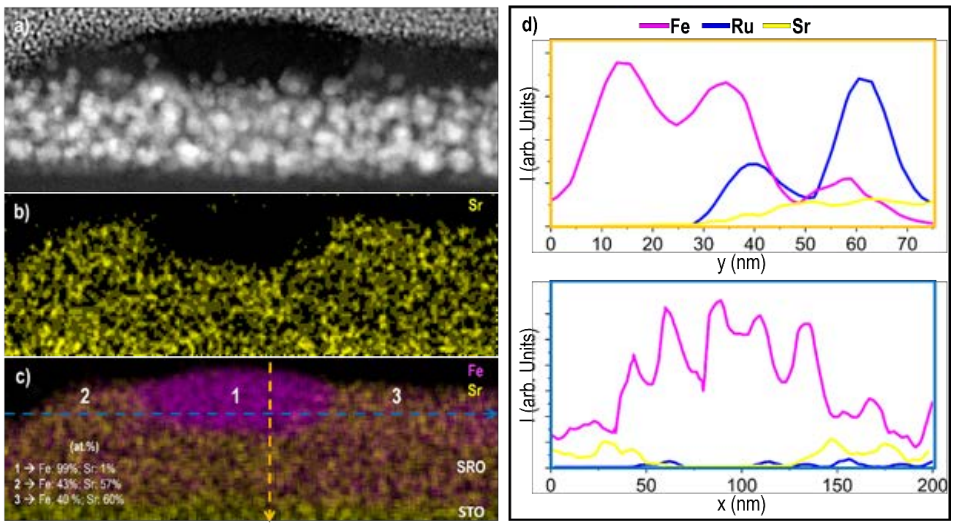

Figure 3.53: (a) low magnification image and (b-c) EDX mapping of the island/buffer/substrate ensemble, (d) composition profiles of the orange (up) and blue (down) lines of (c).

These results suggests that the nanoislands, which at the beginning seemed to be BFO are mostly composed by the Fe_2O_3 detected on the x-ray diffractograms. In view of these results, we performed SEM-

EDX analysis of samples exhibiting different island morphologies including the sample prepared at 650ºC, where the Fe_2O_3 peak was not observed. The EDX analysis for sample BFSS_06 (*figure 3.45a*) is shown in *Figure 3.54*. This sample was selected as it contained low density of dendritic structures. The line profile reveals a decreasing amount of bismuth coinciding with the centre of the island, while at the flat areas this quantity is higher. This is confirmed by the EDS quantitative analysis done in the areas surrounded by a rectangle. The ideal ratio between bismuth and iron should be 1:1. However, the ratio in the red rectangle is 0.7:1, while on the yellow one is decreased to 0.3:1. These results agree with the TEM analysis confirming that the nanoislands are mainly formed by iron oxide at their cores.

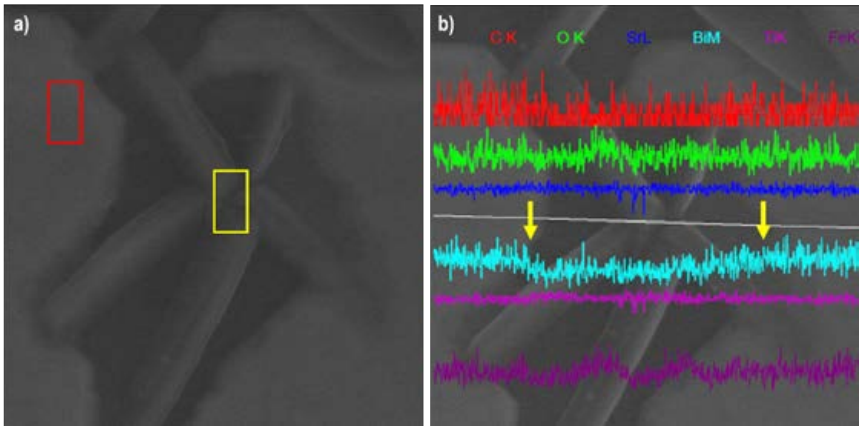

Figure 3.54: Morphology of sample BFSS_06. (a) Secondary electrons image (b) composition profile of the different elements. The yellow arrows indicate the decrease in Bi ratio.

On the other hand, the EDS analysis of sample BFSS_02 (*Figure 3.55a*), deposited at 650ºC, presented a Bi:Fe ratio around 0.7:1 (*Figure 3.55b*). A similar relation was found for this sample on GALAXIES beamline (*Figure 3.55c*). These results prove that even at lower deposition temperatures there is a bismuth deficiency. But this time the bismuth its homogenously distributed along the sample.

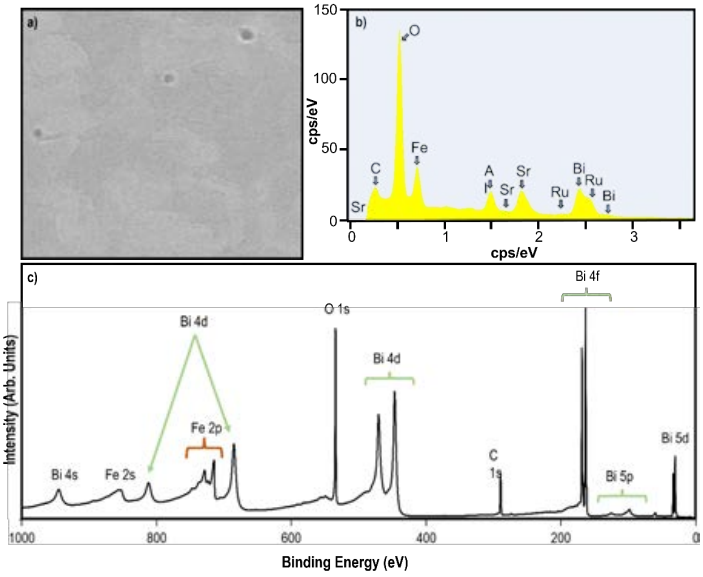

Figure 3.55: (a) Secondary electrons image, (b) EDS quantitative analysis and (c) XPS spectrum measured in GALAXIES beamline (hv = 2500 eV ,Estep=1 eV) of sample BFSS_02.

3.4.2. $BiFeO_3$/SRO on STO (111)

The interest of growing BFO along the [111] direction resides in the fact that this is the polarization direction. Therefore, this orientation provides the maximum polarization value along the film normal. Moreover, from symmetry arguments it is expected that the morphology and domain configurations of islands grown in this orientation will differ from that obtained along [001]. Our previous results on (001)-oriented substrates show that the growth temperature is critical in the formation of BFO islands. Therefore, we explored a range of temperatures comprised between 625ºC and 725ºC at 100mTorr and 2Hz. The list of samples investigated throughout this section is displayed in *Table 3.7*. $BFSS_1$ corresponds to BFO/SRO/STO (111) films. P corresponds to the 2θ position of the BFO (222) reflection in and h is the height of the islands measured with AFM.

Label	Temperature (ºC)	P (º)	Surface morphology	h ±2 (nm)
$BFSS_1$_01	600	-	Inhomogeneous particles	25
$BFSS_1$_02	625	83.51	Triangular islands	35
$BFSS_1$_03	650	83.53	Triangular islands	30
$BFSS_1$_04	675	83.51	Triangular+rectangular islands	48
$BFSS_1$_05	700	83.44	Rectangular islands	53
$BFSS_1$_06	725	83.43	Rectangular islands	51

Table 3.7: Summary of the BFO samples grown on SRO/STO (111)

The x-ray diffractogram presented in *Figure 3.56* shows that the SRO grows epitaxially with the STO (111) substrates. The BFO (222) reflections are present for all samples, except those prepared at 600ºC. The α-Fe_2O_3 is detected for the samples deposited at the high temperature range of 675ºC-725ºC (Inset in *Figure 3.56*). Thus, 625-650ºC is the best range of temperatures to avoid the de segregation of Bi and Fe from the (111) BFO islands.

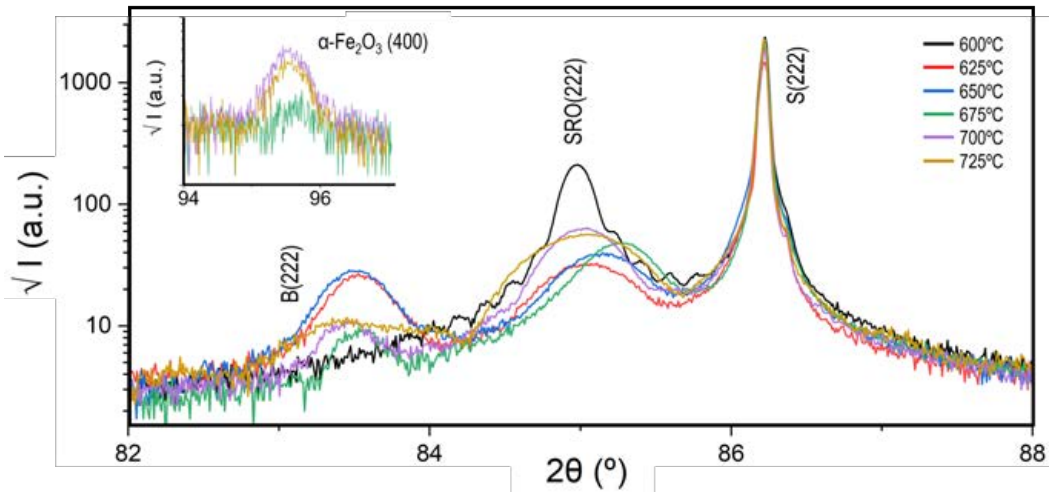

Figure 3.56: HR XRD θ-2θ scan of BFO samples deposited at a different temperature

The AFM images presented in *Figure 3.57* shows a wide range of different surface morphologies. $BFSS_1$_01, grown at 600ºC, presents a very rough surface (*rms* ~2.35nm) formed by inhomogeneous particles of different sizes and heights. In the 625-650ºC range, the surface is covered by flat and regular triangular islands with an average length of 300nm. The triangular shape is consistent with the projected 3-fold symmetry of the rhombohedral BFO structure along <111>. At 675ºC the triangular islands start to disappear, they become less defined and new rectangular shapes begin to appear. This morphological change is probably associated with the thermal destabilization at 700ºC where the surface is filled by big rectangles. Finally, at the highest temperature used (725ºC) a morphology similar to that at 700ºC is obtained, but with rectangular dimensions greater than one micron. These results show that homogeneous distributions of homogeneously shaped triangular islands, free of Fe_2O_3 impurities, are obtained at 625ºC or 650ºC. We selected 625ºC as the best option to minimize thermal decomposition effects.

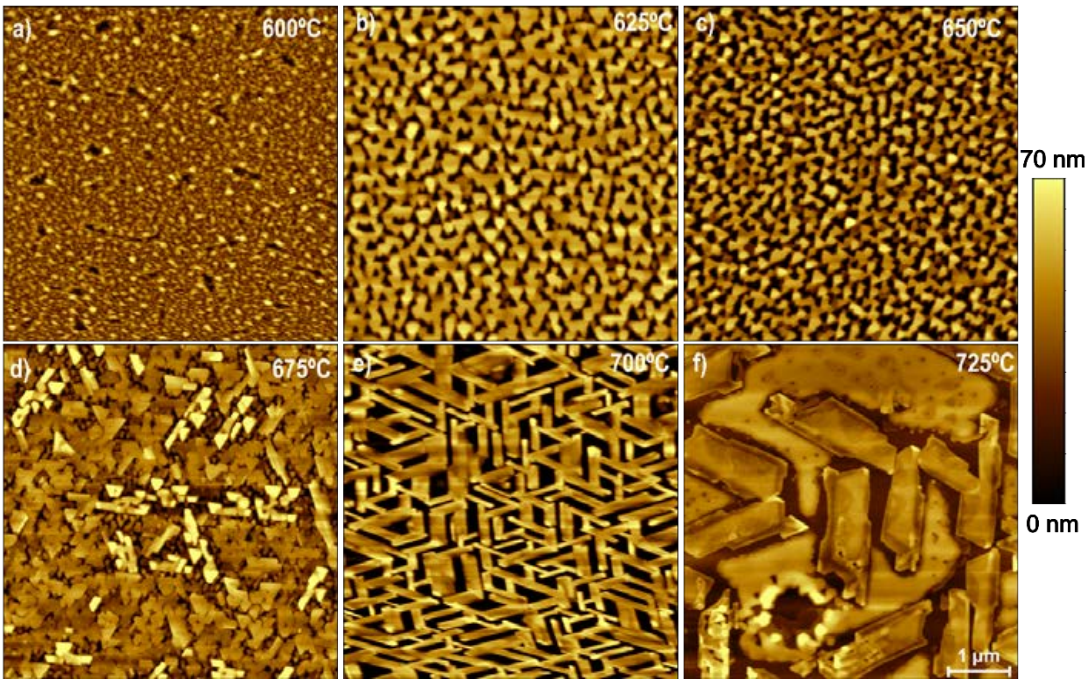

Figure 3.57: 5x5 µm² AFM images of BFO films prepared by PLD showing the evolution of their surface morphology as a function of the growth temperature (600-725ºC).

In view of the previous composition results for the BFO grown on STO (100) a SEM EDX analysis was carried out on the sample deposited at 625ºC. The SEM image with the elements line profile show that the Bi quantity clearly increases when it is on the islands, whereas it decreases on the holes between them (*Figure 3.58*). The Bi:Fe ratio obtained for this sample, once again, presents a deficiency on Bi around 0.7:1 within the islands. This ratio is similar to the one obtained for the fully covered surface of the BFO grown on STO (100).

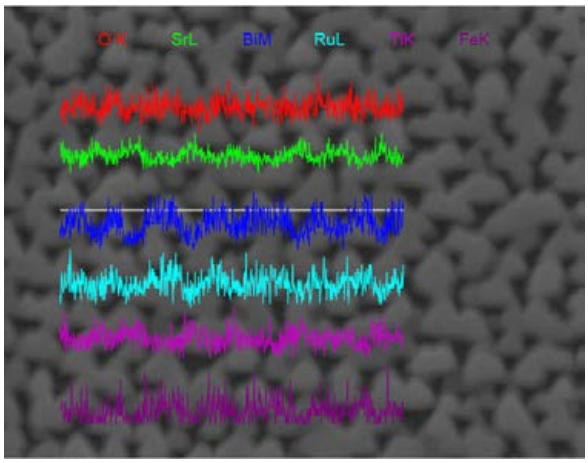

Figure 3.58: Secondary electron image with EDS composition profiles of sample BFSS$_1$_02, deposited at 625ºC.

3.4.3. Discussion

The results obtained for BFO heterostructures grown on STO (100) and (111) prove that the BFO thermal stability has become a relevant variable during the deposition of heteroepitaxial BFO/SRO/STO films. In an ideal scenario, where the properties of the films remain unchanged, the $BiFeO_3$ phase should be pure. However, this is not our case where the BFO decomposes, which can be detrimental to the multiferroic behavior of the material. Following the phase diagram of BFO precursors, Bi_2O_3/Fe_2O_3 presented in *Figure 3.59*[182], it can be observed that there is a narrow gap between sillenite ($Bi_{25}FeO_{39}$) and mullite ($Bi_2Fe_4O_9$), which usually appear as secondary phases in the synthesis of BFO.

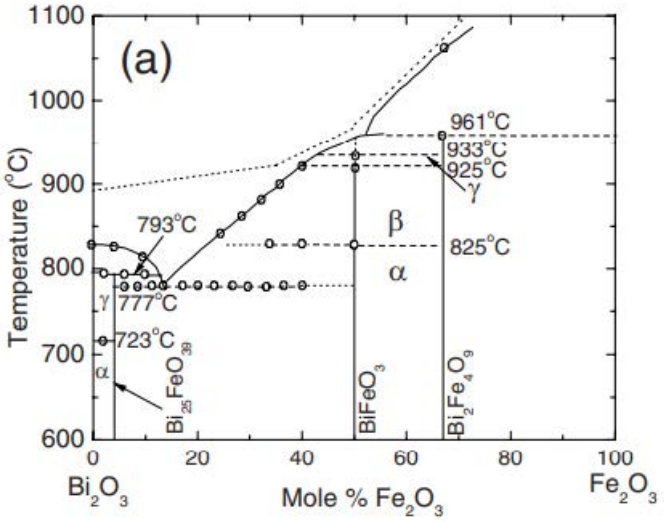

Figure 3. 59: $BiFeO_3$ phase diagram adapted from Palai et.al.[182]

The existence of Fe_2O_3 islands in our samples is consistent with the investigation of Arredondo M. et. Al. In their work the interfacial chemistry of secondary iron oxides phases in a BFO layer was investigated. They deposited BFO on STO (100) selecting LSMO as a buffer layer at 900ºC to deliberately obtain Fe_2O_3 phases. Their XRD data show the presence of BFO, LSMO and STO phases, as well as a peak around 49º assigned

to the α- Fe_2O_3 similar to our XRD data. AFM scans of their samples present dendritic structure comparable to the morphologies that we have obtained. However, their HRTEM and STEM images reveal that the Fe_2O_3 structures are located over a BFO layer. Additionally, they found the presence of iron-deficient structures inclusions inside the Fe_2O_3 phase also suggests that tiny variations in the growth conditions could trigger BFO growth. Nonetheless, our HRTEM and STEM images did not reveal any BFO layer, and it seem that all the layer is not present.

3.4.4. Conclusions

We have explored the deposition of BFO on two differently oriented STO substrates (100) and (111). The obtained results show that achieving pure $BiFeO_3$ phases is a very complex process, and, in most cases, there will be Fe_2O_3 impurities indicating BFO decomposition. Small variations in temperature results in notable changes in the surface morphology and stoichiometry. The bismuth amount decreases with higher temperatures. However, no clear correlation has been found. It appears that there is not a perfect range of temperatures to grow BFO with preserved stoichiometry, but the 625-650ºC give the best Bi:Fe ratios. Around 700ºC BFO decomposes, and bismuth seems to segregate into small particles, while iron appears in the form of islands. Nonetheless, the appearance of those islands is an indicative that BFO is starting to decompose, despite the fact the reflections seen on the x-ray diffractograms are on the positions typically assigned to BFO. This behavior indicates that the interdiffusion preserves the BFO structure in a wide range of compositions.

3.5. Heterostructures

The use of titania films for photocatalytic applications appears to be a potential solution for renewable energy generation and for environmental remediation[8,12]. However, its efficiency is limited by the short lifetime of the charge carriers caused by their fast recombination[183]. The combination of the titania photocatalytic properties with the electric field arising from the polarization of a ferroelectric material has arisen as one option to slow down the charge carriers recombination which leads to an enhancement of the photocatalytic activity[15]. Heterostructures formed by a photocatalyst layer deposited on a ferroelectric material layer is one of the possibilities to use the polarization of that material to favour a photocatalytic process. For these reasons, the preparation of high quality epitaxial thin films is crucial to fully understand the effect of the polarization on the photocatalytic processes.

This section will be centred on the deposition of TiO_2/BTO/STO heterostructures. The final objective is to enhance the anatase (001) photocatalytic properties by growing it on a ferroelectric layer to use its polarization to increase the lifetime of charge carriers. The objective of this chapter is to obtain fully epitaxial anatase (001) oriented on a BTO ferroelectric film.

3.5.1. TiO_2 growth conditions on BTO/STO

The starting growth conditions, as explained in the previous sections, were 700ºC and 1 mTorr for the BTO film and 875ºC and 85mTorr for the TiO_2 keeping the same laser fluence (1.8 J/cm^2) and deposition rate (2Hz) for both films. The thicknesses were 100nm for BTO and 120nm for the TiO_2. Hereinafter, all the deposition conditions will be addressed only for the TiO_2, since the BTO growth conditions are not changed.

The first deposition led to the appearance of (100)-oriented anatase as illustrated in *Figure 3.60.* The x-ray diffractogram of those samples contain reflections coming from the STO substrate, the BTO and the TiO_2-anatase film (100).

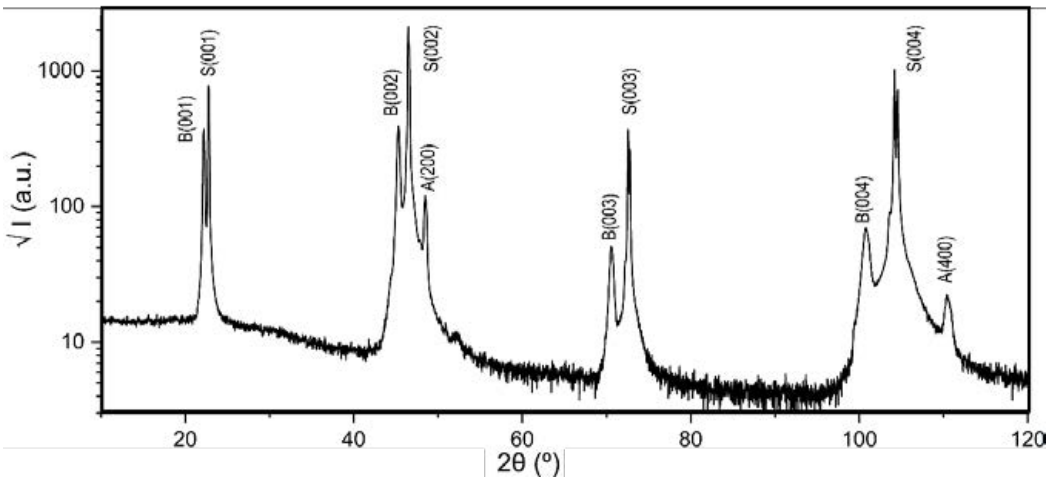

Figure 3.60 : X-ray diffractogram of a TiO2/BTO/STO film. (A), (B) and (S) correspond to anatase, BTO and STO reflections, respectively.

A flat terraced-like morphology with islands size of about 130 nm. is observed on the AFM images of *Figure 3.61*. These kind of morphology looks like the obtained for TiO_2/STO samples deposited at the same temperature (875ºC) with similar islands size, 120 nm and 130 nm for the TiO_2/STO samples (*Figure 3.10e*) and the heterostructure, respectivley. This behaviour suggests that the islands size is more dependent on the deposition temperature than on the layer used to deposit the titania.

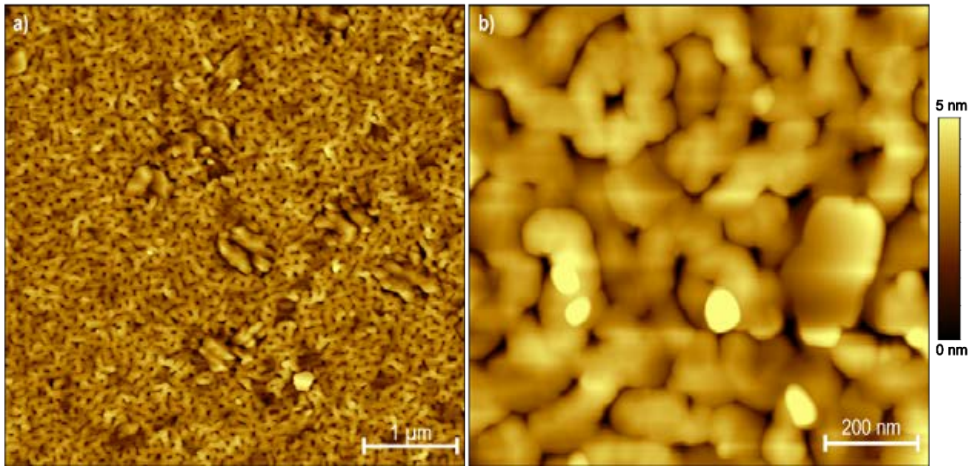

Figure 3.61: (a) 10x10µm^2 and (b) 5x5µm^2 AFM images of a TiO_2/DSO (110) sample.

The bigger lattice parameter of BTO results in a greater mismatch of the TiO_2 compared with the TiO_2 anatase/STO mismatch (3.1%). To check if the lattice parameter of BTO was the feature leading to the appearance of (100) oriented anatase we decided to grow TiO_2 on DyScO3 (DSO) (110) substrates, with the same deposition conditions (875ºC, 85mTorr, 50nm thick). DSO has an orthorhombic crystal structure with a pseudo cubic lattice parameter of 0.395nm[184] which results in a 4.5% lattice mismatch. The resulting x-ray diffractogram (*Figure 3.62*) shows that TiO_2 grows as (001) oriented anatase. However, the anatase (004) reflection is not as intense as expected for a sample of this thickness. Additionally, the (008) reflection cannot be observed.

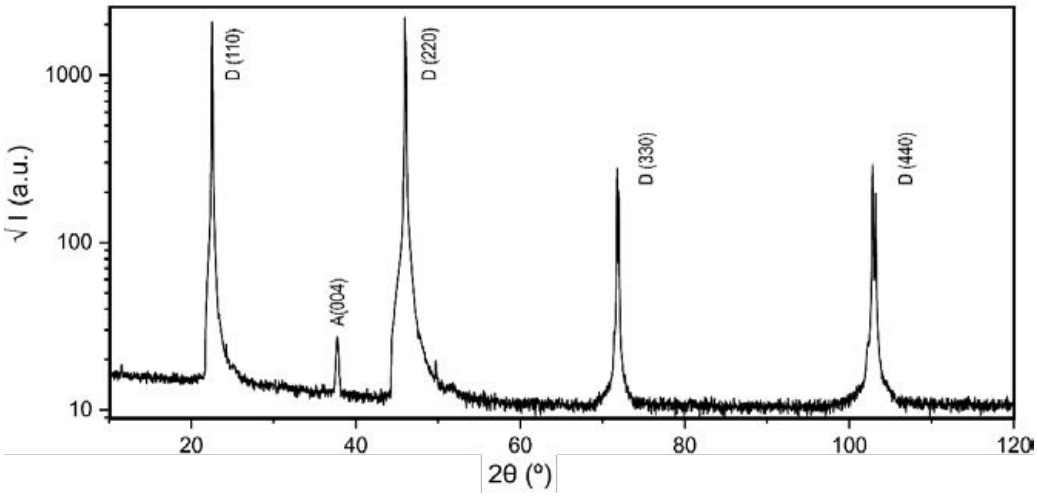

Figure 3.62: X-ray diffractogram of TiO_2/DSO films deposited at 875ºC, 85mTorr, 100mJ and 2Hz.

The morphology of this sample (*Figure 3.63*) shows two kind of structures forming the sample's surface: terraces together with islands. The terraces are flat and have a similar shape to those seen in TiO_2/STO samples (*Figure 3.10e*). On the other hand, the islands seem to have a variation in height within them.

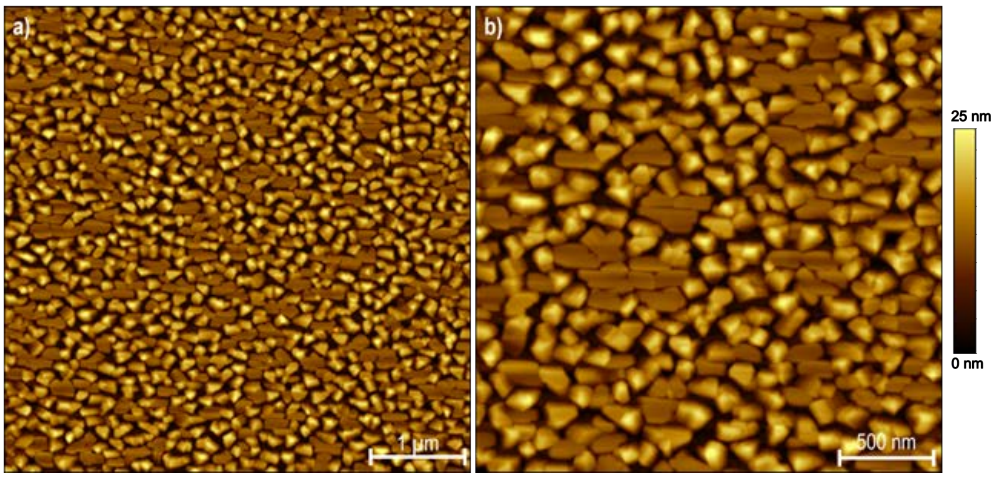

Figure 3.63: (a) 10x10µm² and (b) 5x5µm² AFM images of an as prepared TiO_2/DSO film, (c) 10x10µm² and (d) 5x5µm² AFM images of an annealed TiO_2/DSO film at 900ºC for 6h in air.

These results indicates that the appearance of (100)-anatase oriented is not only affected by the mismatch with the substrate. Thus, the most plausible explanation of this growth comes from the titanium atoms

located at the BTO surface, unlike the DSO substrates, that could be a preferential anchor point for the TiO_2 during the deposition.

In view of the above results, the TiO_2 deposition temperature was reduced to 700ºC in search of pure TiO_2 anatase (001) thin films keeping the same thickness (: ~100nm) and deposition pressure (85 mTorr). The x-ray diffractogram obtained from those preparations (*Figure 3.64*) show the presence of a TiO_2 polymorphs mixture: anatase (001) and rutile (110) with low intensities.

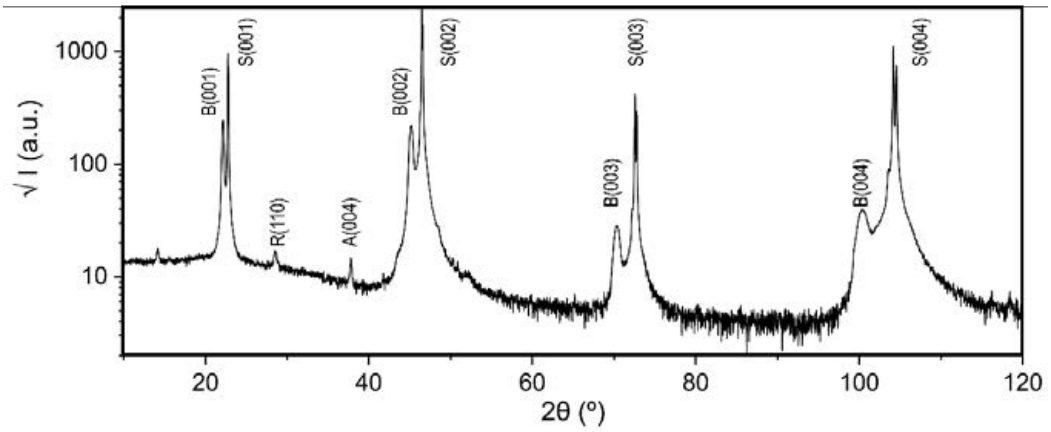

Figure 3.64: X-ray diffractogram of a TiO2/BTO/STO film deposited at 700ºC. (A), (R), (B) and (S) correspond to anatase, rutile, BTO and STO reflections, respectively.

However, it has been reported that the combination of those TiO_2 polymorphs lead to higher photoactivity compared to single-phase titania[28,29,185–187]. That phenomenon is usually assigned to a better charge carrier separation, where electrons are trapped in rutile resulting in less electron-hole recombination[28,188].

Kitazawa S. et.al.[189] obtained mixed rutile-anatase TiO_2 thin films by PLD depositing the samples in the 400-500ºC temperature range and variable oxygen pressures 5 Pa (~40mTorr) and 80 Pa (~600mTorr). The authors explain that the growth mechanisms of both phases is ruled by a competitive process between the epitaxy induced by the lattice misfit and the thermodynamic stability of the crystal growth.

The combination of this phases is proved to increase the photocatalytic activity compared to the. Siah W.R. et. al.[29] studied the photocatalytic activity for the removal of two pollutants: 2,4-dichlorophenoxyacetic acid and 2,4,5-trichlorophenoxyacetic acid of commercial nanoparticles with different anatase: rutile ratios. It was proved that the commercial nanoparticles formed by a mixture of phases lead to an increase of the acid's photocatalytic removal. The results are summarized in *Table 3.8*.

Nanoparticle	Anatase: rutile ratio	Removal of the pollutant (%)
Evonik P25	80:20	90.4
Evonik P90	92:8	93.3
Hombikat UV100	100:0	70.6
Hombikat N100	100:0	73.1

Table 3.8: Summary of the results published by Siah W.R. et. al.[29].

For these reasons, the resulting sample with a mixture of anatase and rutile could be interesting for photocatalytic purposes.

A completely (001) oriented TiO_2-anatase was achieved when the deposition temperature is decreased to 600ºC as confirmed by the x-ray diffractogram (*Figure 3.65*). The diffraction pattern just contains reflections coming from the STO substrate, the BTO (00L) reflections and the (00L) reflections coming from the anatase.

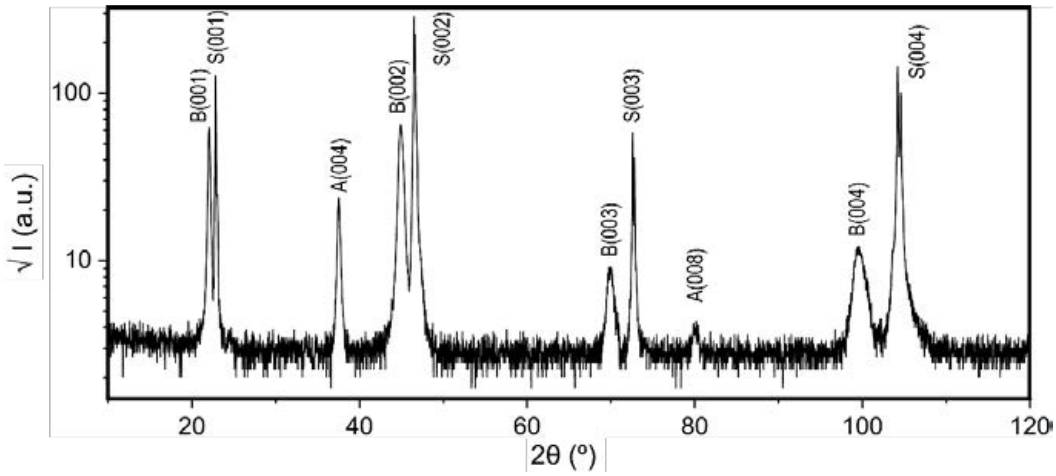

Figure 3.65: X-ray diffractogram of a TiO2/BTO/STO film deposited at 700ºC. (A), (B) and (S) correspond to anatase, BTO and STO reflections, respectively.

The morphological study carried out by AFM is illustrated in *Figure 3.66*. The sample presents a granular-like topography comparable to the one found for TiO_2/STO films (*Figure 3.10a*), with islands sizes around 35 nm.

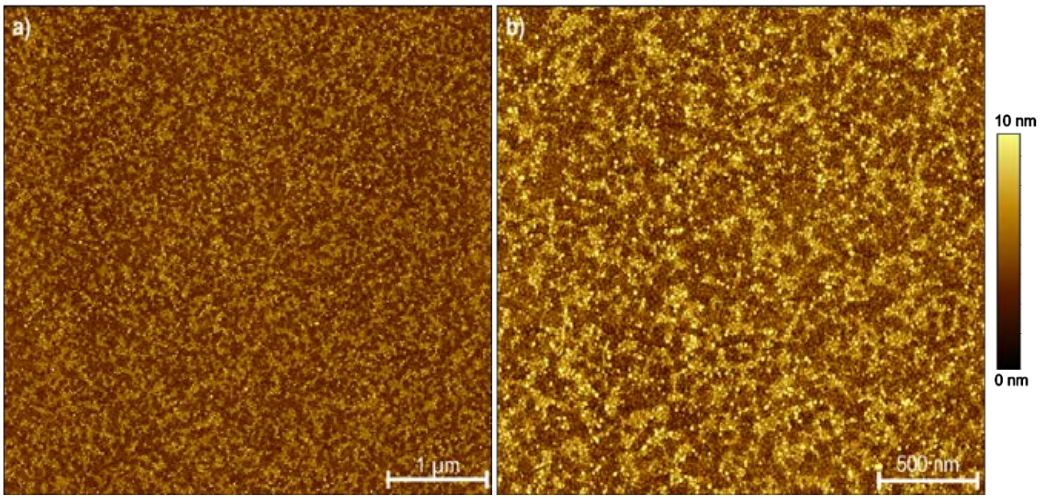

Figure 3.66 (a) 10x10µm² and (b) 5x5µm² AFM images of a TiO_2/BTO/STO film deposited at 600ºC.

These last heterostructures, deposited at 600ºC and 85mTorr, were studied by TEM. Selected area diffraction (SAD) patterns of the heterostructure viewed along the [100] STO zone axis are illustrated in *Figure 3.67*. A splitting of in-plane spots can be seen on *Figure 3.67a* (circled spots) corresponding to the

interface between BTO and the STO substrate which indicates film relaxation. Additionally, the SAD pattern of the whole heterostructure illustrated in *Figure 3.67b* shows sharp spots that indicate perfect epitaxial relationship with basal square-on-square alignment of the three structures. The arrow in Figure 3.67b also shows splitting at the (020)A position indicating relaxation of the TiO_2 film relative to the BTO layer.

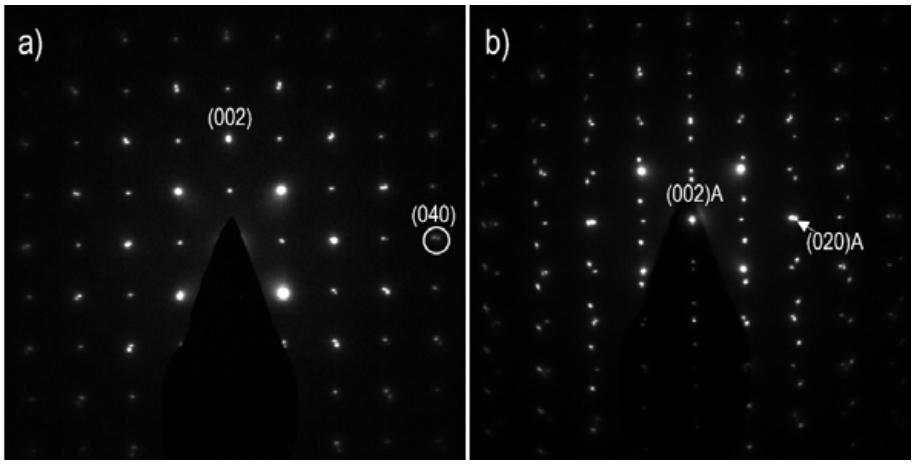

Figure 3.67 SAD patterns of (a) the BTO/STO interface and (b) the whole heterostructure.

The TEM cross-section image (*Figure 3.68a*) of the heterostructure reveals dislocations and strong strains in the TiO_2 anatase layer. Moreover, some areas exhibit periodic contrast modulations which are indicative of oxygen deficiency in TiO_2, as explained in *section 3.2.1.5.TEM characterization*. The BTO layer, on the other hand, shows vertical contrasts coming from the ferroelectric domains of the BTO layer. High-resolution TEM images (*Figure 3.68b* and *c*) allow a better visualization of the BTO ferroelectric domains. This contrast comes from the different crystal orientation of the BTO domains.

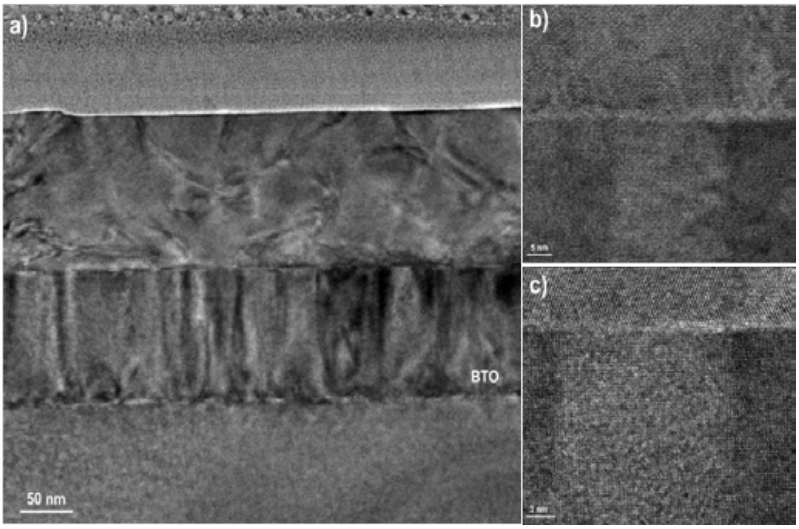

Figure 3.68: (a) cross-section image taken along the [100] STO axis of the heterostructure, (b-c) HRTEM images of the TiO_2/BTO interface. Ferroelectric vertical domains are observed in b) and c).

3.5.2. Summary and conclusions

The growth conditions optimization of TiO_2 heterostructures is preliminary and is still in progress. However, fully (001) oriented anatase thin films deposited on BTO/STO (100) have been grown at 600ºC and 85mTorr. It has been proved that the growth temperature influences the final orientation, as well as the resulting titania phase. At 875ºC, TiO_2 grows (100)-oriented, we assign this change in orientation, to the different mismatch between TiO_2 and the BTO film compared to its mismatch with STO combined with the presence of titanium atoms on the structure of BTO. Additionally, intermediate temperatures (700ºC) lead to films with mixed phases of titania: rutile (110) and anatase (001). Furthermore, the morphological studies show that the islands size evolution follows the same behavior as happened withTiO_2/STO samples, an increase in the deposition temperature leads to bigger islands.

4. Surface structure

This chapter will be focused on SXRD experiments carried out in the ESRF for the TiO_2 films and for the BTO film. The first section is devoted to elucidating the surface structure of the (4x1) (001) anatase. Additionally, the order along a BTO films was investigated. The study of the arrangement of the atoms on the surface of a material is crucial to fully comprehend the processes that take place.

4.1. TiO_2 surface characterization

The promising properties of TiO_2 for photocatalytic applications[23,24,190] has attracted attention to the investigation of its surface structure to understand the photoactivity of this material by studying model single crystal TiO_2 surfaces, such as thin films. Of the three natural polymorphs of titania anatase is considered to be the most photoactive[26,191]. Rutile (110) and anatase (101) are the most studied facets of titania as they are the most thermodynamically stable at high temperatures and the most stable at room temperature, respectively. However, several reports suggest that anatase (001) facet could exhibit more reactivity for photocatalytic reactions[192–195] because it contains higher amount of titanium actives sites at its surface[114,196]. Additionally, the reduction of Ti^{4+} into Ti^{3+} due to the loss of oxygen or the presence of oxygen vacancies can enhance the photocatalytic activity as the Ti^{3+} ions can act as hole traps to promote charge transfer.
Nonetheless, there is still being studied as several reports in the literature have observed that an anatase(001) surface exhibited less reactivity than the (101) facet[32,197]. In consequence, it is crucial to characterize the surface structure of anatase (001) surfaces. The (4x1) surface reconstruction, as those observed in our films (see *Section 3.2.2 MBE growth*), is known to appear in UHV conditions[134,198]. However, determining the reconstruction's atomic structure and the surface's flaws is not straightforward. Several studies have been done to elucidate the (4x1) surface reconstruction structure[134,135,198]. Liang Y. et. Al.[198] proposed an “added” -and- “missing”-row model for the 4x1 reconstruction (microfacets along (103) surface planes). Based on STM, RHEED, LEED and XPS results, a model based on the (1x1) surface structure was suggested. The authors present that each surface unit cell is made of one added Ti-O row, two added oxygen rows and one missing oxygen row, which leads to a stoichiometric and no charge surface (*Figure 4.1a*). However, a different structure for the (4x1) surface structure involving periodically replacements of oxygen rows of the (1x1) surface by TiO_3 species rows was proposed by Lazzeri et al.[134] by density functional (DFT) calculations (*Figure 4.1b*). Additionally, Herman et. al.[135] proposed a missing row model, where every fourth row of oxygens is removed leading to the exposure of the underlying titanium atoms that become threefold coordinated (*Figure 4.1c*).

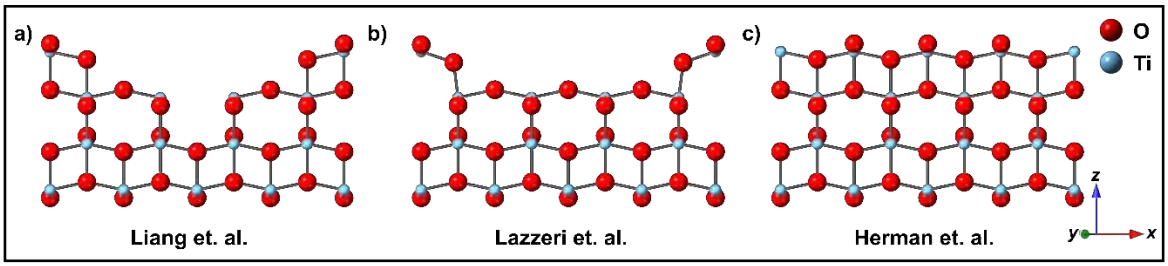

Figure 4.1: Ball and stick model of TiO_2 (001). (a), (b) and (c) illustrates the structure proposed by Liang et.al.[198]*, Lazzeri et.al.*[134] *and Herman et.al*[135]*., respectively.*

The uncertainty about the anatase (001) (4x1) surface reconstruction structure is a limiting factor to understand the mechanisms involved in the different surface interactions of anatase during photocatalytic processes. The previously reported structural ordered models could not fit our experimental data due to the excessive presence of disorder in the surface film. Thus, a new model was proposed to consider the surface disorder reflected in the experimental data.

4.1.1. Experimental procedure

Experimental work was realized at the ESRF in BM32-IF (interface) beamline dedicated to SXRD experiments. The samples selected for this experiment were prepared by PLD (875ºC, P_{O2}= 85mTorr, 2Hz, t=80nm) and by MBE (650ºC, P_{O2} =10^{-6} mbar, t=8nm) similar to the ones presented in *Figures 3.10e* and *3.21*. In situ cleaning involved repeated cycles of Ar^+ bombardment (5 minutes,10^{-6} mbar, 5 μA emission current) and annealing (30 minutes, 700ºC, P_{O2}=$5\cdot10^{-7}$ mbar). Once prepared, the films were transferred to the analysis chamber mounted on a six-circle diffractometer with the sample surface in the vertical plane. Measurements were done with the sample at room temperature, employing a photon energy of 11.7 KeV and an incidence angle of 0.6º. Diffracted x-ray intensity was acquired using stationary scans in where the whole rod over the entire in-plane direction is accepted for the detector for a range of l values.

For selected (h, k), such scans were conducted as a function of l, and then integrated and corrected[199], to enable plots of structure factor versus perpendicular momentum transfer (l) to be produced for both crystal truncation rods (CTRs) and fractional order rods (FORs). For the determination of the structure factors of the (h,k,l) reflections some correction had to be done: (a) the illuminated part area of the surface that participates on the diffracted intensity is related to the slits put before and after the sample[78], (b) the Lorentz geometrical factor which is related to the experimental geometry and in this case defined by *Equation 4.1*[199]:

$$L_s = 1/\sin\beta_{out} \qquad (4.\ 1)$$

(c) the intensity of the emitted radiation from the undulator, as it is almost 100% horizontally polarized, must be corrected by the polarization factor which can be expressed by *Equation 4.2*[200]:

$$P = \sin^2\varphi + \cos^2\varphi\ \cos^2 2\theta \qquad (4.\ 2)$$

4.1.2. Results

The dataset obtained consists of a total 5516 reflections and 2291 for the PLD and MBE samples, respectively, that-using a *P4mm* symmetry (*P2mm* (basic 1x1 cell) + 2 domains rotated 90º) reduce to 3452 non-equivalent points, that correspond to 12 crystal truncation rods (CTRs) and 7 fractional order rods (FORs) for the PLD sample and 1886 non-equivalent points for the MBE sample for a total of 13 CTRs and 5 FORs. The agreement factor between equivalent reflections was about 15% for both datasets. These data are indexed referenced to the anatase bulk unit cell (a_{bulk} = 3.7845 Å, c_{bulk} = 9.5143 Å)[119] defined by three lattice vectors a_1 (100) = a_2 (010) and a_3 (001). The STO's substrate reflections were used to orient the sample, because its reflections are better defined as it is a single crystal. The refinement of the structure was done for the first three cell units, formed by 4 layers of titanium atoms each, to study the variation of the structural parameters as a function of *z*. The reported models were checked generating simulated SXRD data for a possible structure and then refined by different iteration processes to find the best agreement between the experimental data and the model evaluated by the χ^2 value.

After the refinement of the atomic coordinates combined with several non-structural parameters the lowest χ^2 values found for the different models, as well as for our proposed model are summarized in *Table 4.1* together with the minimum and maximum lengths of the Ti-O bonds for the first three unit cells.

Model	χ^2	*nº unit cell*	*Ti-O$_{min}$*	*Ti-O$_{max}$*
Liang et. Al.[198]	1.7	1	1.50	2.37
		2	1.57	2.29
		3	1.57	2.18
Lazzeri et. Al.[134]	2.0	1	1.17	2.43
		2	1.25	2.47
		3	1.53	2.44
Herman et. Al.[135]	1.9	1	1.49	2.47
		2	1.68	2.39
		3	1.76	2.15
Disordered vacancy model	1.1 (1.0)	1	1.67 (1.71)	2.25 (2.30)
		2	1.81 (1.77)	2.14 (2.28)
		3	1.91 (1.81)	2.08 (2.17)

Table 4.1: Obtained χ2 and calculated Ti-O distances of the different models used for the anatase (001) surface structure refinement for the first three unit cells. The values in parenthesis indicate the MBE obtained bond lengths. The error in the Ti-O length is ± 0.01 Å.

Despite the low χ^2 values obtained for the previously reported models, they do not represent good agreement with the experimental data as it can be seen on *Figure 4.2*, where a selection of the obtained CTR and FOR are displayed along with the simulated and refined data for the different models used.

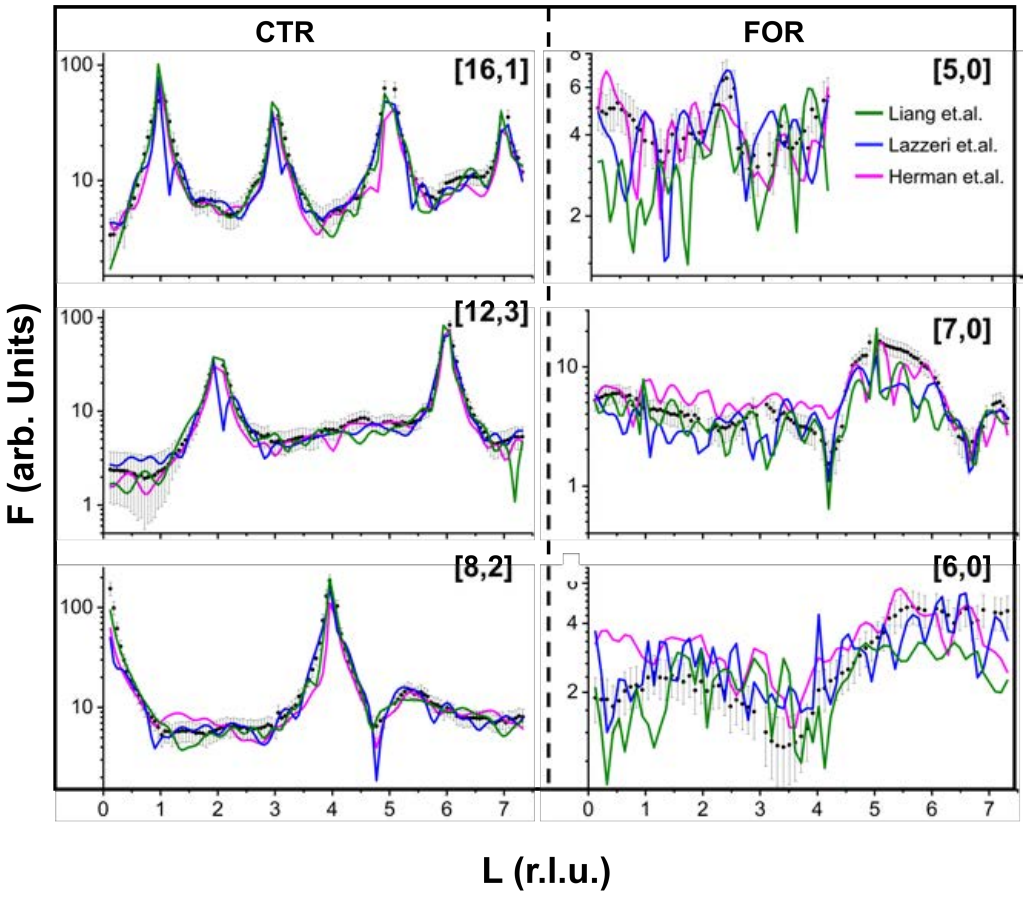

Figure 4.2: Comparison of the experimental data (black dots with error bars) and theoretically simulated CTR and FOR for the reported models.

As previously explained the three models used to check the experimental are ordered vacancy models, where all the atoms' occupancies are 100%, except for the missing rows. The presence of disorder on the anatase (001) surface could give rise to a distribution of atomic vacancies on it. Thus, an alternative model based on disordered vacancies has been found with a χ^2 value of 1.1 and 1.0 for the PLD and MBE data, respectively, which indicates close agreement with the data and the theory as shown in *Figure 4.3* for the PLD dataset and in *Figure 4.4* for the MBE dataset, where the experimental data (black dots with error bars) is displayed together with the optimum structure proposed in this work (red line). The R-factor, known as the unweighted residual[201], has an average 19% and 17% for the PLD and MBE, respectively.

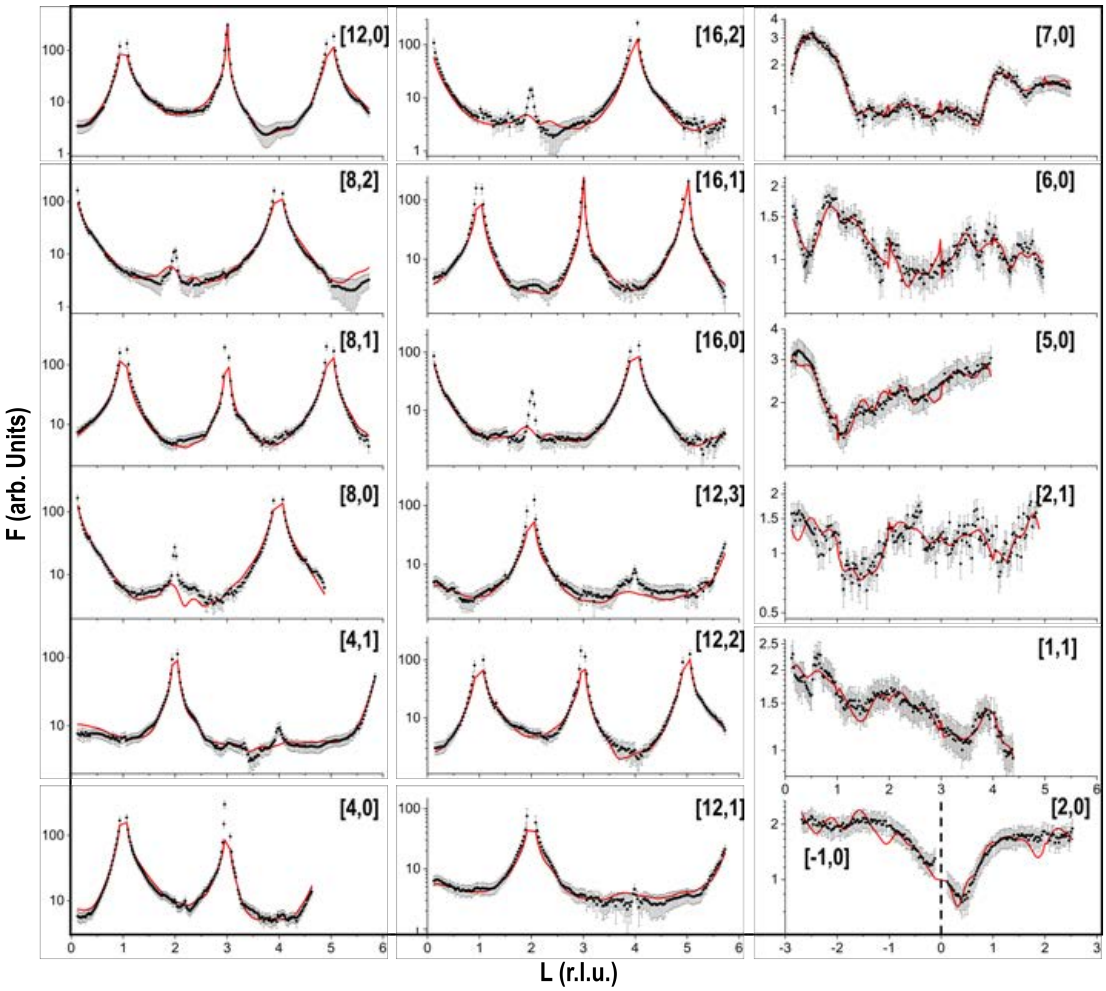

Figure 4.3: CTRs and FORs comparison of experimental (dots with error bars) for the PLD dataset. The red line indicates the best fit (χ^2= 1.1).

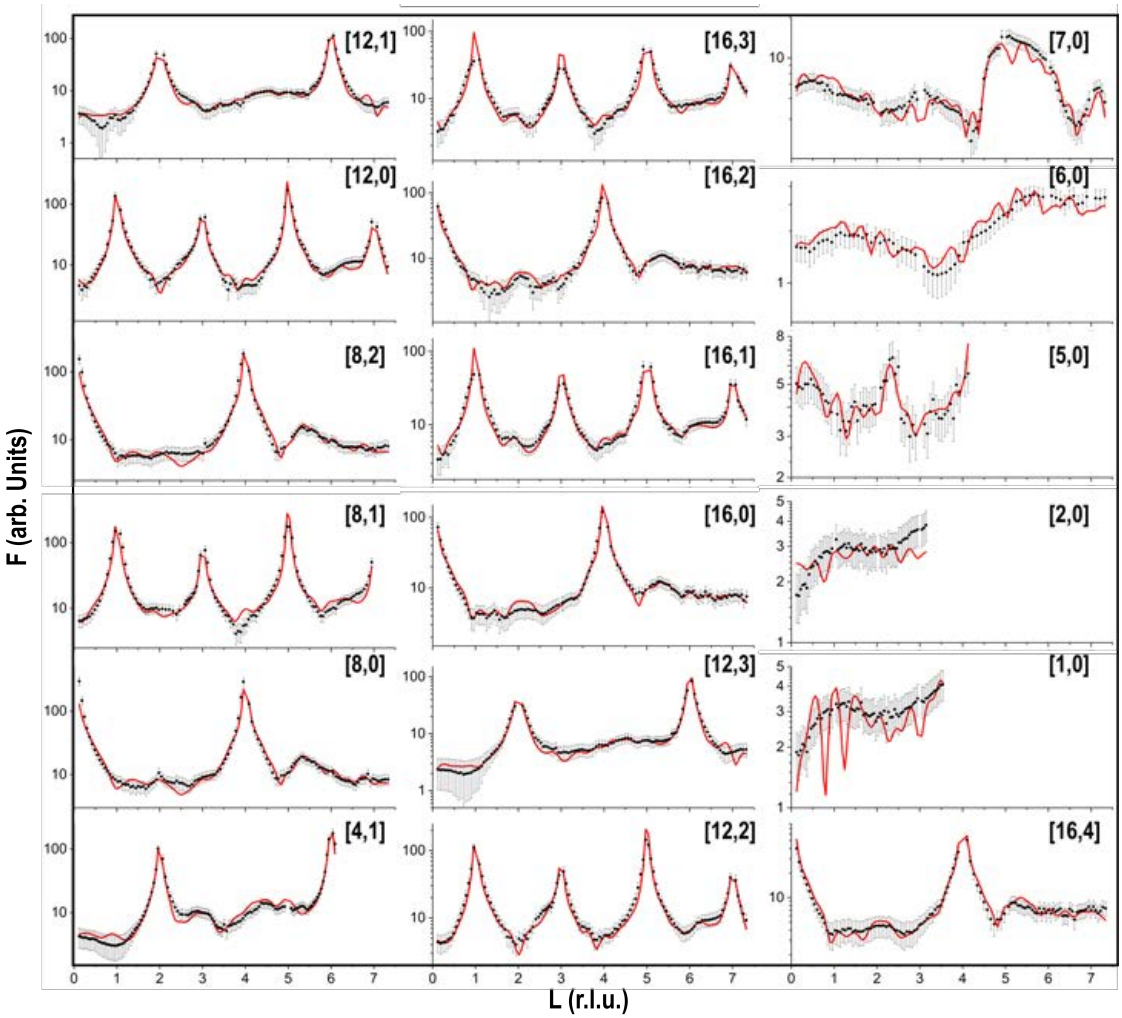

Figure 4.4: CTRs and FORs comparison of experimental (dots with error bars) for the MBE dataset. The red line indicates the best fit (χ^2= 1.0).

Table 4.2 contains the location of the atoms in the structure, expressed as displacements from the bulk (001) TiO_2 anatase, as well as the occupancy of those atoms. The atoms with no occupancy value mean that are fully occupied (100%). 150 parameters (141), including 136 (128) atomic coordinates, 10 (9) occupancies, 2 scale factors, a surface roughness parameter (β) and a surface fraction parameter were optimized to arrive to the proposed structure for the PLD and the MBE, respectively. The smaller number of structural parameters used to refine the MBE data set was due to the use of restraints between some bonded atoms. All the non-structural parameters adopted reasonable values. The small roughness parameter (β=0.03) is small because the surface roughness has already been simulated refining the occupancies of the topmost surface layers. The surface fraction parameter is 96%, indicating that almost all the surface is consistent with the structure obtained in our refinement. The standard deviations (σ_x, σ_z) corresponding to the X and Z atomic coordinate distortions for each model with respect to the anatase bulk model (refined with the PLD or MBE data sets) are summarized in *Table 4.3,* expressed in Å. The standard deviations are averaged mixing the titanium and oxygen atoms and only the titanium deviations,

Atom	Bulk (x,y,z) (4x1) atomic coordinates.(norm. units)	PLD (Δx, Δz) (Å) , Occup. (%) Δ* (0.004, 0.019) Å	MBE (Δx, Δz) (Å) , Occup. (%) Δ* (0.004, 0.019) Å	Atom	Bulk (x,y,z) (4x1) atomic coordinates.(norm. units)	PLD (Δx, Δz) (Å) , Occup. (%) Δ* (0.004, 0.019) Å	MBE (Δx, Δz) (Å) , Occup. (%) Δ* (0.004, 0.019) Å
O (1)	(0,0,4.0424)	(0,-0.409), 22	(0, -0.323), 81	O (20)	(0.5,0.5,3.2076)	(0, 0.228)	(0, 0.162)
O (2)	(0.25,0,4.0424)	(-0.008, -0.276), 22	(0.011, -0.323), 79	O (21)	(0,0,3.0424)	(0, 0.124)	(0, 0.181)
O (3)	(0.5,0,4.0424)	(0, -0.485), 22	(0, -0.323), 81	O (22)	(0.25,0,3.0424)	(-0.004, 0.171)	(-0.045, -0.048)
Ti (1)	(0,0,4)	(0, -0.086), 22	(0, -0.199), 79	O (23)	(0.5,0,3.0424)	(0, 0.0171)	(0, -0.086)
Ti (2)	(0.25,0.5,4)	(-0.008, -0.114), 22	(-0.008, -0.276), 81	Ti (11)	(0,0.5,3)	(0, 0.038)	(0, -0.124)
Ti (3)	(0.5,0.5,4)	(0, -0.133), 22	(0, -0.323), 26	Ti (12)	(0.25,0.5,3)	(0.011, 0.019)	(0.004, 0)
O (4)	(0.125,0, 3.9576)	(0,0), 0	(0, 0.143), 16, 26	Ti (13)	(0.5,0.5,3)	(0, 0.010)	(0, 0.0162)
O (5)	(0.375,0, 3.9576)	(0,0), 0	(0, 0.152), 100	O (24)	(0.125,0.5,2.9576)	(-0.004, 0.181)	(-0.015, 0.133)
O (6)	(0,0.5,3.7924)	(0, 0.219), 26	(0, -0.219), 81	O (25)	(0.375,0.5,2.9576)	(-0.004, 0.105)	(-0.034, 0.029)
O (7)	(0.25,0.5,3.7924)	(-0.011, 0.199), 33	(0.011, -0.276), 79	O (26)	(0,0.5,27924)	(0, 0.209)	(0, -0.001)
O (8)	(0.5,0.5,3.7924)	(0, 0.171), 33	(0, 0.019), 81	O (27)	(0.25,0.5,27924)	(0.011, 0.181)	(-0.019, 0.010)
Ti (4)	(0.125,0.5,3.75)	(0, -0.029), 37	(-0.015, 0.143), 81	O (28)	(0.5,0.5,27924)	(0, 0.143)	(0, -0.234)
Ti (5)	(0.375,0.5,3.75)	(0, 0.038), 37	(-0.015, 0.152), 79	Ti (14)	(0.125,0.5,2.75)	(-0.004, 0.057)	(0.023, 0.095)
O (9)	(0.125,0,3.7076)	(-0.053,-0.029), 57	(0.015, -0.067), 58	Ti (15)	(0.375,0.5,2.75)	(-0.004, 0.038)	(-0.008, -0.114)
O (10)	(0.375,0,3.7076)	(-0-068, 0.057), 30	(-0.068, -0.048), 58	O (29)	(0.125,0.5,2.7076)	(0.019, 0.162)	(-0.015, -0.029)
O (11)	(0.125,0.5,3.5424)	(0.019, 0.057), 70	(-0.027, 0.143), 58	O (30)	(0.375,0.5,2.7076)	(0.023, 0.105)	(0.057, 0)
O (12)	(0.375,0.5,3.5424)	(-0.030, 0.219), 75	(-0.061, 0.152), 58	O (31)	(0.125,0.5,2.5424)	(-0.004, 0.171)	(-0.026, 0.095)
Ti (6)	(0.125,0,3.5)	(0, 0.057), 100	(0.004, -0.067)	O (32)	(0.375,0.5,2.5424)	(-0.004, 0.076)	(0.030, -0.143)
Ti (7)	(0.375,0,3.5)	(0.004, 0.057), 100	(0.008, -0.048)	Ti (16)	(0,125,0,2.5)	(0.004, 0.067)	(0.008, -0.019)
O (13)	(0,0,3.4576)	(0, 0.105), 100	(0, -0.019)	Ti (17)	(0,375,0,2.5)	(0, 0.029)	(0.008, 0)
O (14)	(0.25,0,3.4576)	(-0.011, 0.105), 80	(-0.045, -0.048)	O (33)	(0,0,2.4576)	(0, 0.104)	(0, 0.143)
O (15)	(0.5,0,3.4576)	(0, -0.114), 100	(0, -0.285)	O (34)	(0.25,0,2.4576)	(-0.004, 0.038)	(0.034, -0.181)
O (16)	(0.125,0,3.294)	(0, 0.409)	(-0.049, -0.067)	O (35)	(0.5,0,2.4576)	(0, 0.029)	(0, -0.105)
O (17)	(0.375,0,3.294)	(-0.011, 0)	(-0.068, -0.209)	O (36)	(0.125,0,2.2924)	(0.004, 0.171)	(0.045, 0.181)
Ti (8)	(0,0,3.25)	(0, 0.105)	(0, -0.019)	O (37)	(0.375,0,2.2924)	(0.004,0.038)	(0.019, 0)
Ti (9)	(0.25,0,3.25)	(0, 0.067)	(0.004, -0.048)	Ti (18)	(0,0,2.25)	(0, 0.057)	(0, 0.086)
Ti (10)	(0.5,0,3.25)	(0, 0.038)	(0, -0.086)	Ti (19)	(0.25,0,2.25)	(-0.004, 0.029)	(0, 0.010)
O (18)	(0,0.5,3.2076)	(0, 0.276)	(0, -0.247)	Ti (20)	(0.5,0,2.25)	(0, 0.019)	(0, -0.105)
O (19)	(0.25,0.5,3.2076)	(0.053, 0.152)	(0.042, 0.171)				

Table 4.2: Optimized locations of the atoms in the TiO_2 (001) –(4x1) surface reconstruction obtained from the analysis of the SXRD data for the PLD and MBE samples. Expressed as displacements from the bulk terminated TiO_2 surface in Å. (x,y,z) atomic coordinates for the bulk-terminated structure are also listed. ΔX and ΔZ correspond to the average errors assigned to the in-plane and out-of-plane atomic displacements obtained from the fit, respectively.

	Ti+O (Å)		Ti (Å)	
Dataset	σ_x	σ_z	σ_x	σ_z
PLD	0.015	0.105	0.004	0.048
MBE	0.027	0.133	0.011	0.105

Table 4.3: Summary of the standard deviation values for each dataset PLD and MBE. The errors of the σ_x and σ_x are ±0.003 and ±0.008, respectively.

As displayed on *Figure 4.5*, the structure that we propose presents several differences to those already published. Importantly, our model is based on disordered vacancies, whereas the reported models consist of arrangements of ordered vacancies (missing row or facet model).

This model assumes that in average just one 1x1 cell is fully occupied for each 4 cells (25% occupancy) for the outermost level of the surface. The occupancy on the second level is the 33%, meaning that one 1x1 cell is full for each 3 cells, while the third level has four occupied cells for each 5 cells (80% occupancy). At lower levels all the layers are fully occupied. The models reported in literature do not properly fit the data as all of them assume ordered reported models and our data show some positional disorder of the surface specimens. This behavior could be related to the surface quality of the film. The sample used for this experiment has a maximum island size of 120 nm, which is insufficient for reliable structural statistics that will need island sizes similar to the substrate terraces (~250nm).

Despite the worse fit of the tested ordered vacancy models (*Table 4.1*) compared to the proposed disordered vacancy model, they cannot be completely discarded since the reliability of the experimental data reflects the structural disorder of the film surface. The low number of accessible fractional order reflection rods in the experiment indicate the limitation of the dataset to unambiguously discriminate the final structure of the reconstruction. As the dataset acquired reflects a disordered structure the adjustment with ordered models is not possible. The addition of occupational disorder during the refinement of the reported models shown on Figure 4.1, tends to recreate similar models to our disordered vacancies model. Thus, the occupancies on those models were not optimized.

Figure 4.5 illustrates the proposed model structures of the anatase (001) 4x1 surface reconstruction for the PLD and the MBE datasets. Both structures are very similar in the directionality of the atomic titanium displacements. The main difference between the two models is the atomic occupancy. In the PLD model (*Figure 4.5 up*) the three topmost layers are partially occupied, while on the MBE model (*Figure 4.5 down*) the vacancy distribution is located on the two first topmost surface layers. The different datasets acquired for each sample, mainly the fractional order reflections, can be explained by the variation in the atomic occupancy between both models (*Figure 4.3* and *Figure 4.4*). The error related to the oxygen atoms occupancy is higher than the 10% because of the disorder and its low atomic number, whereas the error associated to titanium atoms is around 2%. The Ti-O bonds follow “regular” periodic tilt angles between Ti : (Ti-O)1 = 89.9º, (Ti-O)2 = 93.6º, (O-Ti)3 = 86.1º, (Ti-O)4 = 91.4º. Subindex 1 to 4 indicating the angle between titanium and oxygen are specified in Figure 4.5.

From these values it is observed that the greatest distortions occur between the first four layers of Ti, which tend to decrease as the film goes deeper. The O-Ti-O chemical bonding angles of the thin film are moderately distorted with maximum/minimum O-Ti-O angles of 109.0º, 115.4º and 74.4º, for the topmost surface layers (*Figure 4.5*) compared to those of the anatase crystal (101º and 77º).

The main differences between the experimental vacancy models adjusted using PLD or MBE data sets are related with the different distribution of atomic vacancies among their topmost surface layers. The grown PLD sample implies a model in which vacancies extend to the top three surface layers, while MBE extends to only two. This difference cold be due to the different preparation methods. PLD involves films grown in very short times, 15 minutes per 50 nm thicknesses and MBE few nm in several hours. This could be an indication of the greater internal structural order of the MBE film with respect to the PLD. This order would imply a flatter surface and, consequently, the same UHV preparation method applied to both samples during the experiment would produce better surfaces in the case of MBE.

The structural atomic displacements are very similar in both cases, as observed in *Figure 4.5*. Despite the worse fit of the tested ordered vacancy models (*Table 4.1*) compared to the proposed disordered vacancy model, they cannot be completely discarded since the reliability of the experimental data reflects the structural disorder of the film surface. The low number of accessible fractional order reflection rods in the experiment indicate the limitation of the dataset to unambiguously discriminate the final structure of the reconstruction. As the dataset acquired reflects a disordered structure the adjustment with ordered models

is not possible. The addition of occupational disorder during the refinement of the reported models shown on *Figure 4.1*, tends to recreate similar models to our disordered vacancies model. Thus, the occupancies on those models were not optimized.

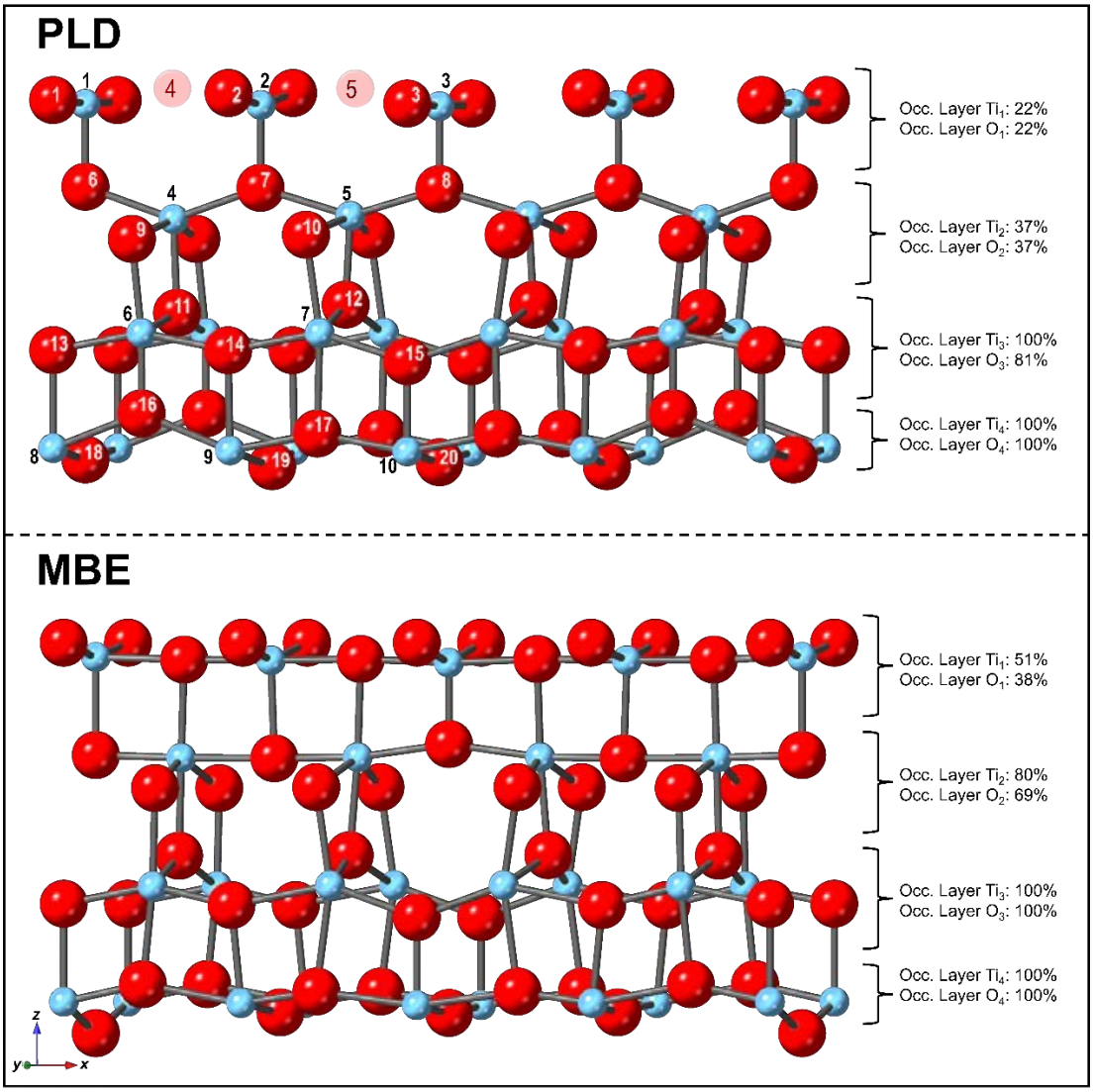

Figure 4.5: Ball and stick models of TiO_2 (001) for the PLD and MBE datasets. Larger red (smaller blue) spheres are oxygen (titanium) atoms. The numerical labelling of the atoms is the same used in Table 4.2 for identification purposes. The with no occupancy are represented with a lighter color.

The coordination number of the titanium present on the three topmost layers for both datasets is schematically illustrated in *Figure 4.6*, where the numbers next to the oxygen atoms correspond to the electrons shared by the oxygen to the neighbour titanium atoms (*Equation 4.3*):

$$n^{o}_{Oxygen\ electrons} = \frac{Occ_O \cdot O_{e^-}}{n^{o}_{coordination}} \qquad (4.\ 3)$$

Occ_O corresponds to the oxygen occupancy of the layer, O_{e^-} is the number of electrons that an oxygen atom can share (nº e^- =2). The total number of electrons from the oxygen atoms is obtained from the sum of the quantity of electrons for the oxygen atoms in the same layer. Then, the number of electrons that a titanium atom can accept from the neighbour oxygens is obtained with *Equation 4.4*:

$$n^{o}_{titanium\ electrons} = Occ_{Ti} \cdot Ti_{e^-} \quad (4.4)$$

Occ_{Ti} corresponds to the titanium occupancy of the layer, Ti_{e^-} is the number of electrons that a titanium atom can accept (nº e^- =4). Then, the amount of Ti^{3+} is obtained by the formula:

$$\%\ Ti^{3+} = \frac{\Delta n^{o}_{e-}}{n^{o}_{Ti\ x\ unit\ cell}} \cdot 100 \quad (4.5)$$

The analysis carried out results in approximately a 26.5% of Ti^{3+} and 24% of Ti^{3+} for the PLD and the MBE proposed models, respectively. This value is consistent with the 25.5% found with XPS (see *chapter 5 Water and oxygen interface with anatase (001) thin films*) for an as prepared PLD sample.

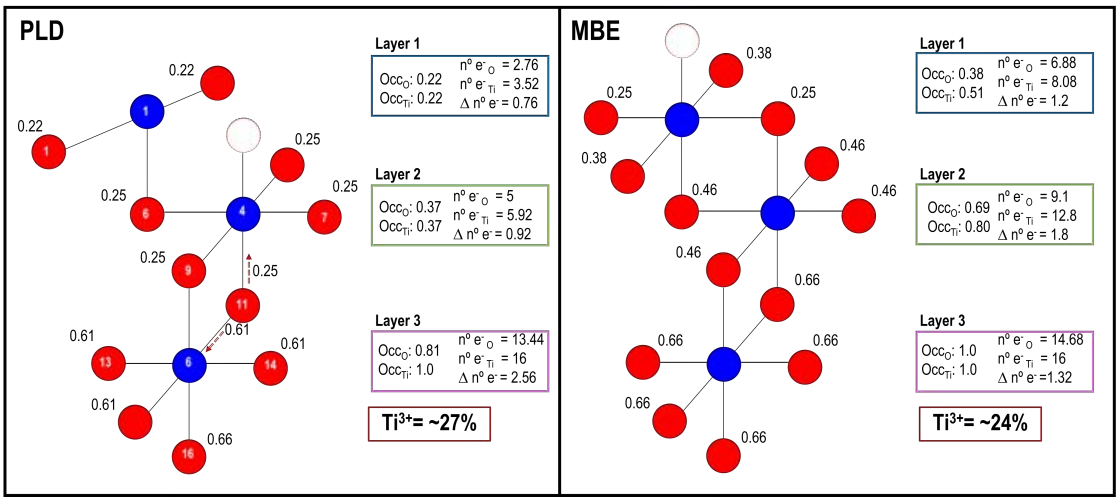

Figure 4.6: Schematic structure of the atoms used to calculate the amount of reduced titanium species. The numerical labelling of the atoms is the same used in Table 4.2 for identification purposes.

4.1.3. Conclusions

The best structural model that agrees with the experimental data considers an ideal anatase (001) terminated surface where the atomic stoichiometry in the upper layers shows partial Ti and O occupation. The distribution of vacancies is maximum at the outermost surface layer and progressively decreases until the fourth layer where the global anatase stoichiometry is recovered. The lack of a greater number of accessible experimental FORs does not allow to discriminate between the different models tested in the literature to fully validate the disordered vacancies model. To achieve this goal, a surface with less roughness and a larger terrace size would be required. However, the vacancy model shows some tracks of the real surface structure of the films. It provides an average picture of the surface structure (4x1) which is not totally unrealistic as analysis of the atomic occupancies of the oxygen and titanium atoms yields about 25% of Ti^{3+} on the upper layers, which is consistent with the percentage obtained through the XPS characterization. Additionally, ab initio calculations should be done to evaluate the energetic stability of the optimized geometry, as well as, for the published structures. This initial structure determination could be

used as initial model to evaluate the interaction between the electrolyte and the catalyst at the interface between both operating under photocatalytic conditions.

4.2. BTO characterization

A BTO deposited on STO at 700ºC and 1 mTorr was studied by SXD to characterize the order within the film. The experiment was carried out at the ESRF in BM32 -IF-interface beamline dedicated to SXRD experiments. The experimental procedure to prepare the sample and treat the data is the same as for the titanium samples explained in section *4.1.1 Experimental procedure*.

4.2.1. Results

The dataset obtained consists of a total 6431 reflections which using a P4mm symmetry reduce to 3468 non-equivalent points, that correspond to 18 crystal truncation rods (CTRs). The agreement factor between equivalent reflections around the 13%. The BTO reflections were measured introducing the experimental lattice parameters of the film in the calculation of the orientation matrix to avoid the re-indexation of the reflections between different bases, i.e., STO to BTO. This procedure involves first orienting the STO substrate according to its lattice parameters and then using this basis to find a set of reflections from the bulk BTO film. The lattice parameters of this set of reflections (indexed in the BTO base) are refined according to their measured angles and x-rays energy. The BTO film lattice values obtained from this process were ($a_{BTO\text{-}f}$ = $b_{BTO\text{-}f}$ = 4,000$_5$ Å, $c_{BTO\text{-}f}$ = 4.150$_5$ Å, α= 89.93$_2$º, β= 90.06$_2$º, γ=89.99$_2$º; subindexes correspond to errors). The set of experimental data described above was measured using this cell to obtain the (HKL) reflections in the base of the BTO. This lattice parameters are slightly larger than those of the tetragonal bulk unit cell (*a*=*b*=3.991 Å, *c*=4.035 Å)[202]. In this BTO film any surface reconstruction was detected, thus the structure has been checked from the ideal structure of the bulk BTO. 34 parameters, including 24 atomic coordinates, 8 isotropic vibrational amplitudes (Debye Waller factors), a scale factor, a surface roughness parameter (β) were optimized to achieve the final structure. All the non-structural parameters adopted reasonable values. The roughness parameter (β=0.7) suggests a rough surface. The measured CTR and FOR, as well as the best fit are shown in *Figure 4.6*, where the experimental data (black dots with error bars) is displayed together with the optimum structure proposed in this work (red line).

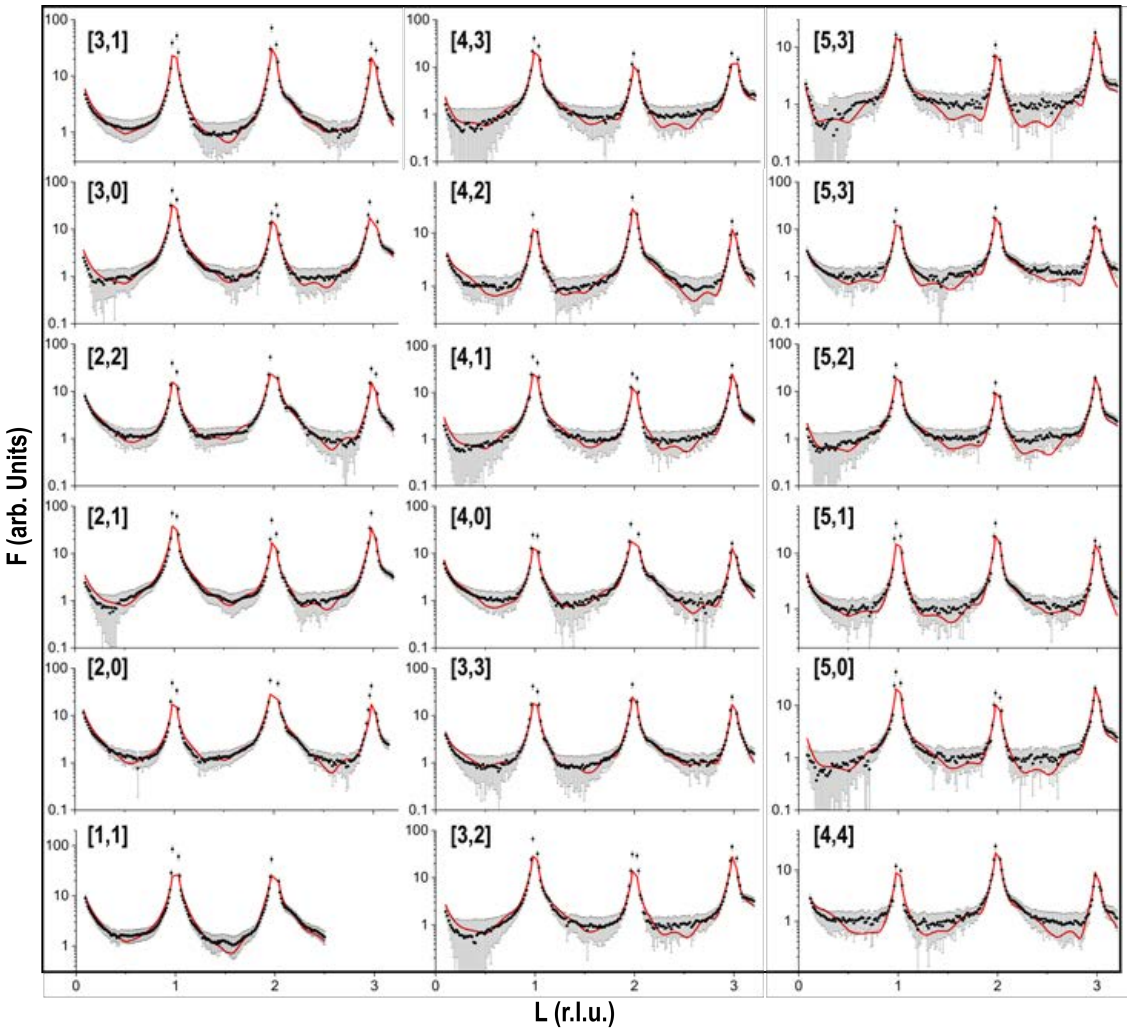

Figure 4.7: CTRs and FORs comparison of experimental (dots with error bars) for the BTO dataset. The red line indicates the best fit (χ^2= 0.9)

Figure 4.8 illustrates the obtained BTO structure. The analysis of the structure shows that the initial 4 units cells present a deformation compared to the bulk BTO. *Table 4.3* contains the average in-plane (green line in *Figure 4.8*) and vertical (yellow lines in *Figure 4.8*) O-Ti-O chemical bonding angles for the first four BTO unit cells. While the in-plane angles are almost 90º, as the bulk BTO, the vertical angles are slightly bigger leading to a distorted BTO unit cell. However, as we go deeper on the BTO structure it stabilizes and reaches angles closer to the expected 90º of the bulk BTO. Below those layers the differences are not significant. Additionally, *Table 4.4* also contains the average Ti-O distances comprised in a range of 1.83 -2.83 Å. These 113engths are comparable to the obtained by Kwei et.al[202].

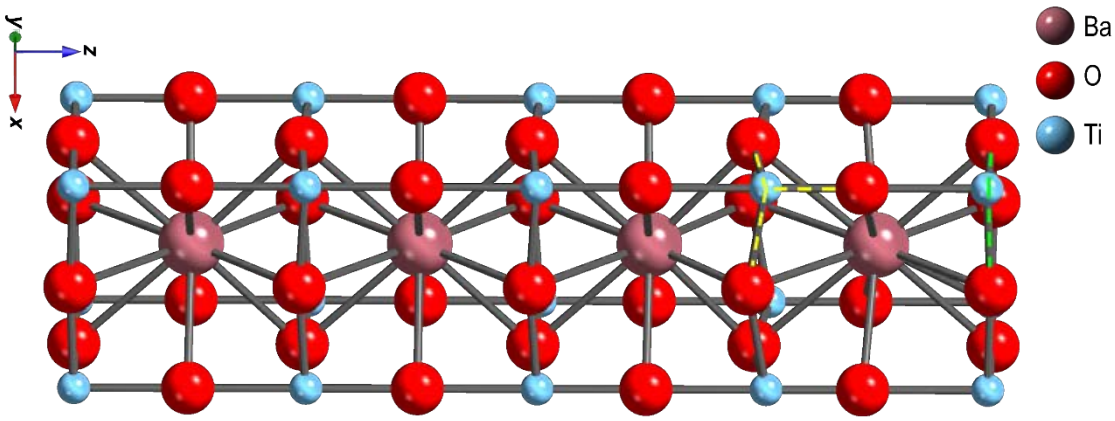

Figure 4.8: Ball and stick models of the obtained BTO.

Nº cell	Ti-O_{min} (Å)	Ti-O_{max} (Å)	Vertical angle (º)	In plane angle (º)
1st	1.754	2.267	95.01	89.40
2nd	1.972	2.178	87.61	89.31
3rd	2.012	2.172	89.22	89.93
4th	2.006	2.139	89.93	89.94

Table 4.4: Calculated Ti-O distances for the 4 first four layers of the BTO. The Ti-O bond lengths are comprised between 1.83-2.83 Å in the bulk. The error in the ΔTi-O length is ± 0.005 Å and of ± 0.05º for the angles.

The roughness value obtained from the structural refinement procedure is very high. It Indicates the presence of vacancies in the two outermost cells of the BTO film with the following distribution of average occupancies per layer from top to bottom on the surface: 0.18 / 0.32 / 0.57. The surface roughness involves some atomic disorder in the three upper surface layers as in the anatase 4x1 structure. In the TiO2 case the atomic occupancies were refined giving an average distribution of vacancies for the two topmost layers of 0.25 and 0.50. The deeper layers show almost complete or total occupation. This different roughness behavior could not be modeled with the beta roughness model[203].

Table 4.5 contains the location of the atoms in the structure, expressed as displacements from the bulk $BaTiO_3$. From these values it is observed that the greatest distortions occur in the second- and third-layer Ti, which tends to decrease as the film goes deeper. The average Δz between the titanium atoms and the basal and apical oxygen atoms is around ~0.5Å.

Atom	Bulk (x,y,z) coordinates (norm. units)	Δz (Å) Δz± 0.004	Atom	Bulk (x,y,z) coordinates (norm. units)	Δz (Å) Δz± 0.004
O (1)	(0,0.5,4.956)	0.221	Ti (3)	(0,0,3.093)	-0.284
Ti (1)	(0,0,5,093)	-0.409	O (6)	(0,0,2.399)	0.425
O (2)	(0,0,4.399)	0.205	Ba (3)	(0.5,0.5,2.5)	0.025
Ba (1)	(0.5,0.5,4.5)	0.006	O (7)	(0,0.5,1.956)	0.131
O (3)	(0,0.5,3.999)	-0.002	Ti (4)	(0,0,2.093)	-0.331
Ti (2)	(0,0,4.093)	-0.279	O (8)	(0,0,1.399)	0.409
O (4)	(0,0,3.399)	0.422	Ba (4)	(0.5,0.5,1.5)	0.029
Ba (2)	(0.5,0.5,3.5)	0.042	O (9)	(0,0.5,0.956)	0.131
O (5)	(0,0.5,2.956)	0.163	Ti (5)	(0,0,1.093)	-0.388

Table 4 5: Optimized locations of the atoms in the BTO surface obtained from the analysis of the SXRD data. Expressed as displacements from the bulk terminated TiO2 surface in Å. (x,y,z) atomic coordinates for the bulk-terminated structure are also listed.

4.2.2. Conclusions

The crystalline quality of the film is rather good. We have detected intensity along the minimums of the CTRs. The film studied had a thickness of 100 nm, but to be used as buffer to other oxides as TiO_2 the interface between them needs to be reduced at one atomic layer. The reduction of the surface roughness could be achieved by reducing the lattice mismatch with other substrates as $NdScO_3$ (110) (a_{pc} = 4.01 Å) or DSO (a_{pc} = 3.96 Å). However, this solution could lead to a reduction in the tetragonality of the BTO, which could reduce the polarization. Thus, to reduce the surface roughness in situ annealing in oxygen at high temperatures in the PLD before growing the TiO_2 heterostructure would allow the possibility of getting a better surface quality.

5. Water and oxygen interface with anatase (001) thin films

This chapter will focus on the exposure of the anatase (001) surface to water and oxygen at various substrate temperatures combined with UV light monitored by XPS. These experiments were used to investigate the effects of oxygen and water adsorption, and temperature on the band gap state (BGS) of the anatase films. The adsorption of those molecules on the anatase surface is crucial to investigate the origin of this material's catalytic activity for example the oxidation of organic pollutants[204,205] or the hydrogen production via water splitting[98,206] .

5.1. Experimental procedure

The experiments were carried out on the TEMPO-B beamline at SOLEIL synchrotron. Some details of the beamline used are previously described in *Section 2.3*. The adsorption of water and oxygen, their combination, the influence of UV illumination, and the influence of temperature on an anatase (001) thin film have been studied by x-ray photoelectron spectroscopy. Spectra of the Ti 2p, O 1s, C 1s and valence band region were obtained with 750 eV of photon energy. Furthermore, widescans were measured through the experiments to control the carbon contamination levels. All the core level positions will be given on the binding energy scale.

The anatase (001) thin film selected for this experiment was grown by PLD (875ºC, 85mTorr, 80nm), as described in *section 3.2 TiO_2 growth conditions*. The cleaning procedure consisted of successive cycles of argon ion sputtering (10 minutes,10^{-6} mbar, 10 mA emission current) and annealing (30 minutes, 1000K, 10^{-6} mbar O_2). This procedure leads to an oxygen deficient surface with a 4x1 surface reconstruction, confirmed by LEED (*Figure 5.1*).

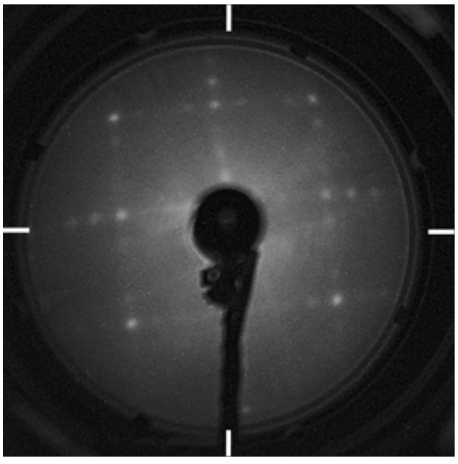

Figure 5.1: LEED pattern of an 80 nm thick anatase film grown by PLD after the cleaning procedure. LEED pattern recorded at 60eV. The solid lines indicate the principal directions [100] or [010].

The sample temperature was monitored using a thermocouple attached to the sample holder. The analysis chamber was purged with nitrogen before introducing the sample to expel the contaminants of the chamber walls during the pump-out. The water used throughout the experiments was contained in a glass vial, coupled to the UHV system, and purified via several freeze-pump-thaw cycles. All gases used in these experiments were introduced into the analysis chamber through a high precision leak valve (O_2 purity: 99.9998%). The cleanliness of the sample was controlled using XPS.

For clarity purposes, relative humidity (RH) is used to express the conditions of the experiment, as it combines two variables, temperature and pressure[207]. The RH is expressed in *Equation 5.1*:

$$\frac{p}{p_v(T)} \cdot 100 \qquad (5.\ 1)$$

Where p_v is the equilibrium vapor pressure at a given temperature (T) and p corresponds to the experimental pressure[208].

Equation 5.2 can be used to get an approximate value of the thickness of the water layer formed on the top of the anatase (001) surface:

$$\frac{I_{Ti}}{I_{0,Ti}} = \exp\left(\frac{d_W^L}{\lambda_W^L cos\theta}\right)\exp\left(-\frac{d_W^G}{\lambda_W^G}\right) \qquad (5.\ 2)$$

Where $I_{0,Ti}$ and I_{Ti} correspond to the Ti 2p intensity for the as-prepared sample and the intensity for the sample when it is exposed to water, respectively. The inelastic mean free path of an electron in liquid water is described by λ_W^L and λ_W^G is the inelastic mean free path of an electron in gaseous water, the angle (θ) defines the angle between the analyser axis and the surface normal, d_W^L is the thickness of the water layer and finally d_W^G the effective thickness of the water vapour that the electrons cross before reaching low vacuum conditions, which is around the distance between the aperture of the first differential pumping stage and the sample (~1mm). Assuming that only a liquid layer is formed, with no water vapour, the previous equation can be simplified[108,209,210]:

$$\frac{I_{Ti}}{I_{0,Ti}} = -\exp\left(\frac{d_W^L}{\lambda_W^L cos\theta}\right) \qquad (5.\ 3)$$

This expression (*Equation 5.3*) is used throughout the chapter to obtain the amount of water monolayers (ML), considering that 1ML is 0.25 nm.

5.2. Results and discussion

5.2.1. As loaded sample and UHV prepared sample

The objective of this part of the experiment was to investigate the consequences of water adsorption on the band gap state of the anatase (001) thin film. The resulting scan of the as-loaded sample after the cleaning procedure described in section 4.2.1 is presented in *Figure 5.2*. The spectrum displays the O, the C and the

Ti core-levels and Auger peaks. A small amount of argon is observed, which is assigned to remnants from the sample preparation process. No other contaminants are detected in the spectrum. The intense O peak is located around 531.0 ±0.15 eV. The non-symmetric shape of the O 1s spectrum indicates the presence of embedded surface species, which were resolved to three peaks at 530.90±0.20 eV, 531.90±0.17 eV, and 532.90±0.18 eV through peak fitting, which correspond to the O1s bulk component, OH and CO_x contaminants, respectively.

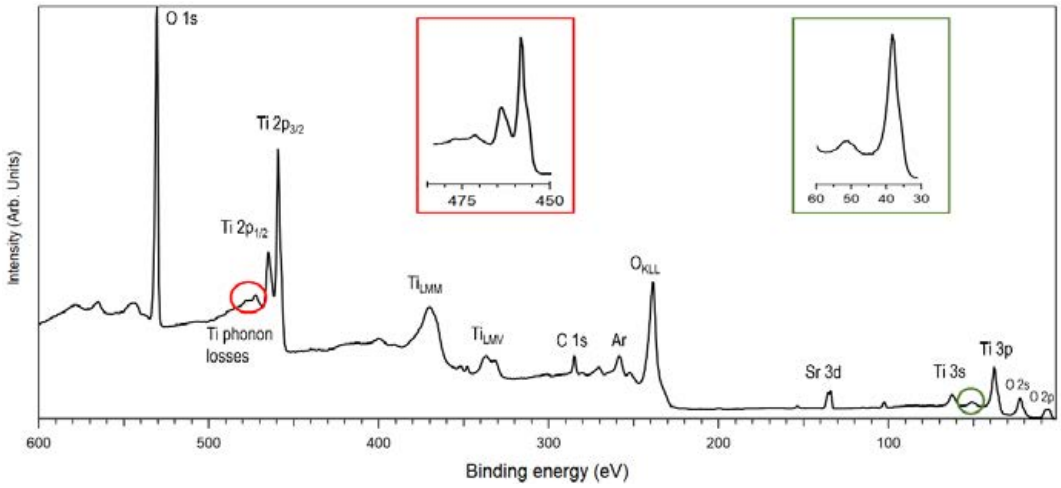

Figure 5.2: XPS spectrum of the as-prepared anatase (001) surface (hv = 750 eV, E_{pass}= 20 eV,E_{step}=0.5eV).

Two peaks corresponding to the Ti 2p peaks located at 459.4eV±0.19 (Ti $2p_{3/2}$) and 465.2eV±0.18 (Ti $2p_{1/2}$) are at similar positions as previously reported in the literature[211,212]. The branching ratio of the Ti $2p_{3/2}$ and Ti $2p_{1/2}$ is constrained to 2:1. Further analysis of the titanium 2p peaks (*Figure 5.3*) reveals the existence of titanium with different oxidation states, which indicates that the surface of our anatase (001) thin film contains a certain degree of non-stoichiometry. The fitting of the Ti 2p spectrum from the as-prepared sample shows contributions from Ti^{4+} at 459.4±0.08 eV binding energy, Ti^{3+} at 457.5±0.09 eV and Ti^{2+} at 456.8±0.05 eV. The delta values between these peaks are at -1.8±0.08 eV and -2.6 eV±0.02, respectively[211,213,214]. At higher binding energies,472.4 ±0.17 eV and 478.5 ±0.18 eV, two satellites appear, which come from phonon losses and have been previously assigned to O ($2p_{eg}$) – Ti ($3d_{eg}$) charge transfer[215,216]. The presence of Ti^{2+} was detected at the beginning of the experiment for the sample as loaded and cleaned before exposure, but once the film was exposed to oxygen it disappeared and was not recovered even after renewing the surface by cleaning the sample with the procedure previously described.

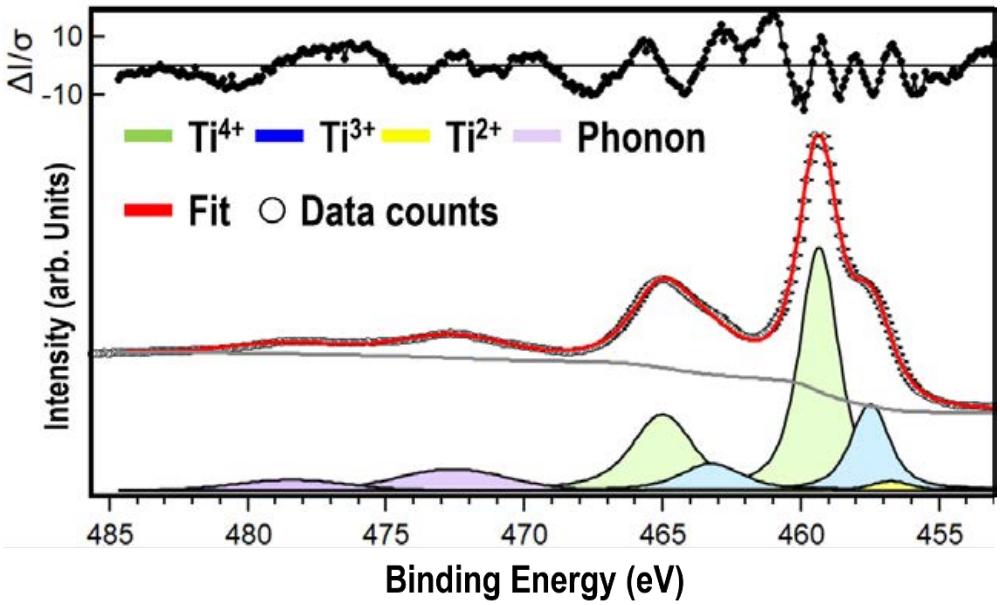

Figure 5.3: XPS spectrum of the Ti 2p anatase (001) surface for the as-prepared sample (hv = 750 eV, E_{pass}= 20 eV,E_{step}=0.1eV).

5.2.2. Oxygen exposure

Anatase (001) thin films were exposed to increasing oxygen pressures to investigate the effects of the oxygen adsorption on the band gap state of anatase (001), as well as the interaction of oxygen atoms with the anatase thin film surface. First, the sample was loaded and cleaned following the procedure described in section 5.1 "*Experimental procedure*" and exposed to oxygen up to 2mbar, keeping the temperature constant at ~273K, and returning to UHV after the exposure (1st sequence).

The increase of oxygen pressure induces changes in the Ti *2p* region as displayed in *Figure 5.4*. At the beginning of the first experiment in UHV conditions the Ti 2p region, as explained in section 5.2.1, presents contributions from three different titanium oxidation states: Ti^{4+}, Ti^{3+} and Ti^{2+}, as well as phonon losses, that will not be shown again for better visualization of the Ti 2p main peaks. Ti^{4+} is the predominant specie with 71.5% compared to the 25.3% of the Ti^{3+} and the 3.2% Ti^{2+}. When the sample is exposed for the first time to oxygen (P_{O2}=10^{-8} mbar), the Ti^{2+} contribution disappears. Further increase in oxygen pressure leads to a reduction of the Ti^{3+} % as it oxidizes to Ti^{4+} (*Figure 5.4*). After exposing the sample to a maximum oxygen pressure of 2mbar, it was returned to UHV conditions. At this point, it is worth to mention that the quantity of Ti^{3+} increases again, we assign this behaviour to possible beam damage of the sample, that induces oxygen desorption and the creation of defects, as reflected by the BGS increase (*Figure 5.7*). The evolution of the percentages between the different oxidation states is shown in the insets of *Figure 5.4*.

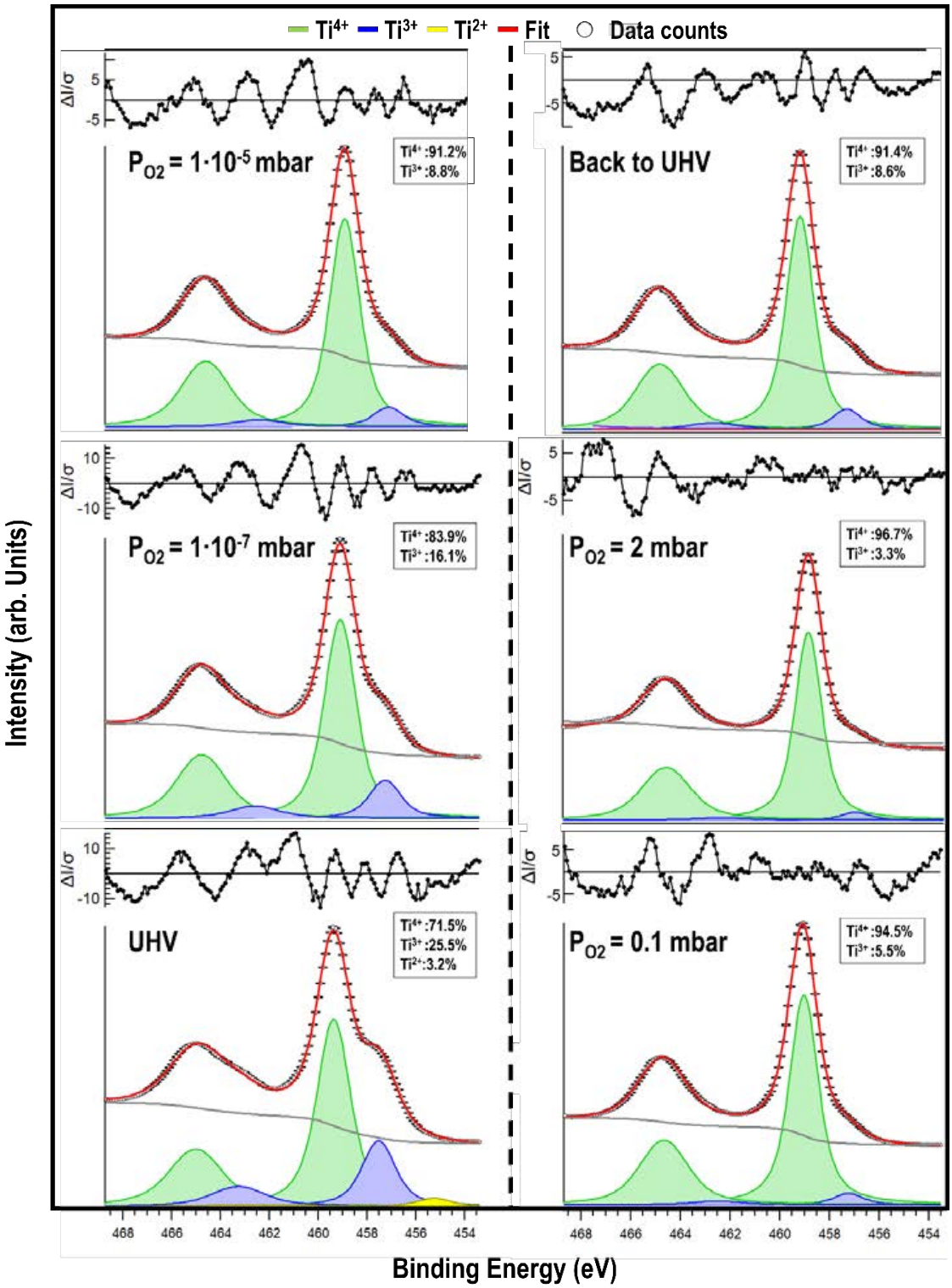

Figure 5.4: XPS of the Ti 2p region of anatase (001) for the 1st sequence (hv = 750 eV, E_{pass}= 20 eV,E_{step}=0.1eV) as a function of oxygen partial pressure.

In a following experiment, the sample was exposed again to a RH of $6.2 \cdot 10^{-7}$ % (10^{-5} mbar H_2O, 500K) and then exposure to oxygen at a range of pressures (P_{O2}=10^{-5} mbar-2mbar) keeping the temperature constant at ~273K without cleaning the sample (2nd sequence). Comparing the Ti 2p region of this experiment (*Figure*

5.5) to the previous experiment (*Figure 5.4*) we can clearly see that there is no presence of Ti^{2+} and that the quantity of Ti^{3+} is much less, as expected since the sample has been exposed to oxygen several times. The ratio between Ti^{4+} vs Ti^{3+} is 96.9% and 3.1%, respectively when the oxygen pressure is below 0.1 mbar. However, when it is increased above 0.1 mbar all the Ti^{3+} oxidizes to Ti^{4+}. Once again when the sample is returned to UHV the Ti^{3+} appears.

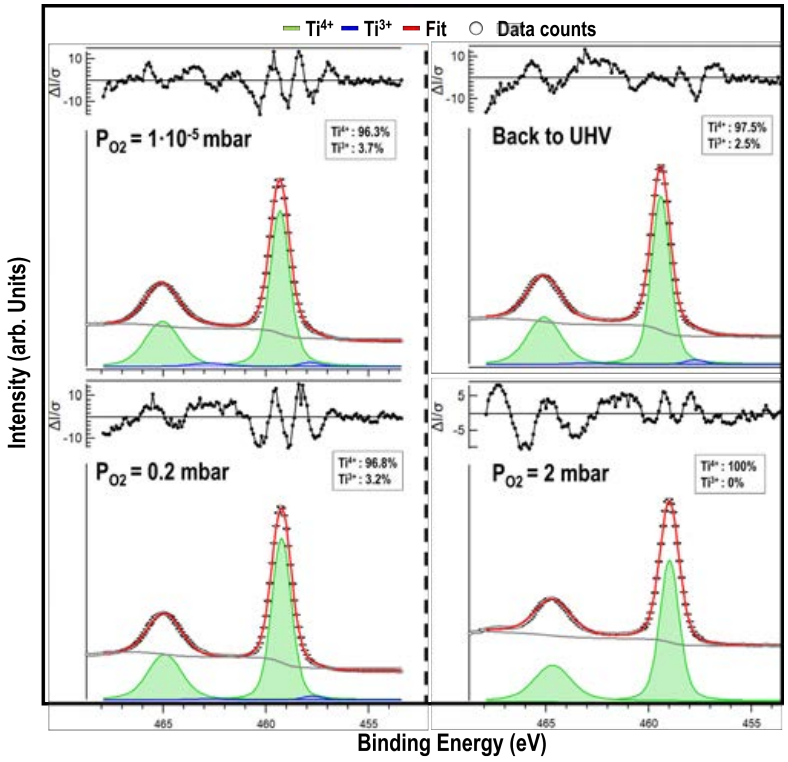

Figure 5.5: XPS of the Ti 2p region of anatase (001) for the 2nd sequence (hv = 750 eV, E_{pass}= 20 eV,E_{step}=0.1eV) as a function of oxygen partial pressure. The exposure to oxygen lead to the complete oxidation of the Ti^{3+}.

Representative spectrum of the O 1s region for both sequences of experiments are presented in *Figure 5.6*. The discussion of the O1s will be done together for both preparations as there are no significant differences between them. The formation of water layers at the surfaces is confirmed by the presence of the molecular water peak (~533.5 ±0.13 eV) in the O 1s core-level spectrum above P_{O2}= 10^{-5} mbar. The appearance of this peak was not expected in the 1st experiment, as the only gas introduced in the chamber was O_2. Therefore, we assign the existence of this peak to possible humidity in the gas injected. On the other hand, the presence of the molecular water peak on the second preparation has been attributed to the remaining water that could stay after the previous experiment. At oxygen pressures above 0.1mbar two peaks corresponding to the oxygen gas phase appear[217] that increase in intensity with the oxygen pressure.

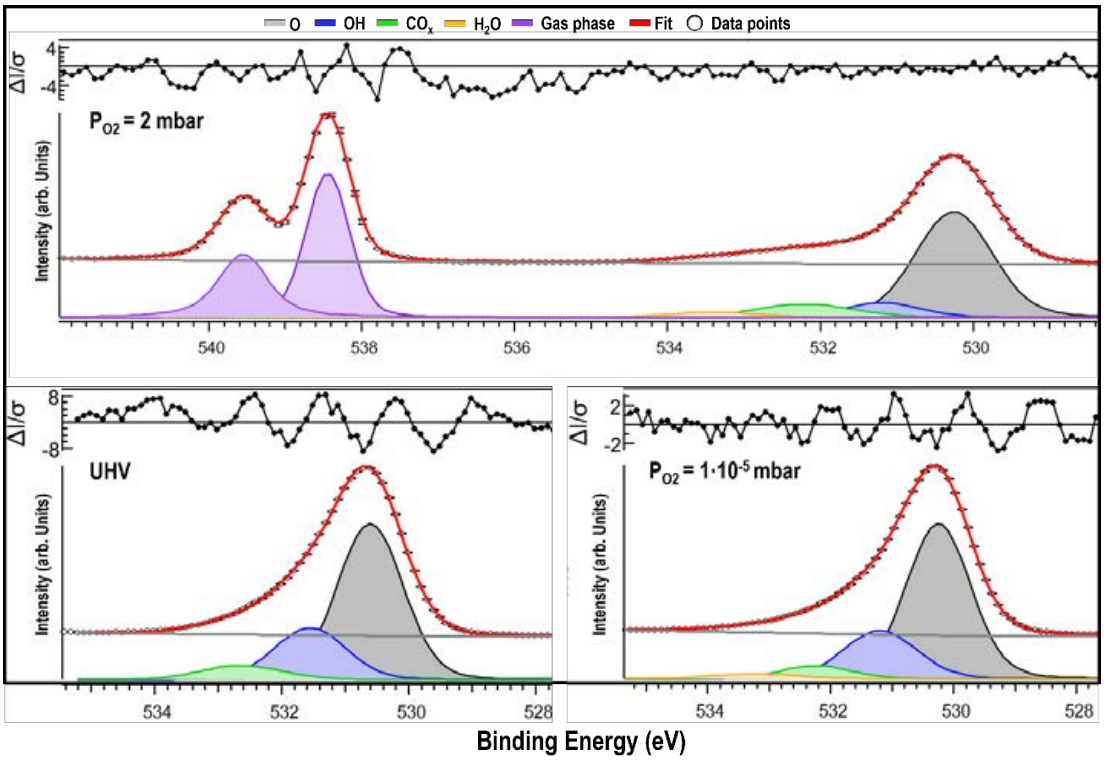

Figure 5.6: XPS of the O 1s region of anatase (001) (hv = 750 eV, E_{pass}= 20 eV,E_{step}=0.1eV) as a function of oxygen partial pressure for the 1st sequence.

5.2.2.1. Valence band

Concerning the valence band region, the introduction of oxygen resulted in the quenching of the defect peak of the band gap state by ~40% at 2 mbar for the 1st sequence (left) ,, while it remained almost constant for the 2nd sequence (right), as illustrated in *Figure 5. 7*. In the 1st sequence, the O_2 molecules have direct access to the oxygen vacancies, OH groups and unoccupied Ti_{5C} sites on the surface which can explain the dramatic reduction of the defect peak[107]. Previously studies suggest that a complete extinction of the band gap state is not possible because of the impossibility to remove all the OH_{br}[218,219]. Furthermore, Bigi et. al.[220] studied the reactivity of the band gap state of anatase (001) where the 2D metallic and deeper lying in-gap states were observed. They showed that with the exposure to oxygen the in-gap states were totally quenched, while the metallic states remain almost constant. The metallic states come from subsurface vacancies whose migration to the surface for recombination with O_2 is kinetically unfavourable on anatase (001), which makes them less sensitive to oxygen exposure. Thus, in this sequence the defects cannot be further reduced.

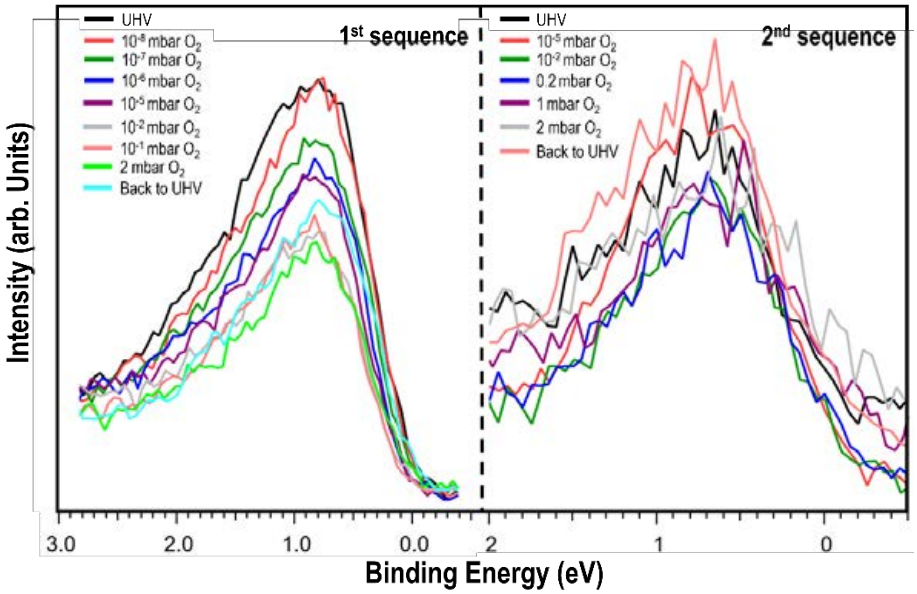

Figure 5.7 XPS of the band gap state region of anatase (001) (hv = 750 eV, E_{pass}= 20 eV,E_{step}=0.1eV) as a function of the partial oxygen pressure. The 1st sequence (left) consisted of exposing the as-prepared sample to oxygen for the first time, whereas on the 2nd sequence (right) the sample had been already exposed to oxygen several times.

5.2.3. Water exposure

The objective of this experiment was to investigate the effect of exposing the anatase surface to water on its band gap state, as well as, to study the interactions between the adsorbed molecules or atoms with the surface. Thus, the sample was exposed to increasing water pressures starting at UHV conditions, right after exposing it to oxygen, up to 2mbar of H_2O, keeping the temperature around 273K. *Figure 5.9* represents a selection of O 1s spectra obtained at increasing H_2O pressures. The evolution of the O 1s spectra indicates a progressive growth of a water overlayer on the anatase surface, where different oxygen species can be characterized at different binding energies: lattice O (530.9 ± 0.20eV), OH (531.9±0.17 eV) as well as CO_x contamination (532.9± 0.18 eV). The OH peak appears just by the exposure of the surface to residual chamber gases, which leads to hydroxylation of the surface. In non-stochiometric TiO_2 surfaces, water dissociates at the surface oxygen vacancies into two OH bridging species (Figure 5.8).

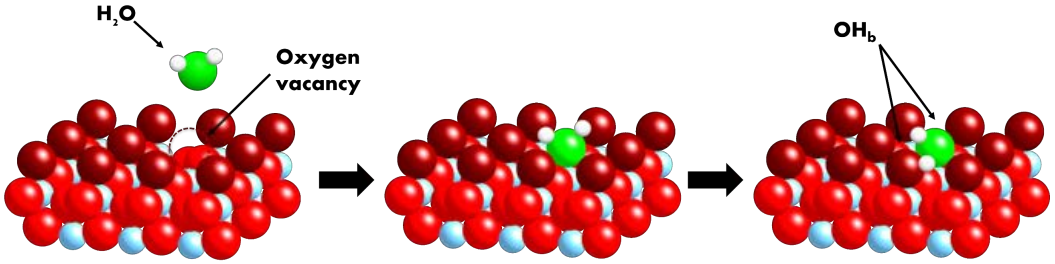

Figure 5.8: Ball model illustration of dissociative water adsorption at an O vacancy on the anatase (001) surface. Red and blue spheres correspond to lattice O and T, respectively. The darker spheres correspond to the bridging oxygens. The white spheres are hydrogen atoms.

These hydroxyls are nucleation points for the incoming water molecules which allows water adsorption and the creation of strong bounded hydroxyl-water complexes[208,221,222]. Thus, the OH peak intensity increases with the water exposure, while the peak assigned to CO_x contaminants remains almost stable until the sample achieves a RH=1.9·10^{-3}% (P_{H2O} = 3·10^{-2} mbar, T=273K). A new peak assigned to molecularly adsorbed H_2O (533.50±0.08 eV) arises when the RH reaches 1.6·10^{-4} % (P_{H2O} = 1·10^{-5} mbar, T=273K), that increases with the RH. At higher RH values the H_2O gas phase peak is observed at 535.7±0.06 eV.

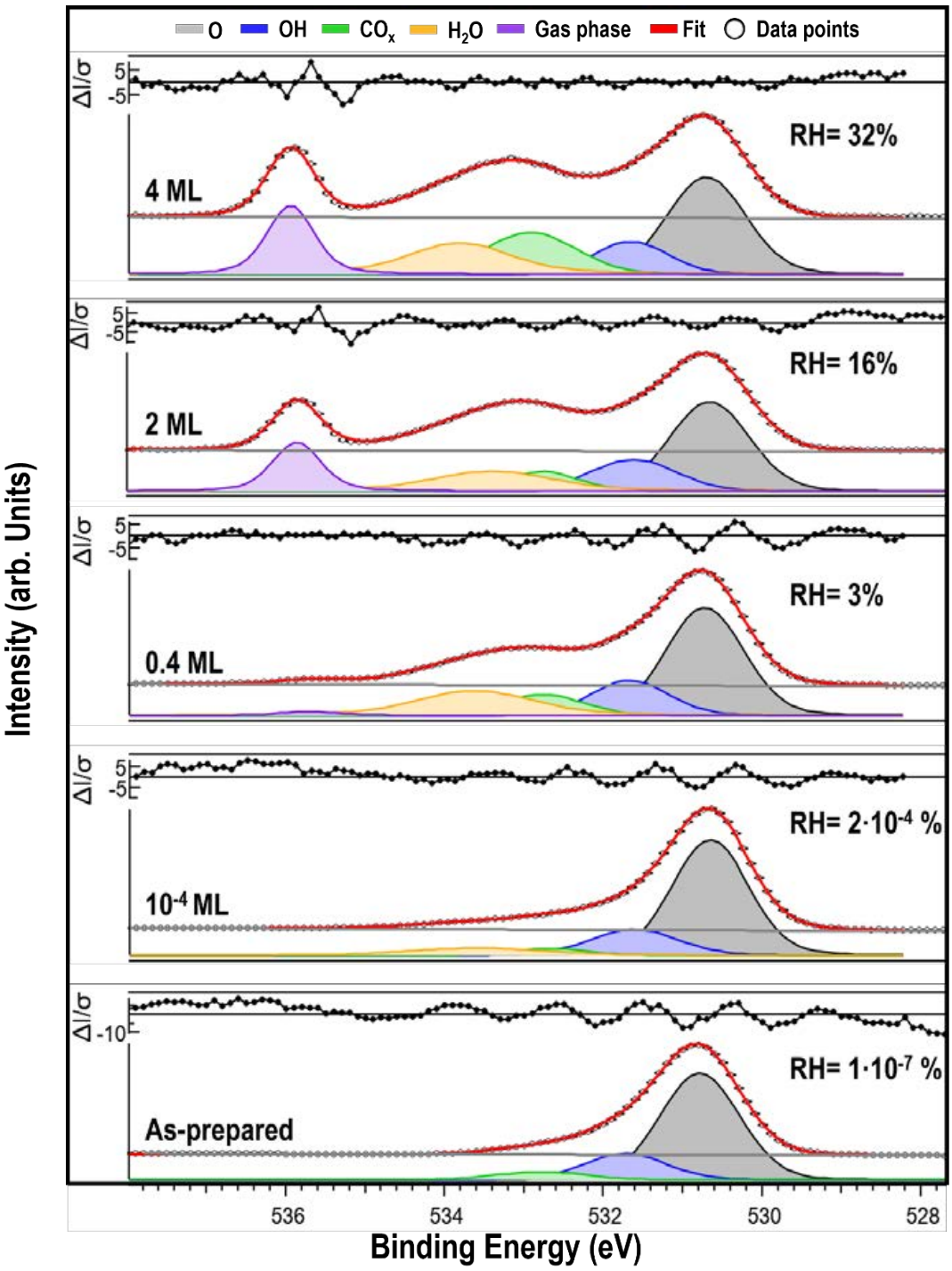

Figure 5.9: XPS of the O 1s region of anatase (001) (hv = 750 eV, E_{pass}= 20 eV,E_{step}=0.1eV) at various RH. The ML of water at each stage are indicated.

On the other hand, the Ti 2p region does not suffer any significant changes. The relation between the two different oxidation states of titanium: Ti^{4+} and Ti^{3+} remains almost constant: 97% and 3%, respectively, independently of the sample's exposure to water pressure.

In near ambient pressure experiments carbon contaminations of the sample is common[208,223,224]. The intensity of the CO_x peaks, monitored by taking survey spectra at each RH, increases with the water pressure. *Figure 5.10* presents the fitting of the C 1s region of the sample at a RH of 16% (P_{H2O} = 1 mbar, T=273K), which has the main carbon peak at 285.1 eV and two other peaks ascribed to oxygen containing carbon species. The maximum amount of carbon was obtained at RH=32% where we have around 0.4 ML of carbon on the sample's surface.[225]

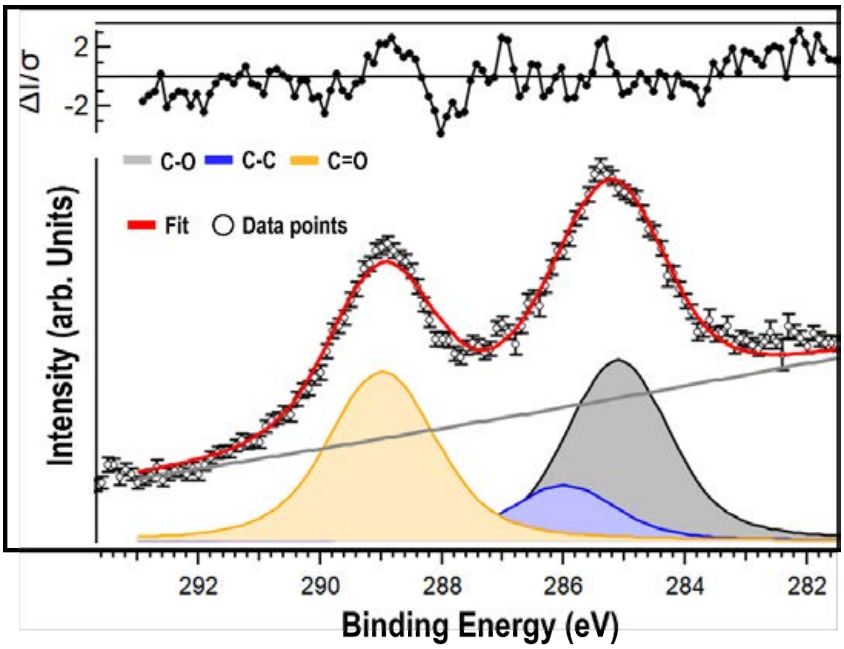

Figure 5.10: XPS of the C 1s region of anatase (001) at RH=32% (P_{H2O}= 2mbar, 273K) (hv = 750 eV, E_{pass}= 10 eV,E_{step}=0.1eV)

5.2.3.1. Valence band

The study of the evolution of the valence band (VB) spectra (hv = 750 eV) with the Ti *3d* electron state (*Figure 5.11*) confirms the presence of water on the anatase (001) surface by the appearance of water molecular orbitals $1b_1$, $3a_1$ and $1b_2$. The $1b_1$ orbital is of nonbonding character and is situated around 7.8 eV below the Fermi level, whereas the $1b_2$ is a bonding orbital, located at about 13.7 eV. The $3a_1$ peak, at approximately 10 eV, contains both bonding and non-bonding character, and is thought to be the orbital that interacts most strongly in bonding to the surface[226,227]. The visualization of the water induced characteristics is achieved by the subtraction of the as-prepared surface spectrum from those obtained after exposing the sample to water. However, this method involves previous corrections before the subtraction. The spectra must be normalized and aligned, which if not properly realized could lead to the appearance of artefacts in the resulting spectra. For this experiment the main problem normalising the data comes from the attenuation

of the signal by the water overlayer, which has been corrected by multiplying the intensity of each spectrum by an empirical value. Similar correction procedures have been previously reported in the literature[208,228]. The subtracted spectra of the region are displayed in *Figure 5.11 (right)*. The $1b_1$ and $3a_1$ molecular orbital peaks display a slight broadening which may be assigned to the superposition of the σ and π hydroxyl orbitals, located at ~10 and ~8 eV, respectively.

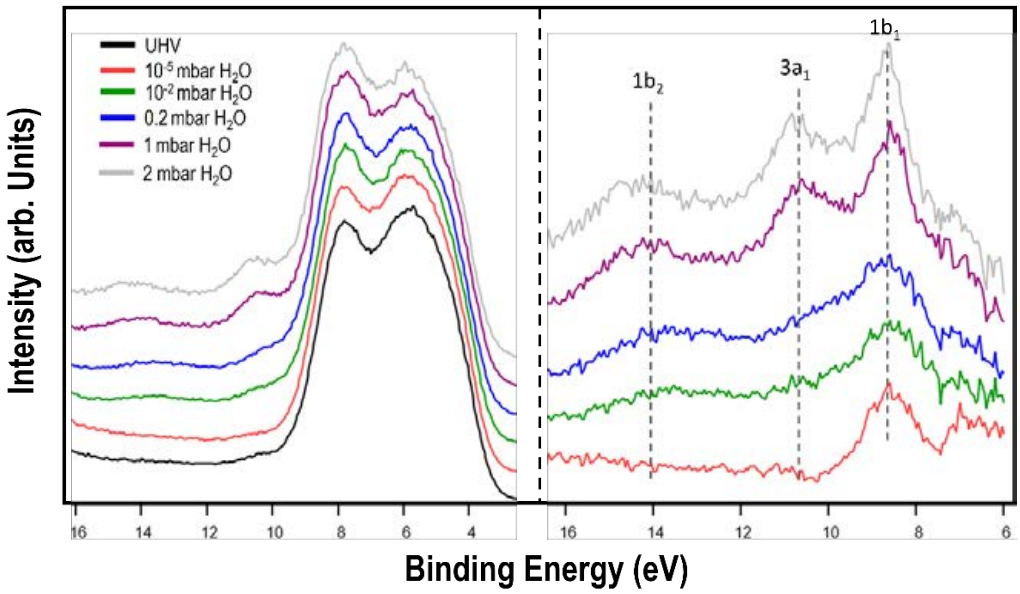

Figure 5.11: XPS of the valence band region of anatase (001) (hv = 750 eV, E_{pass}= 20 eV,E_{step}=0.1eV), before and after water exposure (left). Difference spectra of the photoelectron spectra obtained by subtracting spectrum from the as-prepared sample from spectra acquired after exposing the sample to increasing amounts of water (right).

Figure 5.12 displays the evolution of the band gap state of the anatase (001) thin film with increasing amount of water. The increase in RH does not affect the band gap state that remains almost constant throughout the experiment. This behaviour is consistent with the band gap state coming mostly from oxygen vacancies as the hydroxyl species of the surface are not considered to be electronegative enough to retreat charge from oxygen vacancies or Ti_{5C} sites[229].

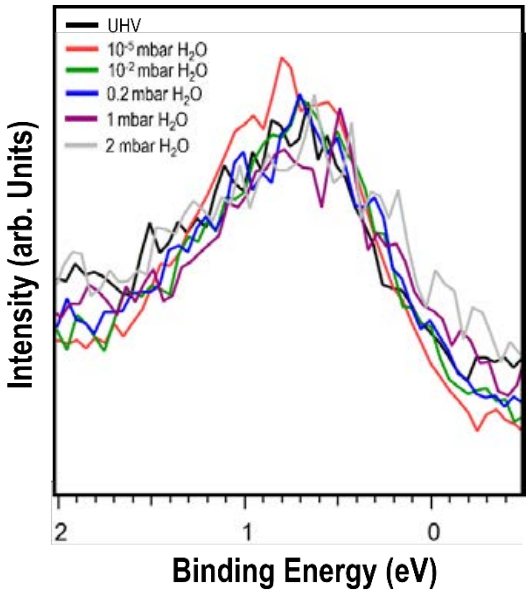

Figure 5.12: XPS of the band gap state region of anatase (001) upon increasing exposure to water (hv = 750 eV, E_{pass}= 20 eV,E_{step}=0.1eV)

5.2.4. Influence of UV illumination

The influence of the sample's illumination with UV light (SOLIS-365C, THORLAB, 365nm, Typical Collimated Power LED Output 4W) was checked by measuring several spectra at different H_2O pressures with and without UV illumination. Nonetheless, we did not notice any differences between the spectra acquired when the sample was illuminated and when it was not illuminated in either region (Ti *2p*, O *1s* and VB) as shown in *Figure 5.13*. We assign this behaviour to the experimental set-up during the measurement, where the UV light was mounted almost parallel to the surface of the sample and most likely did not properly illuminate the sample.

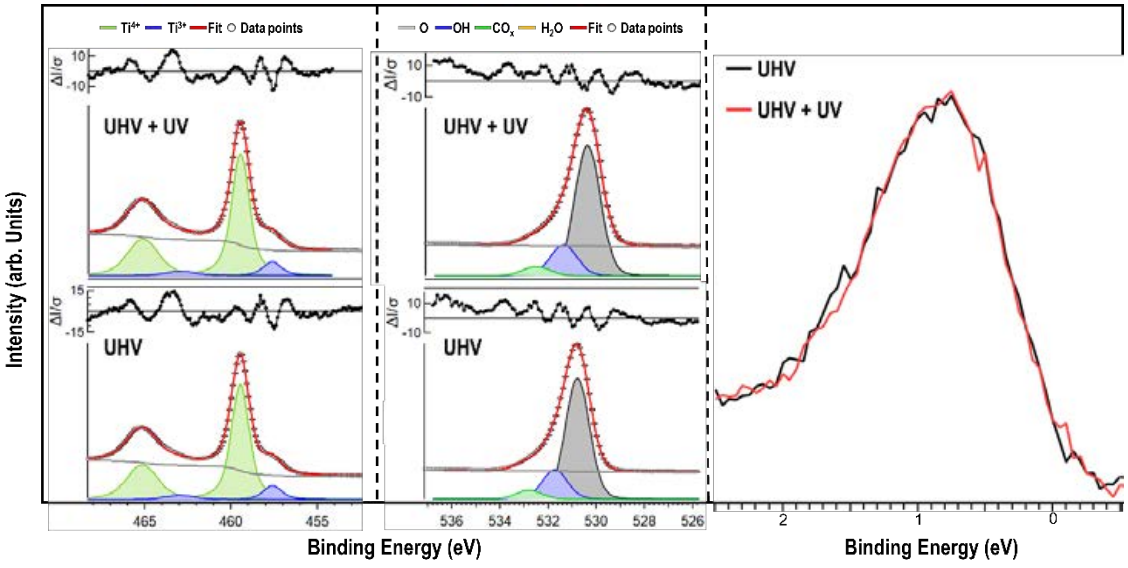

Figure 5.13: XPS of the Ti 2p (left), O 1s (center) band gap state (right) region of anatase (001) at UHV with and without UV exposure (hv = 750 eV, E_{pass}= 20 eV,E_{step}=0.1eV). The sample was exposed to UV for 15 minutes.

5.2.5. Temperature

To study the effect of temperature on the adsorption of the different species, as well as the variations in the band gap state two different experiments were carried out. In the first experiment, the sample's temperature was held at 500K, whereas the water pressure was increased from UHV conditions up to 10^{-5} mbar. The second experiment consisted in heating the sample from room temperature (~273K) to 375K, 400K and 500K in a background water pressure of 10^{-5} mbar. These series of experiments allowed us to differentiate the effects of temperature from the effects of water pressure.

On the first experiment, when the sample temperature is maintained at 500K, the increase in water pressure does not change the O1s core-level spectrum, therefore only the highest-pressure, RH= $6 \cdot 10^{-7}$%, (P_{H2O}= 10^{-5} mbar, 500K) spectra is displayed (*Figure 5.14 left*). As seen in the previous experiments (*Section 3.2.2 Water exposure*), at P_{H2O}= 10^{-5} mbar the peak of the molecular adsorbed water is expected to appear. However, as the sample is previously heated to 500K water cannot adsorb on the surface of anatase, confirmed by the non-existence of the molecular water peak at ~533.5eV. The intensitites of the other peaks remains constant through all the experiment. The band gap state was not expected to vary when the RH is increased, as explained in section 5.2.2. Nonetheless, there is a small decrease of the peak when RH arrives to $6.2 \cdot 10^{-7}$ % (10^{-5} mbar H_2O, 500K), that we attribute to the possible co-adsorption of contaminants displaced from the inner chamber walls through water exposure (*Figure 5.14 right*).

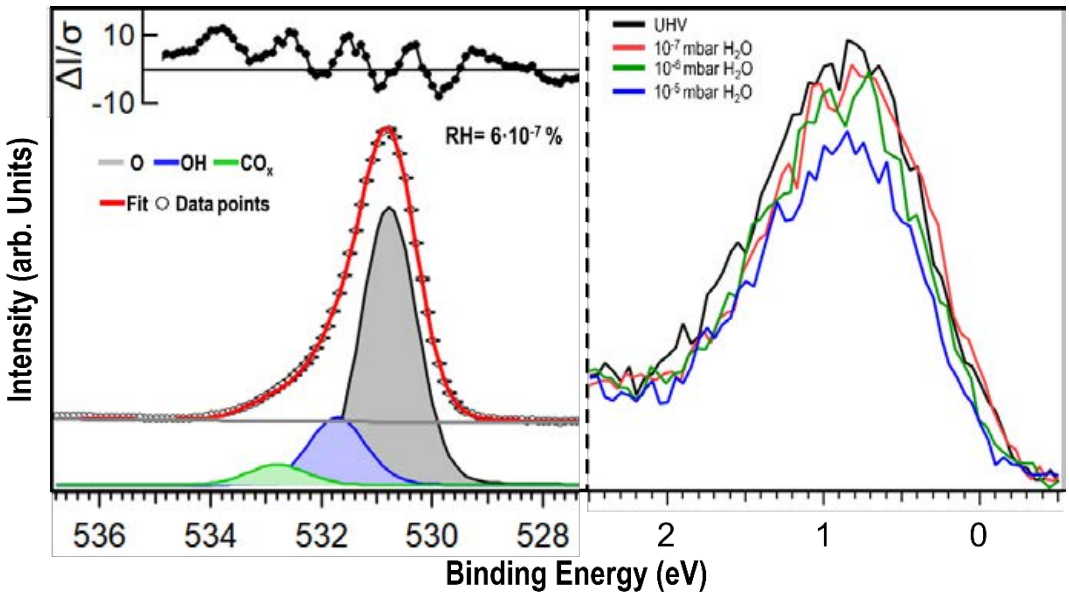

Figure 5.14 XPS of the O 1s at RH= $6 \cdot 10^{-7}$%, (P_{H2O}= 10^{-5} mbar, 500K) (left) and band gap state (right) region of anatase (001) (hv = 750 eV, E_{pass}= 20 eV,E_{step}=0.1eV)

The second experiment showed that when the sample temperature is increased keeping the water pressure around 10^{-5} mbar, water molecules desorb from the surface of the sample when 375K is reached and just the OH species are present on the O1s region spectra. As the spectra are identical once the sample is heated just the starting and the 500K spectra are presented (*Figure 5.15 left*). The Ti 2p core level spectra

displays some interesting features (*Figure 5.15 right*). The percentage of Ti^{4+} slightly decreases from 93.7% to 92% when the sample is heated. This reduction can be associated with the loss of oxygen from the surface of TiO_2, as the desorption of water molecules together with a fraction of the hydroxyl species happens, which could lead to the reduction of Ti^{4+} to Ti^{3+} as it has been previously reported[230] i.e., Guillemot et. al.[231] stated that vacuum annealing could control the rate of Ti^{4+}/Ti^{3+} from low concentrations (~3% Ti^{3+}) at 323K to high concentrations (~21% Ti^{3+}) at 500K. Additionally, the increase in temperature could induce interstitials Ti diffusion towards the surface. Li J. et. al[106] assigned the formation of the BGS to the diffusion of interstitials Ti around 420K consistent with the increase that we observe above 425K in the BGS. Furthermore, a decrease in the CO_x contaminants is observed upon heating the sample, but it does not disappear completely.

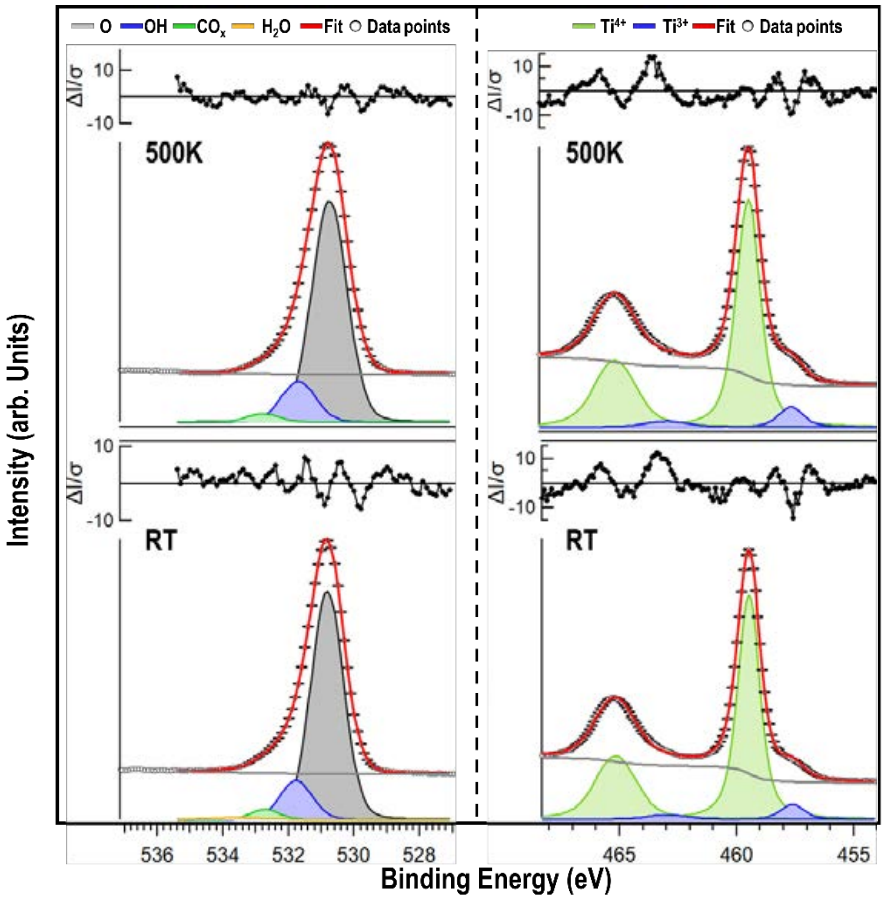

Figure 5.15: XPS of the O 1s (left) and the Ti 2p (right) region of anatase (001) for the sample held at room temperature and 500 K at $P_{H2O}=10^{-5}$ mbar (hv = 750 eV, E_{pass}= 20 eV,E_{step}=0.1eV)

We can observe an increase in intensity on the bandgap state of the TiO_2 anatase thin film as the sample is heated (*Figure 5.16*). This behaviour is consistent with the increment of the Ti^{3+} amount on the Ti 2p core-level region, which is a sign of the Ti 3d nature of the BGS.

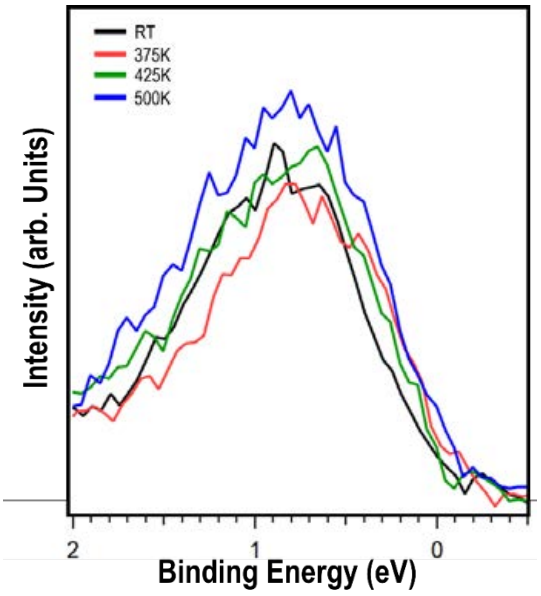

Figure 5.16: XPS of the band gap state region of anatase (001) for the sample held at various temperatures (hv = 750 eV, E_{pass}= 20 eV,E_{step}=0.1eV)

5.2.6. Water and oxygen exposure

The effect of the exposure to water and oxygen combined was also tested on the anatase thin film, as well as the possible effect of UV light. The sample was cleaned and then exposed to increasing water and oxygen pressure at the same time starting at P_{O2}=P_{H2O}=1·10^{-7} mbar up to P_{O2}=P_{H2O}=1·10^{-5} mbar. Firstly, the increase of water pressure led to the appearance of the adsorbed molecular water peak when P_{H2O} reaches 1·10^{-5} mbar in the O1s core-level regions following the same behaviour as *section 5.2.2 Water exposure*. On the other hand, the Ti 2p core-level regions and the BGS evolution is identical to the one previously described in *section 5.2.3 Oxygen exposure* where the addition of oxygen pressure reduced the amount of Ti^{3+} and quenched the defect peak of the BGS by the adsorption of oxygen.

5.3. Summary and conclusions

The spectrum of the as prepared sample displays the O, the C and the Ti core-levels and Auger peaks, a small amount of argon is observed, assigned to remnants from the sample preparation process. The presence of defects in the surface structure was confirmed by the observation of different titanium oxidation states (Ti^{4+}:71.5%, Ti^{3+}:23.2% and Ti^{2+}:3.2%) for the sample before exposure.

The exposure of the anatase (001) surface to water lead to a formation of a water overlayer confirmed by the appearance of water peaks in the O 1s core level and the valence band region. Peaks assigned to the $1b_1$ (~7.8 eV), the $1b_2$ (~13.7 eV) and the $3a_1$ (~10 eV) water's molecular orbitals emerge in the valence band region, while a peak related with molecular water (~533.5 eV) is observed in the O 1s spectra. The BGS located around 0.8 eV remains stable throughout the exposure of the sample to water as the hydroxyl groups cannot withdraw the excess of charge from the TiO_2 surface.

Exposing the sample to oxygen leads to a quenching of the intensity of the BGS peak. This behaviour is due to the possibility of the O_2 molecules to access to the defect sites of the surface (OH groups and unoccupied Ti_{5C}). A diminution on the reduced titanium species has been observed on the Ti 2p core-level spectra, while the O 1s region was maintained and just peaks corresponding to the oxygen gas phase and molecular H_2O appeared at high oxygen pressure, possibly because of humidity of the inserted gas.

The influence of the temperature on the thin film was studied firstly by heating the sample to 500K and then varying the water pressure and secondly by maintaining the water pressure stable at $5 \cdot 10^{-5}$ mbar and gradually increasing the temperature to 375K, 420K and 500K. The first experiment proved that water cannot adsorb on the surface when the sample is heated. Regarding the BGS, there is a small quenching in the intensity when the sample is at a RH of to $6.2 \cdot 10^{-7}$ % (10^{-5} mbar H_2O, 500K), that cannot be owed to the presence of water. Thus, our theory is that is related with the adsorption of contaminants located on the inner chamber walls, that arise when pressure is increased. The second experiment involved heating the sample step by step from room temperature (~273K) to 375K, 420K and 500K at the same water pressure ($P_{H2O}=10^{-5}$ mbar). The spectra taken above RT on the O 1s region showed that the molecular water peak disappears, which is an indicative that water desorption is happening. Furthermore, the increasing in the Ti^{3+} amount with the temperature observed on the Ti 2p core-level spectra is consistent with the gain in the Ti 3d BGS[232].

The effect of mixing water and oxygen on the anatase (001) thin film resulted in similar behaviours to the exposure of the sample to oxygen and water separately. Finally, the impact of UV illumination was tried, but no conclusions have been extracted as the experimental set-up in TEMPO beamline was not adequate to properly focus the UV radiation into the sample.

The purpose of preparing thin films is that they can be used as replacements for single crystals to be employed as models. The results obtained with our anatase (001) film are consistent with reported studies on clean single crystal TiO_2 (001) anatase[227,228] surfaces. Thomas A. G. et.al.[235] present similar behavior on the BGS of anatase (001) single crystal during oxygen exposure which gradually decrease in the intensity of the defect state. Additionally, the amount of reduced titanium species detected for the as-prepared sample, mainly Ti^{3+} (~25%), is consistent with the proposed disordered vacancy model shown in *Chapter 4: Surface structure* (~27%). The main difference of the thin film with a single crystal is the higher concentration of defects observable on the BGS intensity, as well as on the asymmetry of the Ti 2p core level peak related. However, the thin film studied could be used as a replacement of a bulk sample.

For these reasons, there is still work to do to completely understand the BGS of the anatase (001). The time lack in TEMPO beamline did not allow us to solve the UV set-up to study the consequences of the sample's exposure to UV light, however an experiment has been already approved in Diamond to investigate it. Additionally, it would be interesting to repeat this experiment with some of the samples with different grain sizes presented through this work to check the effect of the surface area on the adsorption processes.

6. Conclusions

We have grown high quality TiO_2 (001)-anatase thin films, which could be used as system models for structural determination, by two different CVD techniques (PLD and MBE) with the same crystalline order. It is possible to optimize the terraces size by controlling the growth and annealing temperature. In this way, we have obtained flat terraces size ranging from 120nm up to 650nm. Additionally, an increase in temperature results into an expansion of the out-of-plane lattice parameter, that we assign to the presence of oxygen vacancies along the TiO_2 film. 925ºC has been stablished as the maximum stability temperature of anatase before the transition to rutile begins. Further increase in temperature allows the possibility to control the phase transition.

The LEED characterization revealed a 4x1 surface reconstruction of the films, that could be studied in a surface x-ray diffraction experiment. A disordered vacancies model has been proposed for that surface reconstruction from the analysis of the SXD data. This structure is consistent with the amount of Ti^{3+} got by XPS. The detection of reduced titanium species (Ti^{3+} and Ti^{2+}) confirms the existence of defects on the as-prepared sample surface. The exposure of the sample to oxygen oxidizes those species leading to a reduction of the band gap state of the films.

The changes on the morphological and structural characteristics of $BaTiO_3$ thin films were studied. It has been proved that the partial oxygen pressure is the parameter that affects the most, besides thickness, to the sample's strain. There is a tendency for roughness to increase at higher pressures, while the out-of-plane lattice parameter decreases. 50nm has been estimated as the critical thickness before BTO completely relaxes. Additionally, a layer-by-layer growth mechanism has been identified.

The volatility of bismuth in the $BiFeO_3$ has strongly affected the composition of the films. The appearance of Fe_2O_3 phases, detected by x-rays, are an indicative of $BiFeO_3$ decomposition, even though the reflections typically assigned to $BiFeO_3$ are still observable on the x-ray diffractograms. This behavior indicates that the interdiffusion preserves the $BiFeO_3$ structure in a wide range of compositions. The lack of reproducibility strongly suggests that small deviations in growth conditions out of our control induces large modifications in growth mechanism giving rise to multiple morphologies such as: trapezoidal islands, rectangular islands, or dendritic-like structures.

We have grown fully epitaxial TiO2-BTO heterostructures despite the structural dissimilarity between them. The TiO2-BTO interface typically shows a 2 – 4 unit cell thick slab of disordered material that we interpret as a response to the polar conflict arising from the polar character of the (001) anatase surface and polarization charges on the (001) BTO surface.

6.1. Futures avenues of research

There is still work to do to increase the quality of the anatase (001) films to allow them to be used as surface models. The use of monoatomic oxygen in the UHV chamber of the MBE instead of molecular oxygen could affect the final quality of the films, as the higher reactivity of the monoatomic oxygen would accelerate the growth process. The annealing's temperature range and time should be better defined to better control the transition from anatase to rutile. On this topic an experiment has been already approved to study that transition in the ESRF.

Additionally, BTO films quality could be improved by a step-like deposition with time in between the depositions to allow BTO to restructure, which could lead to even smoother surfaces to have a better starting point to grow TiO_2-BTO heterostructures. Furthermore, the deposition conditions of the SRO buffer layer must be optimized to avoid the appearance of the trenches seen in the AFM images, which sure will affect the properties of the final thin film.

Regarding the BFO, a more accurate temperature control must be done to find the right temperature to obtain fully stoichiometric films.

Next steps should involve the preparation of heterostructures with variable TiO_2 to elucidate the critical thickness where the titania layer would screen the effect of BTO polarization by measuring the photocatalytic activity of those samples. Additionally, further investigation on mixed phases heterostructures prepared at 700ºC could be interesting to compare the photocatalytic performance of those samples with pure anatase (001) films. Furthermore, the preparation of TiO_2-BFO heterostructures should be prepared as the polarization of BFO is higher than the BTO.

Abbreviations

A: electron acceptors

AES: Auger electron spectroscopy

AFM: Atomic force microscopy

BTO: $BaTiO_3$

BE: Binding energy

BFO: $BiFeO_3$

BGS: Bandgap state

BSE: Backscattered electrons

CB: Conduction band

CS: Crystallite size

CTR: Crystal truncation rod

D: electron donors

DSO: $DyScO_3$

EDX: electron dispersive X-ray spectroscopy

E_k: Kinetic energy

FE: Ferroelectric

FFT: fast Fourier transform

FOR: Fractional order reflection

GPA: Geometry phase analysis

IMFP: Inelastic mean free path

LEED: low energy electron diffractometer

MBE: Molecular beam epitaxy

ML: Monolayer

PEC: Photoelectrochemistry

PLD: pulsed laser deposition

P_r, P_s: remanent, saturation polarization

PVD: physical vapour deposition

PWS: Photocatalytic water splitting

RH: Relative humidity

RHEED: reflection high-energy electron diffraction

rms: root mean square

SAD: Selected area diffraction

SC: semiconductor

SE: Secondary electrons

SEM: scanning electron microscopy

SRO: $SrRuO_3$

STM: scanning tunnelling microscopy

STO: $SrTiO_3$

SXRD: Surface x-ray diffraction

T_c: Curie temperature

TEM: transmission electron microscopy

UHV: Ultra high vacuum

VB: Valence band

VB: Valence band

XPS. x-ray photoemission spectroscopy

XRD: x-ray diffraction

7. Bibliography

1. Dincer, I. Green methods for hydrogen production. *Int. J. Hydrogen Energy* **37**, 1954–1971 (2012).
2. Kothari, R., Buddhi, D. & Sawhney, R. L. Comparison of environmental and economic aspects of various hydrogen production methods. *Renew. Sustain. Energy Rev.* **12**, 553–563 (2008).
3. Lan, Z. *et al.* Enhancing Oxygen Evolution Reaction Activity by Using Switchable Polarization in Ferroelectric InSnO2N. *ACS Catal.* **11**, 12692–12700 (2021).
4. Ren, R. *et al.* Controllable synthesis and tunable photocatalytic properties of Ti3+-doped TiO2. *Sci. Rep.* **5**, 1–11 (2015).
5. Nguyen, H. T. T. *et al.* Strain-tunable electronic and optical properties of monolayer GeSe: Promising for photocatalytic water splitting applications. *Chem. Phys.* **529**, 110543 (2020).
6. McNaught, A. D. & Wilkinson, A. A GLOSSARY OF TERMS USED IN CHEMICAL KINETICS, INCLUDING REACTION DYNAMICS. *Pure Appl. Chem.* **68**, (1996).
7. Braslavsky, S. E. Glossary of terms used in photochemistry 3rd edition: (IUPAC Recommendations 2006). *Pure Appl. Chem.* **79**, 293–465 (2007).
8. Yuan, L., Han, C., Yang, M. Q. & Xu, Y. J. Photocatalytic water splitting for solar hydrogen generation: fundamentals and recent advancements. *Int. Rev. Phys. Chem.* **35**, 1–36 (2016).
9. Hisatomi, T., Kubota, J. & Domen, K. Recent advances in semiconductors for photocatalytic and photoelectrochemical water splitting. *Chem. Soc. Rev.* **43**, 7520–7535 (2014).
10. Currao, A. Photoelectrochemical water splitting. *Chimia (Aarau).* **61**, 815–819 (2007).
11. Ismail, A. A. & Bahnemann, D. W. Solar Energy Materials & Solar Cells Photochemical splitting of water for hydrogen production by photocatalysis : A review. *Sol. Energy Mater. Sol. Cells* **128**, 85–101 (2014).
12. Pelaez, M. *et al.* A review on the visible light active titanium dioxide photocatalysts for environmental applications. *Appl. Catal. B Environ.* **125**, 331–349 (2012).
13. Jafari, T. *et al.* Photocatalytic water splitting - The untamed dream: A review of recent advances. *Molecules* **21**, (2016).
14. Kudo, A. & Miseki, Y. Heterogeneous photocatalyst materials for water splitting. *Chem. Soc. Rev.* **38**, 253–278 (2009).
15. Chen, F., Huang, H., Guo, L., Zhang, Y. & Ma, T. The Role of Polarization in Photocatalysis. *Angew. Chemie - Int. Ed.* 10061–10073 (2019). doi:10.1002/anie.201901361
16. Qi, K., Cheng, B., Yu, J. & Ho, W. Review on the improvement of the photocatalytic and antibacterial activities of ZnO. *J. Alloys Compd.* **727**, 792–820 (2017).
17. Szilágyi, I. M. *et al.* WO 3 photocatalysts: Influence of structure and composition. *J. Catal.* **294**, 119–127 (2012).
18. Zhang, K. & Guo, L. Metal sulphide semiconductors for photocatalytic hydrogen production. *Catal. Sci. Technol.* **3**, 1672–1690 (2013).
19. Di, T. *et al.* Review on Metal Sulphide-based Z-scheme Photocatalysts. *ChemCatChem* **11**, 1394–1411 (2019).
20. Hashimoto, K., Irie, H. & Fujishima, A. TiO 2 photocatalysis: A historical overview and future prospects. *Japanese J. Appl. Physics, Part 1 Regul. Pap. Short Notes Rev. Pap.* **44**, 8269–8285 (2005).

21. Guo, Q., Zhou, C., Ma, Z. & Yang, X. Fundamentals of TiO2 Photocatalysis: Concepts, Mechanisms, and Challenges. *Adv. Mater.* **31**, 1–26 (2019).

22. Nakata, K. & Fujishima, A. TiO 2 photocatalysis: Design and applications. *J. Photochem. Photobiol. C Photochem. Rev.* **13**, 169–189 (2012).

23. Fujishima, A. & Honda, K. Electrochemical Photolysis of Water at a Semiconductor Electrode. *Nature* **238**, 37–38 (1972).

24. Carp, O., Huisman, C. L. & Reller, A. Photoinduced reactivity of titanium dioxide. *Prog. Solid State Chem.* **32**, 33–177 (2004).

25. Selcuk, S. & Selloni, A. Facet-dependent trapping and dynamics of excess electrons at anatase TiO2 surfaces and aqueous interfaces. **15**, (2016).

26. Luttrell, T. *et al.* Why is anatase a better photocatalyst than rutile? - Model studies on epitaxial TiO2 films. *Sci. Rep.* **4**, 1–8 (2015).

27. Kavan, L., Gra, M., Gilbert, S. E., Klemenz, C. & Scheel, H. J. Electrochemical and Photoelectrochemical Investigation of Single-Crystal Anatase. **650**, 6716–6723 (1996).

28. Chen, T. Checking the Synergetic E ff ect between Anatase and Rutile. (2019). doi:10.1021/acs.jpcc.9b03381

29. Siah, W. R., Lintang, H. O. & Shamsuddin, M. High photocatalytic activity of mixed anatase-rutile phases on commercial TiO 2 nanoparticles High photocatalytic activity of mixed anatase-rutile phases on commercial TiO 2 nanoparticles. (2016). doi:10.1088/1757-899X/107/1/012005

30. Chen, X. & Mao, S. S. Titanium Dioxide Nanomaterials : Synthesis , Properties , Modifications , and Applications. (2007).

31. D'Arienzo, M. *et al.* Photogenerated defects in shape-controlled TiO 2 anatase nanocrystals: A probe to evaluate the role of crystal facets in photocatalytic processes. *J. Am. Chem. Soc.* **133**, 17652–17661 (2011).

32. Tachikawa, T., Yamashita, S. & Majima, T. Evidence for crystal-face-dependent TiO2 photocatalysis from single-molecule imaging and kinetic analysis. *J. Am. Chem. Soc.* **133**, 7197–7204 (2011).

33. Meng, A., Zhang, J., Xu, D., Cheng, B. & Yu, J. Enhanced photocatalytic H2-production activity of anatase TiO2 nanosheet by selectively depositing dual-cocatalysts on (101) and (001) facets. *Appl. Catal. B Environ.* **198**, 286–294 (2016).

34. Ye, L., Mao, J., Peng, T., Zan, L. & Zhang, Y. Opposite photocatalytic activity orders of low-index facets of anatase TiO2 for liquid phase dye degradation and gaseous phase CO 2 photoreduction. *Phys. Chem. Chem. Phys.* **16**, 15675–15680 (2014).

35. Ren, L. *et al.* The pivotal effect of the interaction between reactant and anatase TiO2 nanosheets with exposed {001} facets on photocatalysis for the photocatalytic purification of VOCs. *Appl. Catal. B Environ.* **181**, 625–634 (2016).

36. Miao, R. *et al.* Applied Catalysis B : Environmental Mesoporous TiO 2 modified with carbon quantum dots as a high-performance visible light photocatalyst. *"Applied Catal. B, Environ.* **189**, 26–38 (2016).

37. Wang, Y. *et al.* Applied Surface Science The e ff ect of composite catalyst on Cu 2 O / TiO 2 heterojunction photocathodes for e ffi cient water splitting. **526**, (2020).

38. H. Lüth. *Solid Surfaces, Interfaces and Thin Films*.

39. Macmanus-driscoll, B. J. L. Self-Assembled Heteroepitaxial Oxide Nanocomposite Thin Film Structures : Designing Interface-Induced Functionality in Electronic Materials. 2035–2045 (2010).

doi:10.1002/adfm.201000373

40. Sci, J. V. Group III selenides : Controlling dimensionality , structure , and properties through defects and heteroepitaxial growth Group III selenides : Controlling dimensionality , structure , and properties through defects and heteroepitaxial growth. **020801**, (2021).

41. Tellekamp, M. B., Miller, M. K., Rice, A. D. & Tamboli, A. C. Heteroepitaxial ZnGeN 2 on AlN: Growth, Structure, and Optical Properties. 10–15 (2022). doi:10.1021/acs.cgd.1c01232

42. Bhalla, A. S., Guo, R. & Roy, R. The perovskite structure — a review of its role in ceramic science and technology The perovskite structure – a review of its role in ceramic science and technology. **8917**, (2016).

43. Aksel, E. & Jones, J. L. Advances in Lead-Free Piezoelectric Materials for Sensors and Actuators. 1935–1954 (2010). doi:10.3390/s100301935

44. Kubo, T. & Nozoye, H. Surface structure of SrTiO 3 (1 0 0). **542**, 177–191 (2003).

45. Radovi, M. *et al.* In situ investigation of the early stage of TiO2 epitaxy on (001) SrTiO3. *J. Chem. Phys.* **135**, 1–7 (2011).

46. Biswas, A. *et al.* Universal Ti-rich termination of atomically flat SrTiO3 (001), (110), and (111) surfaces. *Appl. Phys. Lett.* **98**, 51904 (2011).

47. Yusoff, N. H., Osman, R. A. M., Idris, M. S., Muhsen, K. N. D. K. & Nor, N. I. M. Dielectric and structural analysis of hexagonal and tetragonal phase BaTiO3. *AIP Conf. Proc.* **2203**, 20038 (2020).

48. Phys, J. A., Robinson, R. D. & Herman, I. P. Barium titanate nanocrystals and nanocrystal thin films : Synthesis , ferroelectricity , and dielectric properties. **034316**, (2017).

49. Niu, G. *et al.* Epitaxy of BaTiO3 thin film on Si(001) using a SrTiO3 buffer layer for non-volatile memory application. *Microelectron. Eng.* **88**, 1232–1235 (2011).

50. Posadas, A. B. *et al.* Thick BaTiO3 Epitaxial Films Integrated on Si by RF Sputtering for Electro-Optic Modulators in Si Photonics. *ACS Appl. Mater. Interfaces* **13**, 51230–51244 (2021).

51. Sharma, D. *et al.* Nanostructured BaTiO3/Cu2O heterojunction with improved photoelectrochemical activity for H2 evolution: Experimental and first-principles analysis. *Appl. Catal. B Environ.* **189**, 75–85 (2016).

52. Li, R., Li, Q., Zong, L., Wang, X. & Yang, J. BaTiO3/TiO2 heterostructure nanotube arrays for improved photoelectrochemical and photocatalytic activity. *Electrochim. Acta* **91**, 30–35 (2013).

53. J., C. K. *et al.* Enhancement of Ferroelectricity in Strained BaTiO3 Thin Films. *Science (80-.).* **306**, 1005–1009 (2004).

54. Merz, W. J. The electric and optical behavior of BaTiO3 single-domain crystals. *Phys. Rev.* **76**, 1221–1225 (1949).

55. Wang, N. *et al.* Structure, Performance, and Application of BiFeO3 Nanomaterials. *Nano-Micro Lett.* **12**, 81 (2020).

56. Catalan, G. & Scott, J. F. Physics and Applications of Bismuth Ferrite. *Adv. Mater.* **21**, 2463–2485 (2009).

57. Zavaliche, F. *et al.* Multiferroic BiFeO3 films: Domain structure and polarization dynamics. *Phase Transitions* **79**, 991–1017 (2006).

58. Lebeugle, D., Colson, D., Forget, A. & Viret, M. Very large spontaneous electric polarization in BiFe O3 single crystals at room temperature and its evolution under cycling fields. *Appl. Phys. Lett.* **91**, 10–13 (2007).

59. Phys, J. A. Polarization fatigue in ferroelectric thin films and related materials. **024101**, (2011).

60. Baek, S. *et al.* The Nature of Polarization Fatigue in BiFeO 3. doi:10.1002/adma.201003612

61. Choi, K. J., Biegalski, M., Li, Y. L., Sharan, A. & Schubert, J. Enhancement of Ferroelectricity in Strained BaTiO 3 Thin Films. 1005–1010 (2004).

62. Lyu, J., Fina, I., Solanas, R. & Fontcuberta, J. Tailoring Lattice Strain and Ferroelectric Polarization of Epitaxial BaTiO 3 Thin Films on Si (001). 1–10 (2018). doi:10.1038/s41598-017-18842-5

63. Daumont, C. *et al.* Strain dependence of polarization and piezoelectric response in epitaxial BiFeO 3 thin films. (2012). doi:10.1088/0953-8984/24/16/162202

64. Sun, F., Chen, D., Gao, X. & Liu, J. Emergent strain engineering of multiferroic BiFeO 3 thin fi lms. *J. Mater.* **7**, 281–294 (2021).

65. Venkata Ramana, E., Yang, S. M., Ranju, J. & JUng, M. H. Ferroelectric and magnetic properties of Fe- doped BaTiO 3 thin films grown by the pulsed laser deposition. **187219**, (2020).

66. Kharel, P. *et al.* Structural , magnetic , and electrical studies on polycrystalline transition-metal-doped BiFeO 3 thin films. (2009). doi:10.1088/0953-8984/21/3/036001

67. Phys, J. A. Decisive role of oxygen vacancy in ferroelectric versus ferromagnetic Mn-doped BaTiO 3 thin films. **084105**, (2017).

68. Fujioka, H. *Pulsed Laser Deposition (PLD)*. *Handbook of Crystal Growth: Thin Films and Epitaxy: Second Edition* **3**, (Elsevier B.V., 2015).

69. Asahi, H. & Horikoshi, Y. General Description of MBE. in *Molecular Beam Epitaxy: Materials and Applications for Electronics and Optoelectronics* 23–39 (2019). doi:10.1002/9781119354987.ch2

70. Nunn, W., Truttmann, T. K. & Jalan, B. A review of molecular-beam epitaxy of wide bandgap complex oxide semiconductors. *J. Mater. Res.* **36**, 4846–4864 (2021).

71. Tersoff, J. & Hamann, D. R. Theory of the scanning tunneling microscope. *Phys. Rev. B* **31**, 805–813 (1985).

72. Binnig, G. & Rohrer, H. In touch with atoms. *Rev. Mod. Phys.* **71**, S324--S330 (1999).

73. Binnig, G., Quate, C. F. & Gerber, C. Atomic Force Microscope. *Phys. Rev. Lett.* **56**, 930–933 (1986).

74. Michler, G. Scanning Electron Microscopy (SEM) BT - Electron Microscopy of Polymers. in (ed. Michler, G. H.) 87–120 (Springer Berlin Heidelberg, 2008). doi:10.1007/978-3-540-36352-1_5

75. Gleichmann, N. SEM vs TEM - Technology Networks. *Technol. Networks- Anal. Sep.* (2020).

76. Tang, C. Y. & Yang, Z. Chapter 8 - Transmission Electron Microscopy (TEM). in *Membrane Characterization* (eds. Hilal, N., Ismail, A. F., Matsuura, T. & Oatley-Radcliffe, D.) 145–159 (Elsevier, 2017). doi:https://doi.org/10.1016/B978-0-444-63776-5.00008-5

77. I, R. & Tweet, D. Reports on Progress in Physics Surface X-ray diffraction. (1992).

78. Feidenhans'l, R. . SURFACE STRUCTURE DETERMINATION BY X-RAY DIFFRACTION. *Surf. Sci. Rep.* **10**, 105–188 (1989).

79. Vlieg, E. {\it ROD}: a program for surface X-ray crystallography. *J. Appl. Crystallogr.* **33**, 401–405 (2000).

80. Nicklin, C., Arnold, T., Rawle, J. & Warne, A. Diamond beamline I07: A beamline for surface and interface diffraction. *J. Synchrotron Radiat.* **23**, 1245–1253 (2016).

81. Sant, R. Exploration par rayonnement synchrotron X de la croissance et de la structure de dichalcogénures 2D. *These Dr. Grenoble Alpes* (2019).

82. Niaz, M., Klassen, S., McMillan, B. & Metz, D. Reconstruction of the history of the photoelectric effect and its implications for general physics textbooks. *Sci. Educ.* **94**, 903–931 (2010).

83. Scofield, J. H. Theoretical photoionization cross sections from 1 to 1500 keV. **376**, (1973).

84. Seah, M. P. & Dench, W. A. Quantitative electron spectroscopy of surfaces: A standard data base for electron inelastic mean free paths in solids. *Surf. Interface Anal.* **1**, 2–11 (1979).

85. Tanuma, S., Powell, C. J. & Penn, D. R. Calculations of electron inelastic mean free paths (IMFPS). IV. Evaluation of calculated IMFPs and of the predictive IMFP formula TPP-2 for electron energies between 50 and 2000 eV. *Surf. Interface Anal.* **20**, 77–89 (1993).

86. Philippe, B. *et al.* Photoelectron Spectroscopy for Lithium Battery Interface Studies. *J. Electrochem. Soc.* **163**, A178–A191 (2016).

87. Szajman, J., Liesegang, J., Jenkin, J. G. & Leckey, R. C. G. Is there a universal mean-free-path curve for electron inelastic scattering in solids? *J. Electron Spectros. Relat. Phenomena* **23**, 97–102 (1981).

88. Descostes, M., Mercier, F., Thromat, N., Beaucaire, C. & Gautier-Soyer, M. Use of XPS in the determination of chemical environment and oxidation state of iron and sulfur samples: constitution of a data basis in binding energies for Fe and S reference compounds and applications to the evidence of surface species of an oxidized py. *Appl. Surf. Sci.* **165**, 288–302 (2000).

89. Lazarus, M. S. & Sham, T. K. X-ray photoelectron spectroscopy (XPS) studies of hydrogen reduced rutile (TiO2-x) surfaces. *Chem. Phys. Lett.* **92**, 670–674 (1982).

90. Leprince-Wang, Y. Study of the initial stages of TiO2 growth on Si wafers by XPS. *Surf. Coatings Technol.* **150**, 257–262 (2002).

91. Jagannathan, K., Srinivasan, A. & Rao, C. N. R. An XPS study of the surface oxidation states of metals in some oxide catalysts. *J. Catal.* **69**, 418–427 (1981).

92. Aziz, M. & Ismail, A. F. Chapter 5 - X-Ray Photoelectron Spectroscopy (XPS). in *Membrane Characterization* (eds. Hilal, N., Ismail, A. F., Matsuura, T. & Oatley-Radcliffe, D.) 81–93 (Elsevier, 2017). doi:https://doi.org/10.1016/B978-0-444-63776-5.00005-X

93. Stevie, F. A. & Donley, C. L. Introduction to x-ray photoelectron spectroscopy. *J. Vac. Sci. Technol. A* **38**, 63204 (2020).

94. Siegfried Hofmann. *Auger- and X-Ray Photoelectron Spectroscopy in Materials Science: A User-Oriented Guide*. (Springer Berlin Heidelberg, 2013).

95. Shirley, D. A. High-Resolution X-Ray Photoemission Spectrum of the Valence Bands of Gold. *Phys. Rev. B* **5**, 4709–4714 (1972).

96. Castle, J. E., Chapman-Kpodo, H., Proctor, A. & Salvi, A. M. Curve-fitting in XPS using extrinsic and intrinsic background structure. *J. Electron Spectros. Relat. Phenomena* **106**, 65–80 (2000).

97. Tougaard, S. Background removal in x-ray photoelectron spectroscopy: Relative importance of intrinsic and extrinsic processes. *Phys. Rev. B. Condens. Matter* **34**, 6779–6783 (1986).

98. Lun Pang, C., Lindsay, R. & Thornton, G. Chemical reactions on rutile TiO2(110). *Chem. Soc. Rev.* **37**, 2328–2353 (2008).

99. Mao, X. *et al.* Band-Gap States of TiO2(110): Major Contribution from Surface Defects. *J. Phys. Chem. Lett.* **4**, 3839–3844 (2013).

100. Yim, C. M., Pang, C. L. & Thornton, G. Oxygen Vacancy Origin of the Surface Band-Gap State of

TiO2 (110). *Phys. Rev. Lett.* **104**, 36806 (2010).

101. Henrich, V. E., Dresselhaus, G. & Zeiger, H. J. Observation of Two-Dimensional Phases Associated with Defect States on the Surface of TiO2. *Phys. Rev. Lett.* **36**, 1335–1339 (1976).

102. Schaub, R. *et al.* Oxygen Vacancies as Active Sites for Water Dissociation on Rutile TiO2 (110). *Phys. Rev. Lett.* **87**, 266104 (2001).

103. Deskins, N. A., Rousseau, R. & Dupuis, M. Defining the Role of Excess Electrons in the Surface Chemistry of TiO2. *J. Phys. Chem. C* **114**, 5891–5897 (2010).

104. Petrik, N. G. *et al.* Chemical Reactivity of Reduced TiO2(110): The Dominant Role of Surface Defects in Oxygen Chemisorption. *J. Phys. Chem. C* **113**, 12407–12411 (2009).

105. Finazzi, E., Di Valentin, C. & Pacchioni, G. Nature of Ti Interstitials in Reduced Bulk Anatase and Rutile TiO2. *J. Phys. Chem. C* **113**, 3382–3385 (2009).

106. Li, J., Lazzari, R., Chenot, S. & Jupille, J. Contributions of oxygen vacancies and titanium interstitials to band-gap states of reduced titania. *Phys. Rev. B* **97**, 41403 (2018).

107. Wendt, S. *et al.* The Role of Interstitial Sites in the Ti3d Defect State in the Band Gap of Titania. *Science (80-.).* **320**, 1755–1759 (2008).

108. Polack, F. *et al.* TEMPO: a New Insertion Device Beamline at SOLEIL for Time Resolved Photoelectron Spectroscopy Experiments on Solids and Interfaces. *AIP Conf. Proc.* **1234**, 185–188 (2010).

109. Rueff, J. P. *et al.* The GALAXIES beamline at the SOLEIL synchrotron: Inelastic X-ray scattering and photoelectron spectroscopy in the hard X-ray range. *J. Synchrotron Radiat.* **22**, 175–179 (2015).

110. Connell, J. G., Isaac, B. J., Ekanayake, G. B., Strachan, D. R. & Seo, S. S. A. thermal annealing procedure Preparation of atomically flat SrTiO 3 surfaces using a deionized-water leaching and thermal annealing procedure. **251607**, 10–13 (2016).

111. Tang, H., Prasad, K., Sanjinès, R., Schmid, P. E. & Lévy, F. Electrical and optical properties of TiO2 anatase thin films. *J. Appl. Phys.* **75**, 2042–2047 (1994).

112. Xu, M. *et al.* Photocatalytic Activity of Bulk TiO2 Anatase and Rutile Single Crystals Using Infrared Absorption Spectroscopy. *Phys. Rev. Lett.* **106**, 138302 (2011).

113. Herman, G. S. & Gao, Y. Growth of epitaxial anatase (001) and (101) films. *Thin Solid Films* **397**, 157–161 (2001).

114. Lazzeri, M., Vittadini, A. & Selloni, A. Structure and energetics of stoichiometric TiO2 anatase surfaces. *Phys. Rev. B* **63**, 155409 (2001).

115. Dzibrou, D., Grishin, A. M. & Kawasaki, H. Pulsed laser deposited TiO2 films: Tailoring optical properties. *Thin Solid Films* **516**, 8697–8701 (2008).

116. Hsieh, C. C. *et al.* Monophasic TiO2 films deposited on SrTiO3(100) by pulsed laser ablation. *J. Appl. Phys.* **92**, 2518–2523 (2002).

117. Long, H., Yang, G., Chen, A., Li, Y. & Lu, P. Growth and characteristics of laser deposited anatase and rutile TiO2 films on Si substrates. *Thin Solid Films* **517**, 745–749 (2008).

118. Choi, Y., Yamamoto, S., Umebayashi, T. & Yoshikawa, M. Fabrication and characterization of anatase TiO2 thin film on glass substrate grown by pulsed laser deposition. *Solid State Ionics* **172**, 105–108 (2004).

119. Howard, C. J., Sabine, T. M. & Dickson, F. Structural and thermal parameters for rutile and anatase. *Acta Crystallogr. Sect. B* **47**, 462–468 (1991).

120. Williamson, G. K. & Hall, W. H. X-ray line broadening from filed aluminium and wolfram. *Acta Metall.* **1**, 22–31 (1953).

121. Vera, M. L., Ares, A. E., Rosenberger, M. R., Lamas, D. G. & Schvezov, C. Determination using X-ray reflectometry of the TiO2 coating's thickness obtained by anodic oxidation. *An. AFA* **21**, (2009).

122. Huijben, I. A. M., Kool, W., Paulus, M. B. & Van Sloun, R. J. G. A Review of the Gumbel-max Trick and its Extensions for Discrete Stochasticity in Machine Learning. *IEEE Trans. Pattern Anal. Mach. Intell.* 1 (2022). doi:10.1109/TPAMI.2022.3157042

123. Syarif, D. G. *et al.* Preparation of anatase and rutile thin films by controlling oxygen partial pressure. *Appl. Surf. Sci.* **193**, 287–292 (2002).

124. Mathews, N. R., Morales, E. R., Cortés-Jacome, M. A. & Toledo Antonio, J. A. TiO2 thin films – Influence of annealing temperature on structural, optical and photocatalytic properties. *Sol. Energy* **83**, 1499–1508 (2009).

125. Horazdovsky, T., Drahokoupil, J., Jindra, J. & Vlcak, P. Crystallite size and microstrain evolution in low-temperature annealed titanium. *NANOCON Conf. Proc. - Int. Conf. Nanomater.* **2020**-**October**, 103–107 (2020).

126. Lin, C.-P., Chen, H., Nakaruk, A., Koshy, P. & Sorrell, C. C. Effect of Annealing Temperature on the Photocatalytic Activity of TiO2 Thin Films. *Energy Procedia* **34**, 627–636 (2013).

127. Sankar, S. & Gopchandran, K. G. Effect of annealing on the structural, electrical and optical properties of nanostructured TiO2 thin films. *Cryst. Res. Technol.* **44**, 989–994 (2009).

128. Hanaor, D. A. H. & Sorrell, C. C. Review of the anatase to rutile phase transformation. *J. Mater. Sci.* **46**, 855–874 (2011).

129. Dai, Y., Cobley, C. M., Zeng, J., Sun, Y. & Xia, Y. Synthesis of Anatase TiO2 Nanocrystals with Exposed {001} Facets. *Nano Lett.* **9**, 2455–2459 (2009).

130. Liu, S., Yu, J. & Jaroniec, M. Anatase TiO2 with Dominant High-Energy {001} Facets: Synthesis, Properties, and Applications. *Chem. Mater.* **23**, 4085–4093 (2011).

131. Ciancio, R. *et al.* Magnéli-like phases in epitaxial anatase TiO 2 thin films. *Phys. Rev. B - Condens. Matter Mater. Phys.* **86**, 1–6 (2012).

132. Knez, D. *et al.* Unveiling Oxygen Vacancy Superstructures in Reduced Anatase Thin Films. *Nano Lett.* **20**, 6444–6451 (2020).

133. Gallenberger, J. TiO2 (001)/STO (100) thin film growth and characterization. *ARL, Tech. Univ. Darmstadt* (2020).

134. Lazzeri, M. & Selloni, A. Stress-Driven Reconstruction of an Oxide Surface : The Anatase TiO 2 ˙ 001˚- ˙ 1 E 4˚Surface. 24–27 (2001). doi:10.1103/PhysRevLett.87.266105

135. Herman, G. S., Sievers, M. R. & Gao, Y. Structure Determination of the Two-Domain (1x4) anatase TiO2 (001) surface. *Phys. Rev. Lett.* **84**, 3354–3357 (2000).

136. Hengerer, R., Bolliger, B., Erbudak, M. & Grätzel, M. Structure and stability of the anatase TiO2 (101) and (001) surfaces. *Surf. Sci.* **460**, 162–169 (2000).

137. Babaei pour, M. & Ross, D. K. A determination of the variation in the lattice parameters of Bi2Sr2CaCu2O8+x (Bi-2212) as a function of temperature and oxygen content. *Phys. C Supercond.* **425**, 130–134 (2005).

138. Rudman, D. A. *et al.* Role of oxygen pressure during deposition on the microwave properties of YBCO films. *IEEE Trans. Appl. Supercond.* **9**, 2460–2464 (1999).

139. Zhang, Q. & Li, C. High Temperature Stable Anatase Phase Titanium Dioxide Films Synthesized by Mist Chemical Vapor Deposition. *Nanomater. (Basel, Switzerland)* **10**, (2020).

140. Du, Y. *et al.* In-situ imaging of the nucleation and growth of epitaxial anatase TiO2(001) films on SrTiO3(001). *Surf. Sci.* **606**, 1443–1449 (2012).

141. Liu, G. Q., Jin, Z. G., Liu, X. X., Wang, T. & Liu, Z. F. Anatase TiO2 porous thin films prepared by sol-gel method using CTAB surfactant. *J. Sol-Gel Sci. Technol.* **41**, 49–55 (2007).

142. Li, Z. *et al.* Enhancement of Interfacial Polarization in BaTiO3 Thin Films via Oxygen Inhomogeneity. *Adv. Electron. Mater.* **8**, 2100876 (2022).

143. Hernández, C. Surfaces with switchable catalytic activity in films by inversion of the ferroelectric polarization of the substrate. *TFM, UAB* (2017).

144. Karczewski, J., Riegel, B., Gazda, M., Jasinski, P. & Kusz, B. Electrical and structural properties of Nb-doped SrTiO3 ceramics. *J. Electroceramics* **24**, 326–330 (2010).

145. Karczewski, J. *et al.* Electrical properties of Y0.08Sr0.92Ti0.92Nb0.08 O3−δ after reduction in different reducing conditions. *J. Alloys Compd.* **473**, 496–499 (2009).

146. Mi, S. B. *et al.* Heterostructures of BaTiO3 bilayer films grown on SrTiO3 (001) under different oxygen pressures. *J. Cryst. Growth* **283**, 425–430 (2005).

147. Hiltunen, J., Seneviratne, D., Tuller, H. L., Lappalainen, J. & Lantto, V. Crystallographic and dielectric properties of highly oriented BaTiO3 films: Influence of oxygen pressure utilized during pulsed laser deposition. *J. Electroceramics* **22**, 395–404 (2009).

148. Chen, A. P. *et al.* Strong oxygen pressure dependence of ferroelectricity in BaTiO3/SrRuO3/SrTiO3 epitaxial heterostructures. *J. Appl. Phys.* **114**, 124101 (2013).

149. Shin, J., Kalinin, S. V, Borisevich, A. Y., Plummer, E. W. & Baddorf, A. P. Layer-by-layer and pseudo-two-dimensional growth modes for heteroepitaxial BaTiO3 films by exploiting kinetic limitations. *Appl. Phys. Lett.* **91**, 202901 (2007).

150. Behera, S. & Khare, A. Influence of substrate temperature and oxygen pressure on the structural and optical properties of polycrystalline BaTiO3 thin films grown by PLD. *Mater. Sci. Semicond. Process.* **140**, 106379 (2022).

151. Jones, C. W., Battle, P. D., Lightfoot, P. & Harrison, W. T. A. The structure of SrRuO${\sb 3}$ by time-of-flight neutron powder diffraction. *Acta Crystallogr. Sect. C* **45**, 365–367 (1989).

152. Koster, G. *et al.* Structure, physical properties, and applications of ${\mathrm{SrRuO}}_{3}$ thin films. *Rev. Mod. Phys.* **84**, 253–298 (2012).

153. Spasojevic, I., Sauthier, G., Caicedo, J. M., Verdaguer, A. & Domingo, N. Oxidation processes at the surface of BaTiO3 thin films under environmental conditions. *Appl. Surf. Sci.* **565**, 150288 (2021).

154. Tapfer, L. & Ploog, K. X-ray interference in ultrathin epitaxial layers: A versatile method for the structural analysis of single quantum wells and heterointerfaces. *Phys. Rev. B* **40**, 9802–9810 (1989).

155. Miller, A. M. *et al.* Extracting information from X-ray diffraction patterns containing Laue oscillations. *Zeitschrift für Naturforsch. B* **77**, 313–322 (2022).

156. Shu, X. *et al.* Role of Interfacial Orbital Hybridization in Spin-Orbit-Torque Generation in Pt-Based Heterostructures. *Phys. Rev. Appl.* **14**, 54056 (2020).

157. Xu, J. *et al.* Growth of uniform CaGe2 films by alternating layer molecular beam epitaxy. *J. Cryst. Growth* **460**, 134–138 (2017).

158. Lee, S. A. *et al.* Tuning electromagnetic properties of SrRuO3 epitaxial thin films via atomic control of cation vacancies. *Sci. Rep.* **7**, 1–7 (2017).

159. Lin, M. Z., Su, C. T., Yan, H. C. & Chern, M. Y. High-quality ZnO thin films grown by fast pulsed laser deposition without a buffer layer. *Japanese J. Appl. Physics, Part 2 Lett.* **44**, 995–997 (2005).

160. Choi, J., Eom, C. B., Rijnders, G., Rogalla, H. & Blank, D. H. A. Growth mode transition from layer by layer to step flow during the growth of heteroepitaxial SrRuO3 on (001) SrTiO3. *Appl. Phys. Lett.* **79**, 1447–1449 (2001).

161. Herranz, G. *et al.* Relevance of the 3D to 2D growth mode transition for the transport properties of nanometric SrRuO3 films. *Mater. Sci. Eng. B* **109**, 221–225 (2004).

162. Chae, R. H., Rao, R. A., Gan, Q. & Eom, C. B. Initial Stage Nucleation and Growth of Epitaxial SrRuO3 Thin Films on (0 0 1) SrTiO3 Substrates. *J. Electroceramics* **4**, 345–349 (2000).

163. Bachelet, R. *et al.* Self-Assembly of SrTiO3(001) Chemical-Terminations: A Route for Oxide-Nanostructure Fabrication by Selective Growth. *Chem. Mater.* **21**, 2494–2498 (2009).

164. Chopdekar, R. V, Takamura, Y. & Suzuki, Y. Disorder-induced carrier localization in ultrathin strained SrRuO3 epitaxial films. *J. Appl. Phys.* **99**, 08F503 (2006).

165. Osbourn, G. C. Material Properties of Semiconductor Strained-Layer Superlattices. *MRS Proc.* **25**, 455 (1983).

166. Panish, M. B. & Temkin, H. 3 - Gas-Source Molecular Beam Epitaxy: GaxIn1−xAs1-yPy/InP MBE with Non-elemental Sources. Heterostructures and Device Properties. in *Molecular Beam Epitaxy* (ed. Farrow, R. F. C.) 275–343 (William Andrew Publishing, 1995). doi:https://doi.org/10.1016/B978-081551371-1.50005-6

167. Speck, J. S. & Pompe, W. Domain configurations due to multiple misfit relaxation mechanisms in epitaxial ferroelectric thin films. I. Theory. *J. Appl. Phys.* **76**, 466–476 (1994).

168. Zhao, T., Chen, F., Lu, H., Yang, G. & Chen, Z. Thickness and oxygen pressure dependent structural characteristics of BaTiO3 thin films grown by laser molecular beam epitaxy. *J. Appl. Phys.* **87**, 7442–7447 (2000).

169. Havelia, S., Wang, S., Skowronski, M. & Salvador, P. A. Controlling the Bi content, phase formation, and epitaxial nature of BiMnO3 thin films fabricated using conventional pulsed laser deposition, hybrid pulsed laser deposition, and solid state epitaxy. *J. Appl. Phys.* **106**, 123509 (2009).

170. Béa, H. *et al.* Investigation on the origin of the magnetic moment of BiFeO3 thin films by advanced x-ray characterizations. *Phys. Rev. B* **74**, 20101 (2006).

171. Jiang, Z.-Z. *et al.* Epitaxial growth of BiFeO3 films on SrRuO3/SrTiO3. *Mater. Charact.* **131**, 217–223 (2017).

172. Chen, Z. *et al.* Study of strain effect on in-plane polarization in epitaxial BiFeO3 thin films using planar electrodes. *Phys. Rev. B* **86**, 235125 (2012).

173. You, L., Chua, N. T., Yao, K., Chen, L. & Wang, J. Influence of oxygen pressure on the ferroelectric properties of epitaxial BiFeO3 thin films by pulsed laser deposition. *Phys. Rev. B* **80**, 24105 (2009).

174. Wang, J. *et al.* Epitaxial $BiFeO_3$ Multiferroic Thin Film Heterostructures. *Science (80-.).* **299**, 1719–1722 (2003).

175. Jeon, J. H. *et al.* Selector-free resistive switching memory cell based on BiFeO3 nano-island showing high resistance ratio and nonlinearity factor. *Sci. Rep.* **6**, 23299 (2016).

176. Sun, F. *et al.* Phase transitions in BiFeO3 nanoislands with enhanced electromechanical

response. *Ceram. Int.* **44**, 21725–21729 (2018).

177. Ma, J. *et al.* Controllable conductive readout in self-assembled, topologically confined ferroelectric domain walls. *Nat. Nanotechnol.* **13**, 947–952 (2018).

178. Ma, J. *et al.* Geometry confined polar vertex domains in self-assembled BiFeO3 nano-islands. *Mater. Res. Lett.* **7**, 399–404 (2019).

179. Catalan, G., Schilling, A., Scott, J. F. & Gregg, J. M. Domains in three-dimensional ferroelectric nanostructures: theory and experiment. *J. Phys. Condens. Matter* **19**, 132201 (2007).

180. Schilling, A. *et al.* Domains in Ferroelectric Nanodots. *Nano Lett.* **9**, 3359–3364 (2009).

181. Peng, R.-C. *et al.* Understanding and predicting geometrical constraint ferroelectric charged domain walls in a BiFeO3 island via phase-field simulations. *Appl. Phys. Lett.* **113**, 222902 (2018).

182. Palai, R. *et al.* β phase and γ -β metal-insulator transition in multiferroic BiFeO3. *Phys. Rev. B* **77**, 14110 (2008).

183. Schneider, J. *et al.* Understanding TiO2 Photocatalysis: Mechanisms and Materials. *Chem. Rev.* **114**, 9919–9986 (2014).

184. Kleibeuker, J. E. *et al.* Structure of singly terminated polar DyScO${}_{3}$ (110) surfaces. *Phys. Rev. B* **85**, 165413 (2012).

185. Luo, Z. *et al.* Crystalline Mixed Phase (Anatase/Rutile) Mesoporous Titanium Dioxides for Visible Light Photocatalytic Activity. *Chem. Mater.* **27**, 6–17 (2015).

186. Wei, Y. *et al.* Quantum dynamics origin of high photocatalytic activity of mixed-phase anatase/rutile TiO2. *J. Chem. Phys.* **153**, 44706 (2020).

187. Li, G., Chen, L., Graham, M. E. & Gray, K. A. A comparison of mixed phase titania photocatalysts prepared by physical and chemical methods: The importance of the solid–solid interface. *J. Mol. Catal. A Chem.* **275**, 30–35 (2007).

188. Ohno, T., Tokieda, K., Higashida, S. & Matsumura, M. Synergism between rutile and anatase TiO2 particles in photocatalytic oxidation of naphthalene. *Appl. Catal. A Gen.* **244**, 383–391 (2003).

189. Kitazawa, S., Choi, Y., Yamamoto, S. & Yamaki, T. Rutile and anatase mixed crystal TiO2 thin films prepared by pulsed laser deposition. *Thin Solid Films* **515**, 1901–1904 (2006).

190. Henderson, M. A. A surface science perspective on TiO2 photocatalysis. *Surf. Sci. Rep.* **66**, 185–297 (2011).

191. Fujishima, A., Zhang, X. & Tryk, D. A. TiO2 photocatalysis and related surface phenomena. *Surf. Sci. Rep.* **63**, 515–582 (2008).

192. Gong, X.-Q. & Selloni, A. Reactivity of Anatase TiO2 Nanoparticles: The Role of the Minority (001) Surface. *J. Phys. Chem. B* **109**, 19560–19562 (2005).

193. Vittadini, A., Casarin, M. & Selloni, A. Chemistry of and on TiO2-anatase surfaces by DFT calculations: a partial review. *Theor. Chem. Acc.* **117**, 663–671 (2007).

194. De Angelis, F., Vitillaro, G., Kavan, L., Nazeeruddin, M. K. & Grätzel, M. Modeling Ruthenium-Dye-Sensitized TiO2 Surfaces Exposing the (001) or (101) Faces: A First-Principles Investigation. *J. Phys. Chem. C* **116**, 18124–18131 (2012).

195. Zhang, D., Li, G., Yang, X. & Yu, J. C. A micrometer-size TiO2 single-crystal photocatalyst with remarkable 80% level of reactive facets. *Chem. Commun.* 4381–4383 (2009). doi:10.1039/B907963G

196. Liu, J. *et al.* Quantitative Analysis of the Morphology of {101} and {001} Faceted Anatase TiO2 Nanocrystals and Its Implication on Photocatalytic Activity. *Chem. Mater.* **29**, 5591–5604 (2017).

197. Pan, J., Liu, G., Lu, G. Q. (Max) & Cheng, H.-M. On the True Photoreactivity Order of {001}, {010}, and {101} Facets of Anatase TiO2 Crystals. *Angew. Chemie Int. Ed.* **50**, 2133–2137 (2011).

198. Liang, Y., Gan, S., Chambers, S. A. & Altman, E. I. Surface structure of anatase TiO2 Reconstruction, atomic steps, and domains. *Phys. Rev. B* **63**, 235402 (2001).

199. Vlieg, E. Integrated Intensities Using a Six-Circle Surface X-ray Diffractometer. *J. Appl. Crystallogr.* **30**, 532–543 (1997).

200. Coppens, P., Cox, D., Vlieg, E., Robinson, I. K. & Paufler, P. Synchrotron Radiation Crystallography. Academic Press, London-San Diego-New York-Boston-Sydney-Tokyo-Toronto 1992. 316 p. $ 97.00. ISBN 0-12-188080-X. *Cryst. Res. Technol.* **28**, K10–K10 (1993).

201. Stout, G. H. & Jensen, L. H. *X-Ray Structure Determination*. (Macmillan Publishing Co., Inc., New York, 1968).

202. Kwei, G. H., Lawson, A. C., Billinge, S. J. L. & Cheong, S. W. Structures of the ferroelectric phases of barium titanate. *J. Phys. Chem.* **97**, 2368–2377 (1993).

203. Robinson, I. K. Crystal truncation rods and surface roughness. *Phys. Rev. B* **33**, 3830–3836 (1986).

204. Gao, L., Gan, W., Xiao, S., Zhan, X. & Li, J. Enhancement of photo-catalytic degradation of formaldehyde through loading anatase TiO2 and silver nanoparticle films on wood substrates. *RSC Adv.* **5**, 52985–52992 (2015).

205. Mamaghani, A. H., Haghighat, F. & Lee, C.-S. Photocatalytic oxidation of MEK over hierarchical TiO2 catalysts: Effect of photocatalyst features and operating conditions. *Appl. Catal. B Environ.* **251**, 1–16 (2019).

206. Bashir, S., Wahab, A. K. & Idriss, H. Synergism and photocatalytic water splitting to hydrogen over M/TiO2 catalysts: Effect of initial particle size of TiO2. *Catal. Today* **240**, 242–247 (2015).

207. Buck, A. L. New Equations for Computing Vapor Pressure and Enhancement Factor. *J. Appl. Meteorol. Climatol.* **20**, 1527–1532 (1981).

208. Ketteler, G. *et al.* The Nature of Water Nucleation Sites on TiO2(110) Surfaces Revealed by Ambient Pressure X-ray Photoelectron Spectroscopy. *J. Phys. Chem. C* **111**, 8278–8282 (2007).

209. Tissot, H. *et al.* Cation Depth-Distribution at Alkali Halide Aqueous Solution Surfaces. *J. Phys. Chem. C* **119**, 9253–9259 (2015).

210. Karslıoğlu, O. *et al.* Aqueous solution/metal interfaces investigated in operando by photoelectron spectroscopy. *Faraday Discuss.* **180**, 35–53 (2015).

211. Stefanov, P. *et al.* XPS characterization of TiO2 layers deposited on quartz plates. *J. Phys. Conf. Ser.* **100**, 12039 (2008).

212. Wang, Y. *et al.* Role of point defects on the reactivity of reconstructed anatase titanium dioxide (001) surface. *Nat. Commun.* **4**, 2214 (2013).

213. Zhu, L. *et al.* Ligand-free rutile and anatase TiO2 nanocrystals as electron extraction layers for high performance inverted polymer solar cells. *RSC Adv.* **7**, 20084–20092 (2017).

214. Xie, C., Yang, S., Shi, J. & Niu, C. Highly Crystallized C-Doped Mesoporous Anatase TiO2 with Visible Light Photocatalytic Activity. *Catalysts* **6**, (2016).

215. Yasuhisa, T., Shik, S., Takayuki, U. & Akio, K. Ti 2p-, Ti 3p- and O 1s-Resonant Photoemission Studies of Ti 2O 3. *J. Phys. Soc. Japan* **66**, 3153–3158 (1997).

216. Chermette, H., Pertosa, P. & Michel-Calendini, F. M. Molecular orbital study of satellites in XPS spwctra of BaTiO3 and TiO2. *Chem. Phys. Lett.* **69**, 240–245 (1980).

217. Krishnan, P. *et al.* Characterization of photocatalytic TiO2 powder under varied environments using near ambient pressure X-ray photoelectron spectroscopy. *Sci. Rep.* **7**, 43298 (2017).

218. Zhang, Z. *et al.* Water as a Catalyst: Imaging Reactions of O2 with Partially and Fully Hydroxylated TiO2(110) Surfaces. *J. Phys. Chem. C* **113**, 1908–1916 (2009).

219. Henderson, M. A., Epling, W. S., Perkins, C. L., Peden, C. H. F. & Diebold, U. Interaction of Molecular Oxygen with the Vacuum-Annealed TiO2(110) Surface: Molecular and Dissociative Channels. *J. Phys. Chem. B* **103**, 5328–5337 (1999).

220. Bigi, C. *et al.* Distinct behavior of localized and delocalized carriers in anatase ${\mathrm{TiO}}_{2}$ (001) during reaction with ${\mathrm{O}}_{2}$. *Phys. Rev. Mater.* **4**, 25801 (2020).

221. Yamamoto, S. *et al.* In situ x-ray photoelectron spectroscopy studies of water on metals and oxides at ambient conditions. *J. Phys. Condens. Matter* **20**, 184025 (2008).

222. Wendt, S. *et al.* Formation and Splitting of Paired Hydroxyl Groups on Reduced TiO2 (110). *Phys. Rev. Lett.* **96**, 66107 (2006).

223. Comini, N., Huthwelker, T., Diulus, J. T., Osterwalder, J. & Novotny, Z. Factors influencing surface carbon contamination in ambient-pressure x-ray photoelectron spectroscopy experiments. *J. Vac. Sci. Technol. A* **39**, 43203 (2021).

224. Walle, L. E. *et al.* Mixed Dissociative and Molecular Water Adsorption on Anatase TiO2(101). *J. Phys. Chem. C* **115**, 9545–9550 (2011).

225. Cumpson, P. J. & Seah, M. P. Elastic Scattering Corrections in AES and XPS. II. Estimating Attenuation Lengths and Conditions Required for their Valid Use in Overlayer/Substrate Experiments. *Surf. Interface Anal.* **25**, 430–446 (1997).

226. Henderson, M. A. The interaction of water with solid surfaces: fundamental aspects revisited. *Surf. Sci. Rep.* **46**, 1–308 (2002).

227. Brookes, I. M., Muryn, C. A. & Thornton, G. Imaging Water Dissociation on ${\mathrm{TiO}}_{2}(110)$. *Phys. Rev. Lett.* **87**, 266103 (2001).

228. Kurtz, R. L., Stock-Bauer, R., Msdey, T. E., Román, E. & De Segovia, J. Synchrotron radiation studies of H2O adsorption on TiO2(110). *Surf. Sci.* **218**, 178–200 (1989).

229. Wen, B., Zhang, L., Wang, D. & Lang, X. The distribution of excess carriers and their effects on water dissociation on rutile (110) surface. *Comput. Mater. Sci.* **136**, 150–156 (2017).

230. Xiong, L.-B., Li, J.-L., Yang, B. & Yu, Y. Ti^{3+} in the surface of titanium dioxide: generation, properties and photocatalytic application *J. Nanomater.* **2012**, 831524 (2012).

231. Guillemot, F., Porté, M. C., Labrugère, C. & Baquey, C. Ti^{4+} to Ti^{3+} Conversion of TiO_2 Uppermost Layer by Low-Temperature Vacuum Annealing: Interest for Titanium Biomedical Applications. *J. Colloid Interface Sci.* **255**, 75–78 (2002).

232. Hugenschmidt, M. B., Gamble, L. & Campbell, C. T. The interaction of H_2O with a TiO_2(110) surface. *Surf. Sci.* **302**, 329–340 (1994).

233. Silversmit, G., De Doncker, G. & De Gryse, R. A Mineral TiO_2(001) Anatase Crystal Examined by XPS. *Surf. Sci. Spectra* **9**, 21–29 (2002).

234. Wang, Z., Xiong, F., Sun, G., Jin, Y. & Huang, W. Structural Dependence of Competitive Adsorption of Water and Methanol on TiO_2 Surfaces. *Chinese J. Chem.* **35**, 889–895 (2017).

235. Thomas, A. G. *et al.* Resonant photoemission of anataseTiO_2 (101) and (001) single crystals. *Phys. Rev. B* **67**, 35110 (2003).